# Investigation of the network's robustness upon a single-neuron perturbation

Von der Fakultät für Mathematik und Naturwissenschaften der RWTH Aachen University zur Erlangung des akademischen Grades einer Doktorin der Naturwissenschaften genehmigte Dissertation

vorgelegt von

*Bogdana Cepkenovic, M.Sc.*

aus

*Pristina, Serbien*

Berichter*:* *Prof. Dr. Andreas Offenhäusser*

*Prof. Dr. Marc Spehr*

Tag der mündlichen Prüfung*:* *18.02.2025*

# Abstract

One central goal of current neuroscience is to accurately detect communities of physically and functionally coupled neurons in neuronal networks. Due to the reduced amplitude resolution of the network readouts, connectivity mapping is often restricted to statistical inferences from spontaneous activity, which are confounded by the context in which the activity is observed. Accurate connectivity mapping demands methodology advances and their evaluations, as well as probing experimental approaches other than observational. This work aimed to identify which information about the connectome could be reliably extracted from the current readouts and whether a single-neuron perturbation evokes network-level responses that mark the interconnected neurons.

Chapter 4 addresses how accurately novel 2D+ electrodes convey information about the signal source and network activity. Paired electrophysiology revealed a pronounced variation of the same neuron's extracellular waveforms, resulting in erroneous identifications of detected signal sources. While intracellular waveform variations contributed to the variability of 2D+ electrode signals, an additional contributing factor originated from inconsistencies in the signal transfer. The changes in the transfer function were reversible, occurred at a second timescale, and indicated a physically grounded contribution. Unlike the population-level metrics, pairwise correlation was particularly sensitive to misclassifications. Chapter 4 concludes with analytical challenges in high amplitude records and offers solutions at the spike-sorting curation step.

Chapter 5 evaluates the consistency and context dependence of the calcium-firing code relation in population-level readouts. Benchmarking of the calcium signals by patch-clamp demonstrated that the calcium trace reliably predicts membrane depolarizing events. Accordingly, network synchrony events associated with strong depolarizations were the most reliably detected via calcium imaging. However, detecting isolated firing events was less consistent and depended on the magnitude of firing-evoking membrane depolarizations. The findings inform current firing prediction models about the single-cell short-term translation inconsistencies and position membrane depolarization predictions as the first step toward accurate firing activity inferences from calcium imaging studies.

Chapter 6 investigated the feasibility of topology mapping via single-neuron perturbation. Calcium imaging during the giga-seal patch-clamp revealed that a single-neuron deformation induces calcium influxes in the target that persist through the neurites and propagate to coupled neurons. Calcium influxes were via mechanosensitive ion channels, were further potentiated by L-type calcium voltage-gated channels, and evoked slow membrane depolarizations capable of inducing firing in the target and surrounding neurons. Unlike the single-neuron electrical stimulation, giga-sealing produced robust calcium responses that propagated further in the network and excited the responding ensemble. The findings suggest that targeted deformation of neurons may be a promising approach for the broad mapping of neuronal communities and inform about a biological component to the spatial resolution reduction in deformations. Finally, the potentiation of the responding ensemble following giga-seal informs the optimal time window for reliable activity sampling using patch-clamp.

# Zusammenfassung

Ein zentrales Ziel der aktuellen Neurowissenschaft ist die genaue Erkennung von Gemeinschaften physisch und funktionell gekoppelter Neuronen in neuronalen Netzwerken. Aufgrund der reduzierten Amplitudenauflösung der Netzwerkauslesungen ist die Konnektivitätskartierung häufig auf statistische Schlussfolgerungen aus spontaner Aktivität beschränkt, die durch den Kontext, in dem die Aktivität beobachtet wird, verfälscht werden. Eine genaue Konnektivitätskartierung erfordert methodische Fortschritte und deren Auswertung sowie die Untersuchung anderer experimenteller Ansätze als der Beobachtung. Ziel dieser Arbeit war es, herauszufinden, welche Informationen über das Konnektom zuverlässig aus den aktuellen Auslesungen extrahiert werden konnten und ob eine Störung eines einzelnen Neurons Reaktionen auf Netzwerkebene hervorruft, die die miteinander verbundenen Neuronen kennzeichnen.

Kapitel 4 befasst sich damit, wie genau neuartige 2D+-Elektroden Informationen über die Signalquelle und die Netzwerkaktivität übermitteln. Die gepaarte Elektrophysiologie ergab eine ausgeprägte Variation der extrazellulären Wellenformen desselben Neurons, was zu fehlerhaften Identifizierungen der erkannten Signalquellen führte. Während intrazelluläre Wellenformvariationen zur Variabilität der 2D+-Elektrodensignale beitrugen, ergab sich ein zusätzlicher beitragender Faktor aus Inkonsistenzen bei der Signalübertragung. Die Änderungen in der Übertragungsfunktion waren reversibel, traten in einer zweiten Zeitskala auf und zeigten einen physikalisch begründeten Beitrag. Im Gegensatz zu den Metriken auf Populationsebene war die paarweise Korrelation besonders empfindlich gegenüber Fehlklassifizierungen. Kapitel 4 schließt mit analytischen Herausforderungen bei Aufzeichnungen mit hoher Amplitude und bietet Lösungen für den Schritt der Spike-Sortierung.

Kapitel 5 bewertet die Konsistenz und Kontextabhängigkeit der Kalzium-Zündungscode-Beziehung in Populationsebenen-Auslesungen. Das Benchmarking der Kalziumsignale mittels Patch-Clamp zeigte, dass die Kalziumspur Membrandepolarisationsereignisse zuverlässig vorhersagt. Dementsprechend wurden Netzwerksynchronisationsereignisse, die mit starken Depolarisationen verbunden sind, am zuverlässigsten durch Kalziumbildgebung erkannt. Die Erkennung isolierter Zündungsereignisse war jedoch weniger konsistent und hing von der Stärke der zündungsauslösenden Membrandepolarisationen ab. Die Ergebnisse informieren aktuelle Zündungsvorhersagemodelle über die kurzfristigen Translationsinkonsistenzen einzelner Zellen und positionieren Membrandepolarisationsvorhersagen als ersten Schritt hin zu genauen Zündungsaktivitätsrückschlüssen aus Kalziumbildgebungsstudien.

Kapitel 6 untersuchte die Machbarkeit der Topologiekartierung durch Einzelneuronstörung. Die Kalziumbildgebung während des Giga-Seal-Patch-Clamp-Verfahrens zeigte, dass eine Deformation einzelner Neuronen Kalziumeinflüsse im Ziel induziert, die durch die Neuriten hindurch andauern und sich zu gekoppelten Neuronen ausbreiten. Die Kalziumeinflüsse erfolgten über mechanosensitive Ionenkanäle, wurden durch spannungsgesteuerte L-Typ-Kalziumkanäle weiter verstärkt und riefen langsame Membrandepolarisationen hervor, die Aktionspotentiale im Ziel und in den umliegenden Neuronen auslösen konnten. Anders als die

elektrische Stimulation einzelner Neuronen erzeugte das Giga-Sealing robuste Kalziumreaktionen, die sich weiter im Netzwerk ausbreiteten und das reagierende Ensemble erregten. Die Ergebnisse legen nahe, dass die gezielte Deformation von Neuronen ein vielversprechender Ansatz für die umfassende Kartierung neuronaler Gemeinschaften sein könnte, und geben Aufschluss über eine biologische Komponente der Verringerung der räumlichen Auflösung bei Deformationen. Schließlich gibt die Verstärkung des reagierenden Ensembles für weitere Eingaben nach dem Giga-Seal Aufschluss über das optimale Zeitfenster für eine zuverlässige Aktivitätsabtastung mittels Patch-Clamp-Verfahren.

# Table of Contents

# 1. Introduction

Understanding how networks of neurons compute information is a central goal in neuroscience, as it is crucial for understanding and modulating brain function. While the network activity can be reliably correlated to behavior only by observing or modulating the brain activity in animals, the underlying principles of the neuronal network function and organization have been consistently explored under highly controlled conditions in simpler *in vitro* set-ups.[1-4] One such principle is the network's modularity, the existence of neuron sub-populations that co-activate spontaneously or during a particular task (syn. neuronal ensembles).[5-10] In behaving animals, groups of co-activated neurons correlate with visual tasks, learning and memory,[8, 9] while their disruption is associated with neurodegenerative diseases.[8] *In vitro*, network modules reduce the processing cost by running computations in parallel.[1, 11, 12]

The advances in electrophysiology and optogenetics allowed the screening and manipulation of many neurons at a time. These revealed the key ensemble properties, such as pattern completion and separation,[9] and allowed ensemble-wide manipulations by stimulating only a few cells to imprint new activity patterns and even memories.[9] While the previous studies identified the key ensemble properties, the underlying cellular and circuit principles of ensemble establishment, maturation, and functional dynamics are yet to be fully elucidated. For instance, the mechanisms governing the ensemble establishment and maturation are associated with synaptic plasticity processes,[9, 13] yet the very definition of neuronal ensembles does not require direct connections between the members, as long as they co-activate (Fig. 1A).[5, 9, 14] Such definition arises from methodological limitations in connection mapping from population-level readout, which requires accurate detection of post-synaptic potentials (PSPs), as post-synaptic neurons do not always fire an action potential (AP) upon the stimulus receipt.[15-17]

The multi-cell electrophysiology and functional imaging lack the amplitude resolution required for PSP detection, which is currently achieved only by short-term and few-cells focused intracellular electrophysiology.[15-17] Therefore, network readout strategies are not in capacity to estimate causal relations from spontaneous activity. The ensemble mapping thus focuses on identifying the connected neurons from correlations of their spontaneous activity, under the assumption that more correlated neurons are more likely to be connected (Fig. 1A).[18] However, estimating functional connections from correlations is context-dependent, as network-level synchronizations also recruit non-directly connected neurons.[14] The discrepancy between the physical and functional connections may not only confound identification of ensembles, which is relevant for tracking their origin and dynamics, but also limits the understanding of fundamental mechanisms driving the network's functional organization. An alternative to correlative estimates is observing the network's responses upon the network perturbation. When the stimulus is focused on a single neuron, tracking the neighbor's responses time-locked to the stimulus provides an additional bound to discern the coupled neurons' signals.[19-21] The active readout also engages all coupled neurons, unlike the spontaneous activity mapping which reports

only about the neurons active during the recording session.[22] Indeed, previous single-neuron perturbation paradigms produced detectable responses across the neuronal ensemble. Yet, single-neuron electrical and optogenetic stimulation combined with functional imaging could only map the connections directed from the excitatory target.[20] Even in active connectivity sampling paradigm, the amplitude resolution of the network readout and strength of the output connections dictate the sensitivity of detected output connections. It remains to be elucidated if a different single-neuron stimulation modality could produce more robust responses in the coupled neurons, independently of the connection directionality or the target neuron's type.

This work aimed to identify which information about the network activity and neuronal connectivity could be reliably extracted with the current network readout, and whether the network's sensitivity to a single-neuron stimulation suffices for accurate mapping of the neuronal ensembles (Fig. 1B). I explored the responses of 2D *in vitro* networks of cortical neurons to single-neuron perturbations. Despite lacking the genetically and developmentally defined brain's organization, these networks are self-organizing systems,[11, 23, 24] which makes them a good approximation for tackling fundamental neuroscientific questions in the context of the networks' emergent properties, such as: "*What would happen to the in vitro network if a single neuron is perturbed*?". Besides addressing the ensemble mapping strategies, investigating this question is also relevant for informing the current random network models about the extent of the network's sensitivity to perturbing the basic computational unit.

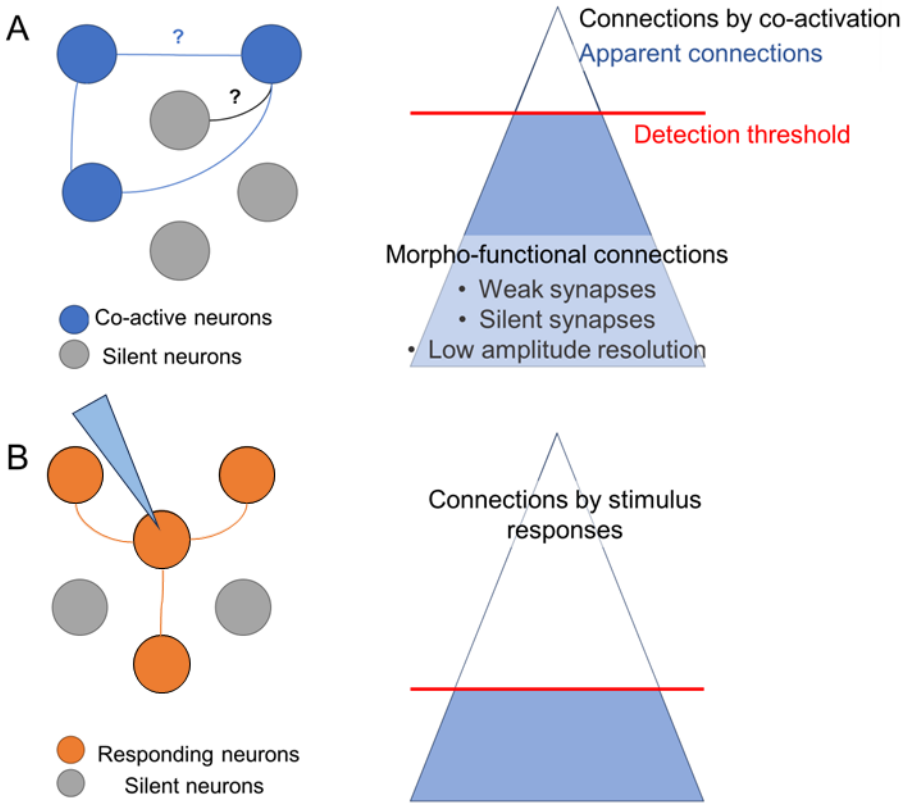

**Figure 1. Single-neuron perturbation to reconcile observed and physical connectivity.** A. Challenges with connectivity inferences from observing the network activity. Left: Neuronal ensemble defined from co-activation; blue denotes correlated, putatively connected neurons; gray denotes neurons with below-threshold activity, or their detected activity did not sufficiently correlate to be included. Right: the iceberg analogy of physical connection mapping under the restrictions of current broad-network activity screening. Neurons whose above-threshold activity correlates enough are defined as functionally connected, yet the correlation is also context-defined (blue question mark). Neurons that are physically connected by weak or silent synapses are not a part of ensemble. B. Stimulating single neurons for accurate connectivity estimates and neuronal ensemble mapping. The goal of this study was to investigate if a single-neuron perturbation can produce visible excitation that propagates through the network of interconnected neurons**.**

Electrophysiology is extensively used to measure APs directly and at fast sampling rates. Intracellular electrophysiology, such as whole-cell patch-clamp, allows accurate and targeted detection of synaptic connections due to a high signal-to-noise ratio (SNR), yet it is short-term and focuses on a few cells at a time. Microelectrode arrays (MEAs) are viable alternative for long-term, high-throughput readout, as the neurons could be grown over the electrodes and measured over days. However, a weak neuron-electrode interface reduces the amplitude sensitivity.[25] In turn, signal attenuation limits the connectivity estimates to correlative, while spike omission from low SNR reduces the accuracy of correlative estimates. Recent bioelectronics advances, including nanostraw-nanocavity (NS-NC) MEAs,[26, 27] surmount this challenge by increasing the SNR through an improved neuron-electrode interface. Chapter 4 characterizes the signal coupling and demonstrates subthreshold resolution of NS-NC MEAs. Nevertheless, MEA electrodes measure non-targeted, and signals detected from a given electrode may originate from multiple sources or *vice versa* if the electrode density allows. Identifying the exact numbers of coupled neurons and each neuron's firing sequences is a pre-requisite for reliable ensemble mapping and network activity inferences, and spike sorting is used to assign the signals to their respective source based on waveform similarity.[28] Current spike sorting pipelines are trained and optimized for low SNR measurements,[29, 30] and the challenges that come with improved SNR are yet to be identified. Given the advantages of high SNR measurements, I benchmarked several current spike sorting pipelines and investigated the underlying sources of the spike sorting errors. The inaccuracies of spike sorting approaches in high SNR measurements, the intrinsic causes of such errors, and their effect on the network connectivity estimates are examined in Chapter 4.

Calcium imaging accurately determines the signal source identity, but reports attenuated, low-pass filtered, and non-linear estimates of internal calcium increases correlating with the neuronal firing.[31-33] The current model proposes a direct and causal relation between calcium fluorescence and neuronal firing, with calcium influx from AP-activated voltage-gated calcium channels regarded as the primary source of calcium signal.[31] The primary goal of functional imaging is to accurately estimate the firing sequence from the fluorescence trace.[34, 35] Several algorithms built to translate the calcium-related fluorescence into the firing code fail to generalize across the unseen datasets, requiring some extent of calibration to the benchmarked datasets or producing the own ground truth. While most prediction inaccuracies could be

attributed to technical differences in optical set-ups and reporters used, recent findings indicate a biological component contributing to inaccurate firing code predictions. For example, the low SNR calcium traces in broad-network calcium imaging showed a surprisingly low sensitivity to isolated APs and inconsistent AP sensitivity within a single neuron, which occurred in short time scales.[36] In Chapter 5., I evaluated how reliably the calcium signal translates into the membrane events and how the context, in synchrony-induced simultaneous inputs, shapes this relation beyond the AP-evoked calcium influxes.

Chapter 6 investigates whether a single-neuron perturbation evokes visible events within the connected community to accurately map neuronal ensembles. While it was previously shown that the single-neuron electrical stimulation effectively maps the strong output connections from excitatory neurons, exploring the network's responses to single-neuron stimulation by alternative modalities could be highly beneficial in mapping connected neurons regardless of synapse directionality, synaptic strength, or the type of target. Among the alternative stimulation modalities, mechanical perturbation is attractive for its non-invasiveness[37] and reliability with which it evokes detectable excitation in neurons.[38] The previous studies identified the key players initiating the mechanical responses in neurons, [37, 39-41] however, it is still unclear if the deformed neurons relay the excitation to the non-stimulated neighbors. The general agreement is that neurons respond to deformation individually, since synaptic block fails to weaken mechanically evoked excitation in network-level stimulations.[37] Yet, mechanical responses disperse non-synaptically between the non-neuronal cells, for instance, gap junctions, also present in neurons. Unlike synaptic transmission, gap junctions spread the excitation to a broader range of interconnected neurons, independently of the target neuron type.[42] Addressing whether and how excitation from single-neuron deformation propagates into the network of interconnected neurons may provide a better strategy for identifying neuronal ensembles. Additionally, understanding if a biological component limits the spatial resolution of mechanostimulation is relevant for advancing the stimulation strategies for clinical purposes. Hence, my thesis focused on the following: "*What would happen to the in vitro network if a single neuron were deformed*?."

Additionally, patch-clamp, widely used in studying the native activity and single-cell electrical stimulation, requires a tight glass-membrane contact achieved in successive membrane-deforming steps. Given that the patch-clamp targets a single cell exclusively while allowing wide-network screening, I investigated the network's responses to a single-neuron deformation *during the establishment of the giga-seal*. Besides understanding the impact of a single-neuron deformation on the local network, investigating this question is crucial for assessing potential confounds introduced by the measurement, particularly when studying native neurons and circuits. Emerging evidence suggests neurons retain a short memory of being deformed, as membrane deformations can impose longer neuromodulatory effects.[43, 44] Building upon findings from network-wide mechanical stimulations, I investigated whether a single-cell mechanical deformation could modulate the target and surrounding network (Chapter 6).

# 2. Theoretical background

## 2.1. From neurons to networks

The first part of this section focuses on neurons, the basic building blocks of neuronal networks. Neurons are highly morpho-functionally compartmentalized cells, comprised of soma containing nucleus and most of the organelles, and neurites: axons and dendrites, with primary relay and recipient roles, respectively. Since neurons represent electrogenic cells whose primary information currency is action potential, the introduction opens with the membrane and ion channel physiology, underlying the resting membrane potential (Section 2.1.1) and electrical signaling (Section 2.1.2). The neuronal operating mode is activity rather than silence. Neurons continuously receive and integrate the inputs to produce an output. The basics of inter-neuronal communication via chemical and electrical synapses is introduced in Section 2.1.3. As my thesis focuses on the network's responses to a single-neuron deformation, the principles and significance of the neuronal mechanosensation are introduced in Section 2.1.4.

The second half focuses on the *in vitro* networks. Grown on 2D and compromised of randomly distributed somas with *de novo* connections, *in vitro* systems lack the anatomical and regional organization of tissue slices and brains. However, they display a few favorable attributes, such as maturation (Section 2.1.5) and self-organization (Section 2.1.6), because of which they are a good approximation to tackle some fundamental neuroscientific questions, under highly controlled environmental conditions. Because of their relative simplicity and accessibility for long-term monitoring, *in vitro* networks found an irreplaceable position in initial network maturation and synaptogenesis studies,[4, 45-47] while recent network neuroscience studies aim to unravel the interplay between the morphology and function underlying the self-organization.[11, 12, 23, 24] This section closes with the networks' convergence towards modular architecture and self-driven organization into the synchronous firing regime as a hallmark of their maturation.

### 2.1.1. Ion basis of the membrane potential

The membrane is a few nm (4-10 nm) thick bilayer composed of amphipathic phospholipids (Fig. 2.1.1.1), with hydrophobic tails sandwiched between the negatively charged, hydrophilic heads oriented towards the cytosol (inner leaflet) or external bulk solution (outer leaflet). The intact membranes are inherently impermeable to ions and are approximated as capacitors (Fig. 2.1.1.2). Because the membrane specific capacitance is $\leq 1$ $\mu F/cm^2$[48], minimal ion fluxes or charge re-distributions are required to induce the membrane potential changes. Nevertheless, the membrane shows the capacity to store charge, which introduces temporal delays in membrane resting potential upon stimulus reception.

The key mobile ions in the membrane potential modulation and maintenance are $Na^+$, $K^+$, $Ca^{2+}$, and $Cl^-$. Ion permeability arises from transmembrane proteins acting as gates. These proteins include ion channels comprising an ion-conducting pore open at both ends and membrane transporters that transfer through conformational changes (Fig. 2.1.1.1). Due to their remarkably high conduction velocity (> $10^6$ ions/s),[49] almost all fast membrane responses are mediated by ion channels. The high conduction velocity is achieved via multiple hydrated ions occupying the channel's pore, as they passively diffuse down the electrochemical gradient. Ion channels open to a certain stimulus: membrane potential changes (voltage-gated), molecule binding (ligand-gated), mechanical stimulus (mechanically gated), pH changes, etc. Once open, the ion channel permeates the particular ion species for which it is specialized. Cation channels show particular selectivity,[49] resulting in $Na^+$, $K^+$, and $Ca^{2+}$ specialists. In contrast, anion channels are usually graded by Eisenmann permeability sequences, although, due to a high mobility and physiological abundance of $Cl^-$, they are canonically denoted as chloride channels[49]. In analogous electrical circuitry, ion channels are modeled as resistors.

Membrane transporters also partake in the maintenance of the resting membrane potential. For instance, Na-K ATP-ase actively maintains the asymmetric distributions of $Na^+$ and $K^+$ [50]: using the free energy of ATP hydrolysis, it pumps $3Na^+$ out and $2K^+$ into the cell, against their electrochemical gradient (Fig. 2.1.1.1, blue rectangle). Other transporters that modulate transmembrane ion gradients include $Na^+$-$K^+$-$Cl^-$ co-transporter (NKCC) and $K^+$-$Cl^-$ co-transporter (KCC). In developing neurons, NKCC1 and KCC2 establish symmetrical chloride gradients,[51, 52] relevant in the early establishment of GABAergic connections during the neuronal development (Sections 2.1.4, 2.1.5).

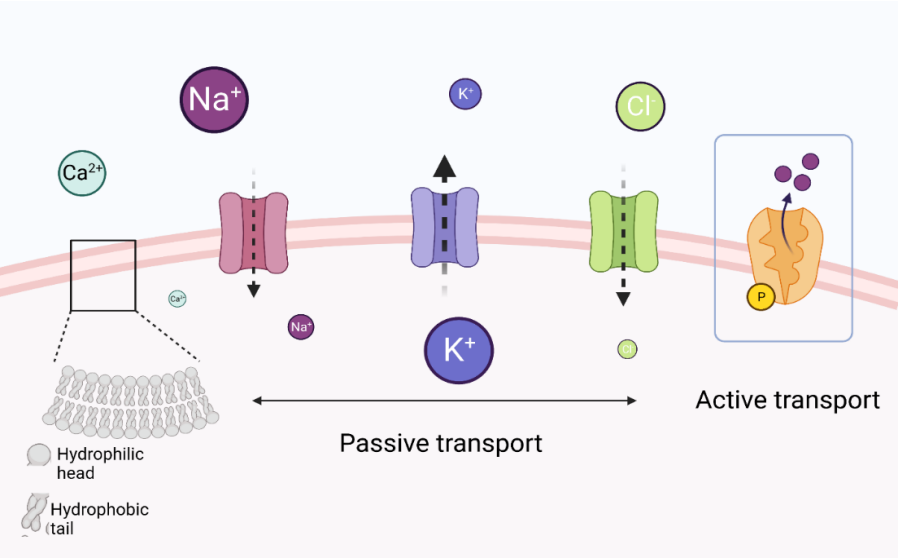


**Figure 2.1.1.1. The key players contributing to the resting membrane potential.** Dashed arrows denote the ion flow across the ion channels and transporters. The ion size depicts their relative abundance across the leaflets. Blue rectangle: Na/K pump. Created with BioRender.com.

The resting membrane potential is governed by a selective redistribution of ions across the leaflets, which arises from the membrane's differential permeability for mobile ion species. The ion flux is controlled by the electrochemical gradient, which is determined by differences in potential and concentration. The equilibrium state for each ion species, in which electrical forces

counteract concentration differences between the two leaflets, is described by the Nernst equation (2.1).

$$E_{N,S} = \frac{RT}{z_s F} \ln \frac{[S]_{out}}{[S]_{in}} \quad (2.1)$$

Here, $E_{N,S}$ corresponds to the Nernst potential for an ion species S, $R$ is the universal gas constant (R = 8.314 J/Kmol), $T$ is the temperature in K, $z_s$ represents the charge of S, F is Faraday constant (F = 96485.33 C/mol) and $[S]_{out}$ and $[S]_{in}$ denote ion concentrations outside and inside of the membrane, respectively. The asymmetrical concentrations across the two leaflets give rise to unique Nernst potential for every mobile ion species. $Na^+$ and $Ca^{2+}$ have strongly positive equilibrium potentials due to their high abundance on the extracellular side, while $K^+$ shows negative Nernst potential. $Cl^-$, abundant on the extracellular side of mature neurons, has negative Nernst potential due to the negative charge (Table 2.1).

Table 2.1. Free ion concentrations and Nernst potential for *Loligo* axon*

| Mobile ion | Extracellular concentration [mM] | Intracellular concentration [mM] | Nernst potential [mV]** |
|---|---|---|---|
| $Na^+$ | 440 | 50 | +55 |
| $K^+$ | 20 | 400 | -75 |
| $Ca^{2+}$ | 10 | 0.4 | +145 |
| $Cl^-$ | 560 | 40 | -66 |

**Values taken from Johnston, Foundations of Cellular Neurophysiology, 1994[53]; ** - calculated for 37°C*

For any given mobile ion species, the ion flux is fueled by differences between the resting and Nernst potential and limited by the membrane's permeability for that ion. At rest, the membrane is particularly permeable for $K^+$ due to abundance of constitutively open pores;[50] in neurons, the inwardly rectifying (Kir) and 2-pore ($K_2P$) potassium channel families are the main contributors to the increased constitutive permeability (syn. "leak conductances") for potassium.[54] This is followed by $Cl^-$, for which the resting membrane shows about 2x less permeability, and $Na^+$ (25-40x less) than that of $K^+$.[55] In rest, the membrane permeability for $Ca^{2+}$ is negligibly low and, as such, excluded from further estimates. Goldman's equation emphasizes the influence of all three key mobile ion species and describes the contribution of their concentration gradients and permeation in shaping the resting membrane potential (2.2).

$$Vm = \frac{RT}{F} \ln \frac{P_K[K^+]_{out} + P_{Na}[Na^+]_{out} + P_{Cl}[Cl^-]_{in}}{P_K[K^+]_{in} + P_{Na}[Na^+]_{in} + P_{Cl}[Cl^-]_{out}} \quad (2.2)$$

$P_K$, $P_{Na}$ and $P_{Cl}$ represent the membrane permeability for potassium, sodium, and chloride, respectively. Setting the permeability ratios to $P_K : P_{Na} : P_{Cl} = 1 : 0.04 : 0.45$ resulted in good fit to the experimental data of Hodgkin and Katz, who studied the *Loligo* axon $V_m$ dynamics upon outside ion concentration changes; hence the equation is also noted as Goldman-Hodgkin-Katz (GHK) equation. Due to the asymmetry in permeability for different ion species, the resting membrane potential is closest to the Nernst potentials for $K^+$ and $Cl^-$. Importantly, at the thermodynamic equilibrium, the membrane potential deviates from the Nernst potential for any mobile ion species, indicating that every ion species is outside the equilibrium. Therefore, only

the total net ion movement equals 0, while the resting membrane potential is maintained through constant individual ion species' fluxes.[55] The GHK equation illustrates the membrane potential at stationary state, and is further expanded by electrical circuit model to describe the resting membrane potential dynamics.

Electrical analog of the unitary membrane comprises of the three parallel branches, each containing a battery defined by the Nernst potential for a given ion species, and resistor, representing the membrane's conductivity for that ion species (Fig. 2.1.1.2 A). The fourth branch connected in parallel denotes the membrane capacitance, $C_m$. Following the injection of the depolarizing pulse, the membrane response experiences an exponential lag, as the current flows both through the capacitor- and resistor-containing branches. In this case, the capacitive current is directly proportional to the membrane capacitance and membrane potential changes according to (2.3):

$$I_C = C_m \frac{dV_m}{dt}, \tag{2.3}$$

where $dV_m/dt$ corresponds to the first temporal derivative of the membrane potential. At the stationary state, $dV_m/dt = 0$ and the current flows exclusively through the resistive branches following the Ohm's law ($I = V_m/R$). Solving this circuitry when the total net charge flux equals zero gives the following expression for the resting membrane potential (2.4):

$$V_m = \frac{g_k E_k + g_{Na} E_{Na} + g_{Cl} E_{Cl}}{g_k + g_{Na} + g_{Cl}}, \tag{2.4}$$

where $V_m$ denotes the resting membrane potential, $g_k$, $g_{Na}, g_{Ca}, g_{Cl}$ correspond to membrane conductivities ($g_S = 1/R_S$) and $E_k, E_{Na}, E_{Cl}$ denote the difference between the membrane potential and Nernst potential each of the ion species ($E_s = V_m - E_{N,S}$)[56].

As described above, the passive membrane properties introduce the membrane potential relaxation arising from the passive membrane's properties. The resistive branches can be further approximated as a single resistive branch containing total unitary membrane resistance, $R_m$ (Fig. 2.1.1.2 Bi). Following the Kirchoff's law, the total membrane current is (2.5):

$$I_m = I_C + I_R = C_m \frac{dV_m}{dt} + \frac{V_m}{R_m}, \tag{2.5}$$

with the first part of equation denoting the capacitive current, while the second part relates to the Ohmic component. Solving this equation for Vm, the following expression holds (2.6):

$$V_m = I_m R_m \left(1 - e^{-\frac{t}{R_m C_m}}\right). \tag{2.6}$$

The formula depicts exponential delay introduced by the membrane's passive properties, characterized by the time constant, $\tau = R_m C_m$. Time constant is the time required for the $V_m$ to reach 63% of the maximal, asymptotic value upon stimulus reception (Fig. 2.1.1.2 Bii). This intrinsic property defines how fast the neuron responds to a stimulus, and the time required for

the membrane to relax following the stimulus end, with important implications in temporal summation of synaptic inputs.

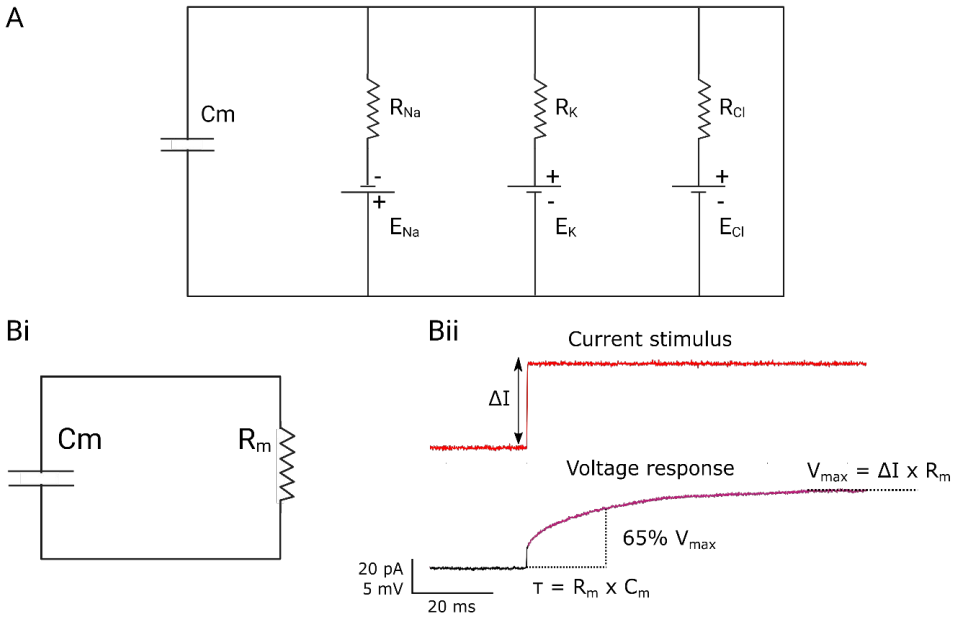


**Figure 2.1.1.2. Passive membrane properties.** A. Electrical analog of the unitary membrane. Adapted from Hodgkin 1952 [56]. Bi. Reduced analog electrical model. Bii. Passive membrane responses (black) upon a step current injection (red). Purple line marks single-exponential describing the neuron's responses. Electrical circuits sketched with BioRender.com.

## 2.1.2. Action potential – the neuronal information currency

Neurons have the property of excitation: a capacity to generate binary, fast, and regenerative membrane potential changes via voltage-dependent modulation of the membrane's ion permeabilities. The key players in action potential generation are sodium and potassium voltage-gated ion channels ($Na_v$s and $K_v$s, respectively),[49, 50] with rectifier-like properties. Both ion channel families feature non-linear voltage-current relationships, with opening probabilities as a function of $V_m$.[49] In the standard model of the neuronal firing, electrotonic, depolarizing membrane potential changes initiated at the dendrites sum up in time and space and trigger the AP generation at the axon initial segment (AIS, also see the following Section), a $Na_v$ rich compartment 30 – 60 µm from the soma[57]; similarly, APs could be evoked by a somatic current injection. From the initiation site, APs regeneratively and reliably propagate along the neuron, acting as a robust bit of information.

APs arise by the *all-or-none* principle; unlike the electrotonic $V_m$ changes that decay in time and space. As shown in Figure 2.1.2. A, weak somatic current injections result in passive membrane responses, and the APs are reliably initiated by above-threshold Vm. The invention of voltage-clamp amplifier by Cole and Marmont enabled the dissection of currents underlying the AP generation in Hodgkin and Huxley's work on space-clamped *Loligo* axons [58]. Through voltage-clamp and ion substitution experiments, Hodgkin and Huxley demonstrated that the total biphasic current representing an AP comprises early-onset, fast-activating inward $Na^+$ current with inactivation profiles, and late-onset, slowly activating outward $K^+$ current (Fig. 2.1.2. B).

The binary property of APs stems from positive and negative feedback of $Na^+$ and $K^+$ membrane permeabilities' dynamics and voltage-dependencies (Fig. 2.1.2. C):

- The positive feedback is manifested by the early onset of depolarization-induced $Na^+$ entry, potentiated by $Na^+$ entry-mediated depolarization (Fig. 2.1.2. B-D);
- The negative feedback loop is established by the inactivation of the $Na^+$ current during the prolonged depolarization (Fig. 2.1.2. B-D) and late-onset of outward $K^+$ current (Fig. 2.1.2. B).

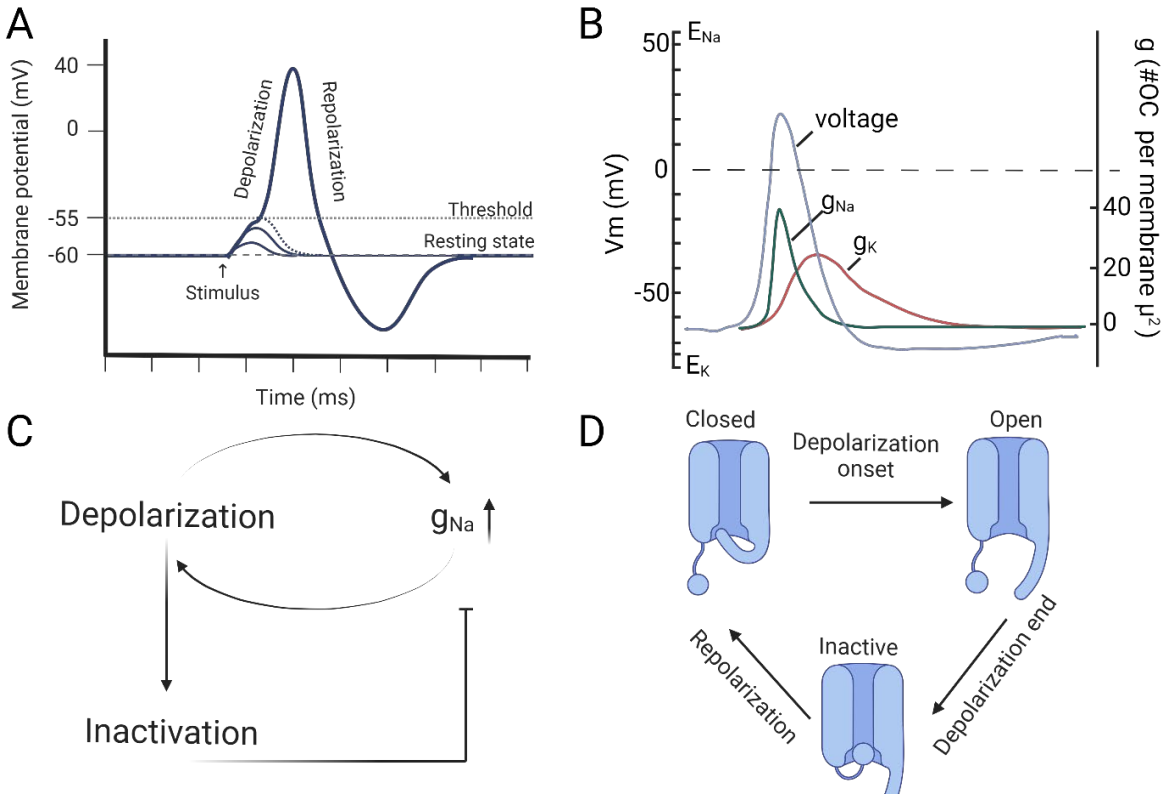


**Figure 2.1.2. Basis of the action potential.** A. All-or-none property of APs. Membrane potential profile upon subthreshold current injection (stimulation time marked by an arrow) and AP generation upon threshold crossing. B. Overlay of an AP and conductivity profiles of the main ion species participating in AP generation: sodium (green, $g_{Na}$) and potassium (red, $g_K$). $E_{Na}$ and $E_K$ mark the Nernst potential for sodium and potassium, respectively; #OC on the right ordinate marks the number of open channels. C. The interplay between the positive and negative feedback loops participating in AP generation. D. Schematics of Nav gating during distinct phases of an AP. Created with BioRender.com.

At rest ($V_m$ = - 60 mV), most $Na_v$s and $K_v$s are in closed state. Membrane depolarization favors the $Na_v$'s activation gate opening, promoting $Na^+$ entry and further depolarization. When the initial stimulus is faster than the $Na_v$'s inactivation and strong enough to allow the $V_m$ threshold crossing[1], the unitary membrane effectively enters the positive feedback loop (Fig. 2.1.2.C). At this step, the membrane abruptly ($dV_m/dt$ = 100-200 V/s)[59] inverts the polarity and approaches

[1] Threshold (syn. onset) potential for most neurons spans from -50 to – 20 mV. Pacemaker neurons with intrinsic oscillatory phenotype have threshold Vm at hyperpolarized potentials (-80 to -70 mV).

about + 30 mV. At the peak of AP, dVm/dt = 0, as the inward $I_{Na+}$ counteracts the outward $I_{K+}$ (Fig. 2.1.2. B). The decline in $Na^+$ entry is due to progressing $Na_v$'s inactivation at depolarized potentials, where a separate inactivation gate imposes a barrier to the ion passage (Fig. 2.1.2. D). The rise in the outward $I_{K+}$ is from the late-onset $K_v$ activation, allowing the $K^+$ efflux. The repolarization phase is characterized by slower ($dV_m/dt$ = 20-40 V/s)[59] decay and return to hyperpolarization. In most neurons, the membrane potential undergoes the after-hyperpolarization (AHP) prior to a complete return to the resting state. $Ca^{2+}$-activated potassium channels of SK and BK family mainly contribute to AHP development in mammalian neurons.[59, 60]

During the repolarization phase, when most $Na_v$s are inactivated, the neurons are incapable of generating another AP; this time window limits the maximal firing frequency and is denoted as the *absolute refractory period*. The absolute refractory period ranges from 0.4 to 1.5 ms,[61] depending on the repolarization kinetics and the neuron's ion channel make-up.[59] The violation of refractory period is widely used as a quality metrics to discriminate extracellular spike unit contamination with spikes from other sources following the spike sorting [62] (Section 2.3.2). As an AP approaches the AHP, the $Na_v$s recover from inactivation and preferentially return to the closed state. Simultaneously, a fraction of $K_v$s return to the closed state. Neurons during this period can fire but require stronger stimulus due to a reduced driving force. This window marks the *relative refractory period*, during which the firing probability is reduced. The total refractory period ranges from 5 to 10 ms[50, 61].

While all APs follow the positive monophasic shape, their waveform varies across the neuronal types [59, 63] and within the same neuron [64, 65]. Ion channel constitution and, in particular, the expression of different $K_v$s across the neuronal types define the kinetics of an AP in different neuronal classes. For instance, GABA-ergic neurons[63] have a fast-spiking phenotype and display faster repolarization compared to glutamatergic neurons (Section 2.1.3), owning to a high expression of fast-activating $K_v3$ isoform.[63] Slight differences in AP waveforms from the same neuron are evident in within-burst APs, where burst-carrying depolarization influences the AP waveform by inactivation of $Na_v$s and $K_v$s [64, 65]. The intracellular waveform variations modulate the neurotransmitter release, in a process marked as analog-digital modulation.[66, 67]

Once initiated at the AIS, APs regeneratively propagate in both directions: towards the soma (back-propagating APs or bAPs) and down the axon. bAPs are detected by intracellular somatic measurements (Section 2.3.1) and successfully invade the proximal dendritic trunk, contributing to spike timing dependent plasticity (STDP, see also Section 2.1.3).[68-70] Forward-propagating APs reach the axon terminals and induce depolarization-mediated vesicle release. Propagation is regenerative: AP initiated at one membrane segment closes a local circuitry with the adjunct membrane segment; the lateral ion flow passively charges the following segment and initiates an AP upon the threshold crossing. This mechanism allows a reliable unidirectional AP transmission along the neurite, since the $Na_v$ refractoriness of the excited segment prohibits back-propagation. The propagation velocity is limited by the initial axial transfer and subsequent

membrane charging and is inversely related to the axonal diameter. Propagation velocity is further elevated by equidistantly spaced myelin sheaths – glial cells' (oligodendrocytes for CNS, Schwann for PNS) processes wrapped around the axon. Acting as an insulator, myelin sheaths promote saltatory conduction, where APs generate exclusively in myelin-lacking membrane segments (Ranvier nodes). In *in vitro* networks of cortical neurons depleted of glial cells, the average propagation velocity is about 1 m/s.

## 2.1.3. Neuronal communication within and beyond synapses

Synaptic transmission is a directed information transfer from the pre-synaptic to the post-synaptic neuron. In the basis of the synaptic communication is the depolarization-induced neurotransmitter release from vesicles docked at the pre-synaptic membranes, which induces electrotonic events (post-synaptic potentials, PSPs) at the recipient, post-synaptic membranes (Fig. 2.1.3). The two membranes are separated by a 20-40 nm cleft[50] that promotes specificity of the information transfer by limiting the neurotransmitter diffusion. The entire process, from the pre-synapse depolarization to the membrane response at the post-synapse, lasts about a few ms. The most of CNS synapses are axo-dendritic, but other arrangements are also present.[71]

Neurotransmitters are classified according to their chemical composition [e.g., acetylcholine (Ach), amino acid ( glutamate, gamma-aminobutyric acid (GABA), glycine), biogenic amines (catecholamines – dopamine, epinephrine, and norepinephrine, and serotonin), and ATP and ATP-derivatives]. Small neurotransmitters are synthetized locally and concentrated into the synaptic vesicles utilizing co-transport powered by proton gradient. While the standard model comprises of individual neurons producing a single transmitter, they are frequently co-released with neuropeptides or other neurotransmitters. In cortex and cortex-derived networks (Section 2.2.1) the most prevalent are GABA and glutamate-mediated synapses.

Neurotransmitter release is a multi-step process. Membrane depolarization at the pre-synapse, standardly triggered by the upcoming AP(s), initiates the $Ca^{2+}$ influx via $Ca_V$s (P/Q and N-type). The localized $Ca^{2+}$ entry triggers the release from already docked vesicles. The vesicle fusion lasts around 0.1 ms,[72] so the events leading to it mainly contribute to the synaptic lag. The amount of the neurotransmitter molecules released is dictated by the magnitude of depolarization and defined by the number of vesicles fused. Since the vesicles contain a defined amount of neurotransmitter molecules, the release is quantal. Vesicle fusion is a multi-step process comprising of several protein complexes. The available pool of primed vesicles is determined by $Ca^{2+}$-driven phosphorylation of the vesicular protein synapsin. The fusion assembly, comprising of the SNARE and Munc13-RIM complexes, lowers the activation energy required to bring the two charged bilayers together; primed and docked vesicles have these complexes assembled prior the fusion. The localized $Ca^{2+}$ increase is sensed by another vesicular protein, synaptotagmin 1 (Syt-1), which triggers the fusion.[50]

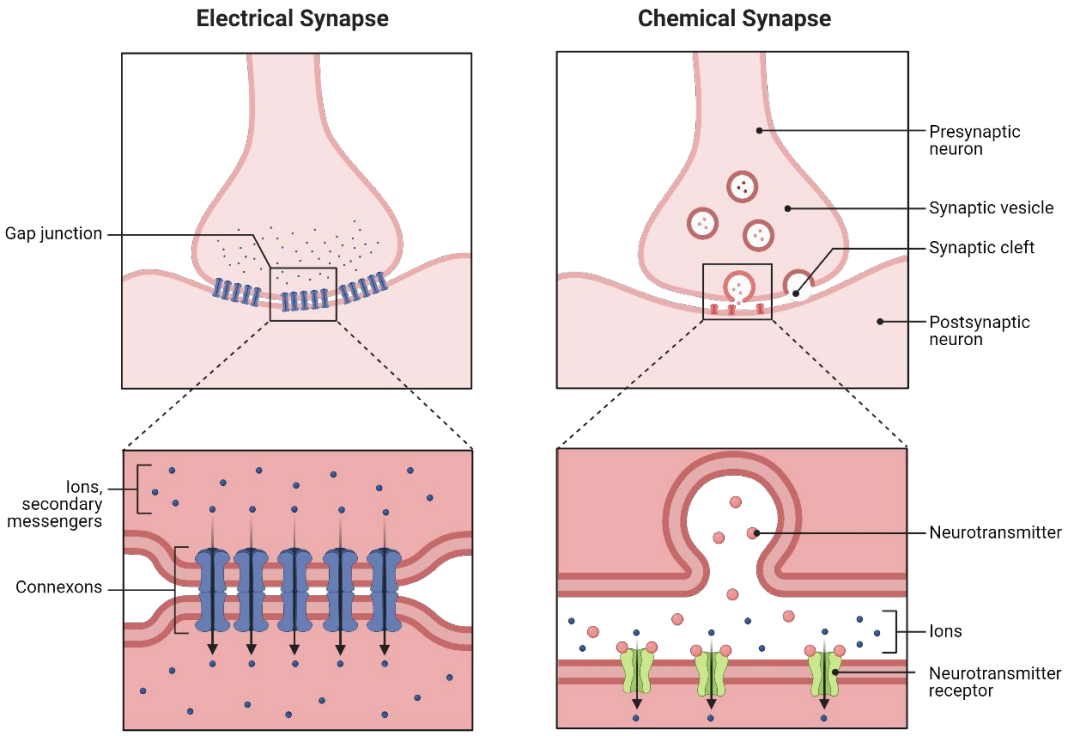


**Figure 2.1.3. Means of interneuronal communication.** Left: Electrical synapses are mediated by the gap junctions. Right: Chemical synapses involve AP-mediated neurotransmitter release and binding to the neurotransmitter receptors at the post-synapses. Created with BioRender.com.

The neurotransmitter released into the cleft diffuses to bind neurotransmitter-specific receptors, inducing the post-synaptic neuron responses. Two classes of neurotransmitter receptors, ligand-gated ion channels (syn. ionotropic receptors) and metabotropic receptors, evoke responses at different timescales. Ligand-gated ion channels (AMPARs, NMDARs, $GABA_AR$s) act promptly, directly inducing the membrane potential changes through ion fluxes. In contrast, metabotropic receptors (muscarinic Ach receptors – mAchR, glutamate – mGluRs, GABA - $GABA_BR$s, dopamine and serotonin receptors) are coupled to the enzymatic activity (G-protein, tyrosine kinase) that triggers signaling cascades, amplified by secondary messengers (e.g., cAMP, IP3) that target many effectors. In turn, metabotropic receptors show slower activation but have long-term and modulatory effect.

The sign of PSP depends on the neurotransmitter type, receptors' ion specificity, and the resting membrane potential. For instance, glutamate binds to the cation-specific receptors (AMPARs, NMDARs), whose opening causes post-synaptic membrane depolarization, excitatory PSPs (EPSPs). Besides acting as ligand-gated channels, NMDARs are rectifiers, as they require depolarization to unblock the conducting pore $Mg^{2+}$. This dual activation (depolarization and glutamate binding) plays a pivotal role in the post-synaptic responses upon synchronous input activation and coincident detection. In addition, NMDARs are capable of generating non-linear NMDA spikes, relevant for dendritic computation and dendrite-soma coupling. Receptors for Gly (GlyRs) and GABA (GABARs) permeate $Cl^-$: in mature neurons $Cl^-$ enters the cells causing

hyperpolarization (syn. inhibitory PSPs, IPSPs). Depending on the transmembrane chloride distribution and resting potential, the standard inhibitory synapses are capable of inducing depolarizing responses. In developing neurons up to the first postnatal week,[73] the symmetrical $Cl^-$ concentrations across the membrane (Section 2.1.1) cause $Cl^-$ efflux, leading to GABA-mediated EPSPs. This feature is found both *in vivo* and *in vitro* and is shown to secure the activity-mediated neurons' survival during the early development. Mature neurons with asymmetric $Cl^-$ distribution also experience depolarization upon strong hyperpolarization from synchronous inhibition;[74] the GABAergic EPSPs may still inhibit excitation through shunting inhibition.

Another means of interneuronal signal transfer are the gap junctions (GJCs). GJCs require physical contact between the neurons via connexons – hexamers of transmembrane connexins (Cxs) that assemble into a hemichannel (Fig. 2.1.3). The two connexons in connecting neurons form a channel connecting the two interfacing membranes distanced by a few nm gaps (hence the name). Having a central hydrophilic pore, GJCs serve as a gateway, exchanging multiple ion species ($Na^+$, $K^+$, $Ca^{2+}$, etc.) and secondary messengers (i.e., cAMP, $IP_3$, $Ca^{2+}$).[75] Since the pore closes the local circuitry between the adjacent membranes, another role of the GJCs is to transmit the electrotonic membrane potential changes, for which GJCs are also known as electrical synapses.[76, 77] Unlike synaptic transmission, GJCs offer bi-directional and fast transfer of analog signals as they are not limited to APs or quantal neurotransmitter releases.[42] Additionally, the sign of electrotonic change in the recipient cell is strictly governed by the electrochemical ion gradient, independently of the relaying cell type;[77] the magnitude of transferred signal scales with the conductivity of the GJCs, but also resistivity and capacitance of the recipient cell (see Pereda 2013[78] and Faber 2018[42], also Bennett 1966[79]). Typical GJC shows conductivity between 0.5 – 5 nS, depending on the Cx composition. The signal transmitted via the GJCs is low-pass filtered: GJC propagating APs adopt attenuated and wider spikelet waveforms, while the slower electrotonic events transmit near linearly.[78, 80] These properties make GJCs particularly relevant in set-ups where a reliable spread of slow excitation is required – such as developing neuronal ensembles,[81-85] and network synchrony.[77, 86-88]

GJCs are prevalent during the neurogenesis and early neuronal development; they are found in radial glia in embryos and radial glia-like cells participating in adult neurogenesis,[89] between the radial glia processes and neuronal precursors with role in radial migration[90], as well as between the early neurons, where they preceded the synaptic connections.[89] Eleven Cx isoforms are expressed in rodents, of which Cx36 is the most prevalent in the brain.[91, 92] The connexin landscape changes as the brain develops and matures. From early embryonic development, Cx26 and Cx43 are abundant in radial glia and neuronal precursors.[93, 94] Developing neurons mainly express Cx26, Cx43, and Cx36, while Cx36, Cx46, and Cx50 are typical for mature neurons (for a recent review, see Talukdar 2022[94]). Cxs are distributed across the neuron. Electron microscopy studies demonstrated the primary localization of GJCs in dendro-somatic,[86] dendro-

dendritic, [86, 95] axo-axonic, [96] and axo-dendritic contact points.[97] Most frequently, GJCs co-localize with synaptic contacts.[98, 99]

It is widely accepted that GJCs are the most abundant during early development,[81] as they precede the synapse formation and get progressively overpowered by further synapse establishment.[100, 101] In this standard overview, GJCs in mature neuronal networks are exclusively retained between the interneurons,[80, 86] forming syncytium relevant for maintaining the basal inhibitory tone. However, the emerging evidence points to silent axo-dendritic GJCs between the pyramidal neurons in hippocampal preparations and adult brains. These GJCs are activated by intracellular application of GJC opener trimethylamine,[97] cytosol acidification, or phosphorylation via kinases.[102] Accordingly, molecular and functional characterization showed a discrepancy between the detected and active GJCs, such that only about 0.1-7% of available GJCs partake in a signal transmission at a time. [87, 95, 103] The findings favor the tightly regulated and inducible GJC opening in mature neurons over their scarcity, and capacity for GJC conductances to be amplified. Indeed, GJC transmission and expression are amplified in several types of brain injuries, such as excitotoxicity from brain ischemia, traumatic brain injury, and epilepsy; in all conditions, GJCs are the primary route for calcium waves and other "death signals", further propagating neuronal damage in a positive feedback loop. [92]

## 2.1.4. Sensing beyond electrochemical: mechanosensation

Mechanobiology consistently demonstrated the neurons' sensitivity to wide ranges of mechanical stimulation modalities such as push, stretch, pull, and capacity to respond to a wide range of mechanical forces, from pN,[39, 41] to nN[40] and μN.[104, 105] Neurons are capable of responding promptly to a mechanical stimulus due to expression of several species of *mechanically gated* ion channels.[106] These channels are specialists,[107] shaped by evolution to promptly open upon the membrane deformation. The Piezo family, comprised of Piezo1 and Piezo2 homologs, is well characterized among the mechanically gated ion channels. Both homologs have 38 transmembrane helices[108, 109], with proximal residues constituting an ion-conducting pore and distal components forming a mechanotransduction blade. Upon the membrane deformation, functional Piezo homotrimers go through a *propeller-like* opening[108], where distal blades' shifts induce small pore conformational changes that suffice for the ion passage (Fig. 2.1.4.1.A). The monomer conformational changes are thought to act in a coordinated fashion.[108] Mechanical gating is also found in multimodal two-pore potassium ($K_2P$) channels, TREK and TRAAK, with vital roles in the modulation of intrinsic neuronal excitability.[110] Similar to prokaryotic mechanically activated channels, MscS and MscL, the gating of TREK and TRAAK is modulated by direct protein-lipid interactions.[111] Through the force-from lipid mechanism, lateral forces open the channels similar to *pupil opening* (Fig. 2.1.4.1 A).[112]

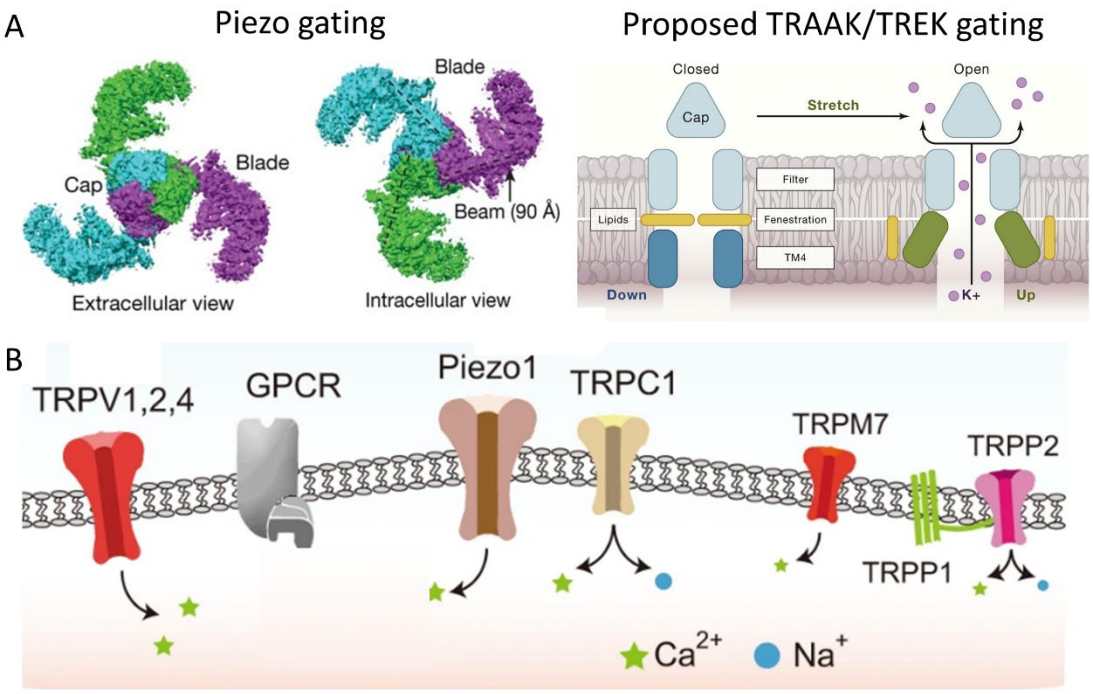


**Figure 2.1.4.1. Mechanically gated and mechanosensitive receptors.** A. Mechanically gated ion channels' opening is directly influenced by membrane deformation. Left: Propeller-like gating of Piezo channels, mediated by the blades' conformational changes acting as a lever. Adapted from Wang 2019.[109] Reproduced with permission from Springer Nature. Right: Proposed iris-like gating of mechanosensitive K2P channels. During the membrane deformation, the upward movement of the transmembrane helix (TM4, green) squeezes out the lipids at fenestration site (yellow), unblocking the channel's pore. Lipid occlusion is one of the proposed mechanisms, along with stabilization of the selection filter and modifications of the cytosolic tail. All three mechanisms share iris-like macroscopic conformational changes. Modified from: Douguet, 2019.[112] B. Both mechanically gated and mechanosensitive proteins contribute to the neurons' excitation to a membrane deformation. Modified from: Yoo, 2022[37]. Reproduced with permission from Springer Nature.

Ion channels and transmembrane receptors whose gating kinetics are affected by the mechanical stimulus are *mechanosensing*. Due to a strong non-covalent protein-lipid interaction, many non-specialized ion channels show some degree of sensitivity to membrane deformation. Ion channels whose gating kinetics are modulated via mechanically evoked signaling pathways also fall into this category. Mechanosensing is extensively shown for voltage-gated[113] and ligand-gated ion channels,[114] G protein-coupled receptors,[115] and multimodal transient receptor potential (TRP) family (Fig. 2.1.4.1. B).[106]

Why are CNS neurons equipped to respond promptly to a membrane deformation? While the neuron's mechanosensation could be a by-product of protein-membrane interactions, several lines of evidence point to the physiological significance behind the neurons' responsiveness to acute membrane deformation. Specifically, acute mechanical stimuli may serve as a cue in the neuronal guidance during the development of the neuronal networks, as the growing neurites respond to a membrane deformation by retraction and turning (Fig. 2.1.4.2. A),[39] while long-term inhibition of MS channels induces aberrant branching of growth cones[116], reduces the

morphological clustering of neurons, as well as the number of synapses.[39] That mechanotransduction plays a vital role in axon guidance is also suggested by a non-random distribution of MS aggregations at point contacts of growth cones.[117] As the growth cone advances, the interactions between the cytoskeleton, transmembrane integrins and cadherins, and extracellular matrix generate forces sufficient for activation of MS channels.[118] MS channels are preferentially found in functional microdomains alongside the point contact proteins,[119-121] where acute mechanical forces generate localized calcium waves that trigger the secondary cascades.[122] That mechanical forces act as a pivotal cue during the neuritic growth is further supported by previous findings from our Institute, where a static 2D+ topography was shown to promote the axonal growth,[123, 124] and was successfully implemented to engineer morphologically defined *in vitro* networks.[125]

In addition to acting as a growth cue, acute mechanical stimuli may directly partake in modulation of the synaptic plasticity, as forces from dendritic spine enlargement actively promote glutamate release from the coupled bouton (Fig. 2.1.4.2. B).[44] Through fine displacement of axonal buttons via the pipette, Ucar et al. demonstrated that acute mechanical perturbations, akin to those from the spine enlargement, amplify the vesicle release through direct interaction of the SNARE (SNAp Receptor) complex with the actin cytoskeleton. The mechanical pre-synaptic responses are postulated to mediate long-term integration mechanisms that persist for tens of minutes following the initial mechanical stimulus from the spine enlargement.[44] On the same token, findings from network-level mechanical perturbations demonstrated the neurons' capacity to store the information of being mechanically perturbed, as ultrasound stimulation (US) led to long-term (> 8h) increases of the intrinsic neuronal excitability.[43] While the mechanisms underlying the mechanostimulation effect on long-term intrinsic excitability modulations remain elusive, they suggest the involvement of several signaling cascades (co)-opted to store a memory of a mechanical stimulus.

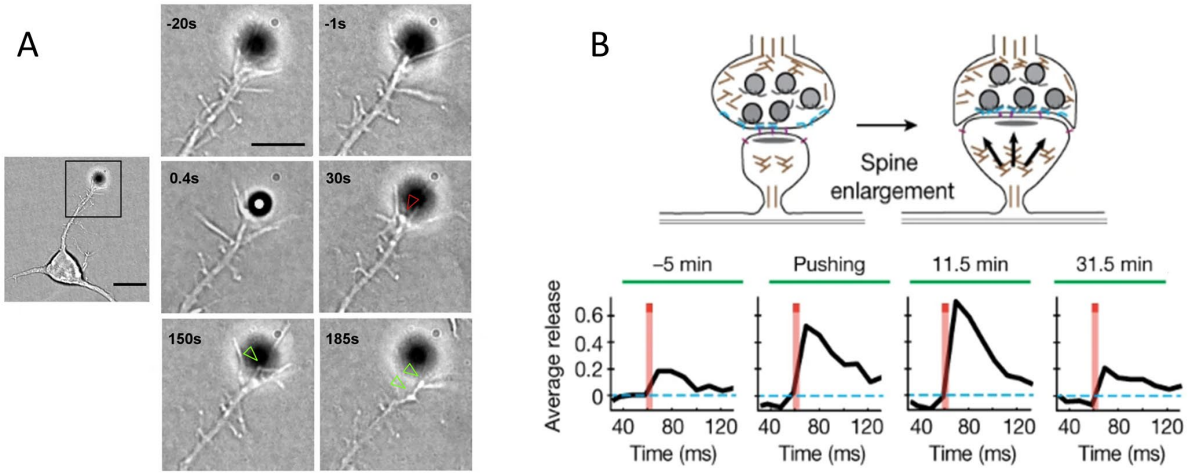


**Figure 2.1.4.2. Acute mechanotransduction has physiological purposes.** A. Growth cone of hippocampal neurons is sensitive to acute and repetitive mechanical perturbations via optically trapped polystyrene beads. Green arrows

denote avoidance, red arrow marks retraction. Adapted from Falleroni et al. IScience 2022[39]. B. Acute mechanical deformation at the synapse promotes elevated vesicle releases. Top: schematic representation of bouton deformation during the spine enlargement. Bottom: Averaged evoked glutamate release from individual bouton prior, during and after acute mechanical deformation. Adapted from Ucar et al. [44] Reproduced with permission from Springer Nature.

## 2.1.5. Morphological organization of *in vitro* networks

*In vitro* neuronal cultures are established via the brain (i.e., cortex or hippocampus) digestion followed by plating on a substrate (Fig. 2.1.5. A). These networks comprise several neuronal types, with incidences akin to those *in vivo* (summary in Table 2.1.5)[126]. *In vitro* networks show signs of morphological maturation. Following enzymatic or mechanical dissociation of embryonic brains, plated neurons adopt spherical shapes as they start adhering to the surface and display several protrusions.[45, 46] About a few hours later, the protrusions grow into a few immature neurites, equal in size and molecular constitution. At 12h from plating, usually one neurite outgrowths the others, having a growth cone at its tip with a directional role; this neurite becomes an axon.[45] The outgrowth is guided by the extracellular signals' gradients from the neighboring neurons that are sensed by the growth cone,[127] and topological cues (Section 2.1.4). During the 1st week *in vitro*, the rest of the neurites develop into functional dendrites, beginning the synaptic communication that would produce emerging activity (Section 2.1.6). After the first week in culture, the extensive neuritic growth and branching are evident, as *in vitro* networks form a dense neuritic net; additionally, dendritic branches form dendritic spines. This timeline, initially described for hippocampal cultured networks,[45] roughly applies to the cortical *in vitro* networks. The main difference is the onset of dendritic outgrowth: in hippocampal cultures, dendritic outgrowth peaks at DIV 14, while cortical cultures exhibit a slower outgrowth, with a significant elevation at DIV 21 (Fig. 2.1.5. B).[46] Fully connected networks form a 2D layer of somas with neurites spanning up to 1 mm. [126]

Table 2.1.5. Distribution of neuronal types in *in vitro* cultures*

| Neuronal type | Fraction (%) |
|---|---|
| Glutamatergic | 72-88 |
| GABAergic | 10-25 |
| Cholinergic | 2-3 |

**Values taken from Marom, 2002.[126]*

The early interneuronal contacts are predominated by electrical couplings,[81-85] which reliably transmit interneuronal calcium signals. In turn, the interneuronal calcium waves guide the neuronal motility[128] and wiring[129], and promote the neuronal survival.[130] Synaptogenesis starts by the end of the first week, and peaks around the 3rd week in culture.[47] In particular, the early excitatory synapses are rich in functional NMDAR-only post-synapses (syn. silent synapses),[131, 132] that gradually get eliminated or replaced with functional NMDAR-AMPAR pairs,[131] allowing for long-term plasticity changes to take place.[132] The synapse abundance and maturation correlate with the network's synchronization onset (see Section 2.1.6 and Chapter 4), emphasizing the connectedness between the morphology and function. Due to symmetric

chloride concentrations (Sections 2.1.1, 2.1.3), GABAergic inputs are excitatory during the first week *in vitro*.[133] The initial excitatory GABAergic effect is essential for inhibitory neuron integration into the circuitry, and thought to partake in orchestration of primordial synchronous events. The quantity of synaptic connections depends on both global and local neuron densities, as well as the brain region from which neurons are extracted.[133, 134] In densely plated networks, where synaptic connection density is higher, neurons typically require multiple coincident inputs to trigger neuronal firing.[134]

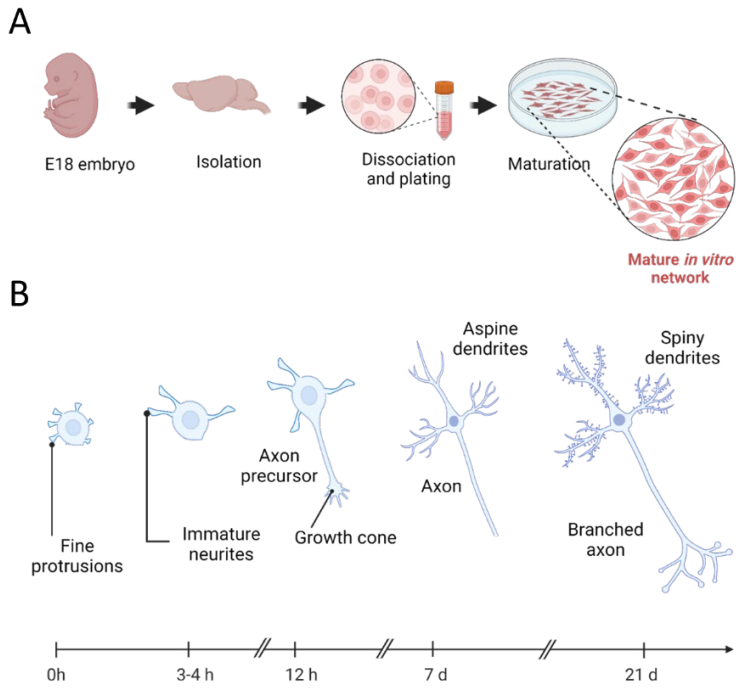


**Figure 2.1.5. Obtaining and culturing *in vitro* networks.** A. Dissociation and plating of neurons isolated from embryonic brains. B. Maturation of neurons and *in vitro* networks during culture: a timeline. Adaptation from Arimura et al., 2007 [45], with timeline adjusted for cortical cultures from Harrill et al., 2015.[46] Created with BioRender.com.

## 2.1.6. The emergence of modular architecture and synchrony

So far, the neuronal growth and synaptogenesis prove the ability of the *in vitro* networks to *mature*. These networks start with a fixed number of somas, yet with highly uncontrolled starting spatial distribution. In contrast to brains with genetically and developmentally defined 3D architecture and regional organization, these networks initially form as a random 2D system. [135] Beyond the predetermined blueprint, brain development is also shaped by spontaneous activity through activity-driven plastic modulation of wiring. [135, 136] The spontaneous concerted activity contributes to the formation of synchronous assemblies in the developing neocortex[137, 138] and hippocampus.[85]

The maturation of *in vitro* networks is governed by the interplay between morphological development and spontaneous activity. Early observations of their topology's self-organized and non-random nature[139] were further supported by recent pharmacologically-driven manipulations of the network's topology [11]. The activity-guided neuronal wiring and migration converge

towards modular architecture, facilitating neuronal cluster creation.[11] In turn, the network's modularity promotes spontaneous activity and shapes the networks' synchrony. Short-range projections connect neurons within modules, while a minority of long-range projections link different clusters. This connectivity supports the small-world architecture demonstrated in cultured mature networks across several regions and species, including networks of the locust *Schistocerca gregaria* frontal ganglia[139, 140], the retinal ganglion cells[141], and cortex.[11] Besides the morphological network properties, the information flow and functional network topology can be estimated from correlation analyses of the neuronal activity. Long-term activity analysis (Sections 2.2.2 and 2.2.3) reveals that the functional topology aligns with morphology, shaping a small-world architecture.[142-144] Additionally, estimates of synaptic connections' distribution verify the non-random nature of the network's connectivity.[145] The resulting functional and morphological modularity enhances the network integration,[143] and favors neurons' engagement in collective network activity [11, 23].

*In vitro* spiking is sparse and irregular during the early stages, gradually evolving to synchronized bursting (Section 4.1).[11, 146, 147] Network bursts (syn. synchronous network events – SNEs) represent a few seconds windows of collective neuronal engagement followed by prolonged epochs of silence. SNEs manifest as prolonged depolarization at the membrane, standardly eliciting a few APs (Sections 4.1, 5.1). In contrast to sporadic firing events, SNEs play a vital role in reliable information transfer and in establishing and maintaining functional neuronal modules. Firstly, neurons in dense networks require multiple coinciding inputs to fire an AP.[144] Namely, the strength of synaptic connections scales inversely with the synaptic density, and excitatory inputs should happen in tens of ms in order to reach above-threshold summation.[144, 148] Secondly, network synchronizations promote synaptic plasticity mechanisms, entraining the neurons within a synchronously firing cluster of neurons.[68, 144] Network oscillations are also captured in cortical organoids,[149] and *in vivo*, in prenatal and early postnatal brains,[85, 150] as well in particular structures (e.g., reticular formation, thalamus, cortex, hippocampus) and states (non-rapid eye movement sleep, memory consolidation, but also stroke, seizures, anesthesia, traumatic brain injury-TBI) of adult brains.[148]

The early investigations of the network's synchronicity with separated but proximal network submodules demonstrated that synchronization requires morphological connections since the segregated neuronal clusters display out-of-phase firing.[151] In the hippocampus[85] and cortex,[150] early neuronal networks synchronize local populations of neurons through non-synaptic GJC-mediated calcium plateaus (synchronous plateau assemblies, SPAs). As the maturation progresses, SPAs get gradually overpowered by synaptic-mediated synchronous events established by dual excitatory effects of glutamatergic and GABAergic inputs.[85, 150] At the membrane, these synchronous events manifest as high-magnitude depolarizations, and are also known as giant depolarizing potentials (GDPs). Developing cortical networks in rodents transition out of the GDP mode via excitatory to inhibitory effect transition of GABAergic inputs. However, wide-network oscillations are also present in neuronal networks after the

GABAergic switch, and are further potentiated by strong activation of $GABA_A$ receptors.[74] The general principle of oscillations comprises the interplay between positive and negative feedback.[148] Two proposed mechanisms drive this phenomenon: one involving emergent synchrony and the other focusing on a few highly interconnected neurons as rhythm generators.

The first mechanism proposes that oscillatory activity emerges collectively from the network. That is, not a single neuron is solely responsible for network rhythm generation, but the individual neurons' rhythms collectively synchronize through interactions.[148, 151] Support for this mechanism comes from observations of sustained network oscillations that persist when individual neurons are clamped at varying membrane potentials.[151] In addition, network-wide measurements of neuronal bursting demonstrated diverse and inconsistent burst initiation sites, challenging the hypothesis of a few pacemaking neurons that generate network rhythms in cultured networks of neurons.[23]

Emergent synchrony relies on a precise spatiotemporal arrangement of excitatory and inhibitory inputs to induce oscillations (Fig. 2.1.6. A). One model proposes recurrent excitatory and feedback inhibitory wiring as a main motif supporting oscillations. Recurrent glutamatergic inputs support the positive feedback that amplifies excitation, while the negative feedback GABAergic inputs shut down depolarization.[148, 151] With updated knowledge on non-linear and compartmentalized dendritic computations, several supporting mechanisms are recognized to contribute to the network's emergent synchrony, including: (1) feedback modulation of intrinsic excitability via leak currents[24] and threshold adaptations,[152, 153] (2) modulation of synaptic plasticity,[68] (3) dendritic amplification[154, 155] and non-linear dendritic computations,[2, 156, 157] and (4) localized excitatory effect of GABA.[74]These mechanisms, working in concert with the network blueprint, promote synchronization in adult brains and underlie the all-excitatory, oscillatory events in developing brains. It is worth noting that several mechanisms work jointly to contribute to synchrony. For instance, clustered and coincident inputs at dendrites trigger non-linear dendritic events, such as NMDA[156, 157] or calcium spikes[2, 158] (3), associated with bursts at the soma.[158] Neurons receiving coincident inputs more readily fire, as a larger pool of available $Na_V$s allows more hyperpolarized threshold (1).[152] Burst-associated APs reliably back-propagate to the dendrites, relieving NMDA receptors from the $Mg^{2+}$ block at the post-synaptic membrane (Section 2.1.3) (2).[70] Besides potentiating the post-synaptic responses, internal calcium increases at the dendrites strengthen the connections through AMPA receptor amplification (syn. AMPAfication) (2). Finally, synchronous GABAergic inputs reliably excite the post-synapses by modulating the local anion gradients (4).[74] These mechanisms amplify feedback at the cellular level, allowing reliable transmission of information and refining the coincident firing; at a long-term scale, they contribute to defining the neuronal ensembles by strengthening connections between synchronously firing neurons.

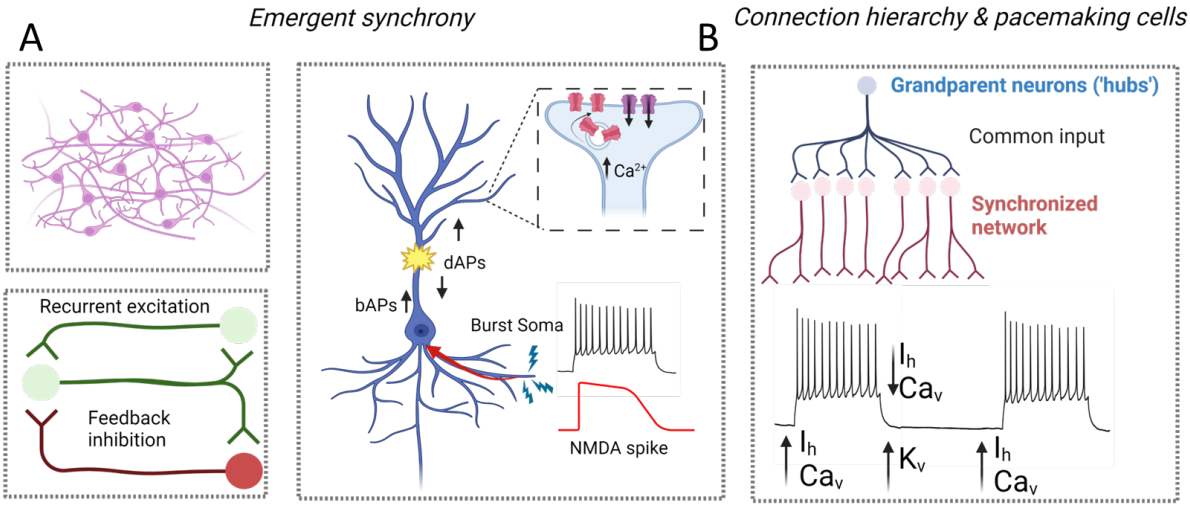


**Figure 2.1.6. Mechanisms underlying the network synchrony.** A. Emergent synchrony proposes SNE formation due to collective network activity (top left square). One of the mechanisms includes synchrony by wiring, i.e., recurrent excitation (green) coupled to the feedback inhibition (bottom left square, red). Right rectangle: Cellular mechanisms contribute to synchronized firing. Coincident and clustered excitatory inputs (green bolts) evoke non-linear dendritic events (NMDA spikes, dAPs), influencing depolarization and bursts at the soma. Somatic APs back-propagate to the dendrites (bAPs), contributing to the generation of dendritic APs (dAPs), further promoting the electrical soma-dendrite coupling. Depolarization at dendritic spines promotes the opening of NMDARs, evoking stronger post-synaptic responses and calcium increases, which contribute to long-term plasticity mechanisms. B. Network hierarchical organization proposes the existence of a few highly interconnected neurons that allow synchrony to act as a common synaptic input. If hub cells show a pacemaking property, they orchestrate the rhythms of the network. Bottom: exemplary intrinsic oscillations and conductivities contributing to the pacemaking rhythms. Ih- hyperpolarization-activated cationic current. Schematics created via BioRender.com.

An alternative mechanism proposes that a small number of intrinsically bursting, highly interconnected neurons act as generators of network rhythms (Fig. 2.1.6. B). This idea was inspired by the functional topology seen in cultured CA3 hippocampal networks, coupled with accumulating evidence that synchronously firing neurons receive converging and coincident excitatory inputs. The recursive structure of converging inputs implies the existence of a few "grandparent" neurons with the capacity to synchronize the parent neurons and, finally, all of the recipient neurons within a functional module.[144] If the grandparent neurons have a capacity to intrinsically oscillate, they can adopt the role of rhythm generators. Indeed, pacemaking cells are found across several brain regions. The intrinsic oscillations emerge from slow membrane depolarization mediated by voltage-gated conductances. In thalamic neurons, these depolarizations start through activation of low threshold, T-type $Ca_v$s (positive feedback) and relax by combining $Ca_v$ inactivation and $K_v$ opening (negative feedback). The pacemaking rhythm continues via hyperpolarization-activated cationic currents, Ih (e.g., via the opening of HCN channels), which supply initial depolarization for T-type $Ca_v$s, and the cycle starts over.[148, 159] A similar mechanism was found for intrinsic oscillatory behavior of CA1 hippocampal neurons.[159] and in reticular formation. Experimental confirmation of rhythm-generating neurons (analogously to conductors in an orchestra) comes from the Cossart group, where a targeted stimulation evoked rhythm changes in the hippocampus *ex vivo*.[159]

## 2.2. Screening and manipulating the activity of the neuronal networks

A high-frequency component of the APs sets the temporal requirements for reliable detection of inter-neuron communication. Electrophysiology methods fulfill this requirement by directly measuring voltage changes at a high (> 10 kHz) sampling rate. This section opens with patch-clamp that provides reliable and targeted intracellular measurements of neuronal signals at the highest signal-to-noise ratio (SNR) (Section 2.2.1). Due to technical limitations, however, patch-clamp is limited to a few neurons at a time, within short recording sessions. Microelectrode arrays (MEAs) are a good approach to screen the network activity at a single AP resolution, over weeks and even months. MEA measurements face two setbacks. Firstly, the poor sealing loses valuable signal to the noise, limiting the information which could be reliably extracted. Secondly, MEA electrodes do not target neurons, and detected signals may originate from multiple sources. The source designation is resolved by spike sorting approaches, whose basics and challenges are introduced in Section 2.2.2. Finally, the imaging approaches are rich in spatial content but lack electrophysiology's temporal resolution and directedness. Calcium imaging, used throughout this thesis, is introduced in Section 2.2.3.

### 2.2.1. Patch-clamp electrophysiology

The patch clamp, invented about five decades ago by Bertil Sakmann and Erwin Neher,[160] remains the golden standard in electrophysiology. In the heart of the technique lies a tight interface between the cell membrane and the glass pipette containing a measuring electrode. This tight contact promotes electrical isolation and thermal noise reduction, allowing acquisition at a very high SNR and detection of the ion currents from individual ion channels.[49, 160] In investigations of the neuronal electrical signaling, patch-clamp provides reliable detection of subthreshold events, granting direct mapping of the functional connections when performed in the multi-neuron regime.[161] As the measuring pipette attaches to the membrane of the neuron, patch-clamp is a targeted, allowing the unbiased identification of the signal's source identity. For these reasons, it found irreplaceable position not only in biophysical studies of the ion channels, but also in studies of basic principles underlying the native intra-neuron computation[162-165] and inter-neuron communication[97, 163, 166, 167], both *in vitro*[164, 165] and *in vivo*[168, 169]. Due to its high temporal and amplitude resolution, patch-clamp is conventionally used to ground-truth the source designation in extracellular recordings (Section 2.2.2)[29, 30, 64, 170] and firing dynamics estimates from functional imaging[34, 36, 171-173] (Section 2.2.3).

A Ag/AgCl electrode in the glass pipette filled with ionic solution measures the ion currents or voltage changes to the bath's Ag/AgCl reference. Both electrodes are connected to the amplifier system via copper pins. Together with the cell, the pairs of electrodes close the electrical circuit and measure the signals via redox reactions. Patch-clamp operates in *current-clamp* and *voltage-clamp* modes. In the former, the membrane voltage responses are detected to injected current,

while the latter comprises measurements of the current responses to voltage injections. When the holding current or potential is set to maintain the membrane potential at a resting value, patch-clamp allows detection of spontaneous activity. To reliably study the dynamics of the voltage-dependent conductivities, the probe is equipped with an op-amp differential amplifier, introduced in electrophysiology measurements by Cole and Marmont (see Nilius 2003[174]). Using a negative feedback loop, the amplifier compensates for the difference between the given and measured potential or current. Patch-clamp amplifier circuitry allows the estimates of voltage-gated conductivities and near-simultaneous tracking of responses to the injected stimuli with a single electrode, unlike initial voltage-clamp design by Hodgkin and Huxley,[58, 175] that required separate stimulation and recording electrodes. The signal is amplified once in the probe and the main amplifier; the latter is also equipped with compensation circuitry and allows signal conditioning.

Giga-seal is one of the most remarkable membrane-material interfaces, with a distance between the membrane and the glass not exceeding a few Å. It persists even after the sequestrated membrane patch is excised from the cell,[176] suggesting stronger lipid-glass than lateral lipid-lipid interactions. At the nanoscale, giga-seal is represented by a membrane-dome structure, with side-lipids interfacing the glass primarily via the Wan der Waals interactions.[177] This interaction is further secured by lateral transmembrane proteins whose extracellular domains denature, forming a high contact area for the glass in a zig-zag structure (Fig. 2.2.1.1. B). Mechanistically, establishing a tight contact requires a close interaction between the pipette and the cellular membrane. The glass pipette containing the measuring electrode is visually navigated to contact the target neuron. Positive pressure is applied during the pipette navigation to keep the pipette tip clean. The latter is further ensured by monitoring the current responses to continuously applied voltage test pulses that read the pipette resistance. A sudden drop in current responses marks the initial pipette-membrane engagement, as the corresponding pipette resistance increases by 10%. Physically, membrane-pipette engagement manifests as an inverted omega dip under the pipette (Fig. 2.2.1.1. A). Following the initial engagement, the pressure is released, and steady suction is applied to protrude the membrane inside the pipette tip. Further suction promotes tight contact with the glass, which is finalized with gigaohm readings (Fig. 2.2.3.1. A, D).[176]

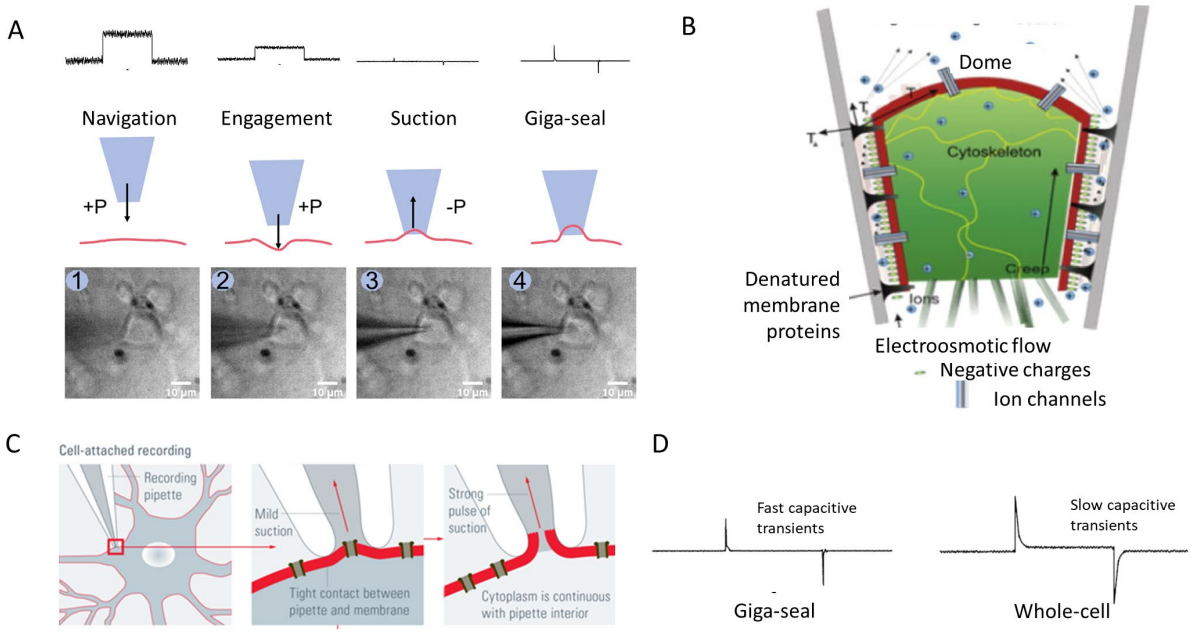


**Figure 2.2.1.1. Mechanistics behind the giga-seal establishment and whole-cell measurement.** A. Pipette-membrane interactions during the giga-seal establishment. Top: pipette currents to voltage test-pulses during the pipette navigation in the bath (1), pipette-membrane engagement (2), suction (3) and giga-seal (4). Middle: schematic overview of membrane-pipette interactions during the giga-seal. Bottom: brightfield micrographs of the neuron-pipette interactions during the giga-seal establishment, showing the onset of dimple formation at the pipette-membrane engagement (2). B. Schematic overview of the pipette-membrane interface following the giga-seal formation. Adapted from: Suchyna et al. 2009, Biophysical Journal[177] C. Acquiring whole-cell configuration following the giga-seal. Schematics adapted from: *https://www.leica-microsystems.com/science-lab/life-science/the-patch-clamp-technique/*. D. Pipette responses to test-pulses after the whole-cell establishment.

Once the giga-seal is established, patch-clamp recording in *on-cell* (syn. cell-attached) configuration can start (Fig. 2.2.1.2. Ai-Aii). If the pipette tip is of a small diameter, this configuration permits measurements from individual ion channels with highly controlled extracellular ionic environment while preserving the composition of the cytosol. *On-cell* provides valuable information on neuronal firing without disrupting the internal milieu. However, the membrane beneath the pipette tip imposes an RC filter causing signal distortion (Fig. 2.2.1.2. B, see also Appendix D for detailed discussion on on-cell filtering effect). Specifically, extracellularly detected APs (EAPs) are about 10x attenuated and 2x wider than intracellularly detected action potentials (IAPs) (Fig. 2.2.1.2. D), while on-cell detected PSPs are 2x attenuated and about 4x wider (Fig. 2.2.1.2. C).[178] Amplitude attenuation causes a valuable signal loss to the noise, while the overall distortion affects the analog information estimates. In addition, on-cell measured $V_m$ is 10-20 mV more depolarized and shows a higher extent of fluctuations, especially when ion leaking is predominant (Fig. 2.2.1.2. B).[178]

In order to reliably detect *whole-cell* membrane changes at a subthreshold resolution, intracellular access is obtained through brief suction pulses or electroporation to rupture the sequestrated membrane patch (Fig. 2.2.1.1. C and Fig. 2.2.1.2. Aiii). In the test pulses, the access to the internal side is manifested via slow capacitive transients, (Fig. 2.2.1.1. D) that arise from

the membrane. Whole-cell circuitry is depicted in Figure 2.2.1.2. Aiii, and comprises of the pipette RC circuit ($R_p$ and $C_p$ connected in parallel), serially connected to the membrane's RC circuit ($R_m$ and $C_m$) via an access resistor ($R_a$, syn. series resistor). Pipette resistance originates from ion flow restrictions imposed by a pipette tip, while the capacitance stems from an insulating glass of the pipette walls sandwiched between the two ionic solutions. The sealing resistor ($R_{seal}$) connected in parallel represents the glass-membrane interface. In whole-cell configuration, the ratio $R_a/R_m$ defines the amplitude accuracy of the whole-cell measurement, due to the voltage drop on the series resistor.

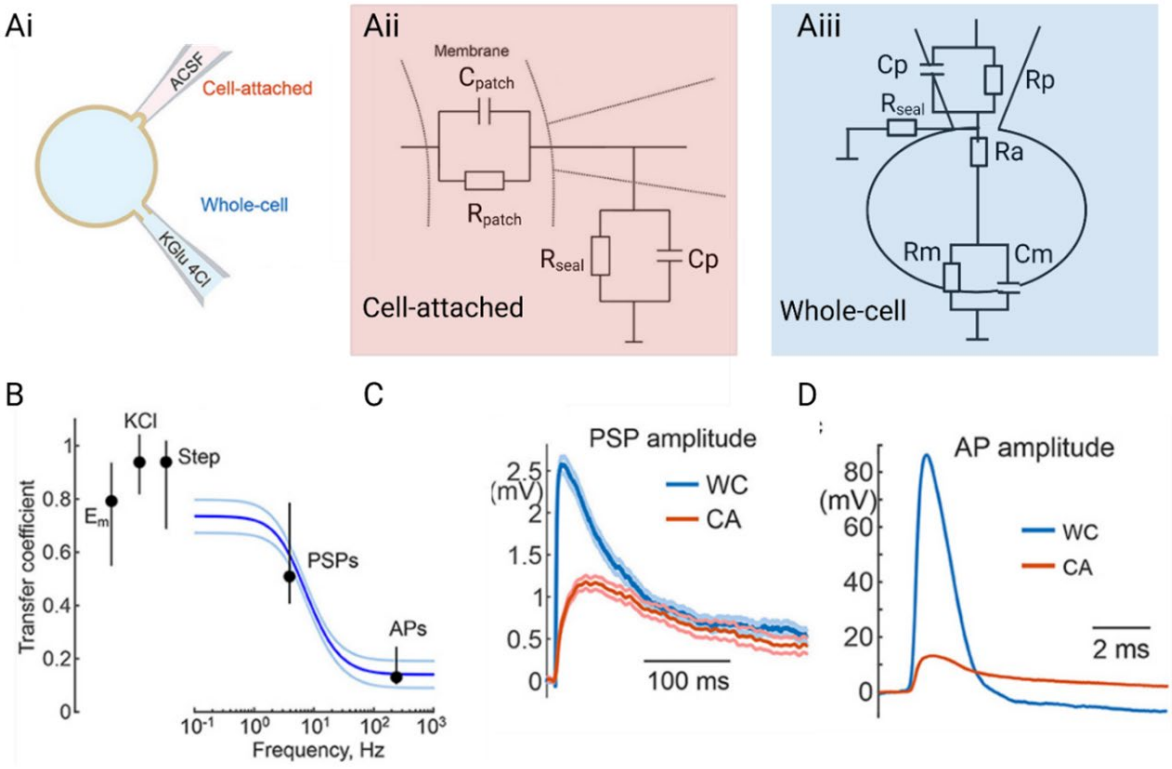


**Figure 2.2.1.2. On-cell vs. whole-cell measurement.** Ai. Schematics of the pipette-membrane interface in on-cell and whole-cell configuration. Aii. Electrical analog of on-cell configuration. Rpatch and Cpatch correspond to an RC circuit for the membrane patch sequestrated by the pipette tip. Rp is omitted because Rpatch >> Rp. Aiii. Circuitry corresponding to whole-cell configuration. B. Amplitude ratio of the membrane events detected in on cell and whole-cell configurations vs. detected signals' frequencies, demonstrating lowpass properties of on-cell configuration. Em – resting membrane potential; KCl – membrane responses to the step extracellular application of 5.5 mM KCl; Step – membrane responses to a 1 s, 50 pA step current injection. X-axis denotes frequency predominating in different membrane events. C. Average PSP waveforms detected in on-cell (red) and whole-cell (blue). D. Waveforms of APs detected in on cell (red) and whole-cell (blue). Figures Ai, Aii, B-D are adapted from Vazetdinova, 2022 [178]. Figure Aiii was created via BioRender.com, according to Molleman 2003.[176]

Giga-seal differentiates the patch-clamp electrophysiology from the classic electrode impalement. In the latter, intracellular access is established through a sharp glass pipette penetration of the membrane, causing ion leakage around the impalement site and membrane depolarizations.[179] In contrast, giga-seal isolates the lateral membrane from the ion leaking leading to a directed ion exchange almost exclusively between the cell and the pipette. In that

sense, patch-clamp is the least perturbing intracellular approach. However, it still suffers from several setbacks. Firstly, the wash-out in whole-cell configuration disrupts the native cytosolic composition, especially in long-term measurements. Although great care is taken to mimic the ionic constitution of the cytosol, the inevitable washout of small signaling molecules is not fully accounted for. This limits duration of the measurements, affecting not only the amount of information extracted, but also introducing bias against the sparsely firing neurons for firing code inferences. Secondly, due to spatial restrictions, patch-clamp limits the numbers of neurons simultaneously investigated (standardly, 2-4[180]). Thirdly, patch-clamp fails to "clamp" the whole neurons, due to a high morpho-functional compartmentalization and axial resistance of the neurites. The space-clamp issue imposes major setbacks when investigating the single-neuron computation and identifying gap-junction coupled neurons. Moreover, membrane deformations associated with the giga-seal formation may impose mechanical stimuli to the target neurons in all patch-clamp configurations. Previous studies on somatotropic pituitary neurons demonstrated the non-negligible calcium responses and membrane deformations.[181] The effects of the membrane deformations during the giga-seal on the target neuron and local circuitry are investigated in Chapter 6.

## 2.2.2. MEA electrophysiology

MEAs allow long-term and direct measurements of electrical signals at a high sampling rate. The activity of the *in vitro* cultures grown on top of the MEAs is sampled simultaneously via multiple electrodes (tens to thousands)[182] organized in a grid. The culture is separated from the contact pads via a glass ring to protect the electronics from salt bridges (Fig. 2.2.2.1. A). Unlike the Ag/AgCl patch-clamp electrode that measures ion fluxes through redox reactions (Section 2.2.1), MEA electrodes are of conductive metals (Au, Pt, TiN, IrOx)[183], detecting via capacitive coupling. APs generated at the electrode-coupled membrane change the local electrical field, inducing the charge accumulations and displacements at the electrode-electrolyte interface. As in the patch-clamp, the measured membrane potential changes are detected with respect to the reference electrode in the bath. An insulating passivation layer covers the non-recording areas, promoting spatial-specific signal detection. Passivation is also absent from the pads that interface and relay the signal to the amplifier. MEA amplifier systems, including the BioMAS developed at our Institute,[184] are represented by the headstage and the main amplifier; the headstage performs initial, hardware-set signal amplification and conditioning, while the main amplifier samples, amplifies and conditions the signal with user-defined parameters.

The cell-electrode interface is represented via a point-contact model (Fig. 2.2.2.1. A).[185] Under the assumption of isopotentiality and non-rectifying conductances at the interface, the junctional membrane is approximated by an RC circuit, comprised of a consistent junctional membrane resistance, $R_j$ (corresponding to the ion channels at the interface), and junctional membrane capacitance, $C_j$ (the interfacing membrane double layer). In planar MEA configurations, a very high $R_j$ closes the Ohmic branch, and the junctional membrane could be further approximated as

a voltage divider.[25, 186] The electrode-cell interface also comprises of an electrical double-layer from the charge separation; this is modeled as cell-membrane electrode interface capacitance, $C_{hd}$. [183, 185] The two capacitors set the high-pass filter that attenuates low-frequency components of the neuronal signals, affecting the detection of the slow and attenuated membrane potential changes, such as PSPs.[25, 185] A strong influence of the capacitive components of the coupling cause EAPs to resemble the first or second temporal derivative of the IAPs.[186] A separate RC circuit ($R_{el}$ and $C_{el}$) models the electrode impedance. $R_{seal}$ connected in parallel models the quality of the membrane-electrode sealing and is inversely proportional to the membrane-electrode cleft. Similar to the sealing resistance in patch-clamp measurements (Section 2.2.1 and Appendix D), $R_{seal}$ influences the proportion of the signal being transferred to the electrode. Besides these parameters, several other interface models detail active interface conductances, membrane-electrode geometry, and the uncovered portions of the electrodes.[183, 187, 188]

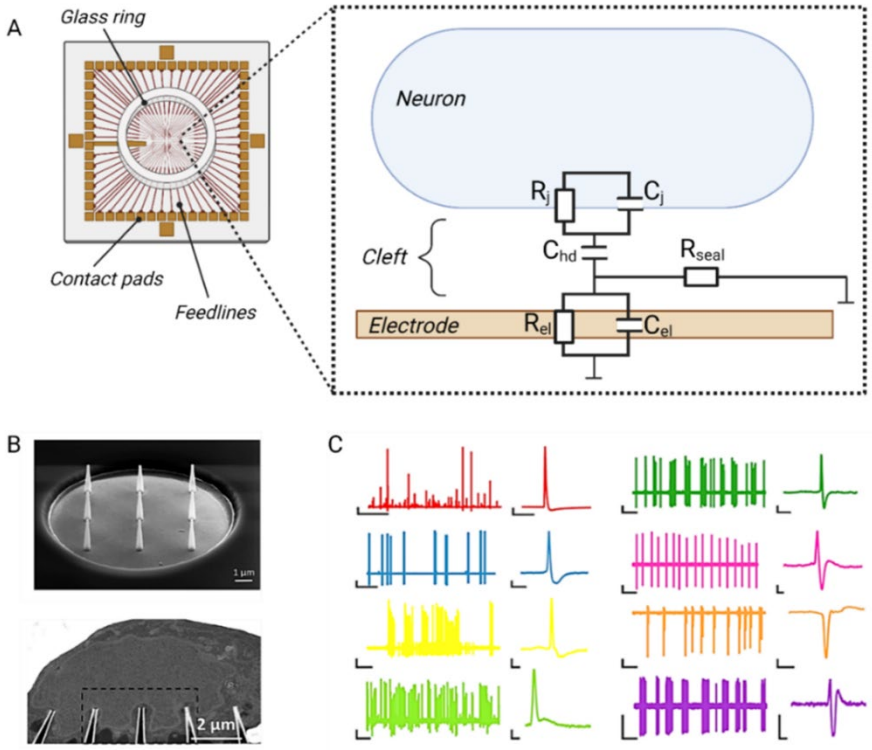


**Figure 2.2.2.1. Basics of the MEA measurement.** A. Left: Standard MEA chip for *in vitro* set-ups. Neuron culture grows on top of the electrode-containing recording area. Pads connect the amplifier and the feedline-connected electrodes. Right: Point-contact model of the cell-electrode coupling (adapted from Joye, 2008 [189]). B. Electron micrograph of the NS-NC MEA electrode (top) and nanostraw-neuron interface (bottom). C. NS-NC MEAs detect high magnitude signals from improved spontaneous cell-electrode coupling. B and C taken from: [27]. Schematics in A created via BioRender.com.

In planar electrodes, the cell-electrode signal transfer shows a significant voltage drop on $R_{seal}$ from a 40-100 nm wide gap,[190] resulting in about 100x attenuation of the signals (EAPs typically < 100 µV).[25] This amplitude reduction imposes a limitation to accurate network activity inferences, as attenuated EAPs are easily overlooked, while PSPs are not visible.[25] The absence of PSP resolution in prevents the direct functional connectivity estimates, and limits the activity inferences to the correlative analyses. These challenges are surmounted by several bioelectronics advances that increase SNR (Fig. 2.2.2.1. B). Among them, the 2D+ geometries[27, 186, 191, 192] arise as long-term and noninvasive solutions, as they promote the spontaneous engulfment of the electrode by the neuronal membrane. Nanostraw-nanocavity MEAs,

engineered at our Institute by Pegah Shokoohimehr,[26] enhance the signal SNR both through promotion of a tight engulfment (nanostraw) and electrode impedance reduction (nanocavity) (Fig. 2.2.2.1. C).[193, 194] Simultaneous patch-clamp and MEA recordings of the electrode coupled neurons, presented in Chapter 4, demonstrated the improved NS-NC electrode's amplitude sensitivity, along with ability to spontaneously detect subthreshold potential changes.

Even with these advances, MEA measurements are non-targeted. Due to a spontaneous, non-guided coupling, a single electrode may detect EAPs from more than one neuron, and, if the electrode density allows, *vice versa*. The unknown signal sources' identities limit the accurate network connectivity estimates and stimulus-evoked responses. As a solution, spike sorting pipelines are applied to the measurements to assign the spikes.[28, 29, 62, 195-197] Under the assumption that a given neuron produces EAP waveforms more similar and collectively distinct from other neurons' spikes, the algorithms sort the spikes based on their waveform similarity. Different flavors of spike sorters share the underlying principle: the found EAPs are sorted such that more similar EAPs comprise a cluster (syn. unit), and follow a similar pipeline[28] (Fig. 2.2.2.2.):

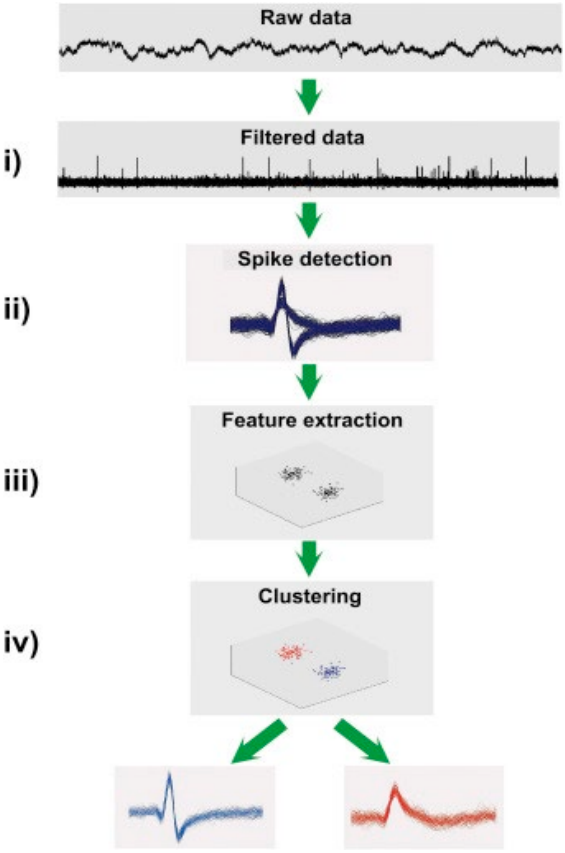


- MEA traces are **filtered**, standardly with a bandpass filter (50 – 4000 Hz) to eliminate slow voltage drifts and high frequency noise;
- Spikes are **detected** by a thresholding algorithm; soft threshold is defined as units of standard deviation of the mean (either of the signal or noise), or median absolute deviation (MAD) (see Table 3.6.4);
- **Feature extraction**–reduces the numbers of the shape features used to estimate similarity; spike waveforms are first aligned to their local maxima and projected to a low-dimensional space via principal component analysis (PCA) or wavelet decomposition;
- **Clustering** on waveform projections in feature space to define clusters of similar spikes.

**Figure 2.3.2.2. Spike sorting pipeline.** From Rey 2015.[28]

The output of the spike sorters are the spike timings labeled by the cluster they belong to. In ideal conditions, a single cluster can be interpreted as a group of EAPs from an individual neuron. However, accurate designation of signal sources is not straightforward since there is no *a*

*priori* information on how many neurons couple to a given electrode. Moreover, EAPs from coincidently firing neurons on the same electrode occasionally merge,[198] while the IAP waveform variations affect the EAP waveform of the single source.[64] The low SNR reduces the spike sorter accuracies both at spike detection and clustering levels: spikes buried in the noise are easily overlooked by thresholding algorithms, and the noise blurs the boundaries between the clusters in the feature space.[199] The misclassification challenges are particularly evident for electrodes engaged in synchronized network activity, since a higher firing correlation during the network synchrony promotes the merging of different sources' EAPs.[198] In addition, neuronal bursts associated with the network synchrony promote intrinsic IAP variations, due to a voltage-dependent inactivation of voltage-gated channels (Section 2.1.2). In turn, network synchrony promotes variation of EAPs and consequent misclassification, even when a single neuron interfaces the electrode.

The accurate signal source designation is relevant not only for fundamental neuroscientific questions, but also when evaluating the efficacy of neuronal differentiation protocols from stem cells. For instance, the overestimation of electrode-coupled neuron-like cells, based on the number of manually curated spike sorter units, may exaggerate the performance of the neurodifferentiation protocols.[200, 201] The unit bias is well-recognized among the spike sorting community, as there are rising community efforts to fully automatize and parallelize spike sorting algorithms (SpikeInterface)[29] and cross-benchmark the current pipelines on existing ground truth datasets (SpikeForest).[30] Many additional features are introduced to increase the spike-sorting accuracy. Some sorters, adapted for standard extracellular measurements, recognize small spikes as biologically relevant and discard artefactual high magnitude spikes (i.e., from movement or light stimulation).[202] Many sorters rely on biological limitations, such as refractory period (Section 2.1.2),[62] to discriminate EAPs from the noise and identify falsely merged clusters. Some sorters implement **template-matching**[2] to deal with overlapping or initially missed spikes.[170, 198, 202-204]The unit bias, most commonly faced in manual clustering and curation steps, is reduced by advanced clustering algorithms that operate without the pre-specified number of clusters,[195-197, 205] and **quality control** steps. The latter integrates quality control parameters, such as presence ratio or cluster distance, to identify when the individual neuron's signals are falsely misclassified into two or more different sorter units.[62]

The advances in spike sorting approaches and community initiatives to optimize, benchmark, and parallelize the spike sorting algorithms led to a striking optimization and streamlining of the process.[29, 30] Accordingly, the SpikeForest consortium reports an accuracy of about 80% for automatized spike sorting algorithms on existing ground truth datasets.[30] However, the current spike sorters are optimized for challenges emerging in canonically low SNR measurements, such

[2] Following the initial pre-clustering, templates are extracted for a subset of waveforms in each found cluster and matched to the original trace; matching signals are removed from the trace, and the process re-iterates until all matching signals are found. This process allows waveform separation of the complex waveforms from two coincident spikes and individual signals' designation to the appropriate cluster.

as those from silicon probes or planar MEAs. With the current advances in bioelectronics promoting amplitude sensitivity, it remains to be elucidated what are the challenges of existing spike sorting pipelines in high SNR traces. For instance, (1) how does a high amplitude resolution affect the spike detection in sorters hard-coded to recognize high signals as artefacts? (2) Does the subthreshold sensitivity affect the accurate spiking sequence estimates, such that both PSPs and APs are clustered in the same unit? (3) Lastly, does a higher amplitude sensitivity cause a higher intra-neuron EAP variability and therefore impact clustering process? As previously stated, answering these questions is not only relevant for understanding the limits of the information extracted about the individual neuron's activities and computations, but also for accurate mapping of functional connections. These questions are further investigated in Chapter 4.

## 2.2.3. Calcium imaging

Calcium imaging is a powerful method for studying the neuronal network's activity using indicators whose emitted light intensity correlates with internal calcium changes. Since internal calcium increases correlate with neuronal electrical activity, the detected light intensity dynamics is a proxy of the neurons' firing. Functional imaging provides a comprehensive overview of the signal's origin by directly visualizing the signal sources and finds a valuable position in *in vitro* as well *in vivo* network neuroscience. In addition to the network activity screening, calcium imaging offers an insight into the single-neuron computations [155, 206] where intracellular recordings fail to inform or are incredibly challenging to obtain. [154, 207, 208] However, as will be discussed in the following paragraphs, calcium imaging provides only indirect, low-pass filtered estimates of the neuronal firing, and one of the current goals is to navigate the translation of the reporter's fluorescence into the neuronal firing code.

The building blocks of the calcium indicators are the $Ca^{2+}$-binding and reporting domain; the binding (or release) of calcium induces conformational changes in the indicator that activate the fluorophore.[3] The $Ca^{2+}$-binding domain, and in particular, the reporters' dissociation constant, determines how sensitive and fast a reporter is.[209] High-affinity reporters show a higher sensitivity for internal $Ca^{2+}$ increases but at the expense of slower fluorescence dynamics. Accordingly, they are most commonly used to report the fractions of responding cells reliably.[172, 209] Vice versa, low-affinity reporters better capture fast calcium transients, such as those associated with the neuronal firing,[210] but at the cost of reduced amplitude sensitivity. The fluorophore defines the excitation and emission spectra of the indicator; the choice primarily depends on the experiment timeline and eventual combinations with other fluorescence

[3] Initially, calcium indicators were based on bioluminescent proteins, such as aequorin. Refer to Grienberger 2012 [32] and Bruton 2020 for a brief and extensive historical overview of calcium indicator development, respectively.

reporters.[171]4 Specifically, indicators that are excited at short wavelengths are more suitable for the short-term recordings, as the long-term exposure induces photodamage.[211]

One of the earliest indicators used a combination of $Ca^{2+}$ chelators and fluorophores, leading to the development of various calcium dyes routinely used in neuroscience,[32, 209] such as Fura-2, Fluo-4, and Oregon green BAPTA[212] (Fig. 2.2.3.1. Ai). These indicators easily permeate the cell thanks to the acetyl ester groups, and do not impose genetic alternations onto the cells. Dye indicators, however, are non-specific to a cell type, invade and chelate organellar $Ca^{2+}$, and gradually reduce the SNR from cytoplasmic clearance.[209, 213] Together with the cytotoxic effect from chronic exposure and interferences with the membrane's physiology,[214] synthetic indicator-mediated calcium imaging measurements are temporally restricted.

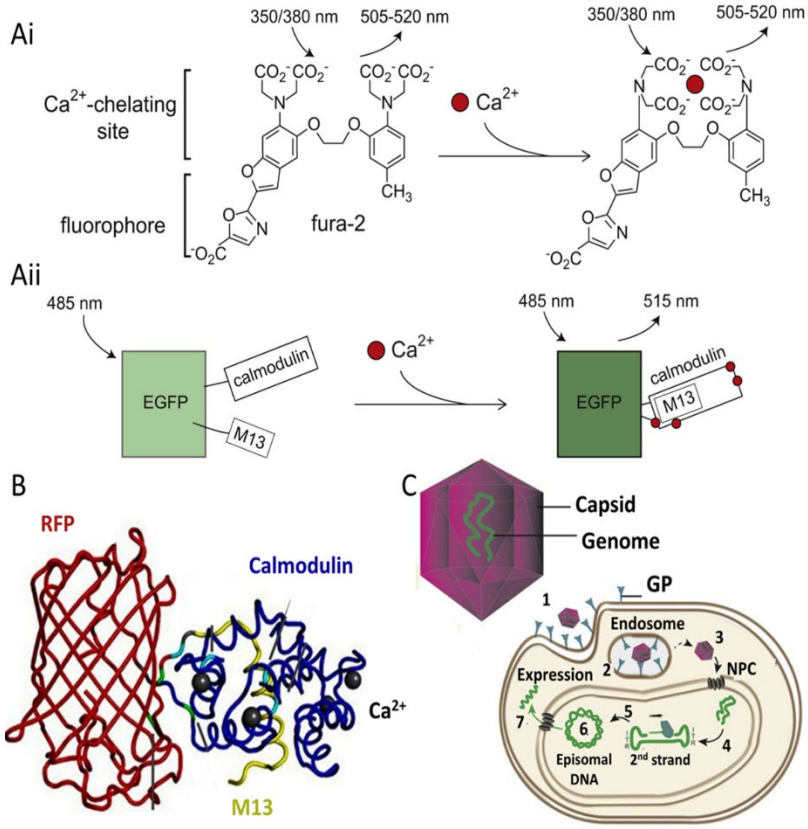


**Figure 2.2.3.1. Calcium indicators.** Ai. Synthetic calcium indicators have the $Ca^{2+}$-chelating site and fluorophore. Depicted the Ca-free (left) and Ca-bound (right) fura-2. Aii. Ca-free (left) and Ca-bound (right) forms of GECI. EGFP: enhanced green fluorescent protein. Numbers on top represent excitation and emission maxima. Adapted from Grienberger 2012. [32] B. Structure of the red GECI in Ca-bound state. RFP – red fluorescence protein. Adapted from Dana 2016. [171] C. Steps leading to GECI expression. Top: AAV containing single-stranded DNA encoding for GECI. Bottom: Infection starts with receptor-mediated endocytosis of the virus (1); GP – glycoproteins. Capsids escape the endolysosomes (2) into the cytoplasm (3). 4. Nucleus entrance via the nuclear pore complex (NPC). 5. Single-stranded DNA acts as a template for the second strand. 6. Circular double-stranded DNA. 7. mRNA synthesis followed by translation. Adapted from Maes 2019.[215]

Genetically encoded calcium indicators (GECIs) are the next generation, recombinant protein-based calcium indicators surmounting some of the challenges. Single protein GECIs represent a hybrid of the calcium-binding (i.e., calmodulin) and reporter domain (Fig. 2.2.3.1. Aii, B). Like the dye indicators, calcium binding induces allosteric changes leading to fluorescence; to further amplify the reporter's conformational changes, GECIs are additionally equipped with calcium-

[4] In in vivo and ex vivo set-ups, the light penetration depth dictates the fluorophore's choice, with high penetrating longer wavelengths being preferred over the short wavelength reporters.

binding domain binding peptide (e.g., M13).[171, 172, 216] The sequence encoding for GECIs is packed into the viral vectors (i.e., lentiviral vectors or adeno-associated viruses (AAVs)), introduced via infection, followed by the read-out and protein expression by the cell (Fig. 2.2.3.1. C). In addition to the GECI-encoding sequence, the recombinant DNA contains the upstream promoter allowing the cell-type specific expression (i.e., synapsin promoter used for neuron-specific expression)[33].

The most frequently used GECIs rely on the green fluorescent protein (GFP) and belong to the GCaMP family[172, 216]; such indicators are excited in the blue light spectrum and emit at the green spectrum. Recent advances in bioengineering bore several GCaMP variants with balanced sensitivity and kinetics, making them especially useful in interrogating neuronal firing. For instance, GCaMP6 variants, developed around a decade ago by Chen,[172] show incredibly high sensitivity to single APs (up to 80-99%, depending on the variant),[5] and rising and decay kinetics faster or comparable to those of the synthetic indicators ($\tau_{rise}$ = [0.05 – 0.18 s] and $\tau_{decay}$ = [0.15 – 0.55 s], depending on the variant).[172] The initiative for long-term all-optical experiments, and the requirements for higher penetration depths *in vivo*, contributed to the development of fast and sensitive red-spectrum GECIs. About a few years ago, comparably sensitive and fast red GECIs were developed jRGECO and jRCaMP[6] (Fig. 2.2.3.1 B depicts the calcium-bound conformation of the jRCaMP1b, which is used in this thesis).[171]

Acquisition settings, including the optical set-up and camera sampling, additionally contribute to the SNR.[209] As the scanning depth and depth-related contaminations do not impose a significant challenge in 2D *in vitro* networks, a standard fluorescent microscope suffices for somatic activity estimates. The primary optical factors universally affecting the spatial resolution and sensitivity of the measurements are the objective's numerical aperture[217] and magnification. The latter determines the field of view (FOV) and photon fluxes collected per soma and influences the SNR. Recent benchmarking of the network-wide, GECI-mediated calcium imaging demonstrated a dramatic reduction in the reporter's sensitivity, as less than 30% of isolated APs could be reliably inferred from the calcium traces (Fig. 2.2.3.2. B).[36]

Fluorescence dynamics which standardly serves as a proxy of the neuronal firing is estimated from the somas, due to their proximity to the AP generation site and large area which yields more photon fluxes per neuron at reasonable illumination settings. Under the native imaging conditions, healthy somas manifest as donuts due to a predominant reporter's expression in the cytosol (Fig. 2.2.3.2. Ai, Bi). This property has been exploited to construct automatic region of interest (ROI) detection pipelines. Automatic ROI detection is often supplemented by manual curation to correct for overlapping ROIs, or neuropil contaminations.[218] Pixel intensities within the ROIs are extracted from previously normalized videos (Section 3.2.2), and spatially averaged within each ROI's borders.

[5] The reported single AP sensitivity is for 30x30 µm fields of view (about 73 px/µm); this is about a 100-fold more pixels per soma than wide-network imaging conditions used in this thesis.
[6] "j" standing for Janelia Institute where the variants were developed.

Translating the calcium traces into the neuronal firing code has been a challenging task for several reasons. Transient calcium increases (spikes) in neurons have a sharp onset and slower exponential decay; the acquired signal is low-pass filtered by the reporter, affecting the $\Delta[Ca^{2+}]_i$ estimates. Further, a calcium spike may not correspond to a single, but rather multiple APs (Fig. 2.2.3.2. Ai). Nevertheless, the magnitude and duration of calcium signals correlate with the AP frequency,[36, 171, 172] and a direct and causal relation between the neuronal firing and calcium signals is often assumed. Specifically, the direct causal relationship is grounded on AP-evoked somatic calcium influxes via high-threshold activated (HVA) $Ca_{VS}$[31] and $Na_{VS}$, [219] while the relationship between the subthreshold membrane potential dynamics and $Ca^{2+}$ influxes, although significant, is often attributed to neuropil contaminations.[31] Accordingly, there are several algorithms focused on the calcium trace optimization to estimate the firing code out of the calcium traces. These include **template-matching** with a single-AP $Ca^{2+}$ spike kernel, [220, 221] **deconvolution**,[222, 223], **supervised neural network** (NN)[224] and **biophysical spiking models**.[35] While these are adequate for the datasets they have been tested on, they can not generalize equally well to novel, unseen datasets, owing to dataset and intercellular differences.[20, 31, 34, 36] Consequently, prior knowledge of the calcium trace-firing code relation is required to calibrate these algorithms. For instance, using template-matching or deconvolution algorithms requires the prior knowledge of the single-AP corresponding kernel, NN models require either re-training or acquisition conditions similar to the training datasets, while the biophysical model demands careful parameter adjustments. While technical differences, such as FOV size, sampling rate, and reporter used, impact the SNR and calcium trace-firing rate inconsistencies across the datasets,[36] they are not the sole contributor.

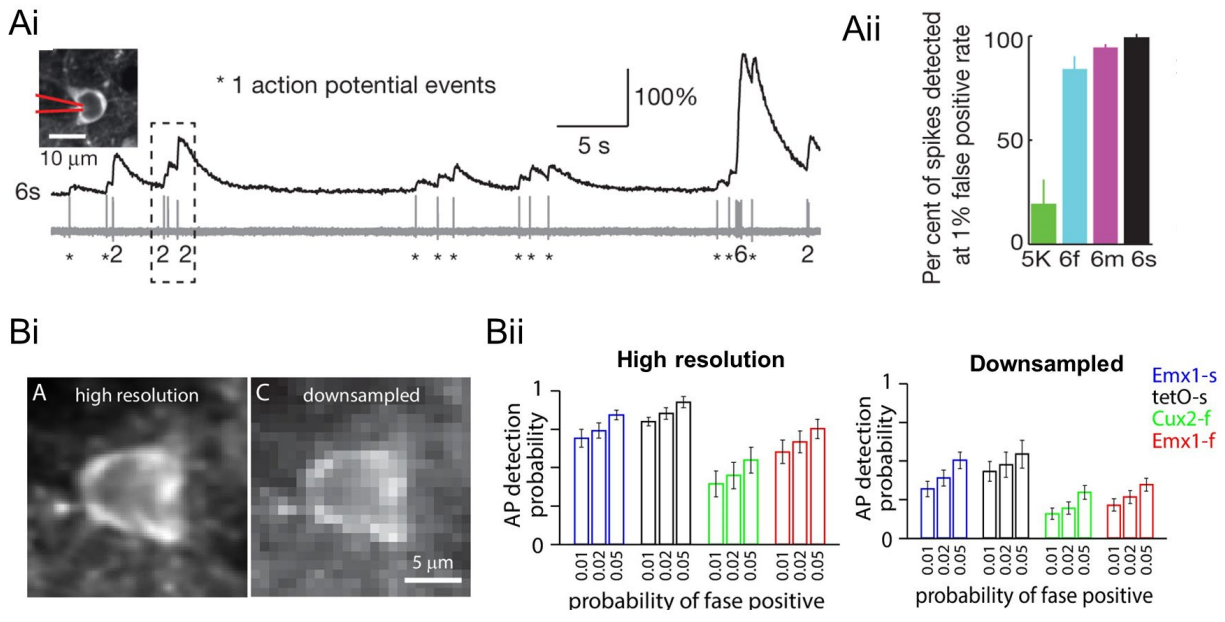


**Figure 2.2.3.2. Calcium fluorescence – firing code relation depends on acquisition.** A. Comparison of the single-AP sensitivities of GCaMP5K, and then-designed GCaMP variants, 6f, 6m and 6s. Ai. Benchmarking of calcium trace-firing rate relationship by simultaneous loose seal cell-attached recordings (gray trace) and calcium imaging

(black trace denotes fluorescence of GCaMP6s) in 30x30 µm FOVs (top left micrograph). Numbers correspond to the numbers of APs, with asterisks denoting single-AP events. Aii. Fraction of single-APs that manifested as visible calcium signals at 1% false positive rate (also see Section 3.6.2. for pipeline details). From Chen et al. 2013b.[172] Reproduced with permission from Springer Nature. B. Single AP detection probability as a function of spatial resolution. Bi. Micrographs of original, high-resolution acquisition (left; 19.3x19.3 µm FOVs) and downsampled micrograph to match 412x412 µm FOVs. Bii. Single-AP sensitivity of high-resolution (left) and downsampled videos (right), as a function of different false detection rates. Color code denotes different mouse lines expressing GCaMP6s (Emx1-s and tetO-s; abbreviations denote promotors under which the indicators were expressed) and GCaMP6f (Cux2-f and Emx1-f). Adapted from Huang et al. 2021.[36]

Firstly, somatic calcium spikes and neuronal firing do not have a one-to-one relation. Calcium is a secondary messenger in signaling cascades that do not directly cause the soma to fire. These include the regenerative synaptically-driven events: dendritic calcium [225, 226] and NMDA spikes[2, 156]. When occurring at proximal dendrites, these events show the capacity to back-propagate to the soma and maintain the membrane in plateau-depolarized state, contributing to additional somatic calcium influxes. Secondly, the contribution of AP-driven calcium influx through high-threshold activating (HVA) $Ca_V$s to the somatic calcium signal may be overestimated, since somas also have low-voltage activated (LVA) calcium channels, such as low threshold activated L-type,[227] R-[228] and T-type $Ca_V$s.[229] Thus, calcium influxes triggered by PSPs, GDPs or UP states, could significantly contribute to somatic calcium signals. Moreover, network-wide synchronization engages additional calcium increases from internal depoes, further contributing to synchrony-related calcium signals that are not directly caused by APs.[230-232]

The recent findings from Huang et al.[36] beg revisiting the chicken-egg question when interpreting the neuronal firing activity from calcium signals. In this work, reduced calcium signal amplitude due to larger FOVs dramatically reduced the sensitivity of calcium traces to single APs (1APs). Importantly, 1AP calcium visibility was inconsistent between the cells and the mouse lines, but also within the same cell. While the differential reporter expression and calcium buffering kinetics account for intercellular differences in 1AP calcium signal visibility, they do not account for inconsistent firing sequence translation within the same cell. On the same token, technical aspects of the same-cell measures, such as slow-paced and gradual bleaching effects, can not explain the reversible and short-term inconsistency in detecting 1AP calcium events. Instead, the inconsistent calcium visibility–firing relation within the same neuron suggests an underlying biological cause. This cause is likely rooted in calcium mechanisms unrelated to firing, as an AP represents a conservative voltage event. While AP waveform variations[66, 67] occur, they should not affect the calcium influx enough to produce inconsistent visibility of 1AP calcium signals (see Section 2.1.2). This is because such sensitivity to the subtle and transient voltage changes would always grant above-threshold 1AP related calcium signals. Rather, the history of the origin of a 1AP may be multi-fold: an AP can originate from a synaptic noise, individual PSPs or UP states that carry different extent of calcium increases[59]. In this case, the membrane electrotonic changes leading to a firing event could be a more reliable representation of internal calcium dynamics co-occurring with an AP. In Chapter 5, I investigate

the membrane potential-calcium dynamics relationship as a step toward more accurate firing estimates.

## 2.2.4. Neuronal responses to mechanical perturbation

The neurons' mechanoresponsiveness (Section 2.1.4) has been majorly exploited to excite and modulate the neuronal networks. Accordingly, several stimulation strategies demonstrated the neurons' sensitivity to a membrane deformation. These range from single-membrane deformations (Fig. 2.2.4. A) via optical tweezers[41] and membrane indentations via magnetic beads[39] or AFM probe[40], to multi-neuron stimulations (Fig. 2.2.4. B) via acoustic waves.[37, 43, 104] In both, the *in vitro* mechanical responses are monitored via imaging,[37, 39, 104, 233] and preferably on platforms mimicking the Young's modulus of the extracellular matrix.[37] These demonstrated the stimulus-induced membrane depolarizations[37] and/or internal calcium increases,[37, 40, 104] whose amplitude scales with the stimulation magnitude,[37, 40] indicating that neurons not only respond to a mechanical stimulus, but are also sensitive to the magnitude applied. While both the single-cell and network-level stimulations demonstrated immediate excitation of neurons, the former focused on the individual neurons' responses,[40, 41] while the latter gave the insights into the collective network's responses.[37, 104]

Among different mechanostimulation modalities found to reliably excite the neurons, ultrasound modulation arises as a particularly promising alternative for a targeted and non-invasive stimulation.[38, 234, 235] Ultrasound neuromodulation bases on administering acoustic waves beyond the hearing frequency (standardly, 0,25 – 43 MHz)[38]. When administered pulses are interspaced by a few ms,[38] ultrasound waves impose mechanical stimulus onto the affected membranes, inducing an immediate excitation[37] followed by long-term neuromodulation.[43] Several properties make US a particularly interesting avenue for neuromodulation. Firstly, US has a fast temporal (< 1 ms) resolution and a high spatio-lateral (< 1 mm) precision[7], allowing fast and precise control over the neuronal populations. Unlike the electrical stimulation, it does not require a close proximity (200 μm) to the target neurons, but readily permeates the brain and even cranium, allowing the neuromodulation without an operational procedure. The US does not require alternation of the genetic make-up for introduction of actuators, providing yet another advantage over optogenetic approaches to manipulate the native brains.

Originally, there were several proposed mechanisms of US-mediated stimulation: membrane cavitation, thermal modulation via dissipated energy, or membrane deformation (for review, see Kamimura 2020[235]; brief discussion also provided in Yoo 2022[37]). Recent *in vitro* studies from Shapiro group confirmed the main excitation mechanism is via the membrane deformation.[37] At the membrane, mechanically gated $Ca^{2+}$ channels; in particular, TRPP1/2, TRPC1, and Piezo1, jointly contribute to the US-induced internal calcium increases, membrane depolarization and

[7] Ultrasound spatio-lateral precision is directly proportional to the US frequency. In contrast, depth precision scales inversely with the frequency of the acoustic waves, where the high-wavelength waves more readily penetrate the tissue.[38]

neuronal excitation.[37] In addition, the neurons subjected to US show long-term (> 8h) increases in intrinsic excitability, likely due to modulation of voltage-gated ion channels and subsequent AP kinetics following the mechanical perturbation.[43] While the mechanisms of US excitation and neuromodulation have been extensively studied, it is still unclear whether the mechanically affected neurons relay the information into the non-target areas, mainly because of the intrinsic multi-cell excitation of the US. The present findings suggested the neuronal mechanoresponses are independent of the neighboring neurons' stimulation, as US-evoked responses do not attenuate in presence of synaptic antagonists.[37] However, the neurons are capable of relaying the signal via alternative means, such as the paracrine communication or gap junctions (Section 2.1.3). It is therefore plausible that a spatial specificity of a mechanical stimulation could be affected by biological component, as mechanoresponses could non-synaptically propagate to the non-targeted areas. In context of mechanical perturbations of individual neurons via the pipette, this question is pursued in Chapter 6.

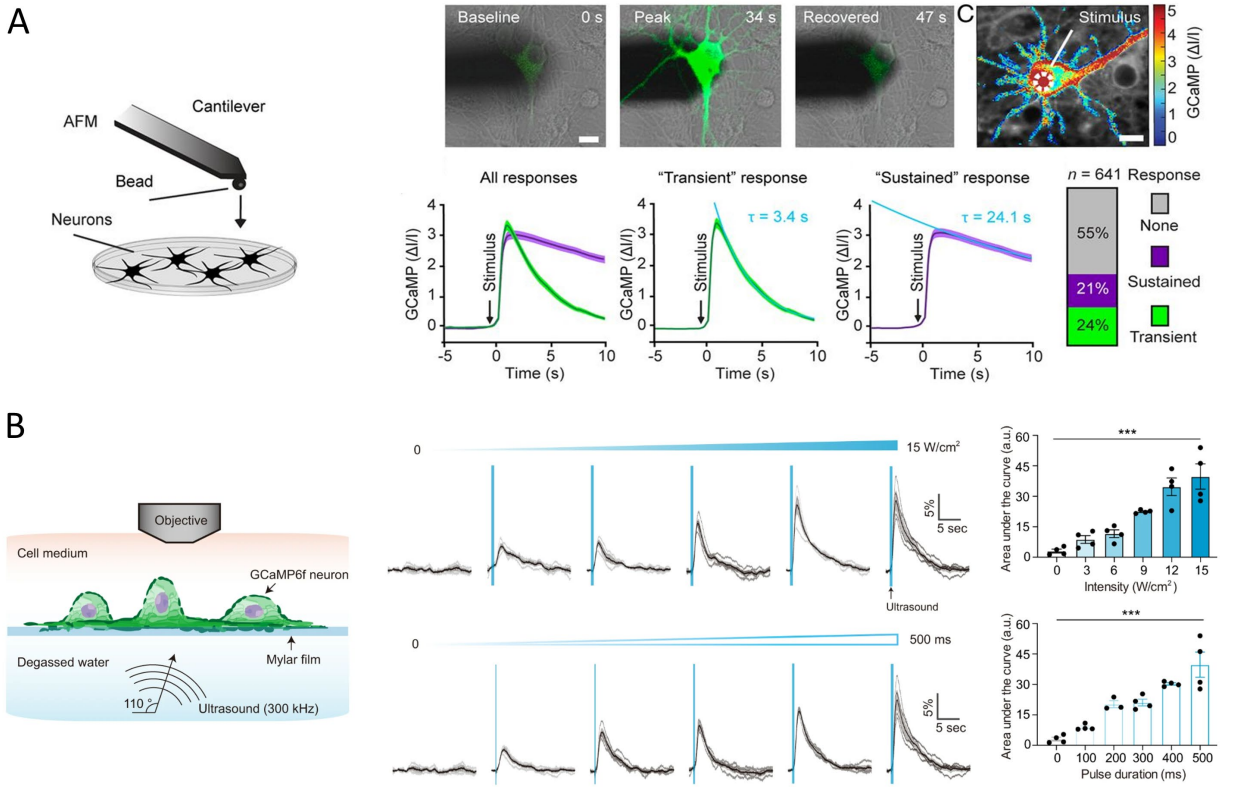


**Figure 2.2.4. Neurons' responses to a single-cell and network-wide mechanical stimulation.** A. Exemplary mechanical responses evoked by AFM-bead membrane indentation (left) of a single neuron. Right: GCaMP somatic responses to membrane indentation. Adapted from Gaub et al., 2020[40]; Copyright (2020) National Academy of Sciences. B. Network responses to ultrasound stimulation (left). Right: Response magnitude scales with US intensity and duration. Adapted from Yoo et al., 2022. [37]

# 3. Materials and methods

## 3.1. Cell culture

### 3.1.1. Substrate preparation

Cell culture samples were sterilized and functionalized up to 7 days before plating, parafilm-secured, and stored at +4ºC. For imaging purposes, neurons were plated on 12mm glass coverslips. Prior to plating, glass coverslips were sterilized by fire. Coverslips were coated through a 1h incubation with 0.01 mg/ml Poly-L-lysine (PLL, Sigma) in Hank's Balanced Solution (HBSS). The residual PLL was removed by a 3x washing in HBSS.

For neuronal cultures grown on MEAs, the chips were re-used. Following the culturing period, the cell layer was removed through a 2x 15-min trypsinization via 0.05% trypsin – EGTA (Life Technologies). MEAs were then treated with 1% Tergazyme (Alconox) for up to 30 min to remove the cellular residuals, followed by a 24-h washout under de-ionized water. Thoroughly cleaned MEAs were either immediately coated and re-used or $N_2$-dried and stored at a room temperature (RT). Cleaned substrates were sterilized either in 70% ethanol, or additionally with 1 h UV treatment (procedure in Appendix B). Chips underwent the same coating procedure as glass coverslips.

### 3.1.2. Neuronal culture

Animal experiments were done according to the Landesumweltamt für Natur, Umwelt und Verbraucherschutz, Nordrhein-Westfalen, Recklinghausen, Germany, Number 81-02.04.2018.A190. Cortices were isolated from Wistar rat embryos at E18 after sacrificing the mother through decapitation under CO2 by trained personnel. Isolated cortices were placed in a non-supplemented Hibernate A medium (Life Technologies, Gibco) and placed at +4ºC. The tissue was enzymatically digested for 10 min at 37ºC via 0.05% trypsin-EDTA (Life Technologies). The digested tissue was 5x washed in a Neurobasal medium (Life Technologies), supplemented with 0.5 mM glutamine (Life Technologies), 1% B27 (Life Technologies), and 100 µM gentamycin (Sigma) (NB). At the last washing step, a gentle mechanical trituration via the 1ml pipette was performed to promote further dissociation. The cells were centrifuged at 1100 rpm for 2 min, and the pellet was suspended in a fresh, supplemented NB-medium. Following the cell count in Trypan blue (Sigma), the desired amount of neurons were plated onto the PLL-coated substrate containing pre-heated NB medium. Neurons were incubated at 37°C and 5% $CO_2$. Culturing conditions favored neurons over glial growth. The medium was half-exchanged twice per week, and measurements started on DIV 21.

### 3.1.3. Transduction

For calcium imaging, neurons were transduced with jRCaMP1b AAVs on the 14th DIV (MOI: $2x10^5$ GC/cell). The desired quantity of viruses was carefully thawed and mixed with the pre-heated NB medium. The total surface/volume area was halved to increase infection probability by removing ¾ of the pre-existing medium and adding ¼ of the AAV-containing medium. This configuration allowed effective infection while preventing eventual osmotic shocks as in full-medium changes. The AAV construct, pAAV.Syn.NES-jRCaMP1b.WPRE.SV40 was from Addgene, via Douglas Kim & GENIE Project (Addgene plasmid # 100851)[171]. The transduction efficiency was 81%.

## 3.2. Imaging

### 3.2.1. Calcium imaging of neurons – recording set-up

Calcium imaging was done on 21-29 DIV jRCaMP1b transduced neurons in bath solution for patch-clamp described in Table 3.3.1. The subcellular localization of the calcium signal, the fluorescence intensity, and the neurons' morphology under the jRCaMP1b filter were indicative of the culture's fitness and served as a reference for designing the exclusion criteria for unhealthy neuronal cultures. Healthy cultures displayed medium-intensity signals abundant in cytoplasm but absent from nuclei (Fig. 3.2.1. A). In contrast, unhealthy neurons showed a strong fluorescence also in the nucleus, indicative of apoptosis-related calcium accumulation. The poorest health cultures also displayed neurite degradation, indicative of the later stages in the cell death (Fig. 3.2.1. B).

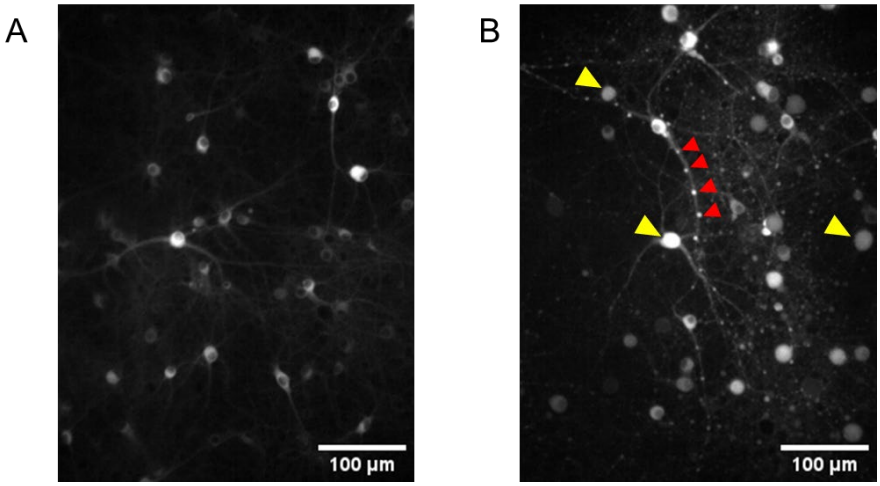


**Figure 3.2.1. Estimating neuronal fitness from jRCaMP1b signals.** A. A micrograph of a native neuronal network expressing moderate fluorescence within the cytoplasm, but not within the nucleus. If visible, neurites form a continuous network. B. Micrograph of the same culture that underwent excitotoxicity due to >1h treatment in Mg-less solution and 50 µM glutamate. The presence of jRCaMP1b signal within the nucleus (yellow arrows) is indicative of the apoptosis onset. Red arrows mark the neurite fragmentation typical for the later stages of neuronal death.

Imaging was under an AxioScope upright microscope (Carl Zeiss AG) coupled to a Zyla sCMOS camera (Andor). For illumination, an HBO 100 W lamp (Zeiss), with 153.7 mW/cm$^2$ power density was used, and the jRCaMP signal was detected through a BP 546±12 nm excitation and LP 590 nm emission filter. A 0.2 mm$^2$ field of view was imaged through a 20x UMPlanFl objective (Olympus), while a 10x air objective Epiplan (Carl Zeiss) was used for 3 mm$^2$. Since the calcium imaging was preferentially done in conjunction with electrophysiology recordings on the same PC, the RAM limitations majorly influenced the quality of the imaging. During the simultaneous patch-clamp and calcium imaging, the acquisition was lowered to 50 Hz with 0.02s exposure to reduce the RAM consumption. Further, the pixels were binned at 4x4 to increase the sensitivity of the weak fluorescence signals and reduce the number of pixel values stored per imaging region. This reduced the time required for image acquisition at the expense of spatial resolution. For 3 mm$^2$ recordings, the air objective caused a fluorescence intensity loss. Here, the exposure was at 0.03-0.04 s to increase the signal sensitivity while preserving the spatial resolution. Accordingly, 3mm$^2$ videos were used exclusively to determine the extent of single-cell stimulation influence on the network.

A subset (N = 34) of calcium imaging only records of spontaneous activity was on inverted Axio Observer.Z1 microscope (Zeiss) coupled to the 5.5 sCMOS camera (PCO) and Colibri.2 LED (Zeiss) illumination at 63.75% of the maximal intensity. Here, the jRCaMP1b signal was detected with the 43 HE filter set (Zeiss) (538-562 nm BP excitation, 570 nm FT dichroic mirror, and 570-640 nm BP emission filter), through a 10x Plan-Apochromat (Olympus) objective. A similar FOV of 0.2 mm$^2$ was ensured by adjusting the recording area size (160 x 260 px at 0.39 px/µm). Pixel binning, exposure and acquisition rate were the same as in the AxioScope imaging. Since both imaging conditions gave rise to similar SNR and activity profiles (Fig. 3.2.2), the two datasets were merged for evaluating the network synchrony and spontaneous calcium spike properties in Section 5.1.

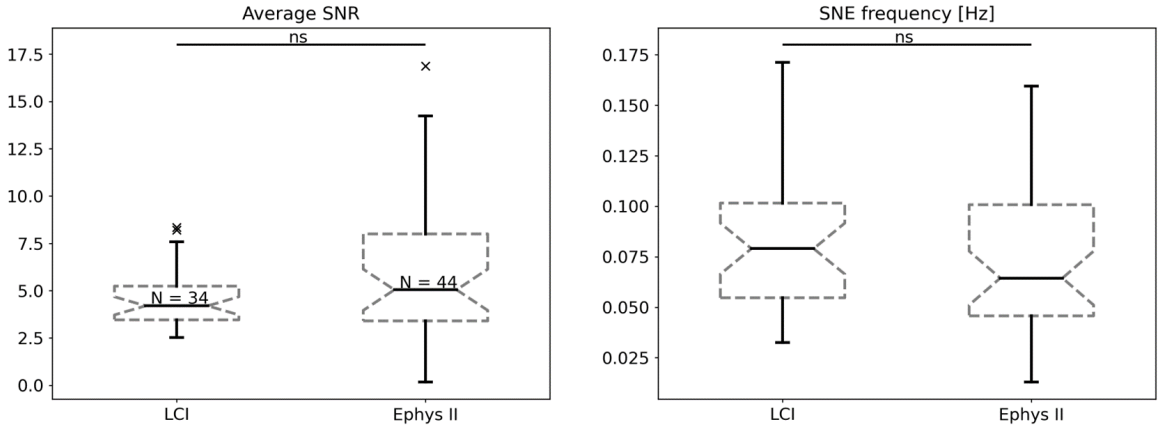


**Figure 3.2.2. Calcium activity imaged with the two set-ups.** SNR and SNE frequency obtained by jRCaMP1b imaging on AxioObserver inverted microscope (on LCI set-up) and AxioScope upright microscope (on Ephys set-up).

## 3.2.2. Image processing

Calcium imaging videos were processed through a custom-made analysis pipeline, established at our Institute by Timm Hondrich.[236] ROIs were fist automatically detected through maximum intensity projection (MIP)-defined borders. The MIP was calculated as a 2D (x, y) matrix of maximum intensity for every pixel throughout a movie, previously normalized to a frame-defined median. MIP is then iteratively convolved via the wavelet kernel [1,4,6,4,1], to weigh the pixel intensities by its surroundings. The B-spline wavelet functions aimed to enhance the pixel intensities within the oval shapes of somas and discriminate background fluorescence. In the next iterations, the convolution was performed on differences between the previous convolution's input and a wavelet function, with kernel expanded with zeroes to increase the spatial area. Within this thesis's dataset, the optimal number of convolution rounds was 3. ROI borders were detected from an 8 px- long sliding window on a binarized filtered image from the iteration of wavelet decomposition. On average, the automatic ROI detection accurately detected about 80% of the ROIs. However, automatic detection failed to discriminate between overlapping ROIs, and frequently expanded somal borders to include proximal neurites; these were manually curated in `SamuROI` GUI.[218] Mean intensity traces within each ROI were then normalized to a baseline ($F_0$), the 5$^{th}$ percentile of a 2000 frames wide sliding window. For the automatic calcium spike detection, normalized traces were filtered by a 3Hz Butterworth low-pass filter. In the upcoming chapters, filtered calcium traces were depicted for clarity, while $dF/F_0$ always denotes the signal amplitude of filtered traces normalized to the baseline.

## 3.2.3. Actin cytoskeleton imaging

Actin imaging was performed by Florian Friedland, at IBI-2 (Mechanobiology Institute). Briefly, the actin cytoskeleton was imaged to evaluate the efficacy of actin-disrupting treatment via a 5 h incubation in cytochalasin D. All chemicals were purchased from Sigma Aldrich, except Nuc Blue Fixed Stain (Invitrogen). The cells were fixed with 4% paraformaldehyde for 20 min RT. Cytoskeleton buffer (CB), containing [in mM]: 5 EGTA, 5 glucose, 10 MES, 5 $MgCl_2$, 150 NaCl, 1.72 streptomycin was used for washing, permeabilization and staining. Samples were first washed by RT CB containing 30 mM glycine, and then 3x with cold CB. The samples were permeabilized by 0.1% TritonX for 10 min and blocked with 5% milk powder for 1 h at RT. Following a 3x washing in cold CB, samples were incubated for 1 hour with Phalloidin-488 (1:500) at RT. Samples were stained with Nuc Blue Fixed Stain for 10 min, washed 3x in cold CB and stored at 4°C in darkness. An Airy scan detector in "Resolution vs Sensitivity" mode at an LSM 880 (Zeiss) equipped with a Plan-Apochromat 63x/1.4 Oil DIC M27 objective (Zeiss) was used for imaging.

## 3.2.4. Neurobiotin injection and gap junction visualization

Neurobiotin (ThermoFisher) tracer injection and visualization by streptavidin-Alexa 488 (ThermoFisher) was to visualize electrically coupled neurons. Neurobiotin belongs to small

(322.8 Da) hydrophilic molecules and does not cross the membrane unless injected. Accordingly, the only route of interneuronal propagation is through GJCs. Compared to the small fluorophores, such as Lucifer Yellow or Propidium Iodide, Neurobiotin diffuses to a greater extent because of its smaller size. Neurobiotin treatment requires additional steps to visualize the injected cells. Schematic overview of the procedure is given in Figure 3.2.4. Target neurons were iontophoretically filled with membrane-impermeable tracer via a patch pipette containing 10% (v/v%) neurobiotin. In whole-cell (see Section 3.3.1), 0.5 s 200 pA current pulses, at 1Hz were applied for 5-10 minutes, followed by a 10 min free diffusion. [237] The injected neurons were incubated at 37ºC for at least 1.5 h to allow propagation into the neurites and the neighboring cells. The samples were fixed overnight by 4% PFA at +4ºC. Cells were treated for 1-2 h at RT with a pre-mixed solution for permeabilization, blocking and staining, containing 0.25% Triton-X, 2% BSA, and streptavidin-Alexa 488 (1:300). [238] Visualization was on an AxioVision upright microscope, under 20x objective (Olympus) and BP 450-90 nm excitation and LP 515 nm emission filter. The micrographs were taken via Zyla sCMOS camera.

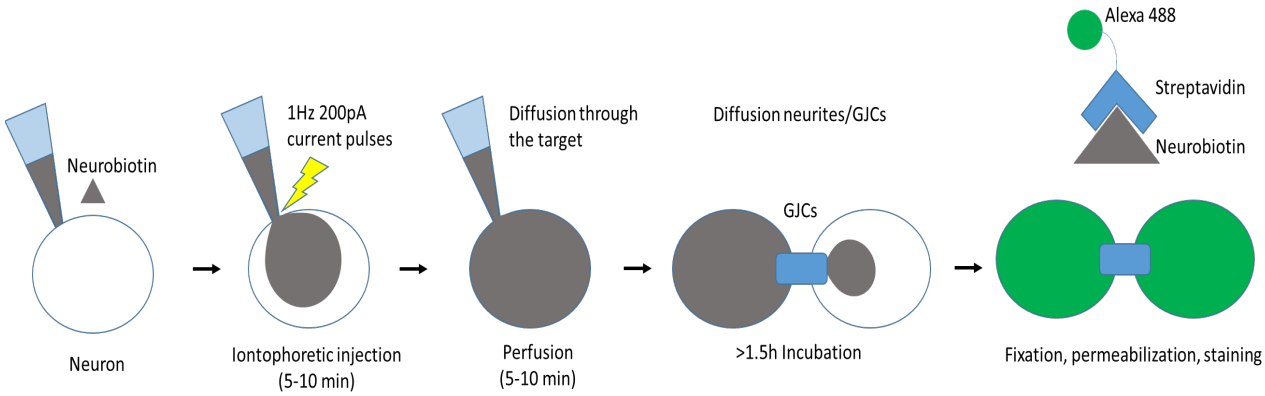


**Figure 3.2.4. Visualization of electrically coupled neurons via Neurobiotin injection.** Neurobiotin is administered through the patch-pipette in whole-cell configuration, through iontophoresis followed by diffusion. After incubation to allow tracer propagation to the neurites and neighbors, neurons were visualized with streptavidin-Alexa488 complex.

# 3.3. Electrophysiology

## 3.3.1. Whole-cell patch-clamp

Patch-clamp experiments were at a room temperature (RT), under the atmospheric (0.04-0.1%) $CO_2$, and were terminated after 2 h. The recording system is comprised of a standard electrophysiology set-up placed on an anti-vibrational table inside the Faraday cage, to reduce the influences of mechanical and electrical interferences (Fig. 3.3.1). Patching was guided by an AxioVision upright microscope under the 20x water objective (Olympus) or 10x air objective Epiplan (Carl Zeiss). This configuration allowed the cell visualization from non-transparent samples. As a reference, a Ag/AgCl pellet electrode was used. Giga seal was established after the pipette was positioned several µm above the target cell via Luigs & Neumann SM I micromanipulator. The pressure was controlled via a 10 ml syringe, connected to a parafilm-

secured tubing system via a T-valve. Whole-cell patch-clamp was done in bath solution (procedure in Appendix B), whose constituents are given in Table B2. Micropipettes were pulled from a fire-polished 1.5 mm borosilicate glass with a laser puller (P-2000, Sutter Instrument) and filled with K-gluconate containing pipette solution, described in Table B3. With these, pipette resistances were in the 5-10 MΩ range. Current responses to 5 ms, 5 mV pulses were used to navigate the experiment.

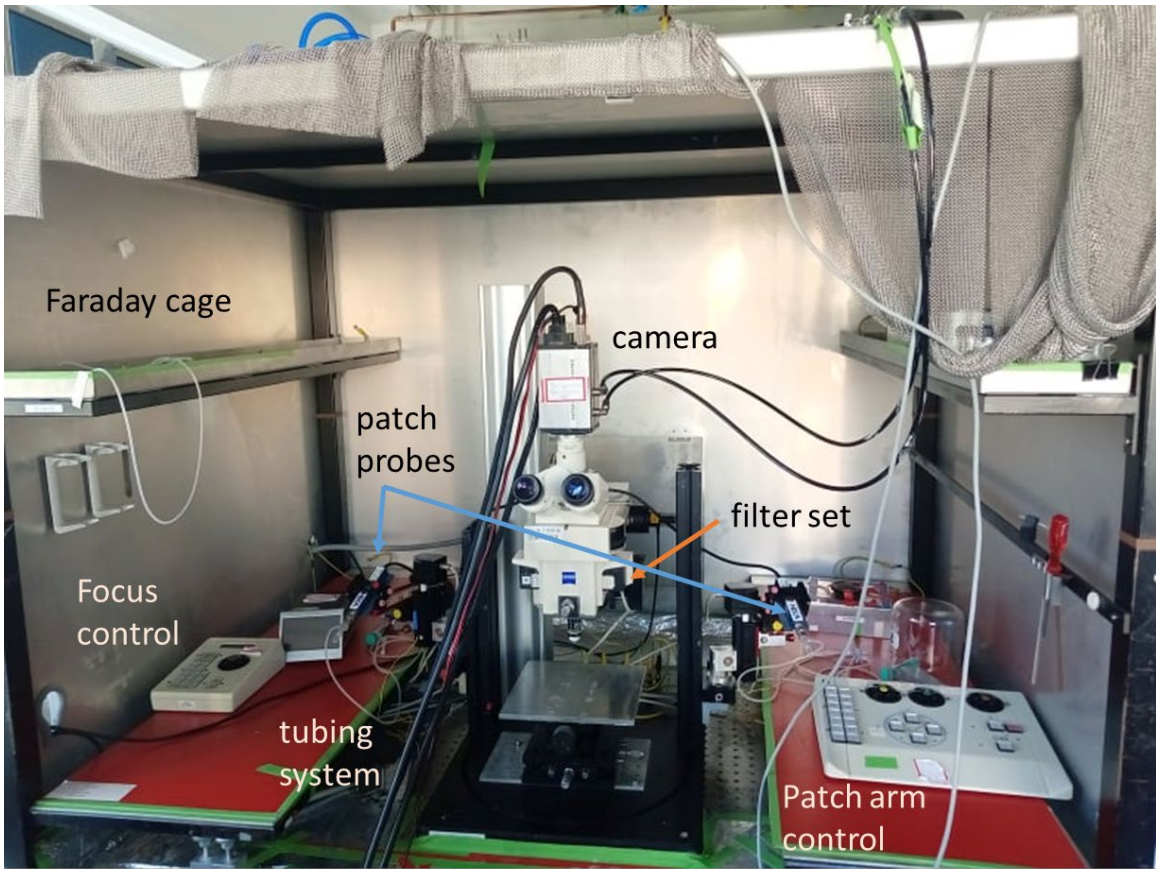


**Figure 3.3.1. Electrophysiology set-up.** Measurements were performed in a Faraday cage, on an air table to reduce the electrical noise and mechanical drifts. An upright microscope was coupled to the camera and equipped with fluorescence filters for simultaneous patch-clamp and calcium imaging. Focus and pipette navigation were via Luigs & Neumann controllers.

When performed under the brightfield, giga-seal was both visually and electrically guided. Here, the initial pipette-electrode engagement was indicated as a dimple formation underneath the tip, while simultaneously the pipette resistance increased by 0.1 - 0.6 MΩ. The subsequent pressure release and slight but steady suction allowed the protrusion of the membrane inside the pipette tip and giga-seal formation. Fast capacitive transients due to the borosilicate glass sandwiched between the two ion solutions were in the 5-7 pF range and compensated after the giga-seal. Brief suction pulses were then applied via a 1 ml syringe to rupture the membrane underneath the tip. Slow capacitive transients due to the membrane bilayer in test-pulse responses were indicative of intracellular access. Membrane capacitance and resistance were either read out from PatchMaster, following the compensation, or estimated *post-hoc* from the uncompensated

records (for details, see Section 3.6.1). Either in voltage- or current-clamp mode, a negative current was applied to keep the membrane potential at – 60 mV.

The liquid junction potential was experimentally determined according to Appendix B, and for this set of solutions was +13 mV. The acquisition was via HEKA EPC 10 dual USB patch-clamp amplifier (Heka Electronics GmbH) coupled to PatchMaster v2.901 software. Signal was sampled at 10-20 kHz and low-pass filtered at 10 kHz (filter 1) and 3 kHz (filter 2) and digitized in +/- 10 V ADC range.

## 3.3.2. Combined patch-clamp and calcium imaging

Synchronization of HEKA EPC10 patch-clamp amplifier and Zyla sCMOS camera was reciprocal and hardware-defined. Both of the instruments shared the same internal clock, as they communicated to the same PC. For combined measurements, EPC10 triggered imaging 10 ms after the start of recording, and Zyla sent electrical pulses to an auxiliary channel of the EPC 10 (Fig. 3.3.2) with every taken frame. To prevent the patch amplifier saturation during the Zyla electrical pulses, EPC10 was connected to Zyla via a 1 GΩ voltage divider. This configuration allowed the post-hoc alignment of electrophysiological signals and calcium traces with respect to the first detected frame on EPC10 from Zyla's input channel, while monitoring the camera's sampling precision.

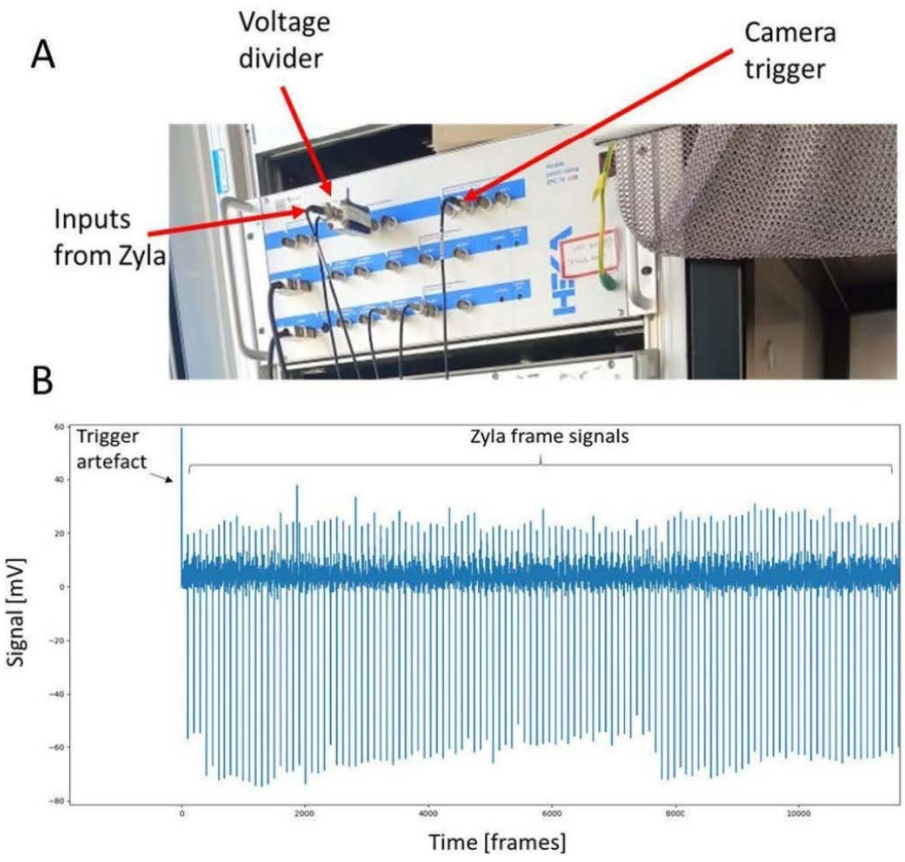


**Figure 3.3.2. Synchronizing the patch-clamp amplifier and calcium imaging camera.** A. Hardware synchronization at HEKA EPC 10 amplifier. The left arrows indicate the camera's input to an auxiliary EPC10 channel with every taken frame. The connection is via a voltage divider to prevent the amplifier saturation. The right arrow points to the EPC10 output to trigger the onset of calcium imaging recording. B. Auxiliary channel containing Zyla's inputs to the EPC10.

The manual switching between the brightfield and jRCaMP was a source of vibrations that could interfere with the stability of patch-clamp measurement. If performed after the giga-seal, these interferences would cause a mechanical drift and risk the formation of an inside-out configuration. In the case of manual filter switch while in whole-cell, the drift could again influence the seal stability, yielding the outside-out configuration. To perform simultaneous patch-clamp and calcium imaging without interferences with the recording stability, a semi-blind approach was performed. Here, the pipette was positioned about 10 µm above the target and centered under the brightfield prior to start of the recording. Relative pipette locations preceding the combined measurements were read out from a Luigs & Neumann SM IV focus control. Following the start of the calcium imaging video, the giga-seal was established under the jRCaMP1b filter, by relying on the pipette responses to electrical test-pulses.

## 3.3.3. Microelectrode array recordings

Microelectrode arrays used in this thesis were designed and fabricated by Pegah Shokoohimehr (the fabrication details can be found in [26] and [27]). The electrode designs were either nanostraw-nanocavity, or nanocavity only. Briefly, the arrays contained 64 electrodes arranged in an 8x8 grid and distanced by 200 µm. In either design, MEAs were fabricated on silicon wafers covered by 1 µm thick $SiO_2$, with 200 nm thick Au or Pt for the feedlines and electrodes adhered to the wafer via a 20 nm thick Ti layer. Chromium was used as an adhesive between the metal and $SiO_2/(Si_3N_4/SiO_2)x2$ (ONONO) passivation, and as sacrificial layer for cavity development. $TiO_2$ nanostraws were engineered to be about 2.4 µm high; their number and pattern depended on the electrode opening, with 5 NS for 6 µm and 9 NS for 10 µm diameter electrodes. In both configurations, a 2 µm pitch was selected to promote a tight engulfment. In their final configuration, NS-NC or NC MEAs had 62 recording electrodes with 30 µm diameter cavity and 6 or 10µm electrode opening (Fig.3.3.3.A), while the remaining 2 unstructured, flat electrodes had a 160 µm opening and served as orientation reference (Fig. 3.3.3. B).

MEA measurements were conducted at RT, in a bath solution described in 3.3.1. As with the patch-clamp recordings, recording sessions terminated after 2h, and the neurons were either put back to a designated incubator for successive measurements, or trypsinized. As a reference, a pellet Ag/AgCl electrode was used. The MEA signal was acquired through the Bioelectronics Multifunctional Amplifier System (BioMAS) (Fig. 3.3.3. C)[184]. The immediate amplification (theoretical gain: 10.1) was at 64-amplifier headstage (MEA III.1), followed by a user-defined 1-100x amplification within the main amplifier. In the scope of this thesis, a total gain of 101-1010 x was used. The signal was acquired at 10 kHz and digitized under a 20 V ADC range via the USB-6255 DAQ (National Instruments). At headstage, the signal was hardware low-pass filtered at 7.2 and 8.8 kHz, to reduce the fast noise component and prevent the signal aliasing. At the main amplifier, the signal was high-pass filtered at 10 or 72 Hz, to accommodate voltage drifts and slow potential fluctuations. Signal acquisition and conditioning were via a LabView script

developed at our Institute. Individual recordings were stored as .dat files with accompanying metadata in .xml.

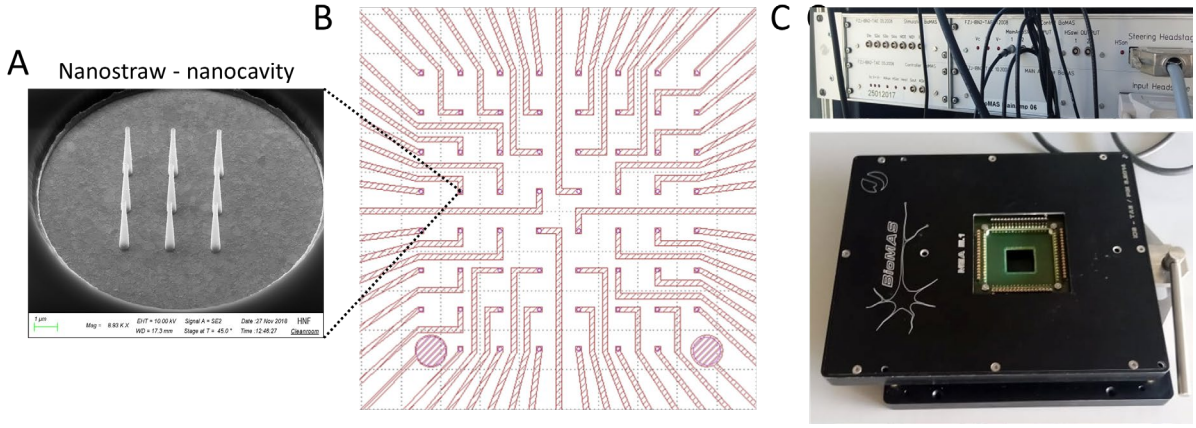


**Figure 3.3.3. MEA measurement set-up.** A. Scanning electron micrograph of nanostraws in recording electrodes of 10 µm opening diameter, engineered by Pegah Shokoohimehr; taken from [27]. B. The layout of 8x8 MEA chip. Two bottom electrodes served as a chip orientation reference and were excluded from the analysis. C. MEA acquisition system. Top: main BioMAS amplifier for conditioning, amplification, and user-defined acquisition through a LabView script. Bottom: MEA III.1 headstage with theoretical 10.1 gain and hardware-defined low-pass filtering.

## 3.3.4. On-chip patch-clamp measurements

Simultaneous MEA and patch-clamp recording were established through a mutual, reciprocal synchronization of BioMAS and HEKA (Fig. 3.3.4). Patch-clamp current and voltage signals were sent to an auxiliary BioMAS channel, and HEKA received a specified channel's signal via an auxiliary input. Both systems were connected to the same PC and shared the internal clock, and no further synchronization steps were required.[182] When performed simultaneously from 64-electrodes, patch-clamp and BioMAS recordings were triggered manually and correlated through reciprocal inputs. While EAPs could be extracted either directly from the BioMAS or the selected BioMAS channel's output fed into the HEKA, the correlation with the intracellular trace was on the latter, to avoid time-shift adjustments and spike omission due to inconsistently triggered intracellular and extracellular measurements Fig. 3.3.4. B. In particular, as long as BioMAS relayed the selected channel's signal in TimeSeries mode, HEKA received the extracellular trace synchronously with the intracellular record, and throughout the whole patch-acquisition. As shown in Fig. 3.3.4. B, EAPs from the HEKA's auxiliary channel show a good match with the BioMAS output, indicating that the patch-clamp amplifier did not distort the received EAP waveform.

Paired recordings were in a bath solution given in Table 3.3.1. In this set of measurements, the pipette solution contained symmetric chloride concentrations, as described in Table B4. The experimentally estimated LJP of +4 mV was not corrected. Both systems shared the same pellet Ag/AgCl electrode as a reference, to avoid multiple reference potentials. Since the main goal was to evaluate the improved amplitude resolution of NS-NC MEAs, patch ROIs were mainly

focused around the electrodes showing spontaneous high-amplitude EAPs prior to the benchmarking. Thus, the paired recordings served to gain an insight into the cell-electrode coupling, and should not be interpreted as an absolute measure of the overall NS-NC MEA performances. Following the experiment, brightfield micrographs of the target neuron were taken to for evaluation of the neuron's size and soma-electrode distance (Section 4.2). Image acquisition was via Zyla or XiMEA camera coupled to the LED Thorlabs light source.

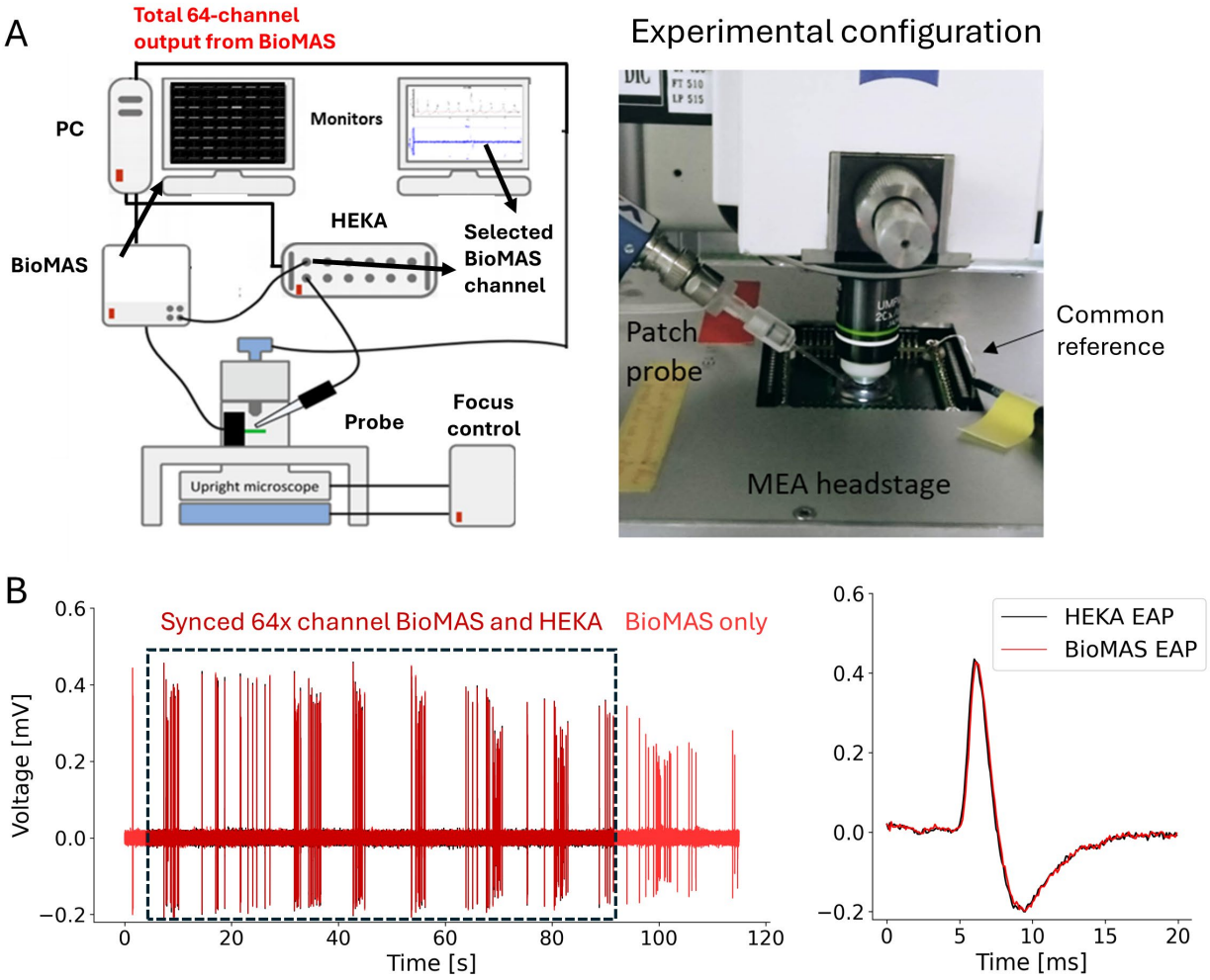


**Figure 3.3.4. Synchronizing patch-clamp and MEA amplifiers.** A. On-chip patch-clamp set-up. Both systems shared the PC to circumvent post-hoc synchronizations of internal clocks. BioMAS received patch-clamp current and voltage signals in auxiliary channels, and the patch-clamp amplifier received a chosen electrode signal. Adapted from: Jäckel, David, et al. *Scientific reports* 7.1 (2017)[182] Right: Recording set-up for an on-chip patch-clamp experiment. B. Target channel's extracellular traces, detected from BioMAS amplifier directly (red) and as the auxiliary input to the HEKA amplifier (black). The rectangle denotes the extracellular trace segments where both systems are detected synchronously. Traces were post-hoc aligned. The effect of uneven triggering is also visible; since the BioMAS acquisition was triggered and shut down manually with some delay to the patch-clamp, extracellular traces directly from BioMAS have flanking segments on both ends (red). Only the segments in the rectangle had simultaneous patch-clamp verification. Right: Zoom on a single EAP shows that the HEKA amplifier does not distort the signal.

### 3.3.5. Dual and double patch-clamp in whole-cell configuration

Dual and double patch-clamp measurements were established through successive patching of the same and neighboring neurons, respectively, separated by 10 min. The former was used to detect the membrane responses of the target during an acute membrane deformation via the approaching second pipette. Double patch-clamp measurements in combination with calcium imaging during the giga-seal formation were to ground-truth the plateauing neighbor's calcium responses during the deformation of a nearby neuron. Double whole-cell recordings in voltage-clamp or current-clamp mode were as well to identify the monosynaptic coupling between randomly chosen pairs of neurons (Section 6.5). To validate the synaptic connections, a neuron was electrically stimulated to track responses in another, held at ca. -60 mV. Post-synaptic potentials (PSP) or currents (PSCs) time-locked to the APs of a stimulated neuron verified a monosynaptic connection. The main criteria to define a post-synaptic deflection as a monosynaptic PSP were the amplitude $\geq$ 0.1 mV and latency $\leq$ 10 ms.[239] The uncoupled pair was considered to share a common input if near-simultaneous PSPs were detected. Finally, double whole-cell in synaptic antagonist cocktail described below was used to confirm the electrical coupling between the well isolated somas. Here, a subthreshold electrical stimulation of one soma evoked the same-sign, but attenuated voltage deflections in the neighboring soma in the current-clamp mode (Section 6.4). The two probes shared the amplifier.

## 3.4. Pipette-membrane interaction during the giga-seal

Mechanical stimulation consisted of a standard giga-seal establishment (Section 3.3.1). The tubing system for pressure control was additionally secured by parafilm to prevent air leaks. A 60-80 mmHg overpressure was applied via a 10 ml syringe, and monitored through a manual manometer CE 0483, (error range: ± 3 mmHg, Bio Plus) attached to the tubing by a T-valve (Fig. 3.4. A). It is worth noting that, even without the syringe-applied overpressure, there's a weak (ca. 0.098 Pa or $7.3 \times 10^{-4}$ mmHg) hydrostatic pressure at the tip, resulting from the height differences between the pipette solution and the bath. Zero-pressure approach in Chapter 4.1 refers to no overpressure applied through the syringe.[240]

For combined calcium imaging and giga-seal formation, the pipette was centered at a target and lowered to ca. 10 µm above the membrane prior to the start of the video. Following the onset of calcium imaging recording, the pipette advanced towards the neuron. Since the numerical aperture of the patch-clamp objective had a theoretical Z-limit of ca. 4 µm, and the microscope was not equipped with an automatic filter shutter, the relative pipette-electrode interactions during the giga-seal formation were extrapolated from the pipette responses to the test-pulses, and not from the brightfield records. Current responses to 5 mV, 5 ms test-pulses, used to navigate the giga-seal establishment, were also stored to post-hoc correlate the timings of pipette-membrane interaction with mechanoresponse dynamics (Fig. 3.4. B). Until the initial pipette-membrane engagement, current responses are maximal, and proportional to the pipette's resistance, according to Ohm's law. The pipette resistance increases by 0.1 - 0.6 MΩ marked the

onset of pipette-membrane engagement. The following steps, pressure release and suction, led to a steeper resistance increases until giga-seal is reached. In Figure 3.4. B, pipette-membrane engagement is marked by a steady drop (6%) in current response, while both the pressure release and suction follow steeper current dynamics. Normalized current response asymptotically approaches 0 as the giga-seal is formed, while the raw trace shows exclusively the remaining, uncompensated fast transients from the pipette. Neurons were initially contacted at 9.2 ± 1.3 s, the pressure was released at 17.0 ± 0.8 s, and, if formed during the recording, giga-seal was at 46.2 ± 3.1 s from the start of the video (average ± SEM). The calculated pipette lowering velocity was at ca. 1 µm/s. However, the pipette lowering was manually controlled using Luigs & Neumann SM I micromanipulator. To locate the patched neuron post-measurement, calcium imaging was followed either by a brightfield snapshot under the same objective, or neuron rupture by positive overpressure.

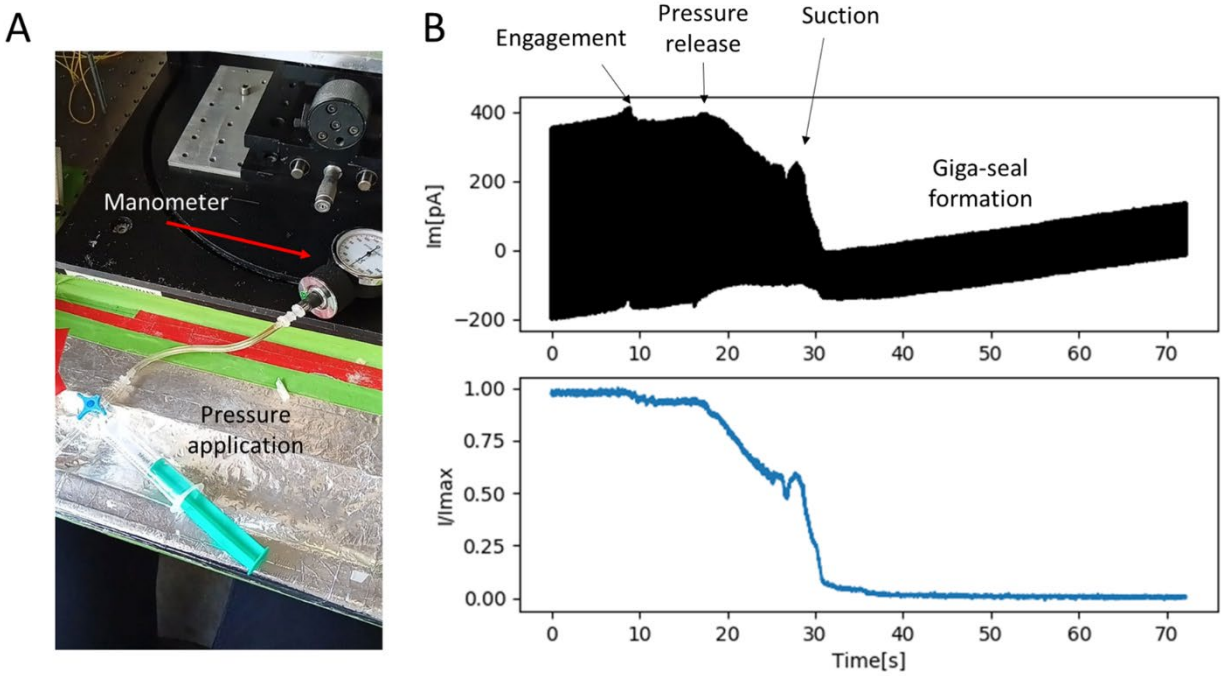


**Figure 3.4. Experimental set-up for tracking pipette-membrane interaction.** A. Pressure application and measurement set-up. Presented is a manual manometer connected to the tubing system via a T-valve. B. Pipette test-pulse responses to estimate relative timings of pipette-membrane engagements during giga-seal formation steps. Top trace depict pipette current responses during the giga-seal formation. The bottom trace represents pulse current normalized to the maximum.

# 3.5. Pharmacology

Unless otherwise stated, chemicals were purchased from Sigma-Aldrich Chemie GmbH, stock solutions were prepared in water, and the neurons were pharmacologically treated by bath application in E-patch solution 5-10 minutes before the measurement started. Incubations > 30 min were done in a drug-containing NB medium at 37ºC, and 5-10 min incubations were in bath-solution for patch-clamp experiments at a room temperature (RT). Where dimethyl-sulfoxide (DMSO) was used as a vehicle, the substance was dissolved through vortexing or ultrasonic bath,

and, when the chemical's temperature sensitivity allowed, gentle heating. For these treatments, the final amount of DMSO (v/v%) is written next to the concentration. Summary of all chemicals used for pharmacology is given in Appendix Table B1.

### 3.5.1. Caffeine-mediated induction of network bursts

Neuron network bursts are pharmacologically inducible. One approach triggers synchronous network bursts by acute network-wide depolarization through addition of 1-11 mM $K^+$ to the bath solution. This approach is short-lived, particularly at > 10 mM concentrations, as a chronic depolarization reduces the AP driving force through inactivation of sodium conductances.[167] Another approach to long-term synchronize the network is through application of caffeine. Caffeine in 8 mM concentrations reliably induces the synchronous network events,[241] primarily through activation of $Ca^{2+}$-induced-$Ca^{2+}$ mobilization from internal stores via Ryanodine receptors (RyRs).[242] In this work, 25 mM stock caffeine was added to an end concentration of 8 mM, following a 5-10 min baseline measurement of spontaneous activity.

### 3.5.2. Pharmacological investigations of mechanoresponses generation mechanisms

Gadolinium (III) chloride ($IC_{50}$ = 1.4 µM) was used as a general antagonist of MS channels at 50 µM[37] to effectively block the mechanosensation without pleiotropic effects on neuron's intrinsic or synaptic excitability.[243] In a free form, gadolinium ions stabilize the membrane through electrostatic interaction with phospholipid heads. Unlike the permeation blocks, this mechanism targets both mechanosensitive and mechanically gated channels.[244] The absence of interferences with the neuron's excitability was confirmed in CC and VC check measurements of the treated cells in whole-cell mode. GsMTx4 in 1-2.5 µM was used to target Piezo 1 and TRPC1 mechanosensitive channels. Ruthenium Red (RR) as a selective TRPV antagonist was not used due to its interferences with the internal calcium homeostasis.[245] As specific antagonist for other mechanosensitive channels are yet to be discovered,[37] pharmacological investigations of TRPM7, TRPP1 and TRPP2 were not possible.

For actin depolymerization, neurons were incubated with 10 µM Cytochalasin D (CytoD) in 0.1% DMSO for 5h. Although the $IC_{50}$ of CytoD reversible inhibition of G-actin polymerization is at nanomolar range, only a long-term treatment at a higher concentrations demonstrates an actin-disrupting effect.[246] To account for the reversible effect, a 5h incubation was followed by a bath application preceding the experiment. Pharmacological interferences with actin motor, myosin, were to test if mechanical responses required an active actin reorganization. Neurons were pre-treated for at least 30 min with 50 µM ($IC_{50}$ = 5 µM) non-muscle myosin heavy chain II (MHC II) ATP-ase inhibitor, Blebbistatin (-) in 0.1% DMSO. Blebbistatin stabilizes the myosin-ADP-Pi complex through non-covalent interactions, inhibiting phosphate release and promoting the ADP-bound state. This leads to a reduction in actin reorganization as the stabilized state has lower affinity towards actin, indirectly interfering with any active actin reorganization

process.[247] Blebbistatin was also bath-applied to account for the drug's reversible effect. In both cases, treated neurons were electrically stimulated while monitoring the membrane responses in whole-cell mode, to estimate eventual drugs' interferences with the neuronal excitability.

For external calcium depletion, neurons were treated in nominally 0mM $Ca^{2+}$ bath solution containing EGTA. Omitting $Ca^{2+}$ does not suffice, as $Ca^{2+}$ in traces (12 µM) is enough to elicit calcium-influx dependent responses,[248] and EGTA was added to bind the residual $Ca^{2+}$. Despite the 2mM EGTA has been the most commonly used concentration, recent discussions have reopened the question of the most efficient EGTA concentrations for binding residual calcium.[249, 250] Gebhardt et al. argue that EGTA concentrations of 1-2 mM are only partially effective in blocking calcium influx due to inefficient chelation of extracellularly-bound $Ca^{2+}$.[249] Conversely, Liu et al. oppose that higher concentrations (10 mM) of EGTA can enter the cell via fluid-phase endocytosis, exit the endosomal compartment, and chelate cytosolic $Ca^{2+}$.[250] Experiments with 10 mM EGTA-treated neurons showed a decrease in baseline calcium signals after a 5-10 min incubation, indicating internal calcium chelation. However, I decided to use 2 mM EGTA, which did not reduce the baseline calcium signal, accepting the assumption that at this concentration, residual $Ca^{2+}$ chelation may be incomplete.

To block calcium conductances, cadmium (II) chloride ($EC_{50}$ = 3-30 µM) was applied at a concentration of 200 µM. $Cd^{2+}$ acts as a competitive inhibitor of calcium channels, with a longer pore-retention time at depolarizing potentials. The block is only 60% at resting membrane potential, but increases to 100% at +20 mV.[251] 2-APB (HelloBio) was used in 100 µM ($IC_{50}$ = 50 µM) in 0.1% DMSO to inhibit calcium entry from internal store depletion. To determine if voltage-gated calcium channels ($Ca_V$s) engage in the development of mechanically-evoked calcium responses, Mibefradil and Nifedipine were used as antagonists for T- and L-type $Ca_V$s, respectively. Specifically, 5 µM Mibefradil[252] was used to antagonize T-type $Ca_V$s ($EC_{50}$ = 2.7 µM), while 10 µM Nifedipine freshly-prepared in 0.05% DMSO ($EC_{50}$ = 0.016 µM) was used to target L-type Cavs.[253] To assess whether electrical activity was required for calcium responses, AP generation was prevented by blocking $Na_V$ channels with 1 µM tetrodotoxin (short: TTX) (Tocris, $EC_{50}$ = 0.53 µM).[254]

## 3.5.3. Pharmacological investigations of dispersion mechanisms

To determine if synapses participated in the propagation of mechanical responses, we first blocked the ionotropic receptors for glutamate (via NBQX-AMPAR antagonist, and D-AP5-NMDAR antagonist) and GABA (via bicuculine, which blocks GABAARs) simultaneously. This was achieved by applying a synaptic antagonist cocktail (cocktail #1) consisting of NBQX (20 µM; IC50 = 0.15 µM), bicuculine (20 µM; $IC_{50}$ = 1 µM) and D-AP5 (80 µM). The cocktail was freshly prepared in the bath solution on the day of measurements.

To rule out that post-synaptic receptors triggering signaling cascades were responsible for the plateau propagation instead of ion conduction, neurons were treated with a second antagonist

cocktail (cocktail #2). This cocktail contained not only the blockers of ionotropic receptors (NBQX, bicuculine, and D-AP5) present in cocktail #1, but also three additional antagonists: AIDA (200 µM; prepared in 1.1 eq NaOH), which blocks type I mGluRs ($IC_{50}$ = 82 nM); CPPG (200 µM; prepared in 1.1 eq NaOH), which blocks type II/III mGluRs ($IC_{50}$ = 3/50 nM); and CGP 55845 (10 µM; 0.1% DMSO), which blocks $GABA_B$ receptors ($IC_{50}$ = 5 nM).

Carbenoxolone disodium (CBX, Tocris) was used as a broad-spectrum GJC uncoupling agent ($IC_{50}$ = 105.2 µM).[85] Though it acts as a universal blocker of connexins (Cx), in concentrations specific to the GJC effect, CBX shows a lower potency than other uncouplers.[255] Neurons were incubated in 100 µM CBX for at least 30 min prior to experiment, and the measurements were conducted in a bath containing the same concentration. Another GJC uncoupling agent, mefloquine, was used to probe the GJC involvement in propagation of the mechanoresponses. In addition to being an antimalarial drug, mefloquine is also used to specifically and potently block Cx36 ($IC_{50}$ = 0.3 µM) and Cx50 ($IC_{50}$ = 1.1 µM), two Cx isoforms ubiquitously expressed in the brain.[256] Neurons were treated with 25 µM (0.05% DMSO) or 50 µM (0.1% DMSO) mefloquine hydrochloride for at least 30 minutes prior to the measurements.[85]

# 3.6. Data analysis

## 3.6.1. Patch-clamp analysis

In whole-cell patch-clamp recordings, series resistance is a critical factor affecting the reliability of the measurements. However, in this work, the series resistance was not readily long-term tracked because the primary mode of acquisition was long-lasting current-clamp. Two exclusion criteria were used: membrane penetration prior to giga-seal establishment and holding negative current larger than 150 pA. Traces were exported from PatchMaster in ASCII format and analyzed using self-made Python scripts. The `find_peaks()` function from the `scipy.signal` module was used to detect both spontaneous and evoked action potentials (APs) as well as postsynaptic potentials (PSPs), with parameters specified in Table 3.6.1. For the corresponding signals recorded from MEAs, a lower prominence threshold was used to include also dendritic APs as ground truth for the detected peaks in the whole-cell recordings.

Table 3.6.1. Spike finding parameters for action potentials and post-synaptic potentials

| Event | Prominence [mV] | Width [ms] | Distance [ms] |
|---|---|---|---|
| APs | 20 (12) | 6 | 2 |
| PSPs | 2 | 18 | 1 |

Capacitance ($C_m$) and resistance ($R_m$) were either read directly from PatchMaster in membrane responses to voltage pulses or estimated offline from saved recordings. Only when slow capacitance was uncompensated, passive membrane properties could be *post-hoc* extracted from the whole-cell membrane responses to the least hyperpolarizing stimuli (-20 pA), to avoid interferences from rectifying conductances. First, $R_m$ was estimated by Ohm's law ($R_m = \Delta V_m/\Delta I_m$) from stationary voltage response ($\Delta V_m$) near the end of a hyperpolarizing current

stimulus ($\Delta I_m$). Membrane constant ($\tau_m$) was extracted from a single-exponential fit of the voltage response at the beginning of the current stimulus. From there, Cm was estimated as (3.6.1): $C_m = \tau_m/R_m$.

Active neuron properties were estimated at depolarizing, suprathreshold current stimuli in CC check. AP parameters were calculated from the first AP at rheobase. Onset was estimated at a first peak of a smoothened third temporal Vm derivative (Fig. 3.6.1)[164, 257] and curated in SpykeClick GUI (Appendix A). When estimation was from intact neuronal activity, only the recordings with a stable potential preceding the rheobase injection were considered, to avoid intrinsic $V_m$-related threshold fluctuations. AP height was estimated from peak to AHP. The local maximum of the first temporal derivative was used as a measure of the AP depolarization kinetics. When the focus was on slow membrane depolarizations associated with giga-seal (Chapter 6), APs were filtered out with Savitzky-Golay filter of 3rd order and 12511 frames (750 ms) window. The UP kinetics of plateau depolarizations was estimated from the local maximum of the temporal derivative of the filtered $V_m$ trace.

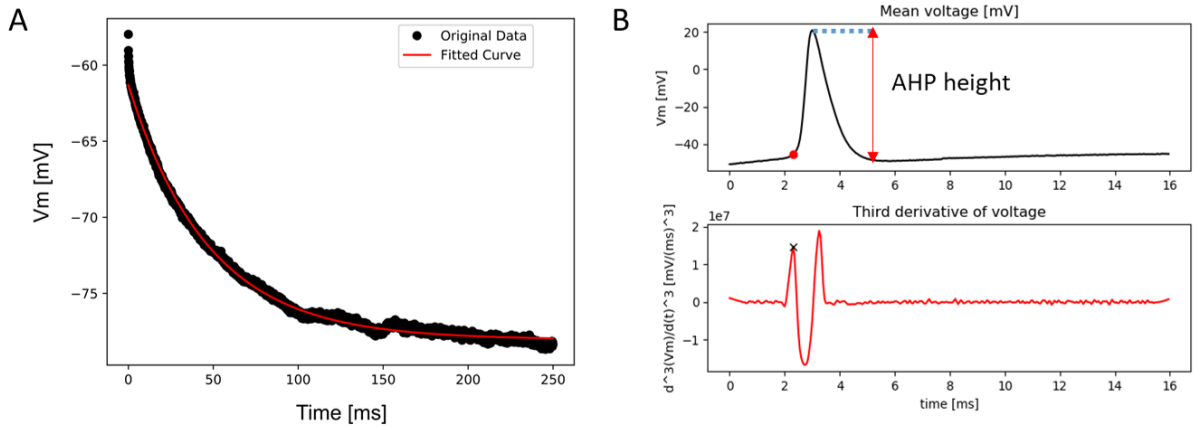


**Figure 3.6.1. Estimation of the neuron's passive and active properties from CC recordings.** A. Non-stationary part of the membrane's response (black) to a -20 pA current injection, and exponential fit (red) to estimate the time constant. B. Neuron's active properties. The threshold (red circle) was determined from the first peak (x) of the third time derivative (red trace). Red arrow marks the height estimate.

## 3.6.2. Analysis and ground truth of calcium transients

### *3.6.2.1. Estimations of the calcium signals*

Calcium spikes and plateaus were automatically detected and manually curated in a custom-made Python GUI. Automatic peak detection was through `find_peaks` function in `scipy` Python package, with the peak parameters specifically adjusted for AP-associated calcium spikes and pipette-evoked plateaus described in Table 3.6.2.

Table 3.6.2. Calcium signal detection parameters in `find_peaks()` function.

| Parameter | Calcium spike | Calcium plateau |
|---|---|---|
| Prominence | Median + STD | Median + STD |
| Width | 0.22 s | 2.2 s |

Automatic onset and end detection was as follows:

1) Baseline was defined as the 5$^{th}$ percentile, and subtracted from the trace of respective ROI's signal;
2) Onsets were defined as a first zero-crossing of the subtracted trace preceding the peak;
3) Ends were calculated as a last zero-crossing following the calcium peak;
4) For superimposed calcium spikes, the end of a calcium signal was re-defined as a local minimum preceding the next spike's timing.

The automatic spike peak, onset and end detection was followed by a manual curation in SpykeClick GUI, written in `Tkinter` (Appendix A). Average signal-to-noise ratio (SNR) from traces containing discernible spiking activity was estimated as a ratio of the mean calcium transient amplitude and baseline variance.[258] Here, the baseline was extracted from the 1 s trace without calcium spikes. Amplitudes were estimated from calcium onsets to peaks, and reported durations were measured from onsets to ends. Integrals of calcium transients were estimated using `np.trapz()` and presented in arbitrary units as multiplies of 100, for clarity.

Network synchrony was evaluated from spontaneous calcium activity as follows. Calcium traces of every neuron were converted to binary values, with ones corresponding to the position of the found calcium peaks. Population-level dynamics was extracted by summarizing all the binary traces. For SNE detection, the binarized summary trace was convolved by gaussian kernel, and population level peaks were detected using a soft-threshold of 3 STD.

*3.6.2.2. Correlating the calcium trace with the membrane events*

$V_m$ changes were correlated with the local network's $Ca^{2+}$ fluorescence to estimate the contextual dependency of the firing and depolarizations causing APs. For this, APs were found by a Vm thresholding (Fig. 3.6.2.1, marked with X) and defined as SNE-participating if they coincided with 2 s windows around the network $Ca^{2+}$ peaks. To correlate the $Ca^{2+}$ events with the numbers of APs (raster windowing), APs were counted in a 0.5 s window (counting window) preceded by 2s of no-firing activity (separation). Due to sampling rate mismatches between the patch-amplifier and calcium imaging camera (10-20 kHz vs. 50 Hz), the reference fluorescence frame was the closest to an AP time point. Calcium traces were cut around the [-1, +5s] windows around the reference point, to match the most prevalent duration of pooled calcium transients (Section 5.2), and averaged out to create an AP template. For each # of APs within a firing event, calcium integrals and amplitudes were evaluated.

Since raster-defined $Ca^{2+}$ windows sporadically omitted far-away APs in neurons with late-burst firing (Section 5.2), single APs were regarded as such if they were unique to a depolarizing event. To remove APs while preserving depolarizing events, whole-cell detected $V_m$ was filtered using 2$^{nd}$ order Savitzky-Golay filter (window size: 2001 frames) (Fig. 3.6.2.1, blue trace). Baseline depolarizations were found in filtered trace using `find_peaks()` function with prominence set at 8 mV and minimal half-maximum width at 8 ms. These parameters were

empirically estimated to minimize the incidence of false positive events (Fig. 3.6.2.1 red traces mark detected depolarizations) at the cost of sporadic omission of brief and subthreshold PSPs (Fig. 3.6.2.1). For accurate onset and end detection, a moving average in 19 s windows was subtracted from $V_m$, to account for slow oscillations. Onsets and ends were detected as the first 0-crossings before and after the peak, respectively. If the event's end preceded the onset of the next event by less than 0.5 s, two events were merged – to account for coincident synaptic inputs. Corresponding calcium windows were extracted by the $V_m$ depolarizing events' onsets and ends.

Since 0 AP events also manifested as suprathreshold calcium spike (Fig. 3.6.2.1), the overall calcium signal detectability was evaluated by the template constructed by averaging all calcium windows corresponding to the membrane depolarizing events, regardless of the firing outcome. To ensure a meaningful template waveform, unequally sized calcium windows were NaN-padded to their end prior to averaging. Following the mean subtraction, templates were normalized to acquire unitary template vectors. Each calcium window was then projected to the normalized template using `np.dot()` function, to obtain a scalar value; these were compared to the baseline projections as a threshold. Baseline segments were defined as fluorescence trace from neurons without any APs, in segments corresponding to stable membrane potentials. Suprathreshold events for a given incidence of false positives (FP) were $Ca^{2+}$ windows whose projections were above $(100 - FP)^{th}$ percentile of the baseline windows' projections. Following the evaluation on all calcium windows projections for different incidences of false discovery, 5% FP rate was chosen as a universal threshold. Thus, calcium windows were considered as suprathreshold if their projections onto the template were above the $95^{th}$ percentile of baseline segments' projections.

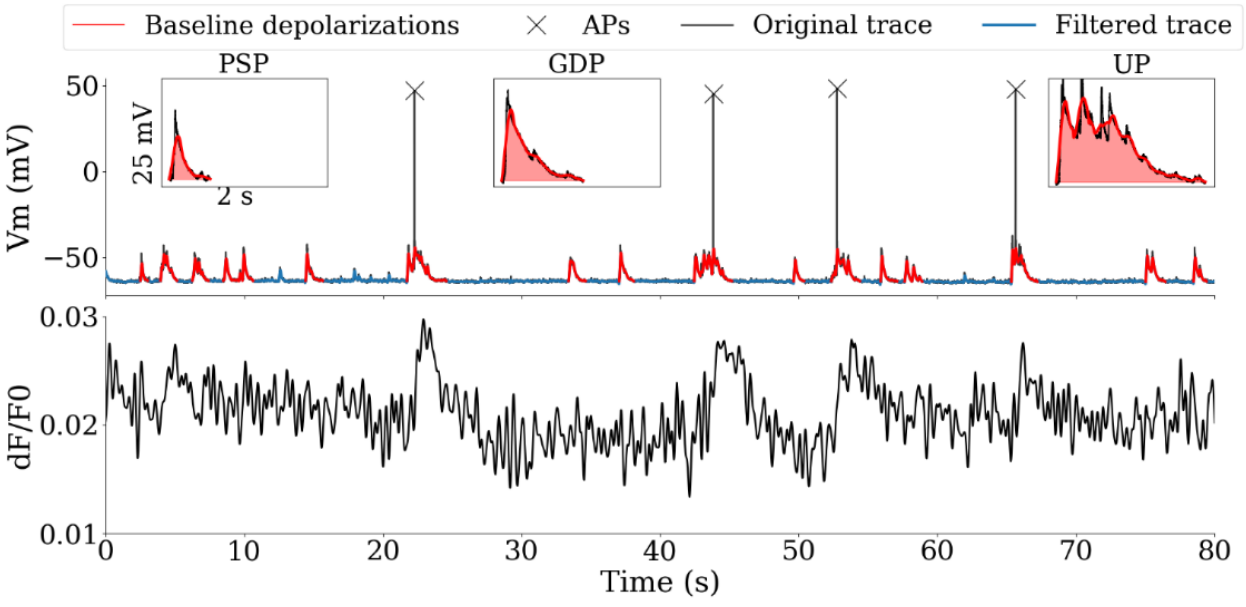


**Figure 3.6.2.1. Correlating calcium fluorescence with subthreshold Vm dynamics.** Top: Extracting slow Vm dynamics from intracellular trace by wide-window fitting (blue trace) and thresholding (red). Insets focus on

different baseline depolarizing events, with shaded areas denoting estimated integrals; X mark filtered out APs. Bottom: corresponding calcium fluorescence.

Individual membrane events were then categorized according to their dynamics (Section 5.3) into PSPs, GDPs and UP states (Fig. 3.6.2.1). Dimensionality reduction was via single-value decomposition (SVD), followed by K-means clustering; both were performed in `scikit` module. Individual traces were not normalized to preserve amplitude content for discriminating isolated PSPs from GDPs. To account for size variations, membrane windows were imputed with the window's average on their end. The number of components for SVD was set to 100, and the initial number of clusters was 10, followed by manual curation.

Besides the calcium benchmarking of spontaneous activity, neurons were also stimulated via +200 pA current pulses interspaced by 1 s. To evaluate the effects of evoked membrane depolarizations on calcium signals, APs were inhibited by 1 μM TTX applied to the bath solution. Plateau magnitudes were calculated from non-negative integrals of total calcium traces, while stimulus-triggered averages were estimated from calcium windows aligned to the electrical pulse onset.

## 3.6.3. Microelectrode array signal analysis

In on-chip patch-clamp measurements, patch-clamp amplifier also detected signals from the electrode via an auxiliary channel. For a convenient comparison with the intracellular trace, both MEA signals and corresponding intracellular trace were exported as ASCII files. Since BioMAS amplification parameters did not propagate to PatchMaster, MEA signal amplitude was adjusted by the BioMAS gain. In BioMAS measurements of the local network activity, BioMAS viewer, a pipeline developed by Fabian Brings and Johannes Lewen, was used for a quick offline overview of the signal quality, as well to convert the MEA traces into csv. [193]

SNR was estimated as a ratio of average ($SNR_{avg}$) or maximal ($SNR_{max}$) spike amplitude and sample-by-sample root-mean-square of the trace ($RMS_{recording}$) for comparison with previous investigations of the MEA waveform variability.[199] It is worth noting that, calculated this way, SNR values are a 2-3 times smaller than those calculated from RMS of epochs without spikes.[199] The estimated SNRs of NS-NC MEAs are only apparently smaller and not directly comparable with those calculated from the baseline, as in characterization of NC MEAs.[193] Noise was estimated from the baseline exclusively for the comparison with NC MEAs. $SNR_{max}$ was used when comparing the overall performance of NS-NC MEAs (Section 3.2). $SNR_{avg}$ was used when estimating MEA waveform variability, and for comparison with benchmarking of the spike sorters, previously done by SpikeForest (Section below and 4.4).[30] The baseline was obtained by excluding the spikes from the recording, and the baseline stability was assessed by calculating the coefficient of variation (CV) within 10 s windows. When necessary, MEA waveforms were plotted as averages aligned by their local maxima, with the shaded area indicating either standard error or deviation.

## 3.6.4. Benchmarking spike-sorters with paired ground-truth dataset

To test the overall accuracy of automated spike sorting on high SNR MEA traces, several spike sorters were benchmarked with paired patch-clamp and MEA datasets using SpikeInterface.[29] Among spike-sorters currently available in SpikeInterface, only 6 were tested. The others were excluded when spike sorting consistently failed (HerdingSpikes)[196], parameters failed to propagate from SpikeInterface to the sorter (IronClust)[205], or due to NVIDIA GPU requirements (all versions of KiloSort[204]). The remaining sorters (Table 3.6.4): MountainSort (ver. 1.0.3), Tridesclous (ver. 1.6.6.1), Klusta (ver. 3.0.16), Spyking Circus (ver. 1.1.0), WaveClus (3.0.3) and Combinato, were run either from the SpikeInterface, or pulling the exact environment from Docker. SpikeInterface was run on a laptop with Intel(R) Core (TM) i5-8250U CPU @ 1.6 GHz, 8GB of RAM and Intel(R) UHD Graphics 620 as GPU.

Table 3.6.4. List of spike-sorters benchmarked via the SpikeInterface

| Spike-sorter | Detection[a] | Feature extraction[b] | Clustering[c] | Template matching[d] | Additional features[e] |
|---|---|---|---|---|---|
| MountainSort4[195] | Threshold ($\sigma_s$) | PCA | ISO-CUT | AS | Bursting, SUA, and MUA classifiers |
| Tridesclous[202] | Threshold ($\sigma_s$) | PCA | GMM | AS | Alien unit identification |
| Klusta[197] | Dual threshold ($\sigma_s$) | PCA | Masked EM | / | Integrated BEER |
| SpykingCircus[170] | Threshold (MAD) | PCA | DBSCAN- K-medoids | ANS | Template-matching spike search |
| WaveClus[259] | Threshold ($\sigma_n$) | Wavelet decomposition | SPC | AS | Integrated quality metrics |
| Combinato[260] | Threshold ($\sigma_n$) | Wavelet decomposition | SPC | AS | Integrated quality metrics |

[a] *Threshold: MAD – median absolute deviation; $\sigma_n$ – units of standard deviation from noise; $\sigma_s$ – units of standard deviation from the signal;*
[b] *Dimensionality reduction: PCA – principal component analysis*
[c] *Clustering: GMM – Gaussian Mixture Model; EM –expectation maximization algorithm; DBSCAN – density-based spatial clustering of applications with noise; SPC – superparamagnetic clustering*
[d] *Template matching: AS – amplitude sensitive; ANS – amplitude non-sensitive*
[e] *Additional feature: SUA – single-unit activity; MUA – multi-unit activity; BEER – best ellipsoid error rate*

While the clustering and template matching parameters were left at their default values, the spike-finding step was modified to account for the higher SNR of NS-NC recordings. A comprehensive list of sorting parameters is included in Appendix A. All spike sorters followed the standard procedure, including pre-processing (filtering), event detection, dimensionality reduction (either PCA or wavelet decomposition), and clustering (Fig. 3.6.4.1). Some sorters utilized template matching to address the issue of overlapping signals in multi-unit trains (Table 3.6.4)

Spike sorting was on concatenated traces from electrodes containing the spontaneous activity of the patched neuron, which were bandpass filtered between 50-4000 Hz (Butterworth filter), using `scipy.signal()`. Since only one neuron was interrogated via patch-clamp, the ground truth (GT) only revealed the identity of a single source and did not provide information on other

sources' spiking times in a multi-unit train. Therefore, the performance was evaluated based on the best-matching unit (BMU), which contained most of the spikes from the patched source and the least spikes from other sources.[29, 30] Following the spike sorting, the spiking trains of each unit were compared with the patched neuron's spike timings, with a 2 ms jitter to account for peak discrepancies between the IAPs and EAPs (Chapter 4).

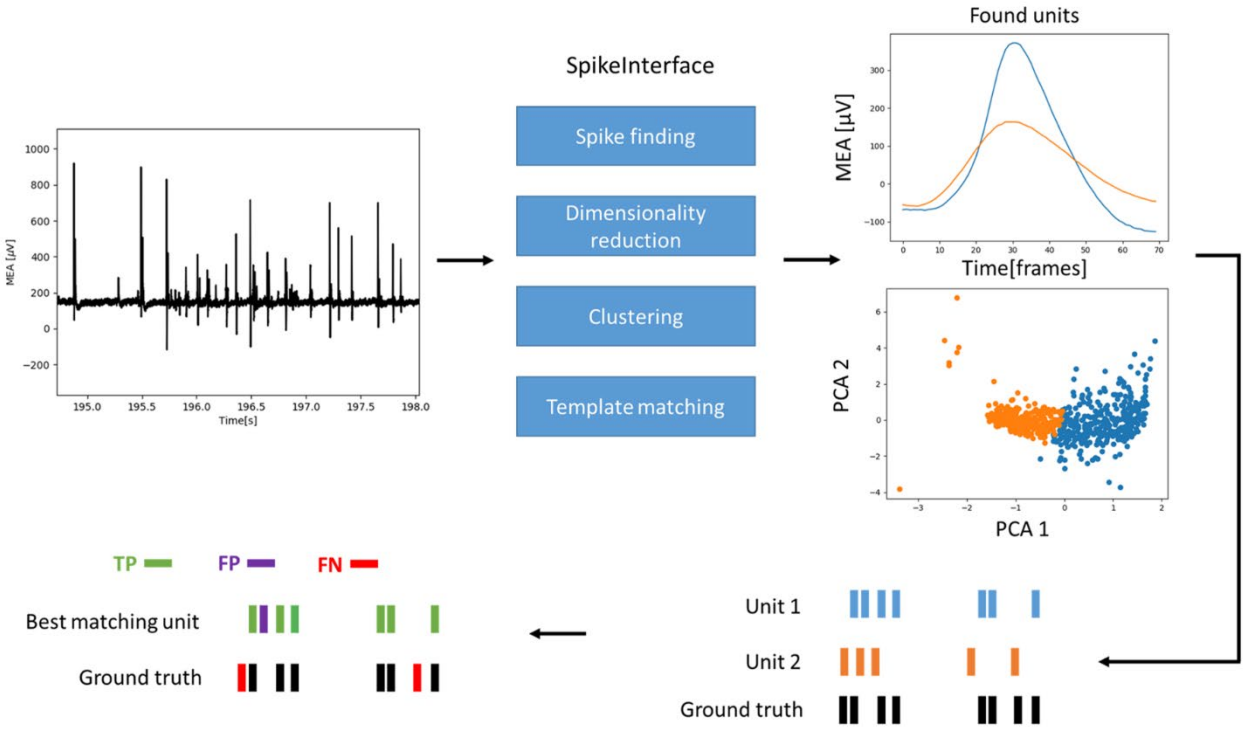


**Figure 3.6.4.1. Pipeline for estimating the spike-sorters' performance.** Spike sorting via SpikeInterface was done on concatenated MEA traces. Within each spike sorting algorithm, spike detection and waveform extraction was followed by dimensionality reduction and clustering. When allowed, clustering was followed by a template-matching step to correct for overlapping spikes and those skipped during the spike detection. The output of spike-sorters was characterized via quality metrics estimates, among which distances between the clusters were compared. Spiking times of every found unit were correlated with corresponding intracellular AP timings, and performance was estimated on the unit with the highest correlation. False positives (FP) account for spikes present in the BMU but not in the ground truth. False negatives (FN) are spikes in the ground truth omitted from the BMU.

Ground truth benchmarking was according to Magland et al.[30] Briefly, for a ground truth spiking train ($t_1$ ... $t_N$) and the spike-train of k-$^{th}$ spike unit ($S_1^{(k)}$ ... $S_{M_k}^{(k)}$), the matches between them ($n_k^{\text{match}}$, syn. true positives (TP)) were counted as (3.6.1):

$$n_k^{\text{match}} = \left(\text{i}, if \left|t_i - S_j^{(k)}\right| \leq 2 \text{ ms}\right). \quad (3.6.1)$$

Accordingly, if a k-th spike-sorter unit contains signals that were not matched to the ground-truth, they were considered as false positives (FP), and counted according to (3.6.2):

$$n_{FP}^k = M_k - n_k^{\text{match}} \quad (3.6.2)$$

where $M_k$ denotes the total number of spikes from the k-th unit. Ground-truth spikes that were not present in a k-th unit, false negatives (FN), were counted as (3.6.3):

$$n_{FN}^{k} = N_k - n_k^{\text{match}}, \tag{3.6.3}$$

where $N_k$ denotes the total number of spikes in ground truth.

Based on counts among the true and false matches, the metrics below was used to find the unit that captures the firing dynamics of the probed neuron.

**Recall (r)**: the fraction of correctly identified TP among all GT spikes. This metrics inversely relates to the FN incidence: $r = \frac{n_{match}}{n_{match}+n_{FN}}$, where $n_{match}$ corresponds to the number of events in GT also found in BMU, and $n_{FN}$ to number of GT events excluded from BMU.

**Precision (p)** represents the proportion of true positives among all spikes identified as positive, and is inversely related to the FP rate: $p = \frac{n_{match}}{n_{match}+n_{FP}}$, where $n_{FP}$ equates the number of events in BMU not found in GT.

**Accuracy (a)** combines precision and recall: $a = \frac{n_{match}}{n_{match}+n_{FN}+n_{FP}}$.

Accordingly, the unit with the highest accuracy was denoted as BMU, and the spike-sorter performance was described from parameters corresponding to this unit.[30] These parameters were also estimated in the process agnostic to unit classification, in SUA recordings to estimate spike sorting errors at the detection step.

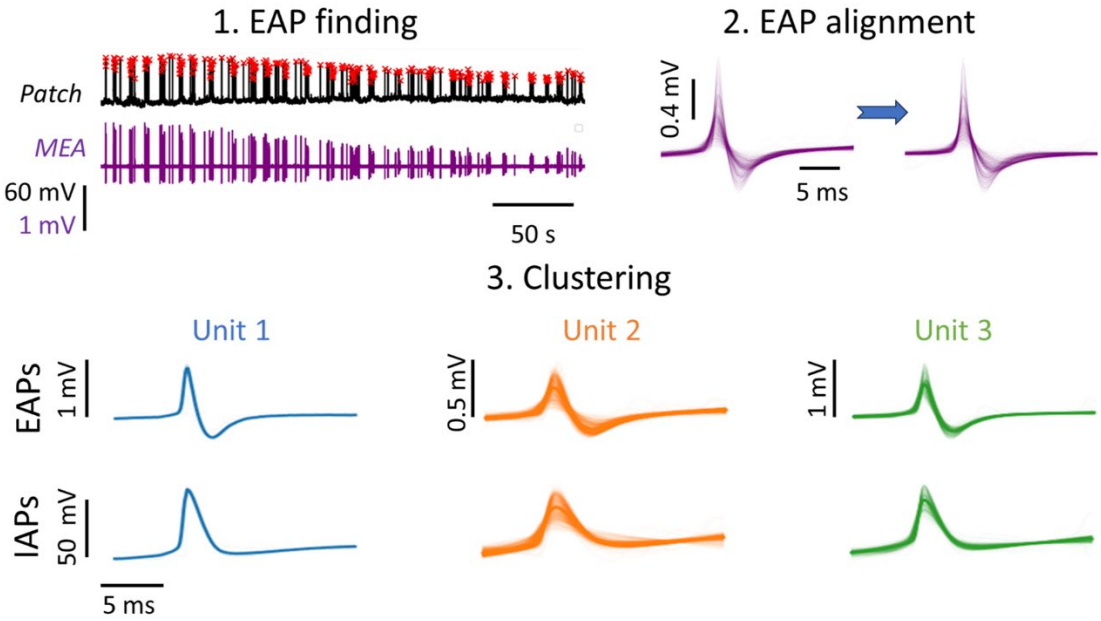


**Figure 3.6.4.2. Pipeline for estimations of misclassification errors.** EAPs of the target neurons were extracted in [-6, 14] ms windows around the intracellularly detected peaks (1) and re-aligned by their local extrema (2). Clustering of the aligned EAPs was done via Waveclus (3).

To estimate the misclassification errors during the clustering process without interferences at spike-finding steps, EAPs were extracted in [-6, 14] ms windows around corresponding IAP

peaks (Section 3.6.1, Fig. 3.6.4.2. ). Due to the EAP resemblance to the 1st temporal IAP derivative, extracted waveforms had a temporal lag as a function of the AP slope (Section 4.2), and required repositioning before the clustering. Following the alignment (Fig. 3.6.4.2 ), EAPs underwent SPC in Waveclus. When Waveclus misclassified EAPs of the same neurons into more than one unit, the best unit (BU) denoted a cluster containing majority of the EAPs, and the rest were merged into a single, other unit (OU).

## 3.6.5. Neuron network inferences

Parallel MEA recordings from 62 recording electrodes were used to determine the local network properties at a single AP resolution. A 200 µm pitch prevented accurate inferences of the network's effective connectivity.[261] Network inferences were thus interpreted as sampling of the network activity at fixed points in space. Accordingly, the metrics extracted from MEA electrodes is not focused on activity-based information flow estimates, but on properties describing the global network's dynamics.

**Individual neuron bursts** were identified from spike trains via an ISI threshold based on intrinsic neuronal firing dynamics as opposed to setting a hard threshold, to account for rhythmic differences between the neuronal spiking types. The pipeline was adopted from Chen et al 2009.[262] For a given spiking train of length N, the mean ISI ($\overline{ISI}$) was calculated as (3.6.4):

$$\overline{ISI} = \frac{\sum_{n=1}^{N-1} ISI_n}{N-1}. \quad (3.6.4)$$

Starting from the whole spike-train, a sequence (Sn) was constructed to have ISIs < $\overline{ISI}$. The mean of Sn, calculated according to the top formula, was set as a soft ISI threshold (MS).

**Synchronous network events (SNEs, syn. network bursts)** were estimated by summation of spikes within a 1 s windows on binarized spike trains. Correlated activity from different channels was considered as SNE if the bin spike count reached at least 60% of the maximum population sum.

**Active connectivity mapping with single-neuron electrical stimulation and calcium imaging.** Electrical stimulation produced slow-building, plateau-like calcium signals in the target. However, calcium responses to isolated electrical pulses were not discernible, likely due to reduced amplitude resolution (Fig. 3.6.5.). Calcium imaging combined with double patch-clamp also demonstrated that single-neuron electrical stimulation failed to produce distinct isolated calcium responses in the post-synaptic neuron. Thus, connections from single-neuron current injections were estimated as follows. Stimulus onsets served as a bound to average the neighbor's traces, and STA amplitudes were calculated by subtracting the pre-stimulus from post-stimulus amplitude. Following Kwan et al. 2012 criterium for connection estimates, the neighbor was regarded as post-synaptic if its STA coincided with the target's and was > 2.3 SEM.[20] To evaluate the precision of using soft-threshold STAs, the incidence of false positives

was estimated from the same neurons' calcium traces in sham stimulation (Fig. 3.6.5.). With this soft threshold, the rate of false positive connections was 0.7%.

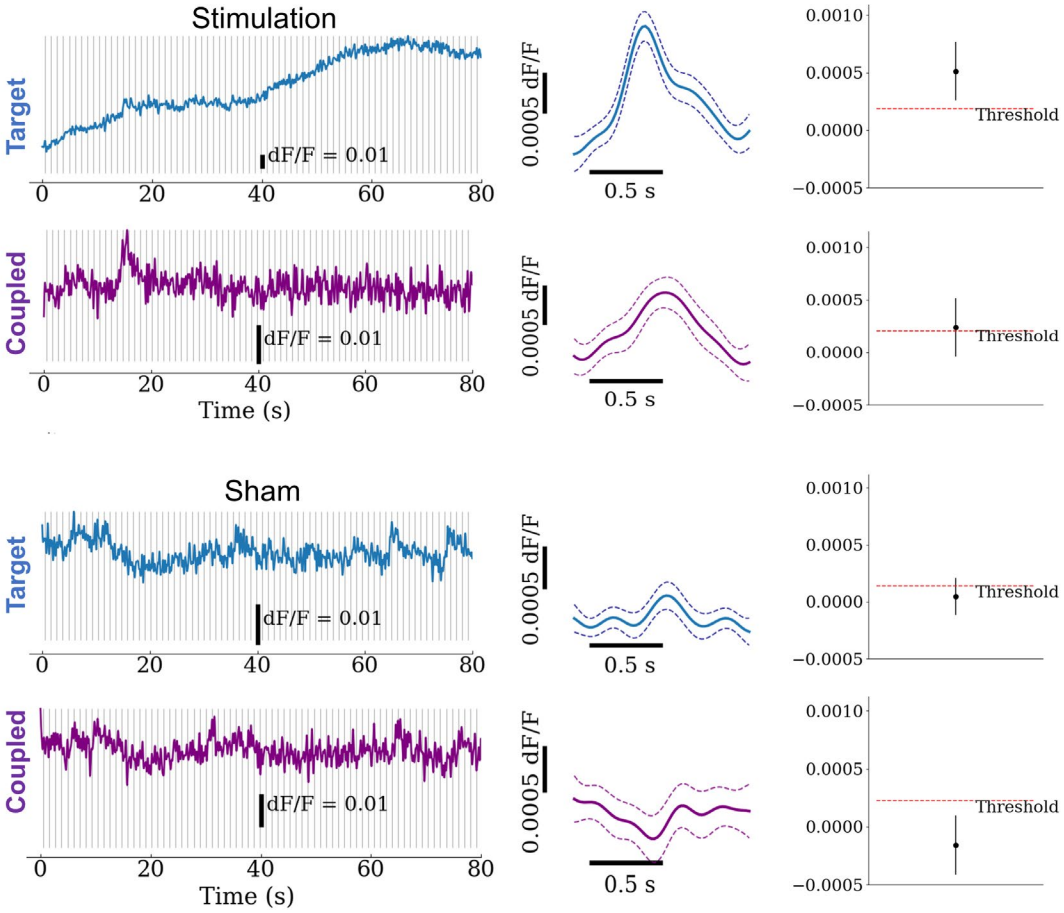


**Figure 3.6.5. Setting the STA threshold for active connectivity estimates.** Depicted are the traces of the target (blue) and putatively coupled neuron (purple) with and without single-neuron stimulation. Middle columns represent mean (solid) and SEM (dotted line) STAs for each case. Right columns denote dFpost-dFpre amplitude distribution and soft threshold (red line).

## 3.6.6. *In silico* Izhikevich network model and simulation of misclassification errors

Izhikevich network in bursting regime was simulated in `Brian2`[288], to evaluate the influence of high spike misclassification incidence on the neuron network estimates. It was chosen due to its versality to reproduce several spiking patterns with low computation demands. The network consisted of neurons whose membrane potential dynamics was described as (3.6.5):

$$\frac{dV_m}{dt} = \frac{k(V_m{}^2 - V_m V_r - V_m V_t + V_r V_t) - U_m + I_{ext} + y}{C_m}, \text{where:} \qquad (3.6.5)$$

$V_m$ represents membrane potential in time ($t$), $d/dt$ –first temporal derivative, $V_r$ – membrane resting potential, $V_t$ – threshold potential, $I_{ext}$ –external stimulus, periodically applied to promote

synchronicity, $C_m$ – membrane capacitance. $U_m$ represents recovery variable that defines the neurons' hyperpolarization, introduced to prevent overshooting of AP to infinity. Its kinetics is defined by Equation (3.6.6):

$$\frac{dU_m}{dt} = a(b(V_m - V_r) - U_m), \text{where:} \quad (3.6.6)$$

*a, b* represent the dimensionless recovery control parameters; *a* defined how fast the recovery was, while *b* defined how sensitive recovery variable was to the $V_m$ fluctuations around the resting value. In Equation 3.6.7, *y* represented a portion of the $V_m$ fluctuations from pre-synapses, and its own kinetics was influenced by the duration of post-synaptic current ($t_{psc}$) after the pre-synaptic spike:

$$\frac{dy}{dt} = \frac{-y}{t_{psc}}. \quad (3.6.7)$$

Membrane potential was re-set after $V_m$ exceeded $V_{peak}$ = +35 mV, according to Equation 3.6.8:

$$\text{if } V_m = V_{peak}, \text{ then } V_m = \text{c}; U_m = U_m + \text{d}, \text{ where} \quad (3.6.8)$$

*c* corresponds to $V_m$ after the reset, while *d* denotes the rate of recovery following the spike.

A comprehensive list of the model parameters is given in Table A4.1, Appendix A. Briefly, a network of 100 neurons was set to have 80% excitatory neurons. Dimensioneless parameters were adjusted to promote bursting, namely: *a* was lowered to 0.001 $ms^{-1}$, and *b* was set to 0.6 $ms^{-1}$. Neurons were randomly interconnected with 0.3 probability of connection for excitatory, and 0.37 for inhibitory neurons. Synaptic weights were randomly chosen between 80-220 mV/ms interval. Simulation was run for 20 s, and parameters were empirically adjusted to match the duration and incidence of *in vitro* cortical networks (Section 4.1). Throughout the stimulation, randomly scaled external current of 80 mV/ms was applied to neurons to promote the bursting activity.

Following the spike sequence generation, the spikes were assigned to bursts and non-bursting epochs, the same as for those of *in vitro* cultures (Section 3.6.5). From misclassification trends characterized for these cultures, probabilistic filter was applied to a generated spiking sequence, by multiplying a random number from 0 to 1 with probability of misclassification within the burst or non-burst epochs. Starting from the average misclassification incidence (MR) of 30% and the burst transition incidence (Mb) of 94%, the average probability of a bursting spike being misclassified was 0.282. Accordingly, the average probability of a non-bursting spike to be misclassified was 0.018 (Section 4.4).

## 3.6.7. Experimental set-up and statistics

In single-neuron perturbation experiments, electrophysiological properties of the surrounding neurons were estimated from dependent sampling, i.e., from comparison of the properties prior and following the perturbation. This approach allowed the estimation of the effect without the sampling bias towards an electrophysiological phenotype in small sample size.[263] Accordingly,

both MEA and calcium screening of the local network's activity following the single-neuron perturbation were compared in paired samples, before and after the stimulus. However, the chosen mechanical stimulus did not allow repetitive deformations on the same neuron. Namely, mechanical stimulus consisted of the same steps preceding the patch-clamp, including the giga-seal formation, and repetitive deformations would introduce membrane tears[179] underneath the pipette tip with every consecutive deformation. Because of this, pharmacological investigations of the initiation and propagation mechanisms were designed to include independent samples, and the overall properties were compared between different fields of view.

Statistical analysis was performed using `scipy.stats`. The Shapiro-Wilk test was used to test the normality of the distributions; for normally distributed datasets, parametric tests were performed, and data was shown as average ± SEM. Otherwise, non-parametric tests were used, and data was shown as median and IQR. For sample sizes over 5000, quantile-quantile (QQ) plots were used to inspect normal distributions. Where applicable, log-normal distributions were presented with logarithmically-binned histograms and fit by a single or multiple Gaussian curves. Multiple pairwise comparisons were then corrected via Bonferroni corrections. Statistical significance was evaluated at $p \leq 0.05$. Box plots for data summation have boxes from the first to the third quartile, the median as a horizontal line, the mean as an x, and whiskers spanning over a 1.5x inter-quartile range. Bar plots represented mean, with whiskers corresponding to 95% confidence intervals. Symbols indicating statistical significance within the figures are: ns: $0.05 < p \leq 1.00$, *: $10^{-2} < p \leq 0.05$, **: $10^{-3} < p \leq 10^{-2}$, ***: $10^{-4} < p \leq 10^{-3}$, ****: $p \leq 10^{-4}$.

# 4. Ground-truth of high SNR MEA signals for accurate network activity inferences

Widely accepted as an elementary unit of neuronal communication, action potentials set the temporal resolution requirement to assay the information flow with high fidelity.[10, 148] Electrophysiology methods, particularly microelectrode arrays, provide parallel and direct screening of neuronal activity with a single-AP resolution. Yet, loose electrode-neuron coupling in conventional planar MEAs results in poor SNR and valuable information loss to noise, leading to the omission of some extracellular APs (EAPs) and a complete lack of PSP visibility. The former limits the accuracy of functional connectivity estimates from correlations of detected EAPs, while the latter limits the neuronal connectivity investigations to only correlative estimates. To that end, estimating true synaptic connection is restricted to intracellular electrophysiology, which is short-term and focused only on a few neurons at a time, but consistently detects at a PSP resolution.[15, 16] Recent engineering advances in MEA electrodes enabled detection with a higher amplitude sensitivity and provided more accurate network inferences due to a better distinction of biological signals. Nanostraw-nanocavity MEAs, developed by Pegah Shokoohimehr,[26, 27] marked a milestone towards non-invasive, parallel recordings of neuronal activity at the high amplitude resolution. In a collaborative project with Pegah Shokoohimehr,[26, 27] I characterized the neuron-electrode interface and demonstrated the electrodes are capable of detecting at the subthreshold resolution without any poration requirements (introduced in Section 4.2 and 4.3).

Even with these advances, MEA electrodes measure non-targeted and do not directly inform how many neurons are coupled. This information is relevant for accurate mapping of neuronal connections, evaluating network responses to a stimulus presentation, and informing neuronal phenotype success in stem-cell differentiation strategies.[200, 201] Furthermore, in cases of multiple neurons coupled to the electrode, an important information is *which neurons fired when,* for proper constructions of connectivity matrices and network response evaluations at a single-neuron resolution. Spike sorting algorithms are applied to the MEA traces to identify the source identity of detected EAPs. Under the premise that every neuron has a unique coupling with the electrode, EAPs of a given neuron are assumed to have similar waveforms that differ significantly from other coupled neuron's EAPs. Currently, several spike-sorters are developed and optimized for low SNR MEA measurements,[29, 30] and the consensus is that SNR improvements should also increase the spike sorting accuracy. However, paired electrophysiology identified a high variation of the single-neuron's EAPs, which reduced the spike sorting accuracy. In Section 4.4., I investigated the performance of the current spike sorting algorithms on high SNR measurements obtained from NS-NC MEAs, as well as misclassification trends concerning the neuron's firing regime and intracellular AP (IAP) properties. Finally, I postulate that a variable intracellular IAP – EAP transfer function

contributes additionally to the variability of the high amplitude EAPs from the same neuron (Section 4.5).

Misclassifications in spike sorting are particularly challenging to untangle since there is no *a priori* information on the number of electrode-coupled neurons, and the downstream handling of the found spike clusters is left to the investigator's judgment. This bias can impact the conclusions when MEAs are used in functional assessments of neuron-like properties following differentiation of stem-cells,[200, 201] and *in vitro* network activity assessments during the pharmacological investigations and targeted drug design.[264] With advances of the probe designs for *in vivo* purposes, similar challenges emerge for neuroscientific questions in *in vivo* set-ups. And while the effects of false negatives from EAP omission have been extensively studied,[265] it is to a lesser extent known how misclassification affects the inferences of network metrics. This chapter concludes with investigation of how misclassifications, prevalent in high SNR MEA measurements, affect the activity estimates of bursting networks, for different decisions post spike sorting (Section 4.6).

Given the advantages of 2D+ electrodes in mapping the functional and synaptic connections, the primary goals of this chapter were to:

1) evaluate whether the localized chronic topology of electrode-coupled neurons affects the network's spontaneous activity (Section 4.1);
2) characterize the neuron – 2D+ electrode interface and origin of high SNR EAPs (Sections 4.2, 4.3);
3) estimate how reliably do high SNR measurements convey the information of the network activity and connectivity (Sections 4.4 – 4.6).

This chapter contains my results partially reproduced from:

- Shokoohimehr, P.[#], **Cepkenovic, B.[#]**, Milos, F., Bednár, J., Hassani, H., Maybeck, V., Offenhäusser, A. High-Aspect-Ratio Nanoelectrodes Enable Long-Term Recordings of Neuronal Signals with Subthreshold Resolution. *Small.* (2022) DOI: https://doi.org/10.1002/smll.202200053 (#-equally contributed)

# 4.1. Spontaneous network activity probed with Microelectrode arrays

2D+ electrodes are a promising platform to study neuronal connectivity, as they allow more accurate activity estimates by promoting amplitude sensitivity. Neurons interfacing the 2D+ vertical structures, however, experience chronic and localized membrane curvatures, along with nuclear envelope deformation.[26] I first investigated if these affected the development of spontaneous network activity, which is relevant for studying native networks of neurons. The spontaneous network activity was sampled at RT, from *in vitro* cultures of dissociated cortical neurons containing about 640 mature somas/mm$^2$. About 17% of the recording area was covered with somas, while the total cell material coverage was 42% (Fig. C1, Appendix C1). A high amplitude resolution of NS-NC MEAs increased the misclassification incidence and impacted the spike sorting performance (Sections 4.4 and 4.6). Thus, the network activity estimates did not include metrics relevant for individual neurons' firings.[266] Individual channels' activity was rather considered as network activity sampled from fixed points in space, and the findings below were reported as such (see Section 3.3.3. for details on the electrode configuration and design).

Long-term activity was screened starting from the 1$^{st}$ week in culture. As shown in Figure 4.1.1. A, 7-14 days old networks displayed sparse and non-synchronized firing. Out of 16 1-2 week old cultures, only 8 showed activity in at least one recording site, with approximately one spiking channel per chip. The incidence of active cultures rose to 70% (N=83) between the 2$^{nd}$ – 3$^{rd}$ week and remained at 68% (N=50) after three weeks. Active cultures displayed activity across 23 ± 2% of channels between the 2$^{nd}$ and 3$^{rd}$ weeks, and the trend persisted a week after (28 ± 4%) (Fig. 4.1.1). Networks of neurons at different maturation stages exhibited distinct network activity patterns, with network bursts emerging after two weeks of culture (Fig. 4.1.1 A). At a single-neuron level, network bursts manifested as slow membrane depolarizations, which elicited APs upon the threshold crossing (Fig. 4.1.1. B). On average, 63 ± 31% of active channels participated in SNEs between the 2$^{nd}$ and 3$^{rd}$ week *in vitro*, with an average incidence of ca. 0.06 Hz. Three weeks and older cultures had a similar fraction of participating channels and SNE frequency (Fig. 4.1.1. C-E). A clear transition from the irregular to bursting regime was well defined from DIV 14, demonstrating the capacity of dissociated networks of neurons grown over NS-NC electrodes to mature into a functional community.[267] Bursting frequency below 1Hz matches the ultra-slow oscillations, previously reported for *in vitro* networks of dissociated cortical neurons grown on flat,[3, 268] suggesting that the 2D+ structures, at least locally, did not interfere with the native progression of the network into the bursting regime, nor with the bursting properties.

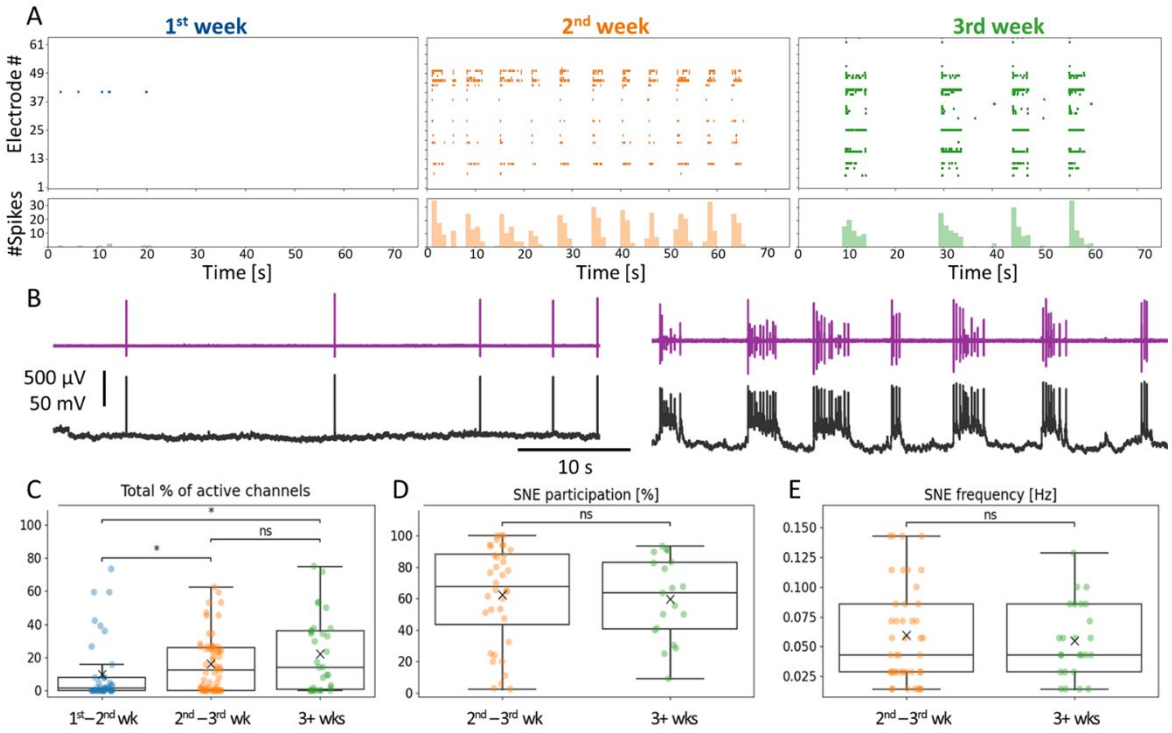


**Figure 4.1.1. Maturation of the primary neuron network activity through weeks *in vitro*.** A. Exemplary raster plots of NS-NC MEA measurements of 10 DIV (blue), 14 DIV (orange) and 21 DIV cultures. Histograms on bottom correspond to the number of spikes in 200 ms bins across all channels. Histogram peaks mark individual SNEs. Color code remains throughout. B. Exemplary MEA (purple) and intracellular traces (black) of a sparse-firing (left) and bursting neuron (right). C. Fraction of active channels for cultures at various stages. D. Fraction of active channels participating in SNEs. E. SNE frequency across DIVs. D and E lack the boxplots corresponding to 1st – 2nd week cultures due to absence of network bursts. Nanostraw-nanocavity MEAs, used throughout this thesis, were developed by Pegah Shokoohimehr.

With active and non-active cultures pooled together, there was an average of 16% active channels per chip. Since the electrode measured from neurites and soma (Section 4.2), the number of active channels was lower than expected by chance, even at the peak of the networks' maturation. Reduced number of active channels per chip increases the time and resources when characterizing novel electrode designs, since more cultures are required to acquire proper sample sizes. While culture-to-culture variations such as the overall neuronal fitness or random distribution of the cell material across the recording area can majorly impact the detection yield, a reduced number of active channels may be due to sparse firing of electrode-coupled neurons. Since network bursts recruit previously inactive neurons, one approach is to measure mature cultures with dominant bursting activity. Yet another approach comprises of electrical stimulation, with only transient excitatory effects. Bursting activity at the network level can be induced pharmacologically without the time required for the network to synchronize spontaneously.

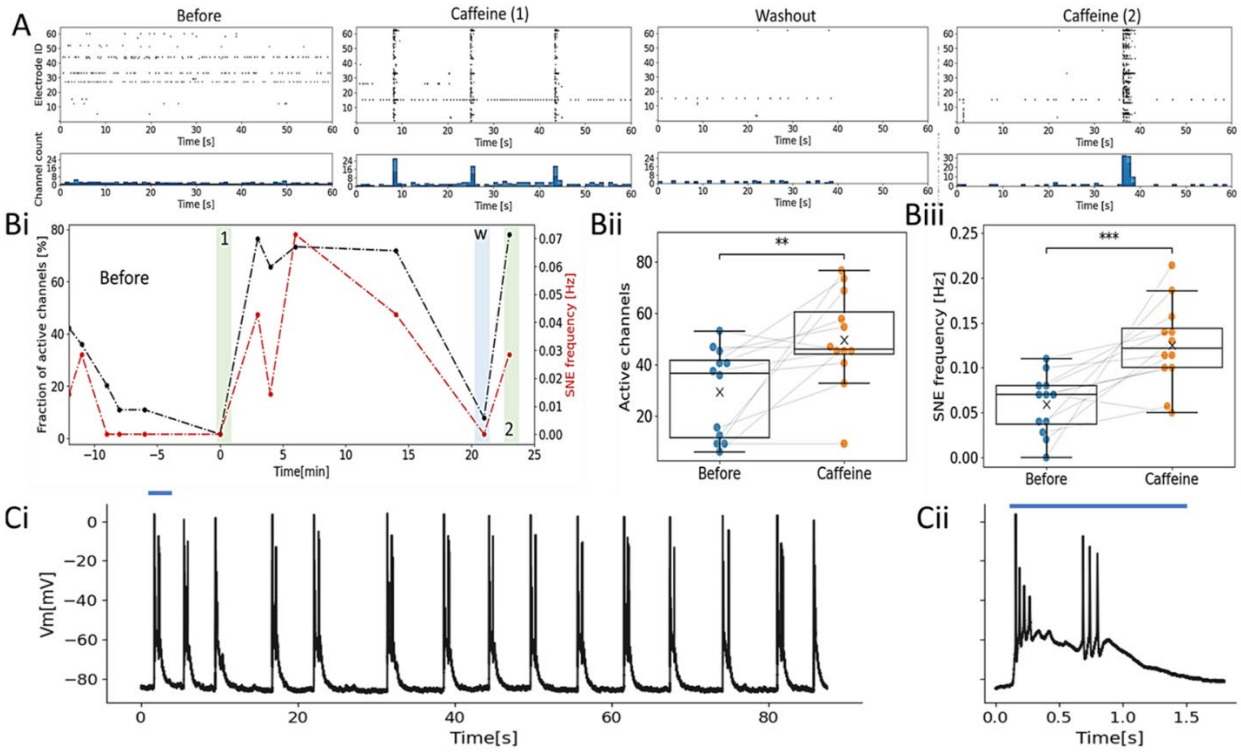


**Figure 4.1.2. Network synchronization via 8 mM caffeine.** A. Raster plots representing individual spike indices from MEA culture during the > 30 min caffeine experiment. Cultures were monitored as control about 10 min prior to treatment. Caffeine (1) denotes first caffeine treatment, followed by washout and second caffeine treatment. Histograms below denote collective spike count. B. Quantification of the collective network activity changes following caffeine treatment. Bi. Dynamics of the fraction of active channels (black) and SNE frequency (red) for recording in A. Green shades denote caffeine treatments (1) and (2), while blue line stands for measurement after the washout in Ep. Zeroth time denotes the first measurement following caffeine addition. Parameter fluctuation at the beginning of the recording session was likely due to the network's accommodation to temperature changes and handling conditions. Bii. Fraction of active channels prior and after addition of caffeine. Biii. SNE frequency before and in caffeine. C. Exemplary whole-cell trace showing response of caffeine-treated neuron. Right: zoom-in on a first giant EPSP.

To estimate if pharmacological interventions are an efficient strategy to increase the number of measuring sites per chip, networks of neurons were treated with 8 mM caffeine (Section 3.5.1) and probed with paired electrophysiology (Fig. 4.1.2. A). Caffeine significantly increased the SNE frequency from 0.07 Hz (median; IQR: 0.04) to 0.13 Hz (median, IQR: 0.07) ($N = 12$, $p < 10^{-2}$, Wilcoxon) starting from 10 min after addition. The average number of active channels rose from 29 ± 5% (5-10 min prior) to 50 ± 5% (5-10 min after, $N = 12$, $p < 10^{-2}$; paired t-test). The overall increase of channels participating in SNEs indicates that the primary mechanism was through recruitment of neurons into the collective network activity. As depicted in Figure 4.1.2 B, the slope for active channels and SNE frequency was higher if these parameters rated low prior to treatment, while there was little to no effect on already active and well-synchronized networks. In one isolated case, the network did not engage in synchronous activity even following the addition of caffeine. This is unsurprising, as this treatment does not correct for the positional or fitness effects. Since the effect is reversible (Fig. 4.1.2 Bi), this approach allows the

combination of chip characterization procedure with screening of the native network activity, following the wash-out. At the membrane, caffeine increased the frequency of spontaneous giant EPSPs, as confirmed by simultaneous patch-clamp. This suggested caffeine effect was likely via the synchronization of excitatory inputs and concurrent modulation of post-synapses for simultaneous inputs (Fig. 4.1.2.C).

In summary, spontaneous activity of neurons grown on 2D+ NS-NC MEAs spontaneously progresses into the bursting regime, starting 14+ DIV in culture. Developed network bursts' frequencies matched those of slow oscillations previously reported for *in vitro* culture. Lower incidence of active channels than expected from coverage area was at least partially from undersampling of sparsely active, non-engaged neurons. Treatment with 8 mM caffeine effectively recruited previously inactive neurons into SNEs and increased the overall incidence of active channels. Giant PSPs detected intracellularly following caffeine addition suggested the primary mechanism of action was via potentiation of synchronous excitatory inputs. This simple but effective intervention could reduce the culturing requirements when characterizing novel neuron-sensing devices.

## 4.2. Ground-truth of action potentials detected by 2D+ MEAs

Simultaneous patch-clamp and NS-NC electrode measurements of the electrode-coupled neurons served to characterize the NS-NC electrode signals and the neuron-electrode coupling. NS-NC MEAs detected at a wide range of amplitude sensitivity, including the signals akin to planar electrodes,[269] NC-only electrodes,[193] and 2D+ electrodes.[26, 27, 192] The aim was to evaluate how the neuron-electrode coupling parameters give rise to high-amplitude extracellular APs (EAPs) and how different amplitude sensitivity shapes the intracellular AP (IAP) transformation.

The use of ground truth enabled investigation of the electrode's amplitude sensitivity with respect to the neuron's localization and coupled compartment, providing insight into the mechanistics of the neuron-electrode coupling. Furthermore, a direct comparison between the IAPs and corresponding EAPs was employed to estimate how the IAP transforms into EAP during neuron-electrode transfer. Ground truth was obtained from whole-cell recordings of spontaneous activity in current-clamp mode (details in Section 3.3.4). Additionally, neurons were injected with 0.1 – 0.25 s current pulses to elicit APs. A neuron was considered to be electrode-coupled if evoked and/or spontaneous APs were robustly detected in both systems (Fig. 4.2.1).[182] When MEA electrode showed EAPs synchronized to the patch-detected IAPs, but also other EAPs non-related to the patched neuron's activity (Fig.4.2.1 B-C) the recording was regarded as a true multi-unit activity (Section 3.6.4). Particularly during the synchronous network events, the true multiunit activity expressed sporadic complex EAP waveforms from merging of the EAPs from two or more highly correlated neurons (Fig. 4.2.1.C). Target neurons near the electrode showed prior spontaneous activity up to 70 min before the ground-truth validation (Fig. C2, Appendix

C1). Of the 74 whole-cell recordings of the neurons near the recording sites, only 21 were coupled with the electrode (Fig. C5, Appendix C1 summarizes all couplings). While the distance of the neuron's soma from the recording site was not a reliable indicator of the coupling outcome, the coupled neurons resided within a 17 ± 4 µm radius, and not always had their soma positioned on top of the electrode (Fig. 4.2.2. A).

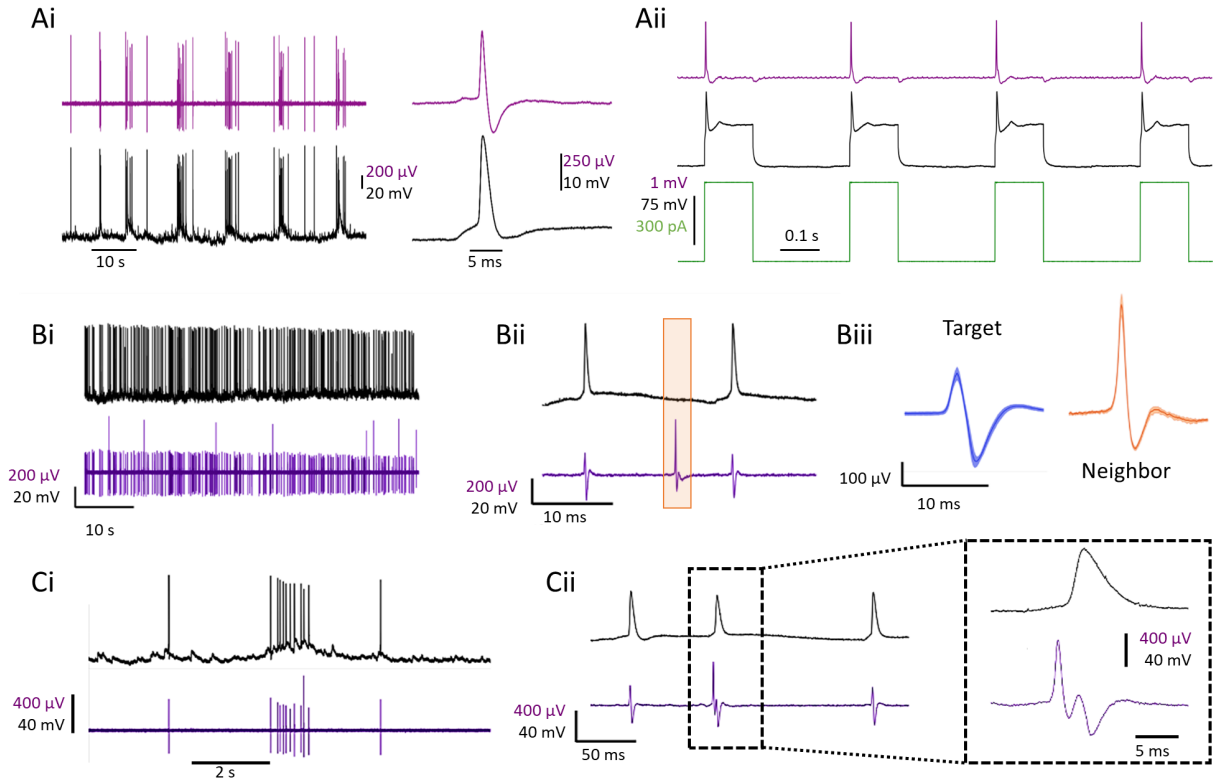


**Figure 4.2.1. Ground-truth of action potentials detected by NS-NC MEAs.** A. True MEA-detected single-unit activity confirmed via the paired patch-clamp (black) and MEA (purple) recordings from the electrode-coupled neurons. Ai. Paired measurements of spontaneous activity showing a robust occurrence of APs in both traces. Right: zoom-in on a single AP. Aii. Paired recordings of neuronal activity evoked by current injection (green). B. True multi-unit activity detected by the MEA electrode and confirmed via the simultaneous patch-clamp. Bi. One minute recording of spontaneous activity. Bii. Zoomed inset showing patched neuron's spikes, along with neighboring neuron's EAPs (orange rectangle). Biii. Averaged EAP waveforms of the target neuron (blue) and neighbor (orange). C. True multi-unit activity during bursts. Ci. Recording segment depicting bursts of APs. Cii. Zoom on intraburst APs, with EAP waveforms from two neurons merging to form a complex one. Right inset: focus on merged EAP waveforms (purple) and IAP (black) of the target. Figure contains my results published in [27]

As also shown in Figure 4.2.1., NS-NC MEA detected EAPs at an exceedingly high amplitude resolution. SNR was first evaluated to relate the quality of the coupling to the physical coupling parameters, such as the distance from the recording site and the neuron's size. When estimated as RMS of the whole MEA trace, the computed noise was 12.2 ± 2.2 µV (N = 21). To calibrate to the previous characterizations of NC only electrodes, the noise was additionally estimated from the baseline (Section 3.6.3). The computed baseline RMS was 3.3 ± 0.5 µV, in the range previously reported for NC MEAs with similar openings.[193] In following sections, the noise was always estimated as $RMS_{recording}$ for comparison with previously published work on EAP

waveform variations,[199] and SNR was estimated from $RMS_{recording}$. The coupled neurons' traces had a range of SNRs, with an $SNR_{avg}$ of 22.5 ± 4.6 (range: 0.6 – 66.2, N = 21) and a $SNR_{max}$ of 64.2 ± 4.6 (range: 4.9 – 230.9, N = 21). It is worth noting that, within this set of measurements, the SNR distribution was skewed towards higher values due to the sampling bias towards the sites showing high SNR spontaneous activity prior to patch-clamp. Thus, EAP characterization in following sections should be interpreted in light of high SNR couplings and may not faithfully represent all coupling configurations in NS-NC records.

Despite the improved membrane-electrode interface and SNR, ground-truthed NS-NC MEA traces exhibited a wide range of amplitude resolution, encompassing signals similar in magnitude to those detected via planar MEAs (SNR < 8),[269] nanocavity-only (8 < SNR < 30),[193] and 2D+ electrodes (SNR > 30)[26, 27, 192] (Fig. 4.2.3). Positive monophasic EAPs particularly predominated >30 SNR signals (7 out of 12), while bi- or tri- phasic (3/12) and negative monophasic EAPs (2/12) were less frequent. Medium SNR spikes were either bi-phasic (2/5), positive monophasic (2/5) or negative monophasic (1/5). Predominantly negative EAPs were frequent in < 8 SNR traces (3/4), while only one low SNR recording had positive monophasic EAPs. A higher incidence of positive monophasic EAPs is in accordance with the previous reports on 2D+ electrodes,[186, 191] as well as loose-patch measurements from different neuronal compartments.[270-272]

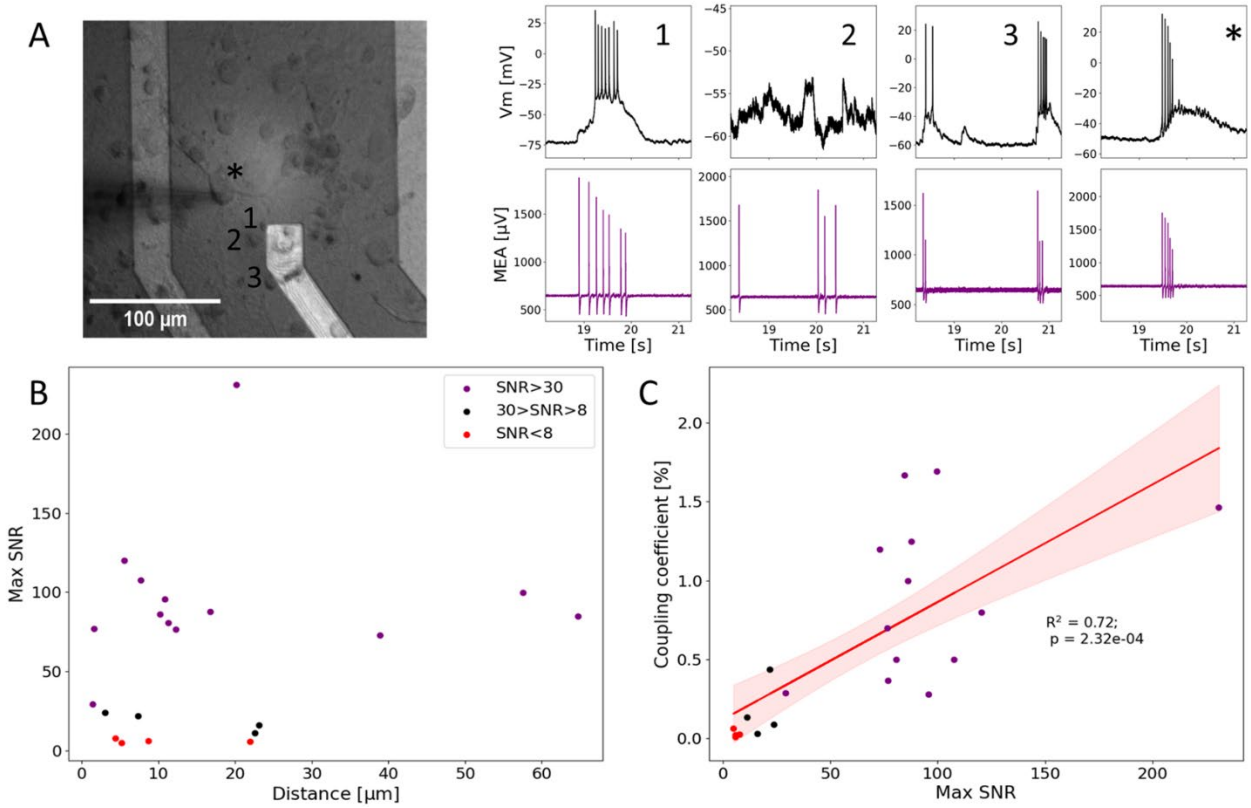


**Figure 4.2.2. Electrode-soma distance and its relation to detected SNR.** A. Proximity of the soma to the recording site is not a reliable indicator of the coupling. Left: a brightfield micrograph depicting patched electrode-coupled neuron (*-ed), and previously patched proximal somas that were not coupled to the recording electrode

(numbered 1-3). Right: Paired traces depicting patch-detected signals of investigated neurons (black) and MEA electrode recording (purple). Symbols in the patch trace match the position of the patch signal sources on the left, indicating the relative positions of coupled (*-ed) and non-coupled neurons (1-3) to the recording electrode. B. Signal-to-noise ratio vs. neuron-electrode distance. C. Coupling coefficient vs. signal-to-noise ratio. The shaded area depicts the 95% CI of the linear fit (red line).

SNR did not linearly correlate with the soma-electrode distance (Fig. 4.2.2. B), while non-linear fits failed to converge (Fig. C3, Appendix C1). This is in contrast with findings previously reported for extracellular recordings *in vivo* and planar HD MEAs *in vitro*, where SNR follows the inverse relation with the distance from the soma and IAP initiation zone.[64, 166] On the same token, hardware-applied 10-72 Hz high-pass filter removed the prevailing frequencies of LFPs,[273] suggesting that contribution of long-range trans compartmental currents is minimal. In fact, some of the > 50 SNR signals were obtained from neurons whose soma resided about 60 µm from the electrode (Fig. 4.2.2 B), close to the limit of the field potential detection.[166] These suggest that the high SNR recordings arise from a stable membrane-electrode coupling, either at the proximal neurites or soma.

The coupling coefficient (CC), which represents the portion of the intracellular signal that persists during the signal transfer,[25] ranged from 0.02 to 1.69 and linearly correlated with the electrode's SNR (Fig. 4.2.2. C, Pearson: $R^2 = 0.72$, $p < 10^{-3}$). This correlation confirms that the critical determinant of the electrode's SNR was the quality of the membrane-electrode coupling. Detected SNR depended on the electrode-membrane sealing, which was an uncontrolled variable. Yet, there was a strong direct correlation between the SNR and the neurons' somal area ($R^2 = 0.78$, $p < 10^{-4}$). This is expected for two reasons. Firstly, larger neurons have a higher current density per unit area, both at the soma and dendrites. Secondly, even with the consistent unitary ion channel density, larger junctional membrane area provides a stronger capacitive current source and allows the better electrode coverage.[187] EAPs had a negative latency to the corresponding IAP, with an average jitter of 1.2 ± 0.3 ms. Absolute delays between the EAPs and IAPs inversely correlated with the UP slope of an IAP, which corresponds to the fast sodium currents. It was also the case for delays between the EAPs and the first temporal derivatives of an IAP (Fig. C4, Appendix C1).

The coupling of the EAPs with the ground truth IAPs was then investigated across different SNRs. For different sets of neuron-electrode couplings, EAPs were compared to the first temporal derivative of the corresponding IAPs. As Figure 4.2.3 shows, particularly low (< 8) and moderate (8 < SNR < 30) SNR EAPs matched the first IAP time derivative. However, EAPs with > 30 SNR were about 2x wider than the IAP derivative, similar to the IN CELL configurations previously reported by Spira.[29] The EAP widening was likely due to increased sensitivity of the coupling towards the $K^+$-driven hyperpolarization phase of an IAP. In addition, IN-CELL couplings were sensitive to the subthreshold depolarizations preceding an IAP. Explicit estimations of the IAP – EAP transfer functions (details in Section 3.6.4 and 4.5), confirmed that the coupling sets the high-pass filter for IAP-associated frequency ranges (1 Hz –

1 kHz).[8][25] Magnitude plots in Figure 4.2.3. B, also indicate the inverse relation between the output signal attenuation and SNR. With SNR improvements, the output is less attenuated across all frequencies, resulting in visibility of slower events in IN CELL configuration, such as those associated with hyperpolarization and sub-threshold pre-depolarizations (Fig. 4.2.3. B).

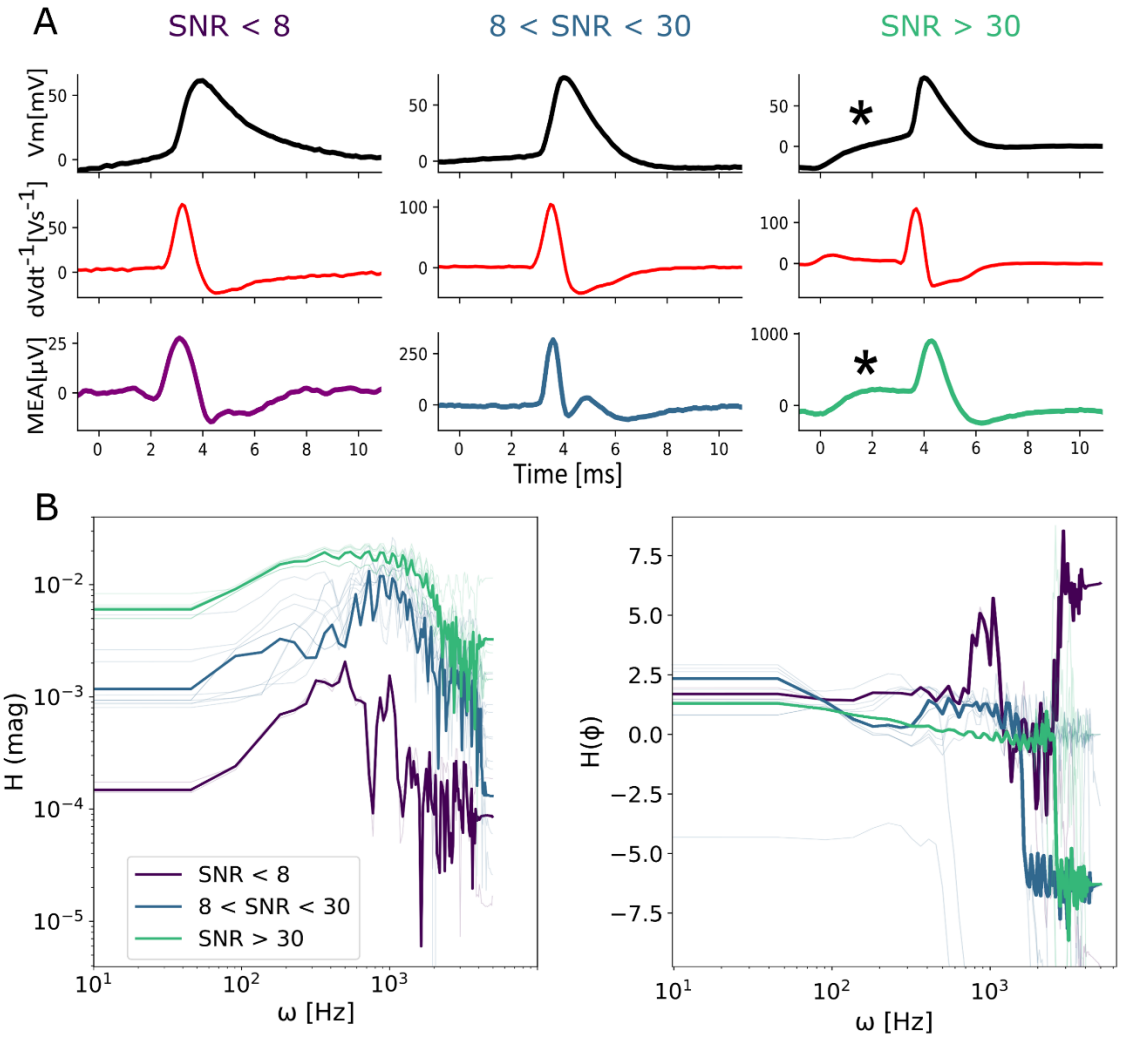


**Figure 4.2.3. Explicit estimation of IAP-EAP coupling.** A. EAP (purple) relation to the IAP (black) and first temporal derivative of IAP (red). Illustrated are exemplary waveforms for different MEA SNR ranges. Different y-scales are to emphasize waveform intricacies within each group. B. Bode plots depicting magnitude (left) and phase (right) of explicitly estimated IAP – EAP transfer functions for three different SNR ranges. Shaded areas depict different transfer functions within each dataset (for details see Section 4.5). Transfer functions were estimated by analysis pipeline developed by Csaba Forro.

In summary, from paired on-chip patch-clamp recordings of APs, I showed that NS-NC MEAs detect with high amplitude sensitivity, and also detected slower subthreshold pre-depolarizations and potassium-driven phases of an IAP. The high resolution stemmed from a stable coupling with the membrane, either of soma or proximal neurites. Explicit estimates of transfer function showed lesser attenuation at lower IAP frequencies for high SNR recordings. For neuron

[8] The apparent low-pass effect > 1 kHz will be discussed in Section 4.5.

network inferences, this sensitivity towards lower IAP frequencies indicates sensitivity to the subthreshold potential changes, such as post-synaptic potentials.

## 4.3. NS-NC MEAs detect at a subthreshold resolution

Simultaneous recordings of the spontaneous neuronal firing demonstrated that NS-NC MEAs also detected individual post-synaptic potentials (Fig. 4.3.1). Along with the EAPs, smaller spikes robustly occurred and were time-locked to the intracellularly detected PSPs (icPSPs). This correlation favors the interpretation that accompanying smaller EAP spikes represented the extracellularly detected post-synaptic potentials (ecPSPs) of the target neuron over the interpretation that they represent the neighboring neurons' EAPs. Coinciding subthreshold events were detected individually at the NS-NC electrode. Due to the symmetrical chloride concentrations of the intracellular solution (see Section 3.3.4), neither patch-clamp nor MEA could differentiate between inhibitory (IPSPs) and excitatory post-synaptic potentials (EPSPs). Here, activation of GABARs in symmetric chloride concentrations also led to membrane depolarizations, as the predominant electrical gradient drove $Cl^-$ outside of the cell. The lack of distinction between the EPSPs and IPSPs rendered their separate characterization, such as possible subtle differences in signal transfer between the faster IPSPs and slower EPSPs. Therefore, the characterization of individual subthreshold events detected by NS-NC MEAs was on pooled EPSPs and IPSPs, while the general guideline for ecPSP detection in NS-NC MEA traces only was exclusively for positive deflections acting as a putative excitatory ecPSPs.

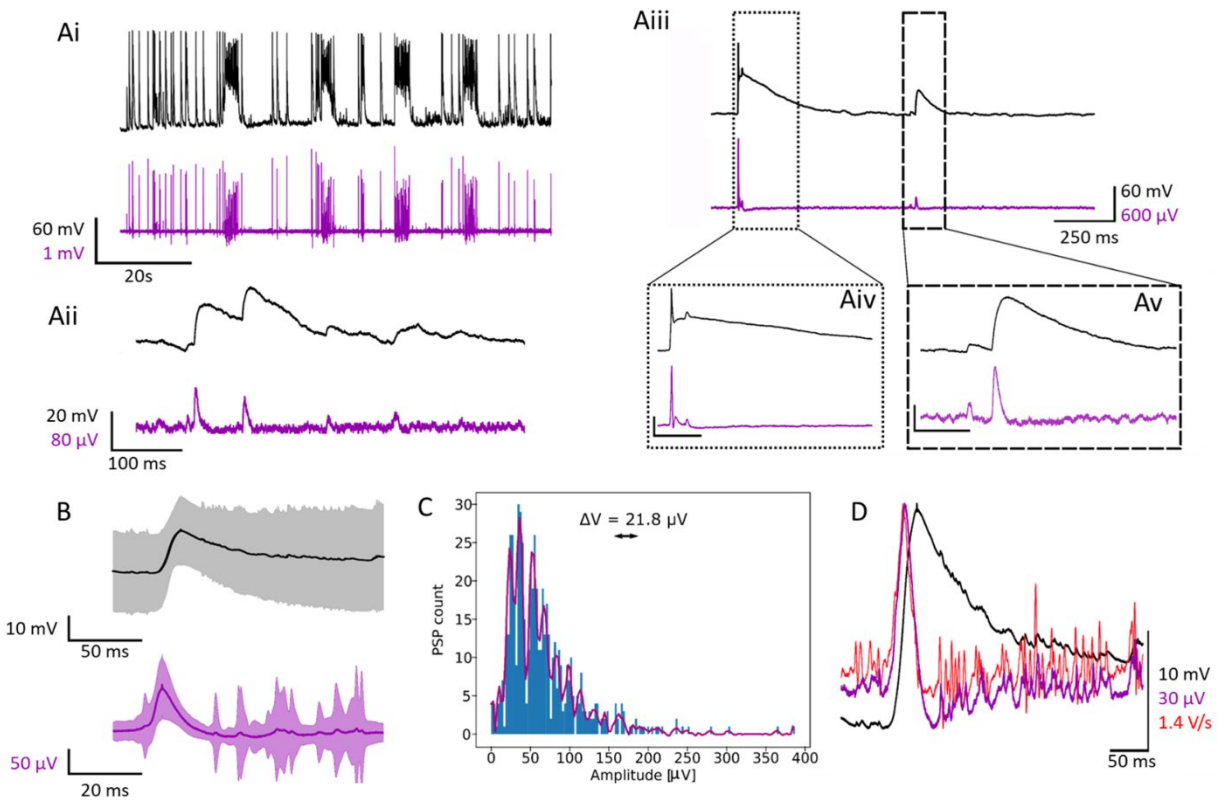

**Figure 4.3.1. NS-NC MEAs record at the subthreshold resolution.** A. Combined patch and MEA detection of the electrode coupled neuron's spontaneous activity. Black trace: patch record; purple trace: MEA record. Ai. A minute recording denoting APs and PSPs. Aii. Individual and coinciding subthreshold PSPs, simultaneously detected by the NS-NC electrode (ecPSPs) and intracellularly (icPSPs). Aiii. Zoomed-in suprathreshold EPSP carrying action potential and a spikelet (Aiv), accompanied with isolated, subthreshold PSPs (Av). Aiv focuses on suprathreshold EPSP, with y-scale corresponding to 40 mV (patch trace) and 400 µV (MEA trace). Av represented two isolated PSPs; y-scale: 20 mV (patch trace) and 100 µV (MEA trace). X-scales in Aiv and Av corresponded to 5 ms. B. Averaged subthreshold icPSPs and ecPSPs. Shaded areas represent standard deviation. Note different time scales, for clear representation of slower icPSPs and faster ecPSPs. C. ecPSP amplitude histogram peaks around multiplies of 21.8 µV. D. Comparison of average ecPSP, icPSP, and first time derivative of icPSPs (red). Figure contains my results published in: [27].

As shown in Figure 4.3.1, NS-NC MEAs detected individual PSPs, as well as giant suprathreshold EPSPs carrying APs and spikelets. In contrast to the isolated PSPs, spikelets emerged following the burst-leader AP, which made them distinguishable even from NS-NC MEA traces. Only the isolated PSPs were used to characterize the relation between the subthreshold intracellular and NS-NC signals. Figure 4.3.1. B illustrates that ecPSPs have standard positive monophasic shape with a steep rise and slower exponential decay. From single-exponential fit, the calculated time constant of icPSP decay was $\tau_{patch}$ = 34.2 ms, while ecPSP displayed 10x faster decay, $\tau_{MEA}$ = 3.6 ms. The onset-to-peak amplitudes of icPSPs were 18.8 ± 9.1 mV, while it was 60.2 ± 52.1 µV (mean ± SD) for ecPSPs. The amplitudes of ecPSPs and icPSPs moderately correlated (Pearson´s, R = 0.55, $p < 10^{-3}$). For the measurement in Figure 4.3.1, the coupling coefficient for PSPs was 0.3%, ca. four times smaller than that of the APs. For others, coupling coefficients ranged from 0.13 to 0.47%, and were half to 1/5 that of corresponding APs (Table 4.3). These results conflict the present-day simulations that predict less signal loss in slower events.[25] ecPSPs were about ten times faster than the icPSPs, and, unlike corresponding APs of the same neuron (Section 4.2), perfectly matched the 1st temporal derivative of icPSPs. Stronger attenuation and derivation of PSPs is unsurprising, given the high-pass transformation and a high prevalence of frequencies below the critical frequency. Similar to the findings of Abbott et al,[274] ecPSP amplitude histogram displayed peaks around multiplies of ΔV = 21.8 µV. While the reported amplitude distribution reflects the quantal nature of synapses, detection of miniature PSPs that arise from stochastic vesicular releases is unlikely due to the attenuated coupling coefficient. Rather, the noted ΔV represents a multiplier of miniature PSP events that reaches the NS-NC detection threshold.

Table 4.3. PSP and AP detected coupling coefficients for a given electrode-neuron pair

| Pair | AP coupling coefficient (%) | PSP coupling coefficient (%) |
|---|---|---|
| 1 | 0.29 | 0.13 |
| 2 | 1.46 | 0.37 |
| 3 | 1.00 | 0.47 |
| 4 | 1.67 | 0.35 |
| 5 | 1.20 | 0.35 |
| 6 | 0.50 | 0.14 |
| 7 | 0.80 | 0.23 |

*APs – action potentials, PSPs- post-synaptic potentials.*

MEA traces that detected PSPs had a high maximal SNR, with EAPs at least 350 µV high, either positive monophasic or biphasic. In a sole case, the electrode detected predominantly negative EAPs with a high (>30) SNR but did not show ecPSPs (Fig. 4.3.2 Ai). As negative monophasic signals are associated with axons[275] that also filter low-frequency passive events,[276] these suggest that the PSP detection yield also depends on the neuronal compartment that couples with the electrode. From the general observations of the ground-truth confirmed PSP incidence in NS-NC MEA recordings, a crude guideline was derived on how to detect ecPSP in high-SNR traces. Firstly, ecPSPs were only detected in paired measurements with SNR over 30, having positive monophasic or biphasic EAPs with predominant first-positive component (Fig. 4.3.2. Aii). Secondly, ecPSPs demonstrated positive monophasic shapes with a sharp up phase, and slower exponential decays, and differed from EAPs in shape (Fig. 4.3.2. B). Finally, the absence of spike merging between the high-amplitude and smaller-amplitude spikes indicated that smaller, accompanying spikes corresponded to ecPSPs instead of neighboring neuron's EAPs (Fig. 4.2.1).

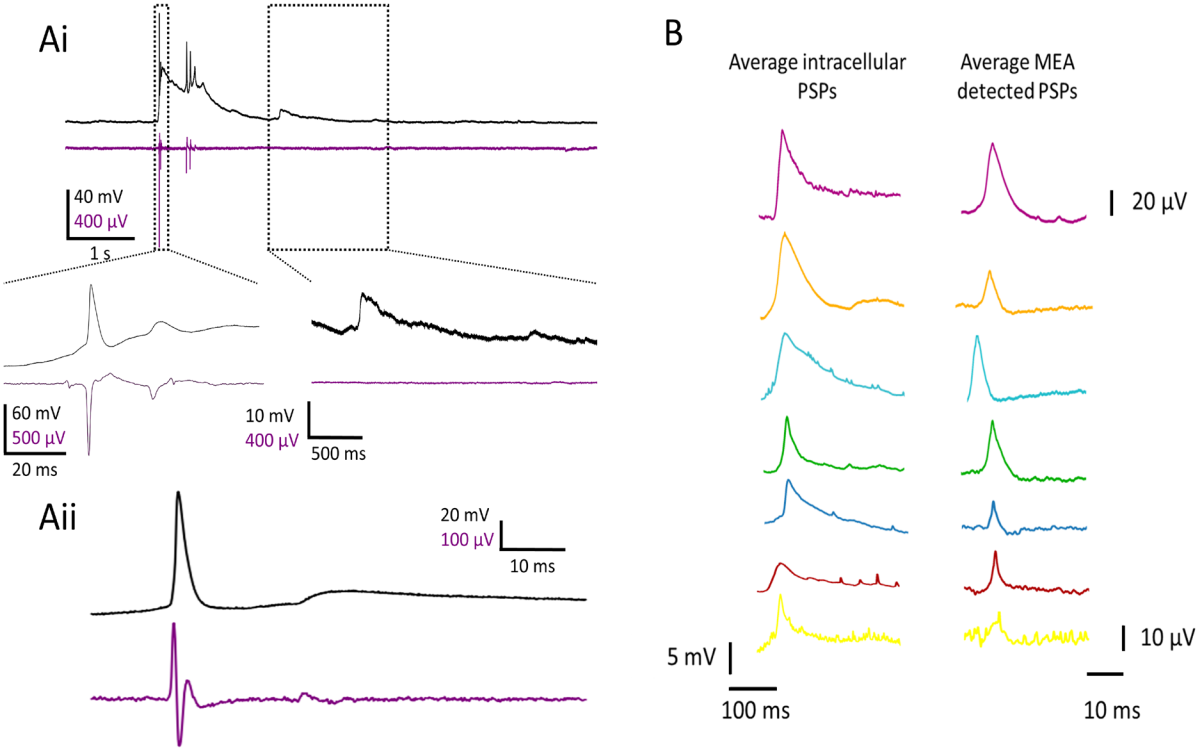


**Figure 4.3.2. Paired electrophysiology to investigate ecPSP occurrence and sensitivity.** A. Representative traces showing the NS-NC MEA's capacity to detect PSPs. Ai. Paired recording of spontaneous activity, with NS-NC MEAs detecting high-magnitude EAPs with predominant negative phase from putative axon. MEA trace shows the lack of ecPSPs (purple) despite the presence of icPSPs (black). Aii. Another paired patch-clamp and MEA measurements showing ecPSPs detected by NS-NC MEAs. Here, the EAP amplitude does not exceed 500 µV throughout the recording. EAPs were strongly triphasic with predominant positive phase. B. Average waveforms of icPSPs (left) and corresponding ecPSPs (right). Note different amplitude scales for ecPSPs to emphasize the shape of more attenuated signals at the bottom rows. This figure contains my results published in [27].

In summary, NS-NC MEAs showed the ability to detect slower membrane potential changes, including spikelets, pre-depolarizations, and post-synaptic potentials. PSPs were detected in

traces containing high SNR (>30) EAPs with predominantly positive phase, similar to IN-CELL[25] configurations. ecPSPs had distinct positive monophasic shapes and matched the 1st derivative of icPSPs. The latter was opposite to EAPs of the same neuron, which fell between the 1st derivative and IAP and experienced less amplitude loss during the signal transfer. The findings are in accordance with the high-pass property of the coupling, with higher attenuation at lower signal frequencies, particularly dominant in subthreshold membrane potential events. These paired experiments directly proved the ability of a non-poration inducing construct to detect at subthreshold potential resolution and provided a guideline to detect ecPSPs in other high SNR MEA recordings lacking the ground truth.

## 4.4. Benchmarking the automatic spike-sorter pipelines on paired recordings using SpikeInterface

High SNR couplings showed a rich catalog of EAP waveforms from individual neurons (Fig. 4.4.1). Here, I investigated if and how the single neurons' EAP diversity affects the performance of the automatic spike sorting pipelines. Ten paired recordings were used to benchmark different spike sorters out of 21 simultaneous measurements with SNRs ranging from 0.6 to 66.2 (Section 4.2). The benchmarking was performed exclusively on spontaneous EAPs to observe native waveform variations and resulting sorting errors. The dataset comprised more than 4.5 minutes of recordings with SNR > 8. One recording was excluded due to the mid-measurement pharmacological intervention with 8 mM caffeine, which caused a single switch change of shape in the EAPs (Fig. C6, Appendix C1). Here, either the coupling between the neuron and electrode, or the neuron and patch pipette changed from the shear stress during the drug application.

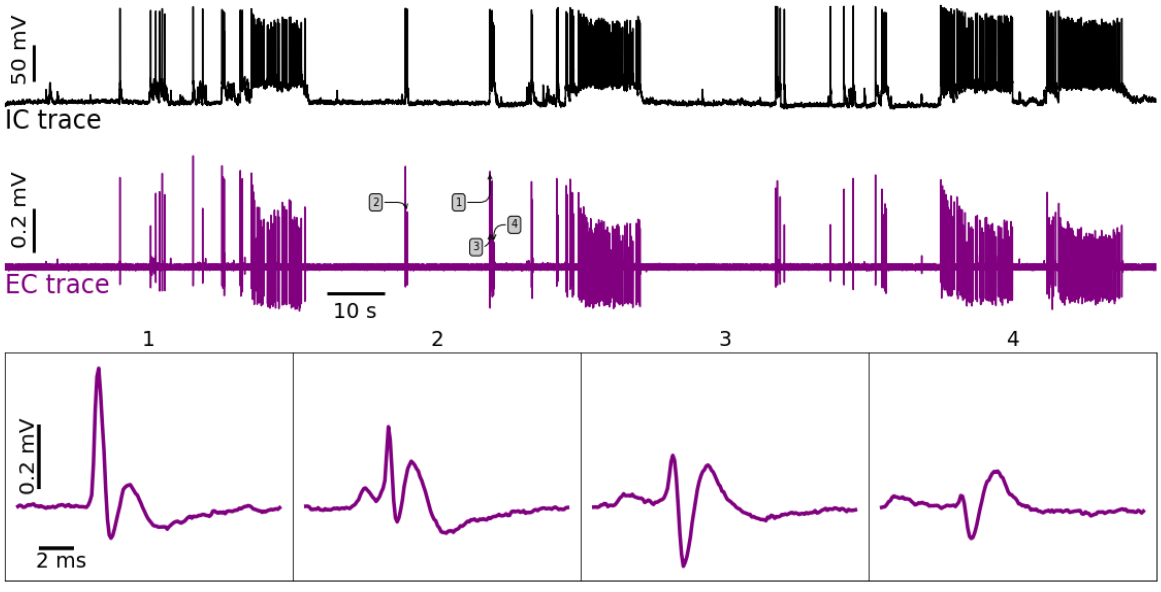


**Figure 4.4.1. Variation of the single-neuron EAPs.** Bottom insets depict exemplary single-neuron EAP waveforms, whose origin was confirmed by on-chip patch-clamp.

Six spike sorters were benchmarked on paired patch-clamp and MEA recordings via SpikeInterface, namely MountainSort4 (MS4), Tridesclous (TDC), Klusta (KL), Spyking Circus (SC), Waveclus (WC), and Combinato (CO). The sorters were run with default clustering, template-matching, and automatic curation parameters (Section 3.6.4). Paired recordings provided ground truth exclusively on the target neuron's signals, and the overall performance was evaluated on the spike-sorter unit with the highest correlation of spike trains (best-matching unit or BMU; for details, see Section 3.6.4). The overall metrics accounted for the incidences of false positives and negatives, with respect to the ground truth. Figure 4.4.2 shows that the average accuracy was below 60% for all investigates spike-sorters. This performance was poorer than previously reported for paired datasets of extracellular traces with lower SNR (80%).[29] While no single sorter emerged as the top performer, Waveclus most frequently showed accuracy over 60%. A detailed table of the spike-sorter performances for every recording is given in Table C1-C2 of Appendix C1.

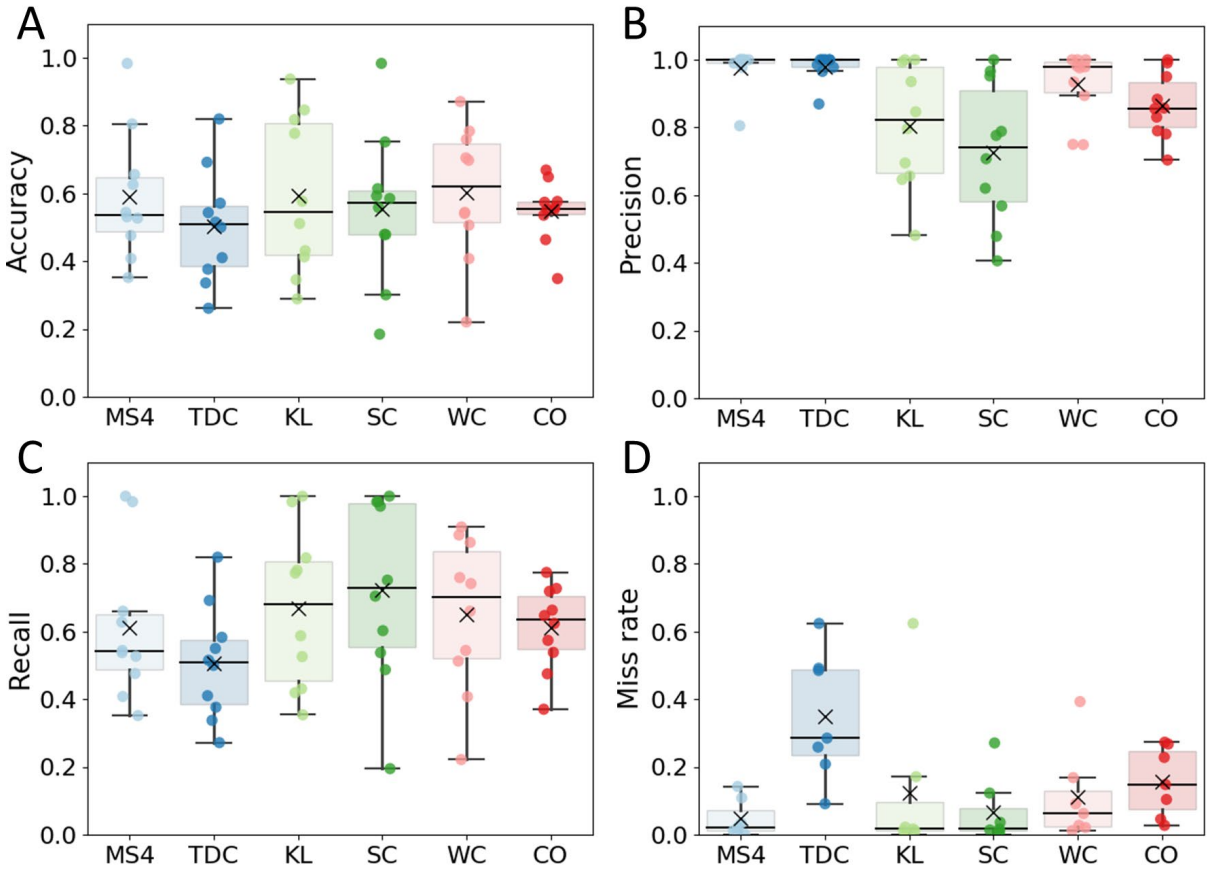


**Figure 4.4.2. Benchmarking the spike sorting performance on paired long-term datasets.** Depicted is the comparison of the overall accuracy (A), recall (B), precision (C) and miss rate during the spike-finding process (D). MS4- MountainSort4, TDC – Tridesclous, KL- Klusta, SC – SpykingCircus, WC – Waveclus, CO – Combinato.

Precision, a parameter inversely related to the incidence of false positives, was high (> 80%) for most of the spike sorters, except for SC (Fig. 4.4.2. B). SC showed the poorest performance in subthreshold-sensitive MEA traces with SNR > 20 (Fig. C7, Appendix C1). Due to amplitude-

robust template-matching process, SC assigned the positive monophasic shapes of the subthreshold pre-depolarizations and ecPSPs to the BMU containing EAPs. Therefore, the primary source of the false positives were non-spiking events of the same neuron. A high overall precision score indicates that committed spikes do not significantly contribute to inaccuracies. A reduced average recall (range: 50 – 74%), similar to the overall accuracy, suggests FNs significantly impact spike sorting performance in high SNR MEA recordings (Fig. 4.4.2.C). Omission errors arise either during the spike-finding or spike misclassification into the unit other than BMU. Benchmarking with 7 recordings containing true single-unit activity confirmed that missed spikes do not majorly contribute to the overall rate of false negatives (Fig. 4.4.2. D). Here, MS4 emerged as the best sorter with an average miss rate of 5 ± 2% , while TDC had the highest omission error rate (35 ± 7%, N = 7) due to its hard-coded recognition of high signals as artefacts (Fig. C8 and Table C2, Appendix C1). For others, the average miss rate ranged from 7% (SC) to 15% (CO), suggesting that, in high SNR recordings, the high omission error rate is primarily due to misclassification errors.

To focus on misclassification trends without interference from other sources of errors, only clustering was done on EAPs extracted from IAP indices. Re-aligned EAPs to their local maxima were submitted to SPC via Waveclus (Section 3.6.4).[259] As all of the EAPs belonged to the ground-truthed neuron, in case of misclassifications, the reference unit contained the most of the spikes and was denoted as “best unit” (BU), to differentiate from the BMU obtained from combined spike-finding and clustering process. Both BMU and BU relate to a spike-sorter unit that shows the highest correlation to the ground-truth. However, BU is deprived of false positives, and represented a unit that would pass the quality check criteria during the curation process due to a higher presence ratio. Among investigated high SNR couplings, only two neuron-electrode pairs had all EAPs clustered into a single unit (Fig. 4.4.3. A). On average, the other eight pairs had 31 ± 5% of the EAPs misclassified into one or two units other than BU (Fig. 4.4.3. B). Neurons with all EAPs clustered into the same unit had a lower firing frequency (0.10 Hz, N = 2) and burst incidence (0.01 Hz, N = 2) than those with misclassified EAPs (firing frequency: 0.88 ± 0.15 Hz; burst incidence = 0.10 ± 0.02 Hz, N = 8) (Fig. 4.4.3. C).

EAP waveform changes and resulting misclassifications were then evaluated with respect to the neurons’ firing. The majority of unit transitions occurred within (77 ± 3%) or at the burst boundaries (17 ± 2%), and only 6 ± 2% of the misclassifications occurred between the bursts. Transition probability, calculated as unit transition incidence per EAP position in the burst, was significantly higher for within-burst (median: 0.115, IQR: 0.397, N = 8) than outside-burst EAPs (median: 0.012, IQR: 0.045, N = 8; $p < 10^{-2}$, Wilcoxon) (Fig. 4.4.3. D). Overall, these suggested that bursting activity is a key determinant of EAP waveform variations and resulting spike misclassifications. Bursting neurons not only had a higher incidence of EAP variations, but waveform changes and misclassifications predominantly occurred within the bursts.

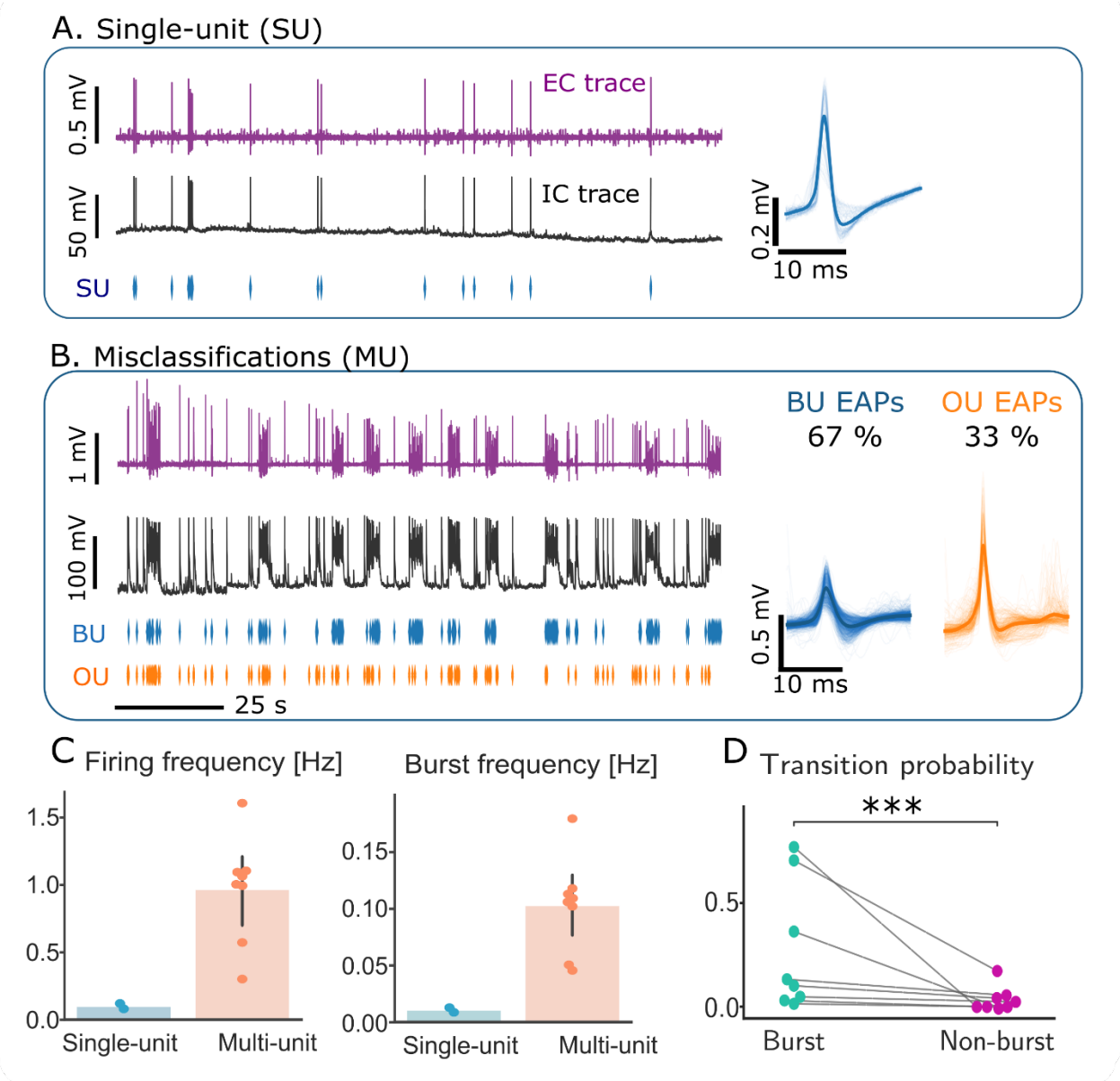


**Figure 4.4.3. Estimating classification error trends**. A. Combined patch and > 8 SNR MEA records of the neuron whose EAPs were classified into a single unit. Time stamps denoted as a raster below the intracellular trace. Right plot depicts average (bold) and individual overlaid EAPs (pale). B. Exemplary paired measurements of neuron whose EAPs were misclassified into more than one unit. Raster plots are below the patch trace, and EAPs of each unit are represented on the right. C. Comparison of average firing frequency (left) and burst rate (right) for neurons with and without misclassified EAPs. D. Misclassification incidences of within and between-burst EAPs.

What causes the individual neuron's MEA waveform variability? A high maximum SNR (56 ± 16, N = 10) suggests the EAP should not be majorly impacted by the noise fluctuations. In addition, hardware-applied filters between the 10 Hz and 8800 Hz captured predominant frequencies of the EAP, suggesting that noted variations were not due to aliasing. A consistent and low coefficient of variation for sections of the trace without the spiking activity confirms that spike variations were not a consequence of the baseline fluctuations (Fig. 4.4.4).

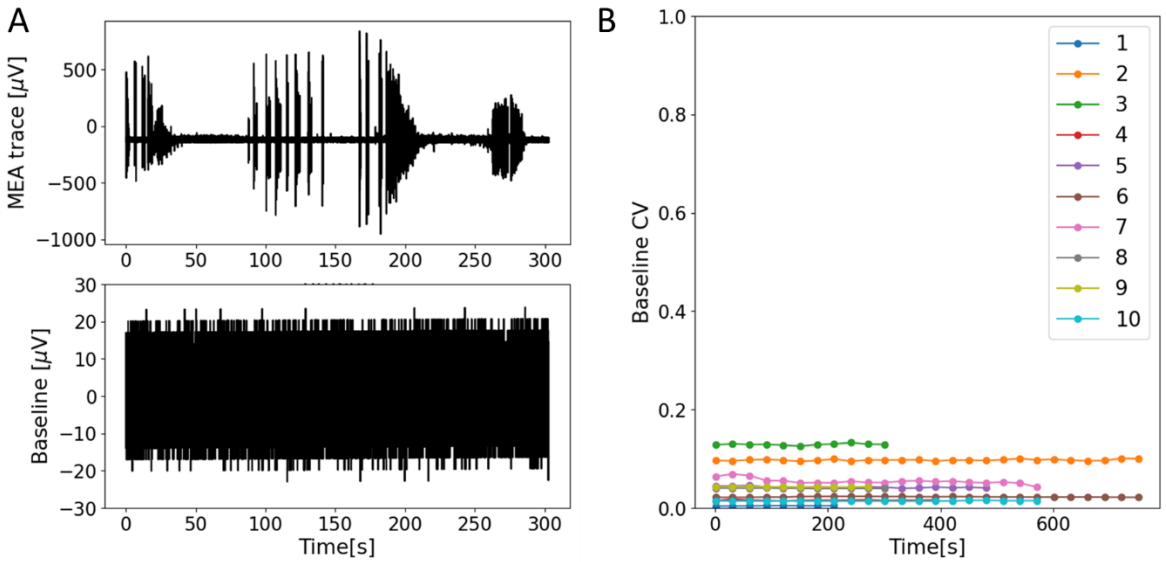


**Figure 4.4.4. Stability of the MEA baseline.** A. An exemplary 10 min NS-NC MEA trace capturing spontaneous activity of a single neuron, as confirmed via on-chip patch-clamp. Bottom demonstrates baseline of the same trace. C. CV dynamics estimated from the baseline.

The misclassification preference towards the bursting regime may be due to intrinsic variations in a given neuron-electrode coupling or interference from neighboring activity during network-wide synchronizations (as discussed in Section 4.1). Since high SNR EAPs arise from direct signal transfer at the coupled compartment (Section 4.2), contaminations by the neighboring activity take place when the neighbors also couple to the electrode. In particular, the waveform interference is expected when the neighboring neuron fires closely (Fig. 4.2.1) to produce complex waveform. However, only three benchmarked electrodes recorded from more than one neuron. Waveform merging affected clustering in only two neuron-electrode pairs, where the neighboring EAPs were comparably high as those of the target (as illustrated in Fig. C9, Appendix C1). In contrast, EAP clustering was unaffected by waveform collision in cases where the target neuron's EAPs were significantly higher than the EAPs of the neighbors. A relatively high misclassification rate (27%) persisted even after omitting multi-unit activity traces, suggesting that the leading cause of EAP variation is intrinsic to a given electrode-neuron pair.

EAP diversity can arise from burst-related IAP waveform variations. As discussed in Section 4.1, a depolarized baseline characterizes complex neuron bursts. Prolonged depolarization reduces the IAP driving force through $Na_vs$ inactivation and attenuates and broadens the IAPs. As the coupling is susceptible to the fast sodium phase of an IAP (Section 4.2), the heights and UP slopes of IAPs were compared between different spike-sorter units from the same neuron (see Fig. C10, Appendix C1, for the first temporal IAP derivatives for different sorter units). Comparison was only in paired measurements where the electrode detected only from the target, or where multi-unit activity and subsequent spike collisions did not affect the clustering process. The amplitudes and UP slopes of IAPs within the BU and OU had distinct distributions (Fig. 4.4.5. B). Whether the best unit and most of the spikes comprised of the faster, higher amplitude

(Fig. 4.4.5. B, first two top rows) or slower, lower amplitude IAPs strictly depended on the neuronal firing dynamics. The former illustrated adaptive multi-spikers that rarely fired within-burst, and most IAPs comprised the taller and narrower burst-leaders. In the latter, neurons readily fired within bursts, resulting in BU comprising of slower and shorter IAPs (Fig. 4.4.5. A). A higher incidence of non-adaptive multi-spikers among the investigated neurons (Fig. 4.4.5. B) resulted in BU most frequently containing within-burst, small amplitude IAPs. The separation extent of IAP amplitudes and UP slopes between different units scaled with the total range of IAP variations defined by the neurons' firing type.

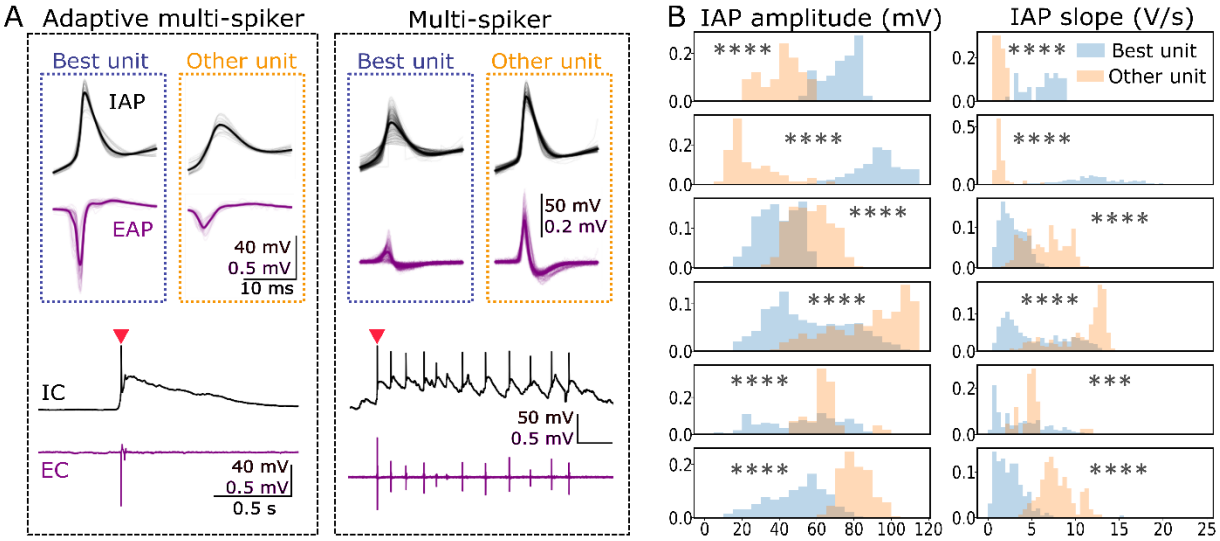


**Figure 4.4.5. IAP properties map to the EAP spike-sorter units.** A. Top: Exemplary IAP (black) and EAP waveform (purple) corresponding to the BU and OU, for two neuron-electrode pairs. Bottom traces show different firing behaviors of the probed neurons in a burst- adapting (left) and non-adapting multispiker (right). Red triangles mark burst leader spikes. B. Weighed histograms of IAP amplitudes (left) and UP slopes (right) for BU (blue) and OU (orange). Note the BU most frequently had distributions skewed towards the attenuated and slower IAPs. Statistical annotation: ***: $p \leq 10^{-3}$, ****: $p \leq 10^{-4}$, Kruskal-Wallis.

In summary, all tested spike sorters showed the low average accuracy for high SNR traces. Misclassifications of the found EAPs primarily contributed to the spike sorting errors. EAP misclassifications were intrinsic to a given neuron-electrode coupling and particularly frequent in bursting neurons. Mapping of the IAP properties to the EAP sorter units suggests the IAP variations contributed to the EAP variability. However, the IAP variations alone do not account for misclassification incidences higher than for the low SNR measurements. Within the dataset, the only low (< 8) SNR long-term recording of spontaneous activity had all EAPs classified into one unit, despite the bursting regime showing increased variations of the IAPs (Fig. C11, Appendix C). In the following chapter, I evaluated if inconsistencies of the IAP-EAP coupling further contribute to the noted MEA spike variations.

## 4.5. IAP-EAP transfer function consistency and its relation to the misclassification

Recent evidence suggests that coupling between the electrode and the membrane, and thus between the IAP-EAP signals, may not be as consistent as previously thought. Mechanical waves associated with firing[277-279] and burst-associated local ion concentration changes[280, 281] may impact how the signal transfers from the neuron to the electrode. The effect may be particularly prominent in 2D+ electrodes due to a high membrane curvature and reduced gap. Here, I investigated how consistent the IAP-EAP coupling is, which could have implications for additional high-magnitude EAP variations and, consequentially, reduced spike sorting accuracy. In addition, the excellent 2D+ electrode sensitivity to slower frequency components of IAPs paves the way toward parallel and reliable analog IAP estimates (Section 4.2). Unraveling analog IAP information directly from EAPs is valuable for high-throughput studies of channelopathies and targeted drug design and explorations of intrinsic IAP variations in the context of network synchrony.[66, 67, 282] Such studies mainly focused on the neurons' somas due to the hard access of intracellular measurements to thin neurites. Therefore, evaluating the consistency of the IAP-EAP signal transfer is also relevant to inform the current cell-electrode interface modeling strategies in pursuit of the IAP analog estimates from EAPs.

Since the main goal was to estimate if a single (consistent) transfer function can describe all the diversity of EAPs solely from the IAPs' variations, a "black box" predictive approach was first adopted (Fig. 4.5.1). Without underlying assumptions on the coupling, several neural network (NN) models were designed in `TensorFlow` to predict the EAPs from corresponding IAPs in each neuron. The consistency of IAP-EAP coupling was evaluated on high-SNR, long-term paired recordings of spontaneous activity (Section 4.4). Models training, validation, and testing were on paired recordings with single-neuron activity to avoid learning the EAP features from the neighboring neurons.

For every neuron-electrode coupling, each model was first trained and validated on a subset of IAP-EAP pairs belonging to the spike-sorter unit with most EAPs (BU), and their prediction performance was compared between the remaining BU subset and IAP-EAP pairs belonging to the other unit (OU). In the case of a consistent transfer function, the IAP changes fully account for the EAP variations, and the black box trained on the IAP-EAP pairs of BU would perform equally well on spike pairs of another unit. A range of models with increasing levels of complexity was constructed to explore whether differences in model performance across different units were due to the different IAP-EAP relations of these units, or if they could be attributed to model generalizability issues. The aim was to ensure that any conclusions about differences in IAP-EAP relations were not the result of using overly simplistic models.

The NN models were designed under consultation with Alina Bazarova and Stefan Kesselheim from Helmholtz AI Center. The catalog included models ranging from one-layered linear

regression models to combined long short-term memory (LSTM) and convolutional layers, and multi-layered densely connected NN with nonlinear, rectified linear unit (ReLU) activation. The simplest linear regression model (Lin_reg) comprised a single layer and approximated the IAP-EAP relationship as a linear function. A single convolutional layer (Conv1D) was used to better capture the non-linear relationships, while combining two convolutional layers (Conv1d_2_l) was used to capture hierarchical features within the data. Although LSTM models are primarily used to capture temporal intricacies of sequential data, in combination with convolutional layers, they are shown to efficiently learn complex patterns,[283] allowing generalizability over time-varying sequences. Similarly, densely interconnected layers with ReLU activation capture more complex relationships, particularly non-linear.

Due to a higher capacitive contribution to the coupling (Section 4.2), the input comprised the 1st temporal IAP derivatives (Fig. 4.5.1. A). The waveforms were isolated in an asymmetric window of [-6, 14] ms to fully capture the slow phases of the IAP and EAP post-peak recovery while maintaining the single-AP resolution. EAPs were extracted according to the first-IAP derivative peak-centered windows and recentered at the more dominant local extremum (minimum or maximum). EAP recentering was to ensure that eventual differences in the models' performance were not due to the variable IAP-EAP delays (Section 4.2). Half of the spike pairs from BU were pseudo-randomly pre-selected while testing and validation were on ½ of the remaining spike pairs for every dataset (Fig. 4.5.1. A; Table C3, Appendix C1 summarizes the IAP-EAP subsets for each dataset). This allowed the training process to capture most of the features among the spike pairs of the same unit while concurrently promoting generalization. The proportion chosen allowed unbiased comparisons of the performances between the two units, as a final subset of spike pairs used for testing within the BU fell within the range of misclassification rate and was comparable to that of the OU (Section 4.4). The NN model was trained using the mean squared error (MSE) loss function with a 0.01 learning rate in all cases. Model training lasted for a maximum of 1000 epochs, and stopped if there were no improvements after 15 consecutive epochs.

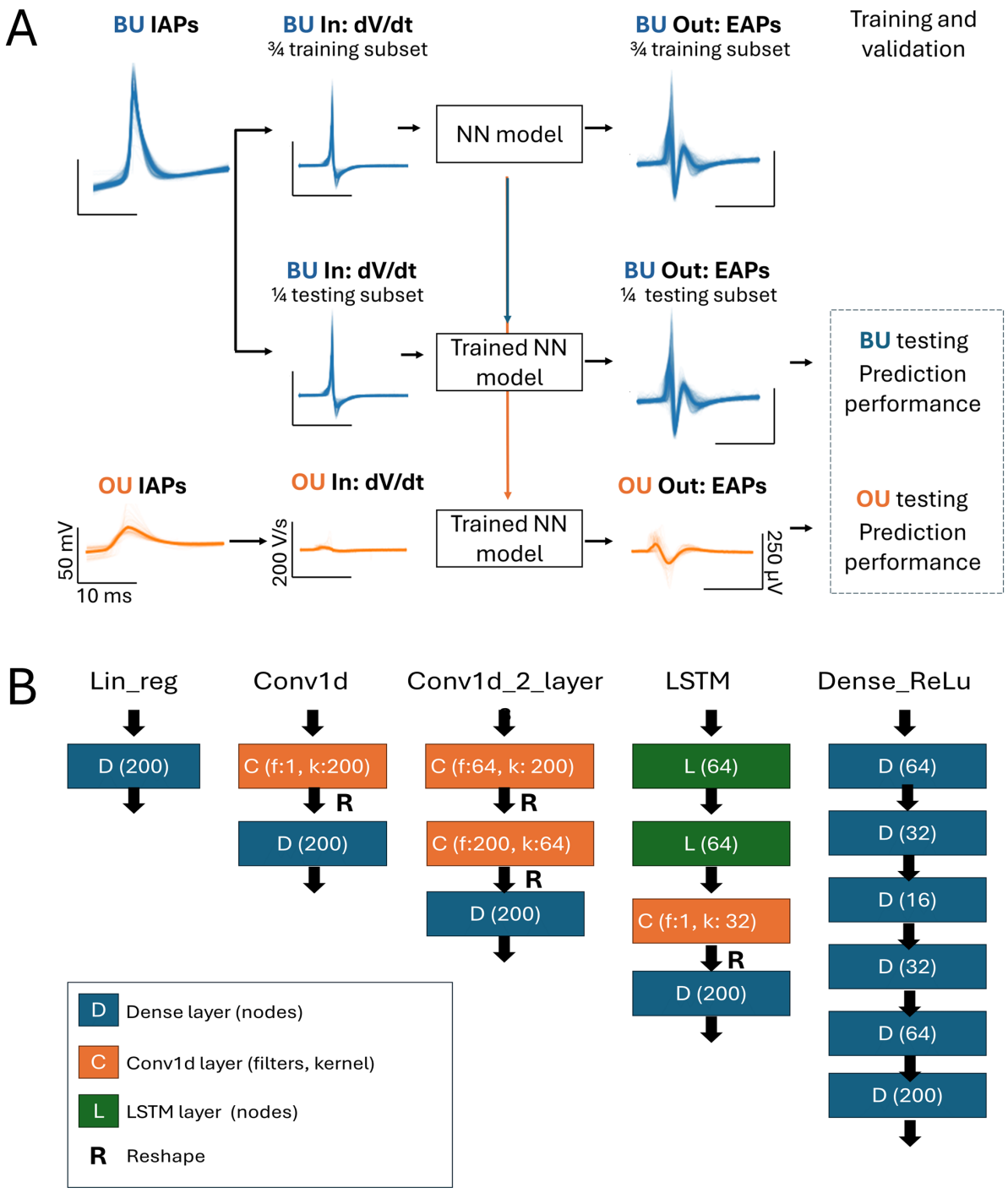


**Figure 4.5.1. Black box approach to investigate the consistency of IAP-EAP relation.** A. Workflow of NN models to predict EAPs from corresponding IAPs. IAP-EAP pairs of the same neuron were first sorted based on EAP WaveClus SPC clustering.[203] For each neuron-electrode pair, training, testing, and validation were on the unit containing most of the IAP-EAP pairs (blue). 1st time IAP derivatives served as a model input, and the output was correlated to corresponding EAPs. Training was done on a pseudorandomly chosen half of IAP-EAP pairs from BU, and validation was on a half of the remaining IAP-EAP subset (in total, ¾ of the BU subset goes into validation and training). The trained NN model was then tested on of the remaining BU subset of IAP-EAP pairs, and all spike pairs corresponding to the OU (orange). Prediction performance for each testing instance was evaluated using MAE

and MSE metrics. B. Different model architectures constructed to predict EAP from the first temporal IAP derivative. Lin_reg: linear regression; Conv1d: 1D convolutional model; LSTM: Long Short-Term Memory; Dense_ReLu: Dense model with ReLU activation. NN models were developed in consultation with Alina Bazarova and Stefan Kesselheim from Helmholtz AI center.

The trained model was again evaluated on the same neuron's spike pairs belonging to other unit, and overall prediction performances were evaluated for BU and OU. The parameters used for comparison of the fit and EAPs were:

1. mean-squared error (MSE), calculated as: $MSE = \frac{1}{n}\sum_{i=1}^{n}\left(Y_i - \hat{Y}_i\right)^2$;
2. mean absolute error (MAE): $MAE = \frac{1}{n}\sum_{i=1}^{n}\left|Y_i - \hat{Y}_i\right|$,

where n corresponds to dimensions of 1D vectors, $Y$ represents detected EAP and $\hat{Y}$ the models' EAP prediction at the i-th frame. Both MSE and MAE were used as quality metrics between the predictions and corresponding EAPs; the former is sensitive to large deviations, while the latter penalizes over- and underestimations equally. As Figure 4.5.2 shows for conv1_d performance on an exemplary recording, the model performs well on the spike unit in the training set (BU) but failed to generalize to another unit of spike pairs from the same neuron.

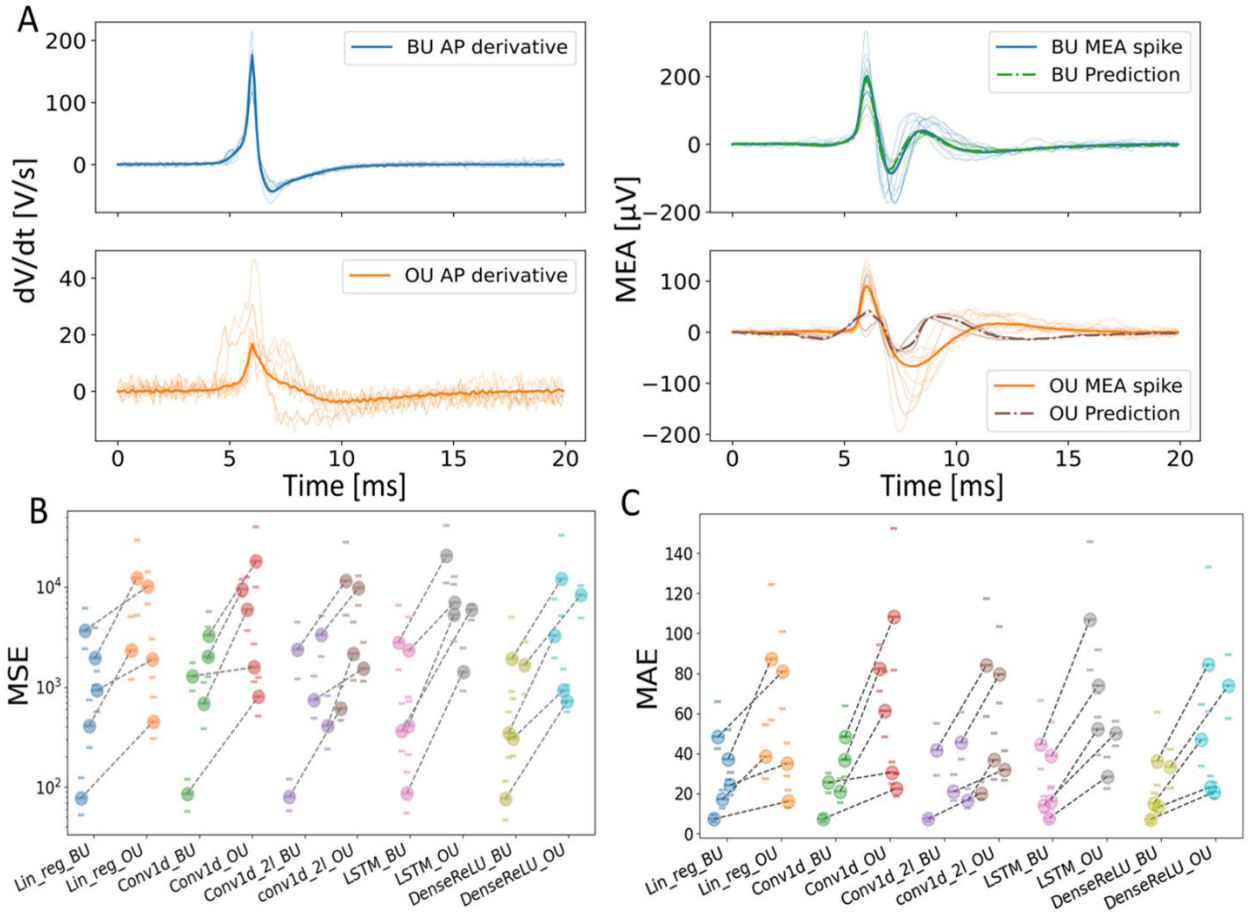


**Figure 4.5.2 NN's prediction performance on different spike-sorter units from the same neuron.** A. Exemplary traces of the first temporal IAP derivatives (left) and corresponding EAPs (right) used for the models' testing on the

BU ($N_{test}$ = 76 spike pairs) and OU ($N_{test}$ = 63 spike pairs). Thick lines correspond to averaged waveforms, while overlaid thin traces correspond to only 10 pseudorandomly chosen waveforms, for clarity. B. Predictive performance for different NN models, estimated by MSE of the fit vs. the corresponding EAP, for BU and OU. Circles depict median, bottom and top lines correspond to the 1st and 3rd quartile, respectively. Dashed lines connect the medians of BU and OU within a given dataset. C. MAE distribution across the different NN models and datasets. Annotation matches that of B. NN models were developed in consultation with Alina Bazarova and Stefan Kesselheim.

The trend persisted for all neuron-electrode pairs, as different NN architectures consistently showed significantly better performance on the BU following the training on its subset (Table 4.5). On average, models trained on BU had a 5x higher MSE and 2.5x higher MAE when predicting OU EAPs (Table C4, Appendix C1). Since the fast phase of the EAPs occupies a part of the window, the observed discrepancy between the MSE and MAE errors indicates fewer points, focused around the EAP peaks (Fig. 4.5.2 A), which suffered worse prediction outcome for OU. Although not a single model emerged as the best performer, dense_ReLU showed more frequently lower prediction errors for BU and slightly better generalization to OU across different datasets (Fig. 4.5.2 B-C). Since ReLU is a non-linear activation, the observed trend may be due to non-linear relations of the IAP and EAP features. As the training was performed separately for every neuron-electrode pair, a consistently higher error in prediction of the EAPs belonging to OU suggests an inconsistent IAP-EAP coupling in each neuron. The same trend persisted following the EAP normalization (Fig. C12, Appendix C1), indicating that the output was robust to the pre-processing steps. A consistently better performance of several investigated models for the EAP spike-sorter unit used for training than for other unit from the same neuron also indicated that inconsistent IAP-EAP coupling may additionally contribute to the EAP variations. However, the distinct features in IAP across the different EAP spike-sorter units (Fig. 4.4.4) challenged to draw such conclusions from this approach alone, as the training exposed the models only to the IAPs from a single unit (BU).

Table 4.5. P-values from MSE and MAE prediction comparisons between BU and OU

| **MSE** | | | | | |
|---|---|---|---|---|---|
| Rec # | Lin_reg | Conv1d | Conv1d_2l | LSTM | Dense_ReLU |
| 0 | 3.38E-08 | 6.90E-03 | 6.24E-08 | 6.98E-21 | 8.88E-09 |
| 1 | 1.22E-39 | 7.77E-55 | 1.15E-37 | 1.19E-53 | 6.05E-51 |
| 2 | 1.46E-38 | 1.40E-53 | 6.10E-36 | 3.54E-48 | 2.58E-34 |
| 3 | 5.20E-09 | 9.92E-14 | 3.66E-10 | 3.88E-08 | 1.26E-13 |
| 4 | 4.83E-22 | 1.30E-25 | 3.77E-25 | 7.69E-26 | 4.74E-25 |
| **MAE** | | | | | |
| Rec # | Lin_reg | Conv1d | Conv1d_2l | LSTM | Dense_ReLU |
| 0 | 1.76E-08 | 2.82E-04 | 2.19E-08 | 1.52E-19 | 1.88E-10 |
| 1 | 3.97E-37 | 3.70E-54 | 6.72E-35 | 4.20E-52 | 5.53E-50 |
| 2 | 4.18E-35 | 5.24E-51 | 3.30E-32 | 5.32E-44 | 5.96E-32 |
| 3 | 1.61E-08 | 1.39E-13 | 2.22E-09 | 8.86E-09 | 8.18E-14 |
| 4 | 1.36E-20 | 1.89E-25 | 6.31E-25 | 8.89E-26 | 1.52E-24 |

*Statistical significance probed with Mann-Whitney for the models' prediction performances across BU and OU, shown in Fig. 3.5.2. B-C. As all the p-values are < 0.05, the noted differences are statistically significant.*

To test the consistency of the coupling regardless of the unit identity, transfer functions ($H(j\omega)$) were explicitly estimated from EAP-IAP relations in Fourier domain (*FFT*), according to the formula: $H(j\omega) = Y(j\omega) / X(j\omega)$, where $Y(j\omega) = FFT\ (EAP)$ and $X(j\omega) = FFT\ (IAP)$. Prior to FFT, patch and MEA traces were two-way filtered via a 3rd order Butterworth bandpass filter (10-4000 Hz). This frequency range reduced the noise bias without affecting the waveforms (Fig. C13, Appendix C1). EAPs had a higher noise component than IAPs (Fig. C14, Appendix C1), resulting in peaks in Fourier spectra at unmatching frequencies. When estimated by the formula above, transfer functions had a higher degree of uncertainty, making it challenging to extract subtle differences between the transfer functions of individual IAP-EAP pairs, despite the pre-processing.

To overcome these limitations, a trainable multiplying NN layer was constructed in `Keras` to find the $H(j\omega)$ from a subset IAP-EAP pairs in Fourier space. The model was constructed by Csaba Forro. Fourier transformed IAP served as an input, and the output was converted into the time domain via inverse Fourier transform ($FFT^{-1}$) for comparison with EAP (Fig. 4.5.3). Because similar-sized IAPs are expected to produce similar-sized EAPs, the fitting was on spike pair subset with IAPs larger than 80% of the maximal IAP amplitude, and a common $H(j\omega)$ was extracted from the weights of the NN layer (Fig. 4.5.3). Choosing a subset over individual IAP-EAP pairs allowed generalization over unique features, while restriction of the size to at maximum 15 pairs was to focus on extracting unique features for similar IAP-EAP relations. The leftover spikes were fitted with the extracted $H(j\omega)$ to account for the spike pairs skipped during the initial fitting but whose coupling was otherwise well captured by the found $H(j\omega)$. Specifically, all spike pairs for which the fit was maximally twice as bad as the best prediction formed a subset. The process re-iterated to find the optimal $H(j\omega)$ on the remaining subset, until the total pool of spikes was exhausted. Finally, every spike pair was fitted by all the found $H(j\omega)$ to evaluate the specificity of the process. In the case of a consistent IAP-EAP transfer function, the model would find a single $H(j\omega)$ in a given neuron-electrode coupling, or multiple similar $H(j\omega)$ that fit all of the IAP-EAP pairs equally well (that is, no specific $H(j\omega)$ spike subsets would be formed). On the contrary, distinct and specific multiple transfer functions for a given neuron-electrode coupling indicates inconsistent IAP-EAP relation. Since the constructed layer acted as an optimizer, the fitting procedure for extracting $H(j\omega)$ occurred during the model training. The model was trained using MSE as loss function with 0.01 learning rate, and stopped if there were no improvements after 50 consecutive epochs. To avoid artificially small penalties for small EAPs, both EAPs and predictions were normalized by the mean and variance of the EAPs, according to the Equation (4.1):

$$Y' = \frac{Y - \bar{Y}_{EAP}}{\sigma_{EAP}} \tag{4.1}$$

In expression above, $Y'$ denotes normalized vector $Y$ (either EAP or fit), while $\bar{Y}_{EAP}$ and $\sigma_{EAP}$ denote the EAP mean and variance, respectively. Normalizing the model's predictions also to the EAPs' mean and variance forced the model's convergence to match both the magnitude and the shape of the EAPs. In contrast, normalizing predictions by the own's mean and variance would have forced predictions matching the shape, but not necessarily the magnitude of EAPs. The fit error was evaluated by the maximum root square error according to Equation 4.2:

$$E = \sqrt{\max\left(Y'_i - \widehat{Y'_i}\right)^2}, \tag{4.2}$$

where $Y'_i$ and $\widehat{Y'_i}$ denote the i-th frame of normalized EAP and fit, respectively.

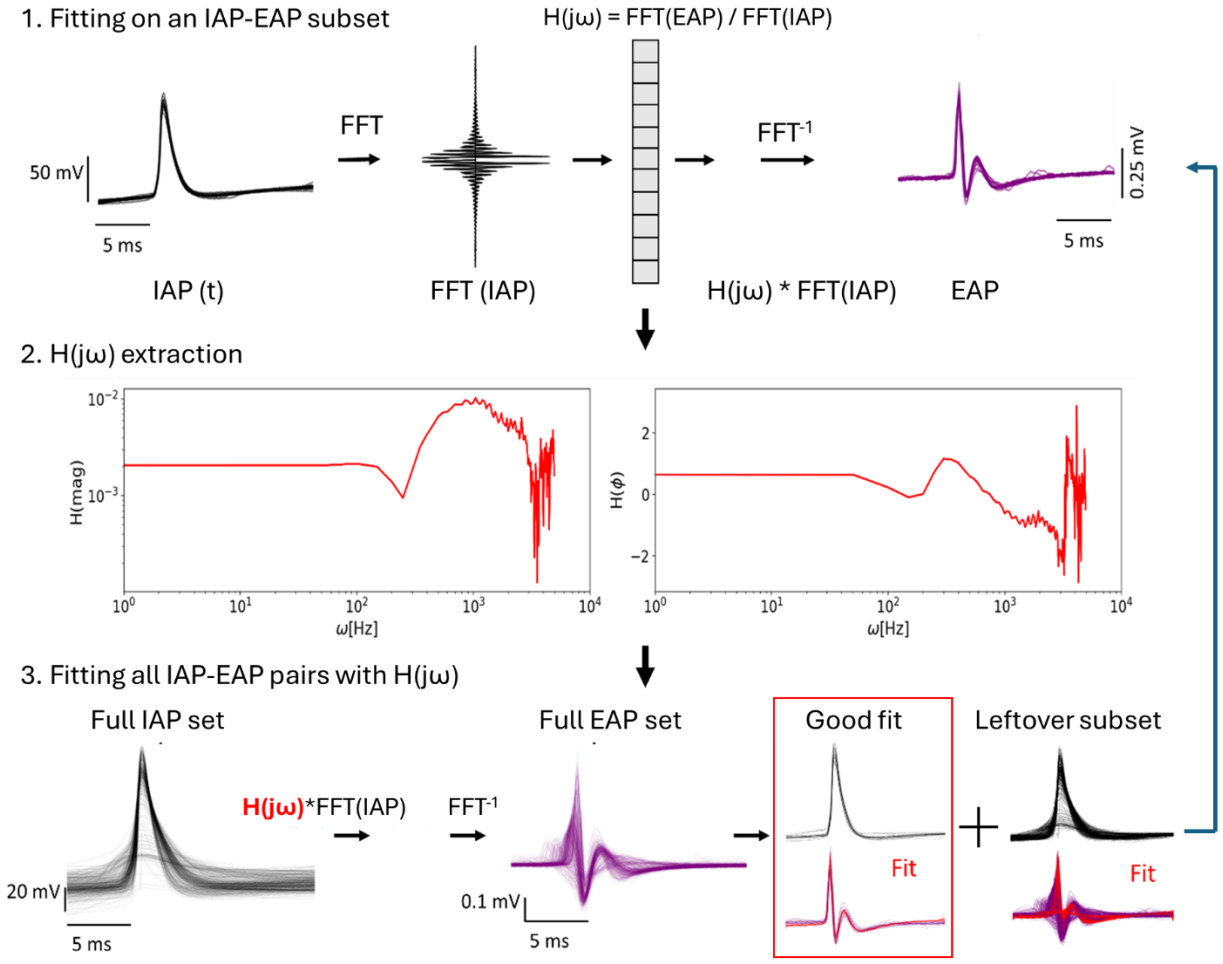


**Figure 4.5.3. The workflow of explicit transfer function estimates using NN layer.** Multiplicative NN layer with trainable weights was constructed to predict FFT of EAPs from FFT of IAPs. As an input, a subset of maximum 15 spike pairs containing highest IAPs was used (1). The transfer function was extracted from the NN layer's weights (2). All present spike pairs were probed with extracted H(jω) to account for missed spike pairs that are well captured by the found H(jω), but are skipped during the fitting (3, red rectangle). The process re-iterates for the leftover subset of spike pairs. The pipeline was developed by Csaba Forro.

As with the previous approach, the consistency of *H(jω)* was estimated on long-term spontaneous activity traces, where the electrode detected exclusively from the target, to disregard apparent transfer function inconsistencies from collisions of multiple sources' EAPs (Section 4.2). The analyzed subset comprised of mainly high amplitude, predominantly positive EAPs that arose either from neurite-electrode (#1, #2) or soma-electrode coupling (#3, #4), and one (#5) soma-electrode coupling with strongly triphasic EAPs (Table 4.5.2). The two cases with neurites coupled to the electrode showed ecPSPs along with positive monophasic EAPs. It is therefore safe to assume the electrode coupled to the dendrites (see also Section 4.3). In putative dendrite-electrode couplings, IAPs were recorded from large somas with thick processes oriented towards the electrode (for instance, see the bright micrograph in Fig. 4.2.2. A). The soma-electrode distance < 65 µm favors the coupling with proximal dendritic branches. Since proximal primary dendrites have lower axial resistance (10-15 MΩ)[284], a similar IAP waveform could be assumed between the patch- and MEA electrode-detection sites.

Multiple IAP-EAP transfer functions were found for a given neuron-electrode coupling (Fig. 4.5.4. B-C), suggesting an inconsistent IAP-EAP relation. IN-CELL configurations with positive monophasic EAPs (Section 4.2) had Bode plots akin to those of a high-pass filter in IAP-associated frequency ranges (1 Hz - 1 kHz)[25] (Fig. 4.5.4 B); high-pass transformation of IAPs was also previously reported for planar electrode-cell interfaces.[185] The coupling with strong triphasic EAPs as well showed stronger attenuations at lower frequencies, but the magnitude had sharp dips at 150, 200, or 250 Hz (Fig. 4.5.4 C), which likely resulted from interactions between the membrane and the flat components of the electrode, the cavity, and straws.[285]

The frequency shifts of magnitude dips associated with triphasic EAPs suggest that the qualitative changes of triphasic EAPs result from the physical coupling inconsistencies. Specifically, apparent transfer function changes from inconsistent IAP detection with patch would manifest as uniform magnitude scaling of the transfer function, since technical setbacks are attributable to the Ohmic changes in detected IAPs. For instance, increased series resistance in whole-cell configuration promote the gradual amplitude drop of patch-detected IAPs. Likewise, the apparent transfer function changes due to signal transfer at the neurites and IAP detection at the soma would cause a magnitude scaling transformation due to the IAP amplitude drop at the axial resistor.[286] However, the transfer function frequency shifts for the triphasic EAPs and the proximity of the detection site to soma (Table 4.5.2) suggest the transfer function inconsistencies were not apparent.

In contrast, IN-CELL-like EAPs emerged from somatic (n=2) and dendritic (n=2) neuron-electrode coupling, and their transfer function changes were not associated with drastic magnitude shifts at specific frequencies. In these cases, the same-neuron EAPs showed quantitative waveform differences but preserved the positive monophasic shape. A slight change in magnitude slope at 150 Hz suggests that even IN-CELL coupling variations are not purely Ohmic (Fig. 4.5.4 C). This conclusion was further supported by an incomplete overlap of

different transfer functions' magnitude profiles following the magnitude re-scaling (Fig. C14, Appendix C1).

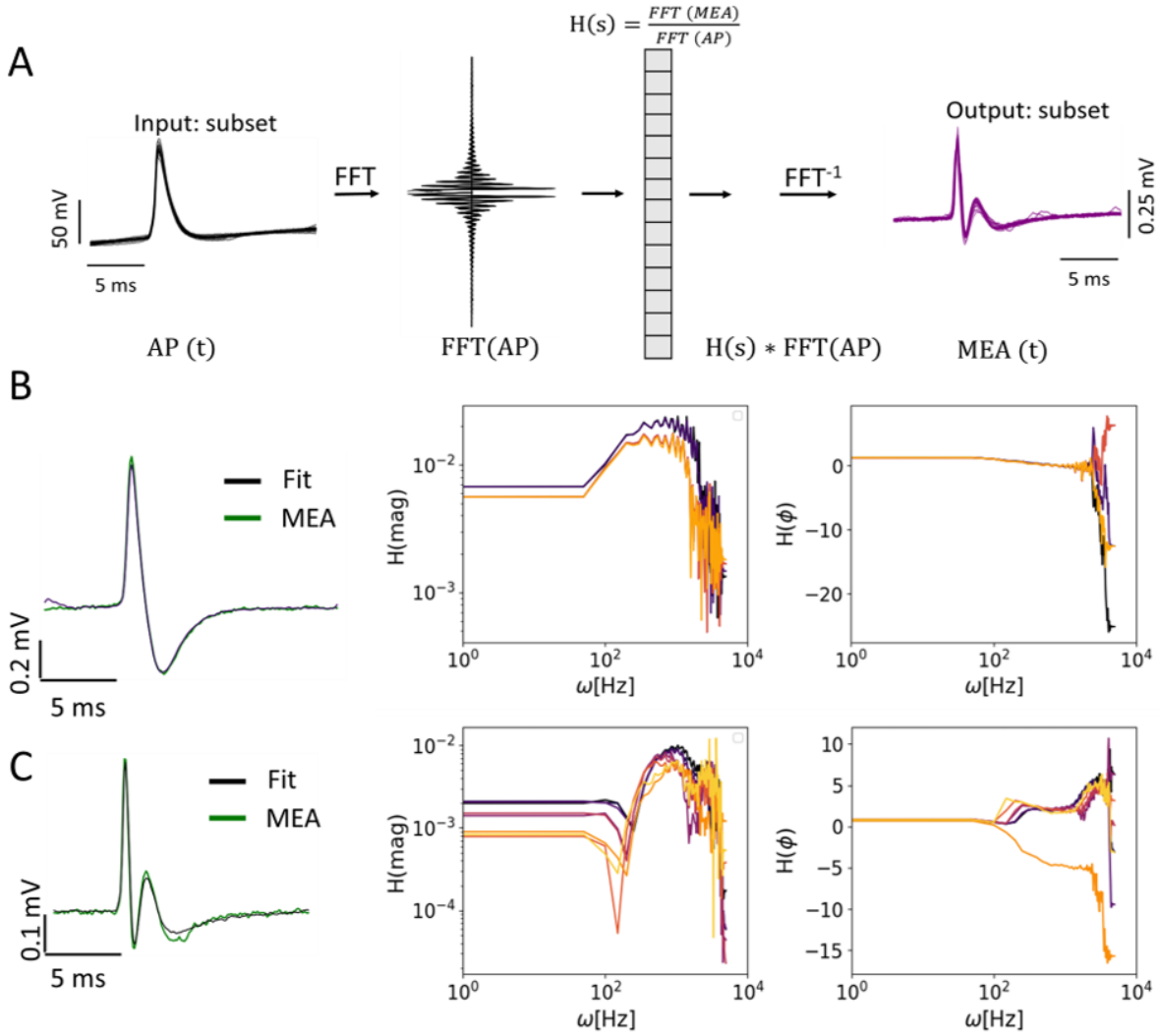


**Figure 4.5.4. Experimental IAP-EAP transfer functions.** A. Schematic overview of a multiplicative NN layer used for transfer function fitting. All same-neuron IAP-EAP pairs were probed with H(jω) to find spike pairs missed during the H extraction. Fitting quality criterium was a threshold of 2*MSE (best fit). The process re-iterates for the leftover subset of spike pairs. B. Exemplary magnitude (left) and phase (right) Bode plots of all transfer functions found for IN-CELL coupling with positive monophasic EAPs. C. Bode plots for all transfer functions describing the neuron-electrode coupling with strong triphasic EAPs.

Table 4.5.2. Coupling properties for high SNR measurements of single-neuron signals

| Recording | Soma-electrode distance [µm] | SNRmax | Soma CC area [µm$^2$] | Waveform |
|---|---|---|---|---|
| 1 | 65 | 86 | 203 | PM |
| 2 | 39 | 73 | 363 | PM |
| 3 | 5 | 120 | 155 | PM |
| 4 | 12 | 77 | 229 | PM |
| 5 | 11 | 96 | 396 | TF |

*Soma-electrode distance: Eucledian distance between the centers of soma and recording electrode. CC area- somal cross-section area, SNRmax – maximum SNR, PM- positive monophasic, TF - triphasic*

While the above *H(jω)* estimates pointed to inconsistent IAP-EAP coupling, the Bode plots still showed a degree of uncertainty due to a considerable number (200) of fitting parameters. An NN layer was constructed to fit the IAP-EAP coupling with only six parameters to extract clearer estimates of the transfer functions. Assuming the coupling is represented via few resistors and, at maximum, two capacitors (representing the junctional membrane and double layer capacitance; see Section 2.2.2), the transfer function is approximated to the second order complex polynomial and adopts the form (4.3):

$$H(s) = \frac{k + l * s + m * s^2}{u + v * s + w * s^2} \tag{4.3}$$

where $s = j\omega$. As the capacitor's impedance scales to $1/ s*C$, parameters $k$ and $u$ denote purely Ohmic components of the coupling (resistors), $m$ and $w$ correspond to the combination of the two capacitors, while $l$ and $v$ represent a combination of one capacitor and at least one resistor. This approach allowed a general assessment of the eventual changes in the coupling without constraints of the specific point-contact model. The expression for the transfer function could be further reduced to 5 unique parameters (Eq. 4.4):

$$H(s) = a\frac{1 + b * s + c * s^2}{1 + d * s + e * s^2} \tag{4.4}$$

where $a = k / u$, $b = l / k$, $c = m / k$, $d = v / u$, $e = w / u$. Using the same pipeline as in Figure 4.5.3, the reduced NN layer finds the optimal transfer functions for IAP-EAP subsets. EAPs were aligned to the maximum inflection point of the soma-detected IAP to account for inconsistent IAP-EAP delays (Section 4.2). Although the delays may have introduced only phase shifts, the temporal alignment facilitated the reduced model's convergence towards a local optimum. Parameters were restricted to positive values by raising them to the power of 10, and initial weights were set to prevent convergence to suboptimal local minima.

As shown in Figure 4.5.5., the output of the reduced model are transfer functions with similar Bode profiles as obtained with 200 parameters NN model, however, with fewer uncertainties and cleaner profiles (Fig. 4.5.5. A-B). One striking difference is less signal attenuation at > 1 kHz for the reduced *H(jω)* expression. In either *H(jω)* estimate, > 1 kHz frequencies are predominated by a high-frequency noise, which persists despite the hardware low-pass filter. As a result, *H(jω)* estimations are biased at > 1 kHz, even more so when extracted from the 200-node NN model, whose weights were initialized with ones. That > 1 kHz frequencies are predominated with noise and are less relevant for EAP prediction, is supported by exact matching of predictions when *H(jω)* was *post-hoc* modified to have steady or rising magnitude at these frequencies (Fig. C16, Appendix C1).

As with the previous model, the output was at least two distinct transfer functions for a given neuron-electrode pair containing EAP misclassifications. Couplings with positive monophasic EAPs had the highest variations of parameters related to the capacitive components (Fig. 4.5.5.

Aii), while those with triphasic EAPs had variations of both capacitive and purely Ohmic parameters (Fig. 4.5.5. Bii). Pooled together across different datasets, the variations of transfer functions describing individual neuron-electrode pairs peaked for parameters *b* and *c* (Fig. 4.5.5. C), suggesting the main factors contributing to the coupling inconsistency related to capacitance changes.

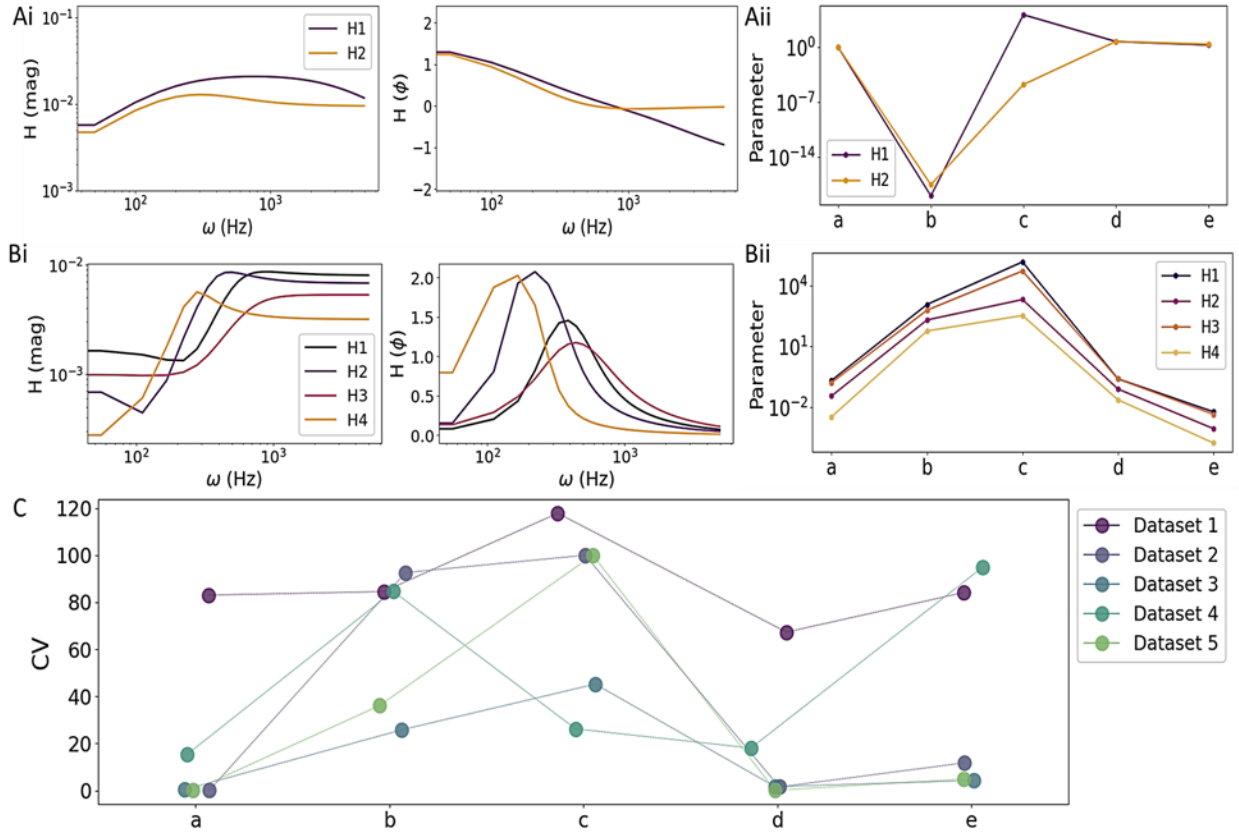


**Figure 4.5.5. Expressing IAP-EAP transfer function as a second-order polynomial.** A. Transfer functions extracted for a single neuron-electrode coupling with positive monophasic EAPs. Ai. Bode magnitude (left) and phase plots (right) of the two transfer functions. Aii. Distribution of second-order polynomial coefficients. B. Transfer functions extracted from the coupling triphasic EAPs. Bi. Bode magnitude (left) and phase (right) diagrams. Bii. Distribution of parameters describing the found transfer functions. C. Coefficient of variation (CV) of parameters describing different transfer functions found for a single electrode-neuron coupling, across five neuron-electrode couplings. Dataset 1 denotes the coupling with triphasic EAPs. Model approximating IAP-EAP transfer function by the second order complex polynomial was constructed by Csaba Forro.

Importantly, subsets of spike pairs for a given H showed larger and significant errors when predicted by other found Hs, confirming that the found transfer functions were specific (Fig. 4.5.6.A for positive monophasic, and Fig. C17, Appendix C1 for triphasic EAPs). Coupling transitions occurred for seconds at a time (median transfer function retention time: 0.967 s, IQR: 4.35 s) in the recording and were reversible (Fig. 4.5.6. B). These suggested that native changes of the coupling were not due to the experimental artefacts, such as mechanical drifts or series resistance increases, as otherwise they would manifest as irreversible, switch-like perturbances (see also Section 4.4. and Fig. C6, Appendix C1) or slower directed gradients, respectively.

Coupling changes were seemingly focused around the bursts, as all of the spike pairs could be explained by a single transfer function in neurons that fired sparsely and had no misclassified EAPs (Fig. C17, Appendix C1). In addition, transfer function spike subsets had distinct and significantly different ISI distribution (Fig. C18, Appendix C1), suggesting that transfer function transition probability relies on the firing dynamics.

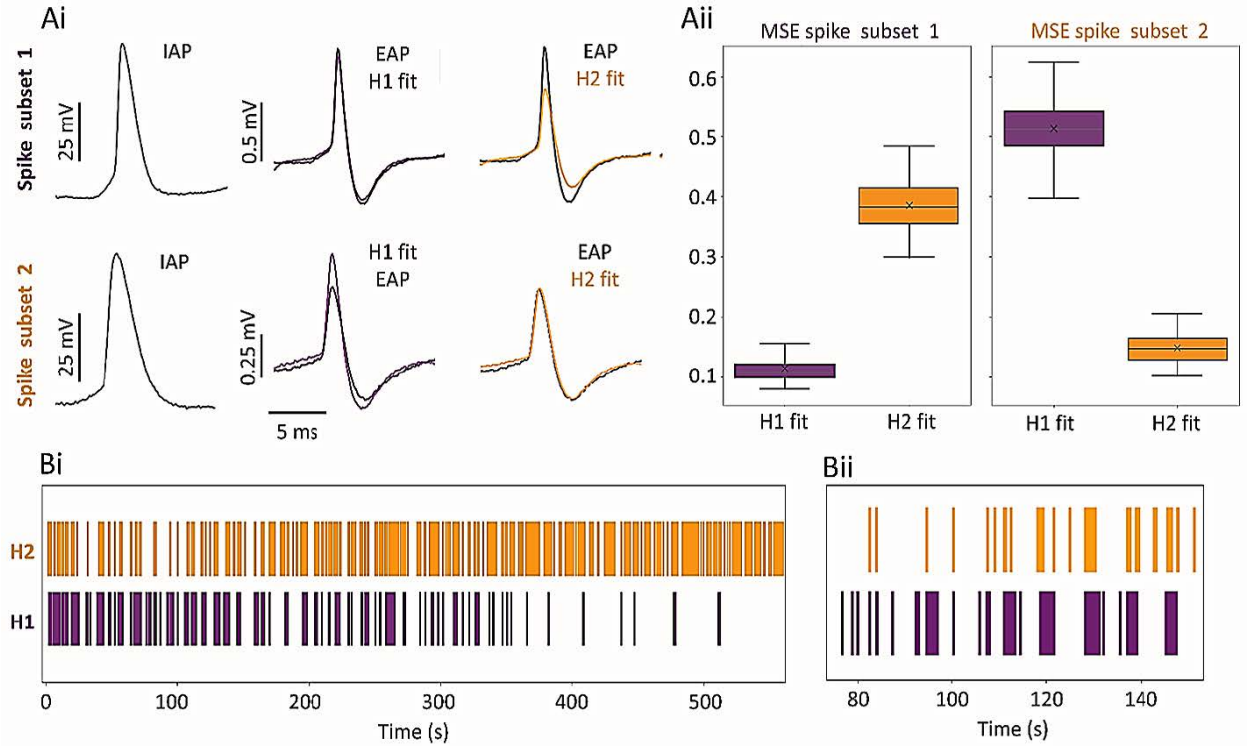


**Figure 4.5.6. Specificity and reversible transitions of IAP-EAP transfer functions.** A. Extracted transfer functions fit well a specific subset of IAP-EAP pairs. Ai. Representative IAPs, EAPs, and fits by found Hs presented in Fig. 4.5.5. A., for each H-spike subset. Aii. MSE distribution for all found H fits across different subsets of spikes. B. Coupling changes are reversible and occur at s time scale. Bi. Raster plots of EAPs belonging to H1 (purple) or H2 subset (orange). Bii. Focus on ca. 1 min trace shows reversible and s-order changes of the IAP-EAP coupling.

In summary, both the 'black box' approaches and explicit transfer function estimates indicated that not all the spike pairs from a given neuron have the same coupling. In the former, several black boxes of different complexities were trained to recognize EAPs from IAPs. These showed that, when trained on the spike pairs in one EAP spike-sorter unit, the models perform consistently worse on the spike pairs from the same neuron, but of another EAP spike-sorter unit. Experimentally estimated IAP-EAP transfer functions show inconsistent coupling in bursting neurons, as different transfer functions explain different subsets of spike pairs from the same neuron. Transfer function changes were reversible, and occurred in a matter of seconds, suggesting the inconsistencies were not due to mechanical drifts or series resistance increases, which would manifest as a switch-like behavior or gradual IAP decay, respectively. Approximations of the IAP-EAP signal transfer to the second-order polynomial revealed that the

main inconsistencies were in the capacitive component of the coupling. The inconsistencies found support additional EAP variations in high SNR measurements.

## 4.6. Network metrics accuracy post spike sorting

Previous studies on spike sorting errors have focused on false negatives that result from missed EAPs.[265] However, with improved SNRs, burst-associated EAP waveform changes and resulting misclassifications were the main source of sorting errors (Section 4.4). These misclassifications primarily result from over-splitting, where a single neuron's spikes are assigned to more than one unit. Contrary to spike omission, which only reduces the number of spikes found per unit, misclassified units are more challenging to identify and may lead to different and often subjective source designation. The main reason for the subjectivity is uncertain number of neurons contributing to each electrode's signal and limited ability of present unit quality criteria to differentiate between the spike units that are wrongfully disjointed and those representing rarely-firing neurons. Accordingly, following the spike sorting on recordings lacking the ground truth, the investigator makes the following decisions when the found units fail to meet presence ratio criteria.

1. *Merge* the smaller unit into a larger unit of spikes; if the smaller unit contains misclassified signals, this scenario corresponds to the ground truth, as initially separated units are merged back together.

2. *Discard* smaller units that do not fulfill presence ratio criteria; discarding misclassified spikes has the same outcome as false negatives from spike omission since it preserves the number of actual units and effectively reduces the number of spikes.

3. *Keep* the unit with misclassified spikes. This outcome increases the number of perceived neurons while redistributing the existing spikes among them.

The effect of misclassification and curation on network activity and connectivity metrics has not been previously investigated. Here, I investigated how these outcomes affect activity estimates in *in vitro* networks, with bursts as a primary mode of activity (Section 4.1). Since my paired dataset focused on a single neuron at a time, network-level ground truth was obtained from a simulated dataset. An Izhikevich spiking network[287] of 100 randomly connected neurons, 80% of which were excitatory, was simulated in `Brian2`[288] to match the bursting regime observed *in vitro* (Section 3.1). Simulated FNs probability was adjusted to the misclassifications distribution of burst and non-burst spikes *in vitro* (Section 4.4 and Section 3.6.7). From the generated sequence, misclassified spikes were assigned via a probabilistic filter, scaled by a randomly chosen parameter [0,1]. Note that estimated this way, misclassifications were considered as independent events (details in Section 3.6.7). With identical distributions of misclassification errors, I simulated three abovementioned scenarios that depended on curation (Fig. 4.6.1. A).

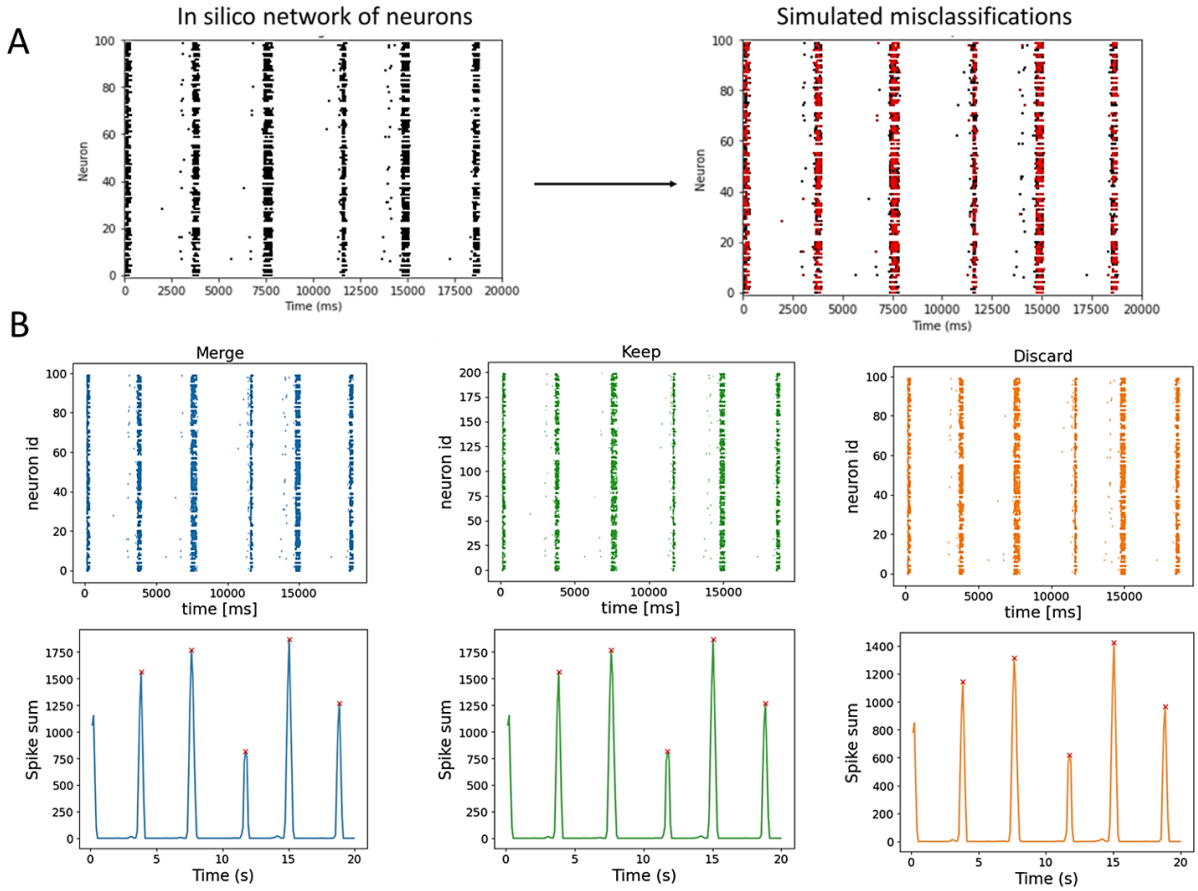


**Figure 4.6.1. The accuracy of network population metrics for different unit curation outcomes.** A. Simulation of the bursting network and burst-related misclassification errors resulting from the MEA spike variations (red). B. Raster plots of the same network following different curation scenarios: merge, keep, and discard. The bottom is cumulative spike counts to capture network bursting events (red x).

Network synchrony and functional architecture were then evaluated for every scenario. The former focused on population firing metrics a network burst time scale, and the latter on the connectivity estimates from pairwise correlations of firing sequences. SNE detection was robust to the misclassification errors, regardless of the outcomes (Fig. 4.6.1. B). As expected, the number of spikes per SNE decreased in the Discard. However, the high network synchrony suffices to detect SNE peaks at a high accuracy, despite the missing spikes. Keep and Merge yielded the same numbers of spikes per SNE since both outcomes preserve the network-level spiking sequence and differ only in distribution of the signals across the putative neurons. The findings suggest that the least relevant attribute in population firing metrics is the signal source designation, as long as the signals are correctly found.

Network connectivity estimates were susceptible to misclassification. Patches of highly synchronous modules were preserved in cross-correlograms across different scenarios (Fig. 4.6.2), suggesting that the network synchrony is detected even at 3 ms resolution. In addition, retaining the misclassified units disrupted highly correlated clusters of neurons. The overall cross-correlation coefficient (CC) significantly reduced from 0.27 to 0.21 and 0.15 ($p < 10^{-4}$, t-test)

for Discard and Keep outcomes, respectively. These also suggested introducing the new units impacted the correlative estimates more than spike exclusion. As normalized and thresholded CCs are standardly used in estimates of functional connections, I also evaluated if CCs uniformly declined. As shown in Fig. 4.6.2 C, discarding the misclassified spikes and, more prominently, retention of misclassified units reduced the normalized weights as well. Since normalized weights are used to define a putative connection as statistically significant and a proxy of functional connection strength, the findings indicate fewer connections for the same network, particularly when the misclassified spikes are regarded as individual units.

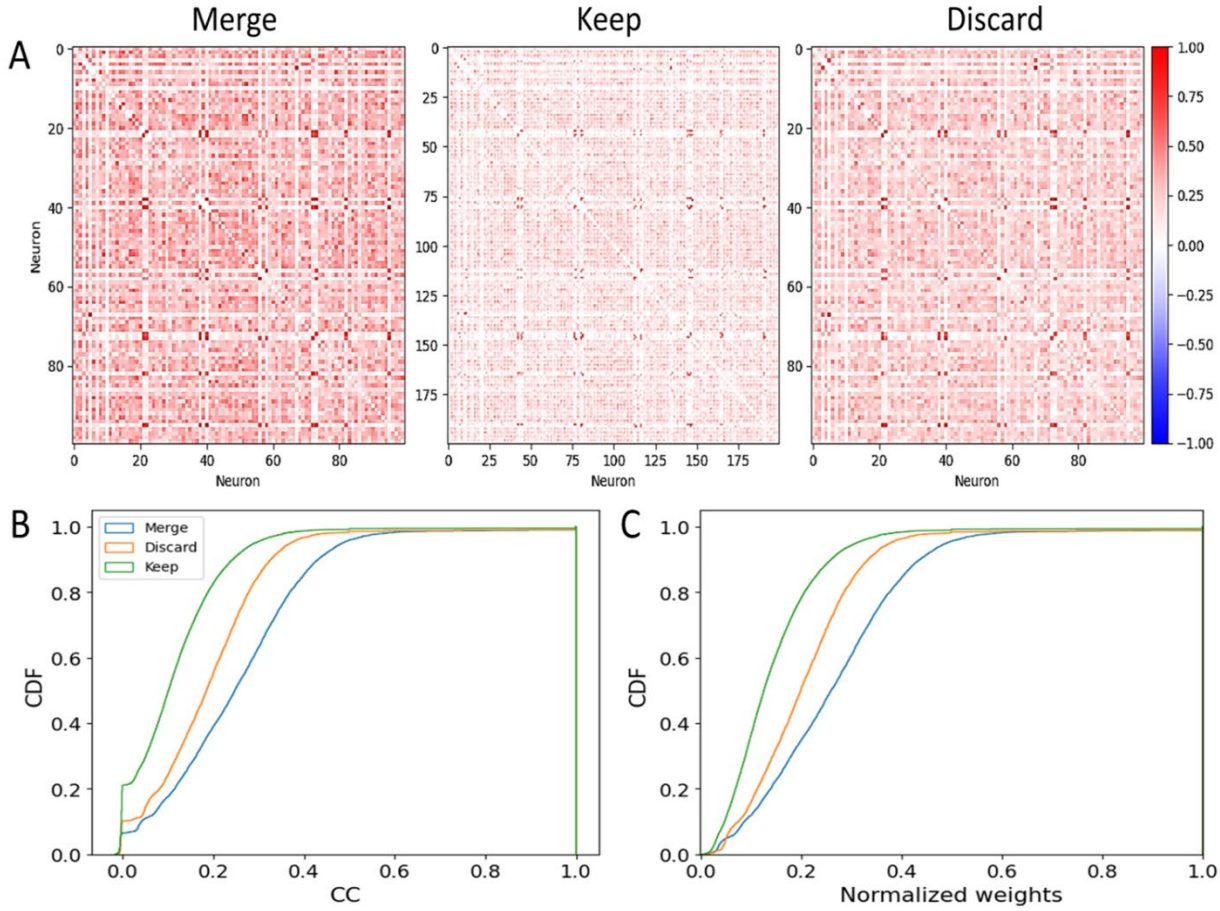


**Figure 4.6.2. The effects of misclassification errors on functional connection estimates.** A. Cross-correlation matrices obtained from spike trains of the same network in Figure 4.6.1, for misclassifications that were re-included into the main neuron unit (Merge), kept separately as different neurons (Keep), or discarded from the estimates (Discard). Colormap depicts normalized CCmax. [289] B. Cumulative density function of the CC. C. Cumulative density function of CC following normalization and cutoff.

To fully examine the effect of misclassification handling, functional network topology was estimated from unidirected network graphs (Fig. 4.6.3, details in Section 3.6.5.2). Maximal cross-correlation coefficients (CC) for a given neuron pair were extracted from 3-ms binned binary spike trains[289] in `Elephant`.[290] Two neurons were considered to be functionally connected if weights normalized by the maximum CC for a given network were above the 90$^{th}$

percentile. For orientation purposes, the *in silico* network was distributed across a 10x10 grid, resembling the configuration of the network on a chip. The overall network architecture was described by the concepts of graph theory. Omission of spikes reduced the global efficiency by 20%, due to exclusion of a number of direct connections. Inversely, introduction of nodes containing misclassified spikes along each electrode slightly increased the number of direct connections (Table 4.6) and global efficiency by 4%. The number of connections per node decreased slightly in Discard, and significantly in Keep. Although the overall number of links increased, these also included spurious correlations that were filtered by thresholding, due to significant reduction in the normalized weights. In turn, the existing connections re-distributed across newly created nodes.

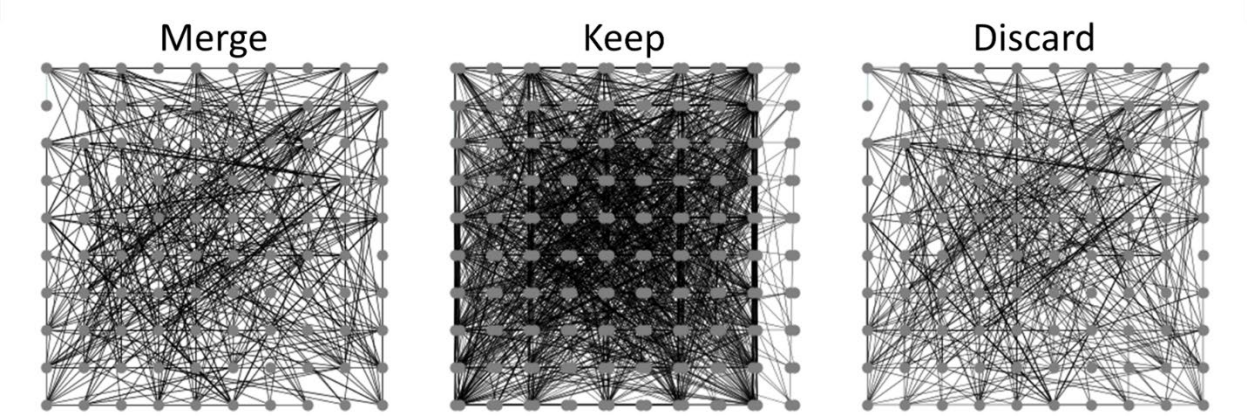


**Figure 4.6.3. Functional topology is shaped by curation decisions following spike sorting.** Network graphs generated from the simulated network and misclassification outcomes. Weight of links scales with the normalized weight between a given neuron pair. Note duplicated nodes in Keep configurations; these represent units with the highest number of spikes, along with the misclassified unit accounted as different neurons.

Table 4.6. Neuron network properties for different misclassification outcomes

| Network parameter | **Merge** | **Keep** | **Discard** |
|---|---|---|---|
| Avg norm weight | 0.49± 0.09 | 0.31± 0.08 | 0.38± 0.08 |
| Global efficiency | 0.64 | 0.67 | 0.51 |
| Density | 0.08 | 0.07 | 0.08 |

Overall, misclassification errors and curation decisions did not influence the network-wide synchronicity measures. At a single AP resolution, bursting activity is preserved in cross-correlograms irrespective of misclassification outcomes. Estimates of functional connections, however, were susceptible to the curation of the misclassified units. Both the CC and normalized connection weights were reduced, mainly when the decision was to keep the misclassified unit. Spurious correlations significantly reduced the network's density due to the increased number of nodes while concurrently elevating the global efficiency due to artificial increases of direct links. These suggested that omitting the units that dissatisfy the standard quality metrics provides more accurate estimates of the network activity than unit retention, following spike sorting in bursting networks.

# 4.7. Discussion and conclusions

Accurate mapping of causal neuronal connections requires signal detection at a PSP resolution, which has so far been achieved reliably by intracellular electrophysiology. Conventional MEAs used for long-term and non-invasive screening of neuronal network activity, however, suffer from reduced SNR and omission of not only PSPs but also APs. The 2D+ electrodes, such as NS-NC MEAs, surmount the challenges of low SNR in planar MEAs, allowing reliable AP detection and showing promise in direct connectivity estimates. This chapter aimed to evaluate the applicability of NS-NC MEAs in native connectivity estimates, both from aspects of invasiveness and the reliability with which they inform the activity of coupled neurons.

## Networks on 2D+ MEAs maintain native progression toward bursting regime

Networks grown on structured electrodes showed signs of activity maturation similar to those grown on planar MEAs (Section 4.1),[1, 3] suggesting that neurons with very localized and sparse chronic membrane curvature converge to a similar activity regime as those grown on flat. The bursting activity of mature networks comprised oscillations below 1 Hz, which current network models explain through modular connectivity of neurons and maturation of NMDAR-mediated signaling (Section 2.1.6). A lower yield of active channels than by chance was partially due to electrodes sensing from neurons not engaged in synchronous activity, which simple pharmacological interventions with caffeine could improve. These findings confirm the undersampling of sparsely firing neurons in short-term recording sessions as a setback of electrophysiological measurements in network activity and connectivity estimates.[10]

## NS-NC MEAs detect by signal transfer at the cell-electrode interface

On-chip patch-clamp measurements demonstrated that NS-NC MEAs detect from the soma and proximal neurites (Section 4.2). NS-NC EAPs did not attenuate with increased distance, while some of the largest spikes were detected tens of microns away (Fig. 4.2.2). Since typical juxtacellular signals sharply attenuate from IAP origin site and are hardly measured > 30 µm from the soma,[271] NS-NC electrodes detected via the signal transfer at the coupled compartment, rather than local electrical fields arising near the IAP generation sites. To that end, NS-NC detection shows the highest similarity with the loose-patch extracellular records, which successfully report spikes from any neuronal compartment as long as the electrode interfaces with the membrane tightly.[270-272]

Though direct signal transfer suggests that NS-NC electrodes could measure from coupled neurites at any distance from the soma, the benchmarked neurons had their somas in < 70 µm radius around the electrode. The proximity requirement is likely due to a reduced probability of neurites establishing effective coupling with electrodes at higher distances, given a higher passivation/sensing ratio at larger radii and random neuritic growth on mainly flat substrates.[123, 124] Thus, although 2D+ electrodes can measure from neurites, the high electrode pitch limits

detection to proximal ones. Accordingly, the full electrode ability for sensing neuritic signals should be explored in the context of topological neuritic guidance[124] or high-density 2D+ MEAs.

However, the finding that relatively thin neurites produce millivolt signals holds relevance for modeling the cell-electrode interface, which often assumes attenuated signals for partial electrode coverages. In particular, the equivalent circuit models predict the optimal signal acquisition when the electrode is fully covered, as otherwise, a portion of the signal is leaked to the bath.[183, 187, 291] Assuming the maximal primary neurite diameter (3 µm)[286, 292] and neurite spanning across the whole electrode diameter, the neuritic membrane covers half of the electrode opening at maximum.[9] Hence, improvements in other coupling parameters, such as increased sealing, could compensate the signal loss across the uncovered electrode. Future cell-electrode models should thus account for the interplay between gap size and electrode coverage when estimating neuron-2D+ electrode interfaces.

The SNR correlated with the size of the neurons, akin to previous findings in high-density silicon probes[64] and juxtacellular pipettes.[293] Since larger neurons have a higher membrane area, the coupled area and electrode coverage are expected to increase, thus promoting sealing and capacitive transfer. These matter for two reasons. Firstly, they emphasize the undersampling of EAPs from smaller neurons, particularly in low SNR measurements. Secondly, the correlation of the neuronal size to the SNR introduces a confounding variable when reporting and calibrating the amplitude sensitivity of the recording devices. Interestingly, one of the pioneering works on 2D+ electrodes, golden nano mushrooms from Spira's group, reported IN-CELL configurations most frequently from *Aplysia* neurons, about 10x larger than mammalian.[191] These emphasize the necessity of supplementing the electrophysiological findings with the soma size of neurons within the maximum detection radius (Section 4.2) for transparent and consistent reports of the device's performance.

## 2D+ electrode – neuron coupling detects the signals at a subthreshold resolution

NS-NC MEAs are capable of detecting subthreshold events, paving the way toward direct connectivity mapping from spontaneous detected activity. Although previous pharmacological interventions and spike shape analyses on 2D+ MEAs indicated PSP detection,[186, 274] the on-chip patch-clamp allowed a direct correlation of intracellularly detected PSPs with corresponding NS-NC MEA signals. In particular, the direct benchmarking revealed that high SNR (> 30) traces most often had positive monophasic signals and showed sensitivity to subthreshold changes, such as pre-depolarizations, hyperpolarizing phases of an IAP (Section 3.2), and PSPs (Section 4.3).

[9] Assuming that a cylinder of a maximal primary dendrite radius spans the whole electrode diameter and interfaces the electrode with a half of its total area.

The subthreshold resolution and prevalent positive monophasic signals may suggest that vertical nanostraws porate the membrane. Since the previous electron microscopy investigations did not confirm the membrane poration,[26] the ground truth of NS-NC signals served to verify whether the IN-CELL records originated from intracellular access or a tight engulfment. Based on previous signal validation on active porating constructs, intracellular access is expected to produce attenuated versions of IAPs.[294] In contrast, IN-CELL couplings produced spikes about 2x faster than IAPs despite the improved sensitivity for the slower IAP components and subthreshold events (Section 4.2). This indicates capacitive signal transfer at a tightly coupled, intact membrane, rather than membrane penetration – similar to loose-patch detection.[270-272]

Transfer function estimates showed that the coupling sets a high-pass filter at IAP-related frequencies (1-1000 Hz),[25] similar to previous models of planar electrode-cell interfaces.[185] Unlike the planar electrode interface models, experimental transfer functions show magnitude attenuation above 1 kHz, giving the impression of a band-pass filter (Fig. 4.2.3). However, > 1 kHz ranges are predominated by a high-frequency noise, which persists despite the hardware filtering. Thus, these frequency ranges are less relevant for the EAP-from-IAP predictions, introducing bias in transfer function estimates above 1 kHz. The latter is evidenced by similar EAP predictions when transfer functions were modified to be consistent or rising above 1 kHz. High-pass transfer function profiles further support that IN CELL records are established by a tight engulfment instead of poration; otherwise, intracellular access would manifest as linear magnitude plots that are consistent across all frequencies.

The magnitude of the transfer function was less attenuated at lower frequency ranges for higher SNR couplings. The increased sensitivity towards slower components of an IAP allows more accurate inferences of another important property, the IAP shape, opening parallel estimates of analog signal information[66, 67, 282] to fundamental cellular neuroscience and targeted drug design. At the network level, the subthreshold sensitivity allows direct inferences of connections, shifting the observational network analysis from correlative to causal.[295] Subthreshold events detected with NS-NC MEAs also showed a good match with the 1$^{st}$ intracellular time derivative, although they had a higher attenuation. Given a higher content of slower frequencies in subthreshold events and a predominant high-pass property of the coupling, a reduced coupling coefficient for PSPs is unsurprising. The future electrode design advances should thus focus on improving spontaneous engulfment to increase the yield of PSP detection for parallel, long-term, and non-invasive direct connectivity inferences.

## High SNR comes at a price of pronounced single-neuron EAP variability

Despite these advances, MEA electrodes detect non-targeted, and the information on how many neurons are coupled to the electrode and which neuron fired when is not directly provided. As a result, spike sorting algorithms are required to assign detected EAPs to appropriate signal sources. While the enhanced amplitude sensitivity of NS-NC MEAs overcomes spike sorting challenges associated with EAP detection, high magnitude EAPs of the same neuron showed an

exceptionally high variability. These variations reduced the accuracy of spike-sorters optimized for the low SNR extracellular measurements. Benchmarking of 6 different spike-sorters on high SNR MEA traces showed an average accuracy below 60%, majorly impacted by misclassifications of EAPs of the same neuron (Section 4.4). A misclassification rate of about 30% was exceptionally high for bursting neurons, and misclassified EAPs were primarily assigned to the neuronal bursts. The underlying EAP variations were accompanied by IAP waveform changes, similar to the findings of Henze et al.[64], and are well explained by the biophysics of sodium voltage-gated channels. During the bursts, prolonged depolarizations inactivate $Na_vs$, reducing the pool of available channels for the upcoming IAPs, and resulting in attenuation and broadening of the IAP waveform (Fig. 4.7. A). These IAP variations are reflected in the EAP changes; due to the dominant high-pass properties of the coupling, the height of the EAP scales to the fast sodium-driven part of an IAP. However, the variations of the IAP waveform alone could not fully explain the EAP variations and the consequential high incidence of misclassifications for the high SNR measurements.

## Inconsistent IAP-EAP transfer promotes the EAP variations

Explicit estimates of the transfer functions revealed that an additional factor contributing to the high amplitude EAP variations is inconsistent IAP-EAP coupling in each neuron (Fig. 4.7. A). Different transfer functions for a given neuron-electrode pair were specific for a subset of IAP-EAP pairs. Their reversible transitions occurred in seconds, supporting that the observed changes did not arise from technical limitations in benchmarking; the latter typically manifests as an irreversible switch or gradual waveform decay. The observed inconsistencies could be attributed to variant signal transfer at the electrode or be only apparent due to different compartment detection by patch-clamp and MEA. However, changing transfer functions were found both in soma-on-electrode and putative dendrite-on-electrode configurations (Section 4.5). Since dendrites have relatively low axial resistance (15 MΩ) up to 100 µm from the soma,[154, 284] propagating IAPs are not expected to attenuate drastically. Finally, all the causes of apparent transfer function changes would lead to primarily Ohmic changes and equal scaling of the transfer function magnitudes across all frequency ranges. Unmatching magnitude profiles even after the scaling correction suggested the differences were not from different IAP detection. Therefore, the primary cause of the changing transfer function is inconsistent EAP detection.

The parameters related to the capacitive component of the coupling had the highest degree of dispersion (Section 4.5). At the cell-electrode junction, the capacitive component is represented at least by the junctional membrane capacitance and the capacitive double layer (see also Section 2.2.2).[25, 189] One plausible explanation for the capacitive coupling changes relates to activity-associated variations of local ion concentrations. Particularly during bursts, the immediate neuronal surrounds experience up to 10 mM $K^+$ elevations lasting over seconds.[296] Increasing ion concentrations, particularly in the reduced cleft, may induce ion adsorption at the Helmholtz layer and transiently increase double-layer capacitance, affecting the signal transfer. While accumulated ion channels at chronically curved interfaces have been suggested as a mechanism

to reduce the junctional membrane resistance in 2D+ electrode coupling,[25] future studies should evaluate the ability of junctional membranes to produce extracellular alternations comparably to the free membrane.[296] Another mechanism concerns the junctional membrane area alternations. Since chronically curved membranes are abundant with docked vesicles,[297, 298] activity-guided vesicle dynamics could alter the membrane area.[299] Although the mechanism of transfer function changes is yet to be identified, the findings confirm that transfer function inconsistencies, which are prominent in high SNR measures, further contribute to the single-neuron's EAP variations. The findings also hold relevance for the IAP-from-EAP prediction, since the current cell-electrode models assume consistent coupling parameters and signal coupling for a given neuron.

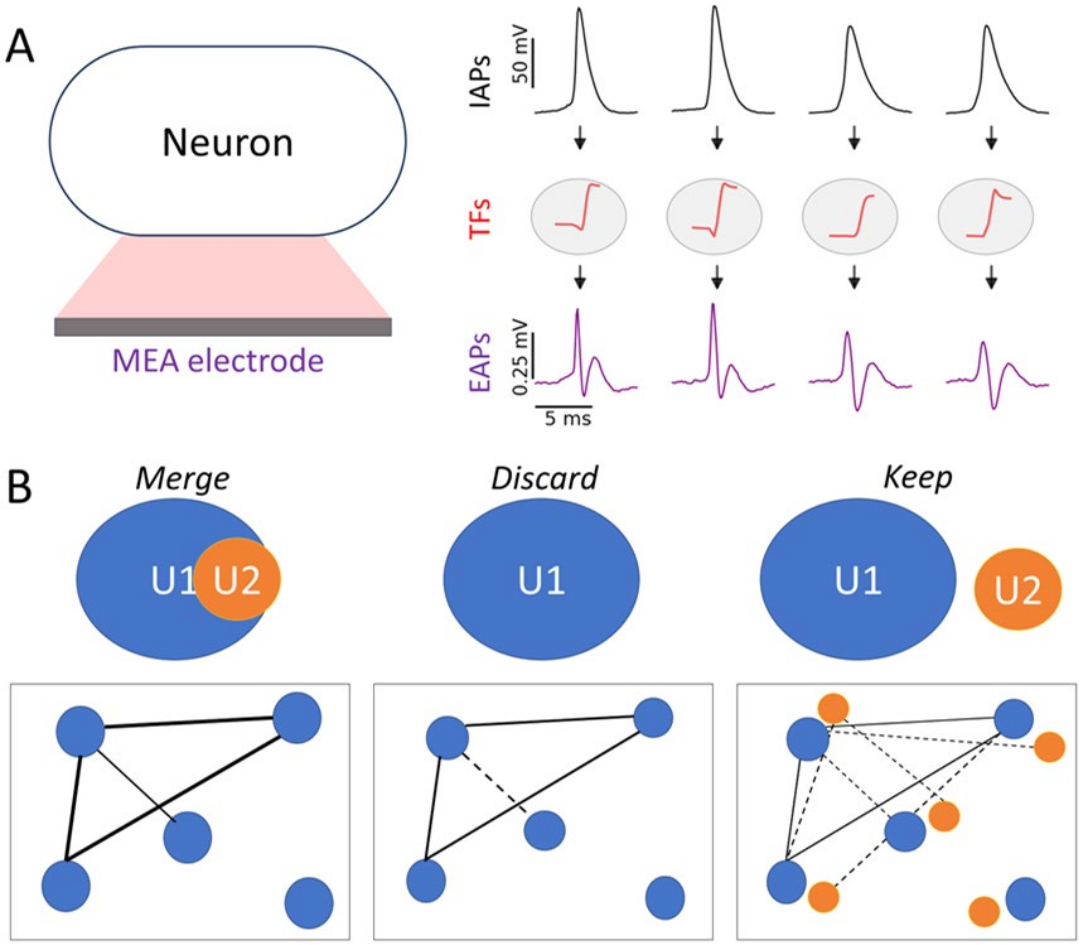


**Figure 4.7. EAP waveform variability: origin and implications for functional connections.** A. Dual origin of EAP waveform variations. Left: neuron-electrode interface (red). Right: Single-neuron IAP waveform and IAP-EAP transfer function variability promote EAP variations. B. Network connectivity from pairwise correlations is sensitive to misclassification. Top: different curation outcomes after misclassifying the single-neuron EAPs into more than one unit: the two units may be merged, the smaller unit may be discarded, or kept as a separate neuron. Bottom: network functional topology for each outcome. Nodes represent putative neurons corresponding to spike sorter units. The thickness of vertices denotes the strength of connections estimated from pairwise cross-correlations.

## Spike-sorting curation steps influence the functional connectivity estimates

Spike omissions, frequently occurring in low SNR MEA traces, consistently impact the network connectivity estimates by causing the loss of information within the conserved unit landscape. In contrast, spike misclassifications from single-neuron EAP variability can have varying outcomes depending on the unit curation process, which relies on chosen unit quality criteria and the investigator's judgment. *In silico* benchmarking of the bursting network with misclassification incidence comparable to *in vitro* networks showed that the population metrics are robust to the spike sorting errors as long as the spikes are correctly detected (Section 4.6). However, estimates of functional connections from cross-correlation of the spike-timings were sensitive to the curation outcomes (Fig. 4.7. B). In particular, retaining and interpreting smaller, disjointed units of EAPs as separate neurons had the most reductive power on estimated functional connectivity. The reduced density of connections and increased global efficiency due to the introduction of weak, spurious connections for unit retaining demonstrate that conclusions drawn about the functional network's topology from MEA measurements are susceptible to misclassifications. In contrast, discarding smaller units that did not satisfy the presence ratio criterion had a lower impact on the network density, as only some EAPs were omitted from the preserved unit landscape. In light of increased misclassification incidences in high SNR records, the findings favor excluding all units that do not satisfy quality criteria over their retention.

## Study limitations and outlook

The spatial profiles of neuron-electrode coupling were extracted within the limitations of the brightfield imaging. Although brightfield micrographs reported relative soma-electrode distances, maximal electrode coverage by the coupled neurites was inferred from previously reported neurite dimensions. [286, 292] Future benchmarking studies should aim to identify the neuronal compartments coupled, for instance, by live-cell markers. In addition, the relation between the sealing and coverage area should be verified on the measured neurons, to get an insight into the cleft dimensions. Benchmarking of spontaneous EAPs demonstrated inconsistent IAP-EAP relation, which further contributes to the EAP variability and reduces the accuracy of spike source designation. While approximated transfer functions indicate that the capacitive component is most prone to variation, a holistic cell-electrode model is essential to clarify which variable physical component of the coupling produces inconsistencies in signal transfer. Such a model should be generalized to all EAP waveforms and should consider neuronal compartmentalization and complex spatial interactions that may arise between the neuronal membrane, nanocavity, and nanostraws. Since several physical causes of transfer function changes are plausible, experimental verification is needed to determine the main contributors. Examples of such investigations include correlating transfer function changes with local ion concentration shifts,[296] or actively modulating local ion concentrations, for instance, by optogenetic stimulation of the coupled neuron.[300] In addition, future microscopy analyses could be employed to verify activity-related modulations of chronically curved interface membranes.

Demonstrating which parameter of the physical coupling shapes the IAP-EAP transformation is relevant for understanding the dynamics of cell-electrode interfaces and should also increase predictive power about transfer function changes. The latter is crucial for developing spike sorter adjustments to excess EAP variations arising from transfer function inconsistencies and accurate analog IAP-from-EAP estimates.

# 5. Somatic calcium signals are context-dependent predictors of neuronal activity

Due to the rich spatial content and source specificity, calcium imaging and particularly genetically-encoded calcium indicators are widely used to infer neuronal network activity. One main goal is to accurately translate the $Ca^{2+}$ signal into the firing code, for high-resolution estimates of the network's rhythms and functional connections. However, accurate translation is not straight-forward for several reasons.[34] Firstly, the binding kinetics of calcium indicators causes the non-linear addition of coincident 1AP-associated transients.[34, 213] Secondly, $Ca^{2+}$ is involved in secondary signaling cascades that occur alongside firing, but may not directly reflect action potentials.[301] Thirdly, spontaneous neuronal signaling introduces non-linear $Ca^{2+}$ events from dendritic calcium APs and NMDA spikes.[156-158] Finally, synchronous network events contribute to additional calcium pool by imobilizing cacium from internal reservoirs.[231, 232] These are only indirectly related to the firing of the observed somas, although they are relevant in single-neuron computations and synaptic plasticity.[207] Nevertheless, it was previously demonstrated that somatic $Ca^{2+}$ signals reliably report the neuron's firing sequence, especially when a high spatial resolution allows amplitude sensitivity that suffices for reliable 1AP detection. The current state-of-the-art models assume a causal relation between the firing code and calcium signals, with APs contributing to somatic $Ca^{2+}$ increases by activating high-threshold L-type Cavs.[31] Accordingly, $Ca^{2+}$ signals are widely accepted as a robust proxy of neuronal firing.

In the light of the assumed causal relationship, decoding neuronal firing directly from $Ca^{2+}$ signals has been addressed as an optimization issue, using approaches ranging from deconvolutions[222, 223] to supervised NN models.[224] However, these methods have limited scope and often fail to generalize the firing activity across multiple datasets. Models that combine $Ca^{2+}$ dynamics and voltage-gated channel kinetics led to spiking inferences based on biophysical processes;[35] however, they suffer from expanded parameter space and require tedious parameter adjustments. In addition to the lack of a generalizable pipeline to predict the neuronal spiking rhythm, recent studies pointed to a surprisingly reduced sensitivity to isolated APs in broad-network activity screening, requestioning which information about the neuronal firing could be reliably extracted from $Ca^{2+}$ signals.[36] The current standpoint for the overall reduced 1AP sensitivity and $Ca^{2+}$ signal-firing code inconsistencies focuses on the technical aspects, such as the low-pass filtering of the signals from reduced sampling rate, delays from the reporter, and low photon-per-pixel yield in the wide network screenings.[36] While the technical setbacks causing the low 1AP sensitivity have been systematically studied, the inconsistent visibility of 1AP events in the same neuron's $Ca^{2+}$ trace indicated an additional, biologically grounded contribution to the variable firing – $Ca^{2+}$ signal relation. In particular, the technical aspects and intercellular differences, such as the bleaching effect or variant reporter expression and $Ca^{2+}$ buffering, respectively, can not account for short-term and reversible inconsistency in 1AP visibility in single-neuron $Ca^{2+}$ traces. Moreover, a single firing event represents a robust, binary change of the membrane potential.[59] If an AP were mainly or solely responsible for $Ca^{2+}$

influxes at the soma, the 1AP $Ca^{2+}$ visibility would be binary and consistent within the cell. Conversely, if $Ca^{2+}$ signals were sensitive to subtle AP waveform variations (Chapter 4),[66, 67, 282] the acquisition would certainly be sensitive enough to detect individual APs.

Here, I postulated that the major contributor to the reported firing prediction inconsistencies are context-dependent, synapse-driven $Ca^{2+}$ non-linearities and that the $Ca^{2+}$ traces are a better predictor of the membrane potential changes than the firing sequence. The former is inspired by the evidence accumulated on dendritic $Ca^{2+}$ events propagating to the soma, and contributing to the somatic $Ca^{2+}$ increases and depolarizations, as well as synchrony-evoked $Ca^{2+}$ mobilizations from internal $Ca^{2+}$ pools.[2, 157] Since the membrane acts as a thin capacitor ($\leq 1 \mu F/cm^2$),[48] the neuronal membrane potential is sensitive to small charge fluxes or re-distributions, contrary to the APs whose binary occurrence relies on the threshold crossing, membrane resting potential preceding the depolarization and ion channel constitution.[59] The unknown source of inter- and intra-trial variability in the detection of 1APs could be due to limited information from the previous juxtacellular and loose-patch benchmarking that reliably reported only spiking sequences. [34, 36, 171-173] Since a single AP can arise from the synaptic noise, or PSPs and UP states, discernible 1AP $Ca^{2+}$ transients may reflect isolated AP events carried by stronger membrane depolarizations. Investigating a direct membrane potential- $Ca^{2+}$ trace relation is not only informative for which information could be reliably extracted from $Ca^{2+}$ traces but could reduce the parameter space within current biophysical models and increase the generalizability of optimization-driven spike estimation pipelines.

This chapter investigates how reliably calcium imaging conveys information about the local network activity compared to MEA sampling of the network-wide activity estimates from the previous chapter.

In accordance with this, the main objectives of this chapter are:

1. Investigate the context-dependency of neuronal somatic $Ca^{2+}$ signals;
2. Estimate which information about the membrane potential could be reliably extracted from $Ca^{2+}$ fluorescence traces.

This chapter contains parts of working manuscript:

**Bogdana Cepkenovic**, Vanessa Maybeck, Andreas Offenhäusser. Decoding Neuronal Firing Rates: Unraveling the Interplay Between Calcium Signals and Membrane Events.

# 5.1. Calcium imaging reliably captures network synchrony

To test how calcium imaging maps the local circuitry dynamics compared to MEA electrophysiology, spontaneous neuronal activity was probed with calcium indicators in ca. 0.2 $mm^2$ (acquisition details in Section 3.2.1). jRCaMP1b was used to screen the calcium activity of 21+ DIV cultures, representing the peak of network maturation (Section 4.1). As $Ca^{2+}$ spike waveform serves as a primary predictor of the observed neurons' firing, the general properties of the pooled $Ca^{2+}$ transients were analyzed with respect to the local network's activity. In addition, a comparison of jRCaMP1b-mediated $Ca^{2+}$ signals with previously characterized gCaMP6f spikes at our Institute[302] evaluated the consistency across the reporters.

SNEs were the primary mode of mature cortical network activity, occurring at a frequency of 0.07 Hz (Fig. 5.1.1. A, median; IQR: 0.05; 78 fields of view, 3967 cells). In 0.2 $mm^2$, approximately 82 ± 3% of jRCaMP1b-expressing neurons showed $Ca^{2+}$ signals, and 74 ± 3% contributed to at least one SNE. The frequency of SNEs detected via calcium imaging within the local circuitry was comparable the MEA-detected SNEs in 2 $mm^2$ (Section 4.1). This suggested that local neuronal circuits reflect network-wide synchronization during the network bursts and that calcium imaging accurately conveys information transfer during SNEs. A higher incidence of active neurons in the calcium-screened cultures could be due to activity sampling differences, as the incidence of active MEA channels depended on the cell coverage area (Section 4.1).

The amplitude of $Ca^{2+}$ spikes followed a log-normal distribution, with the Gaussian peak at 0.03 $dF/F_0$ (N = 22490 transients). A similar distribution was found for $SNR_{avg}$ of $Ca^{2+}$ traces with clear $Ca^{2+}$ signals, which ranged from 0.6 to 299.1 and showed a log-normal Gaussian peak at 5.6 (N = 3967 traces). The full width of $Ca^{2+}$ transients ranged from 0.3 s to 72.0 s and followed a log-normal distribution peaking at 5.4 s. The log-normal distribution suggests that most traces had a low SNR, and the majority of detected $Ca^{2+}$ signals had small amplitudes and short durations (Fig. 5.1.1. B). Similar amplitude distribution was also reported in previous characterizations of neuronal $Ca^{2+}$ transients from our Institute using GCaMP6f,[302] suggesting a universal trend in $Ca^{2+}$ fluorescence across different reporters.

At the level of individual neurons, the average integral of $Ca^{2+}$ spikes inversely scaled with the $Ca^{2+}$ spike frequency (Fig. 5.1.1.C, black). A high incidence of attenuated transients in high-frequency traces is a leading cause of the pooled distributions' skewness towards small signals. The neuron's $Ca^{2+}$ spiking rate and fraction of its $Ca^{2+}$ spikes that participated in SNEs had a significant inverse relation (Fig. C1, Appendix C2). This relation suggests that slow-frequency neurons are most often engaged in SNEs, whereas high-frequency neurons had, in addition, $Ca^{2+}$ spikes outside the SNEs. Frequently $Ca^{2+}$ spiking neurons also showed a greater magnitude variation of $Ca^{2+}$ spikes (Fig. 5.1.1. C, red), and thus most often had a mixture of small and high-magnitude $Ca^{2+}$ signals. However, the distribution of $Ca^{2+}$ spike magnitudes was not random. As depicted in Figure 5.1.1. D, the integral of transients participating in SNEs was almost 2x larger (median: 0.14, IQR = 0.21, N = 13331 transients) than for those outside of SNEs (median: 0.08,

IQR = 0.1, N = 9159; $p < 10^{-4}$, two-tailed Mann-Whitney). These not only explained a higher CV for neurons exceeding the SNE frequency but also suggested that the $[Ca^{2+}]$ increases and corresponding $Ca^{2+}$ fluorescence are context-defined.

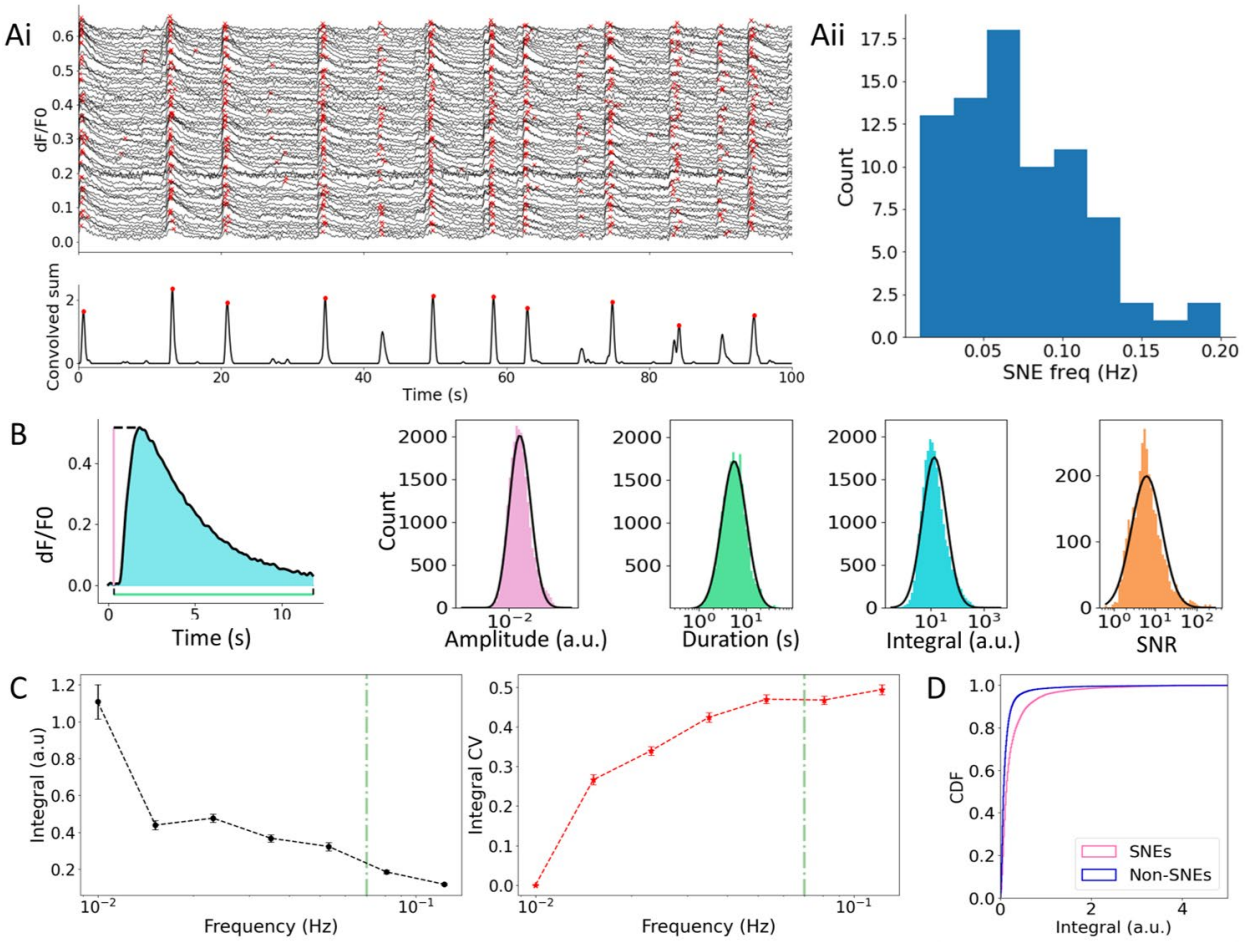


**Figure 5.1.1. Spontaneous activity sampled by calcium imaging.** A. Synchronous network activity of 21+ DIV neurons detected in 0.2 $mm^2$. Ai. Exemplary $Ca^{2+}$ traces (top). Red x marks the local maxima of $Ca^{2+}$ transients. Bottom: convolved sum of network-level $Ca^{2+}$ events. Red circles mark SNEs, defined through the 3 SD threshold. Aii. SNE frequency distribution (N = 78 fields of view). B. Properties of spontaneous $Ca^{2+}$ transients. Exemplary transient and estimates of amplitude (pink), duration (green), and integral (blue). Right: log-normal histograms depicting $Ca^{2+}$ signal amplitudes, widths, integrals (N = 22490 transients), and SNRavg of $Ca^{2+}$ traces (N = 3967 cells). Distributions of each parameter were fit by the Gaussian curve (black). C. Integral distribution for $Ca^{2+}$ transients of individual traces as a function of the average firing frequency. Green line denotes the median SNE frequency at the network level. Right: $Ca^{2+}$ integral CV vs. the average $Ca^{2+}$ frequency. Symbols denote the mean of every bin, with standard error of the mean. Note that 0.01 Hz frequency (which equals 1 $Ca^{2+}$ spike per 100 s trace) was kept in the CV plot for consistent comparison with integral-frequency relation; however, this point is not reliable, as CV estimated on a single $Ca^{2+}$ event per neuron always amounts to 0. D. CDF of integrals of SNE and non-SNE $Ca^{2+}$ transients.

In summary, spontaneous *in vitro* activity screened via calcium imaging showed network synchronizations at frequencies similar to MEA-detected SNEs, suggesting that calcium imaging is comparably accurate for detection of network synchrony. $Ca^{2+}$ spikes showed log-normal distribution of widths, amplitudes, and integrals, due to a high prevalence of attenuated signals in fast $Ca^{2+}$-spiking neurons. $Ca^{2+}$ fluorescence depended on the context, as high magnitude $Ca^{2+}$

signals concentrated around SNEs. The origin of pronounced internal $Ca^{2+}$ increases may be two-fold. First, multiple APs typically accompany SNEs (Chapter 4), and potentiated $Ca^{2+}$ influxes may be from pronounced firing. However, neurons during SNEs also receive stronger, coincident synaptic inputs capable of eliciting regenerative $Ca^{2+}$ events.[6, 147] Further, SNEs are typically characterized by $Ca^{2+}$ mobilization from internal $Ca^{2+}$ pools.[231, 232] In turn, these can increase the cytosolic $Ca^{2+}$ pool, which may or may not contribute to neuronal firing. Defining which factor has a predominant role in somatic $Ca^{2+}$ signal generation is relevant for firing predictions and connectivity estimates, since non-firing related $Ca^{2+}$ increases may contribute to context-dependent inconsistencies in translations of $Ca^{2+}$ fluorescence into the firing. The question of how $Ca^{2+}$ transients translated into the firing, and whether this translation was context-dependent, was explored in the following section.

# 5.2. Context-defined calcium signal-firing relation

Calcium waveforms are a complex, non-linear predictor of neuronal firing. Intuitively, the most prevalent small-amplitude spikes (previous Section) should correspond to a single AP.[302] However, the recent benchmarking of *in vivo* $Ca^{2+}$ traces revealed a surprisingly low sensitivity of network-level imaging to isolated APs that varied between and within the cells' traces.[36] The latter points to the indirect relations of neuronal firing and $Ca^{2+}$ dynamics since APs represent robust voltage events. The cause of such variations is likely biological, but remains elusive, presumably due to the limitations of the targeted extracellular benchmarking.[36, 171, 303] I mapped the jRCaMP1b fluorescence to the somatic membrane potential detected simultaneously in whole-cell. The main goal was to evaluate how reliably the $Ca^{2+}$ signal translates into the spiking activity, focusing on context-dependent spontaneous neuronal activation and associated membrane potential dynamics.

Spontaneous activity was detected simultaneously with whole-cell patch-clamp and calcium imaging, as described in Section 3.3.2. The whole-cell was used to accurately identify spiking of the target neuron and to correlate $V_m$ with $Ca^{2+}$ dynamics. Correlating the membrane events with the $Ca^{2+}$ traces gave insight into spontaneous, communication-related background processes contributing to $Ca^{2+}$ increases, since these processes reflect on the membrane potential. Short recording intervals accounted for possible biases due to the cytoplasm perfusion with the pipette solution. Out of 54 obtained >1.5 min paired measurements, six neurons were without APs, and the rest fired at least one AP.

Like the calcium imaging-only observations, $Ca^{2+}$ transients participating in SNEs (Fig. 5.2.1. A, blue rectangles) had a higher magnitude than the non-SNE signals (Fig. C2, Appendix C2). $V_m$ events were first correlated with the local network's $Ca^{2+}$ fluorescence to estimate the contextual dependency of the firing events and depolarizations eliciting APs. Briefly, the found APs were defined as SNE-participating if they coincided with 2 s windows around the SNE peaks (Fig. 5.1.1. A). Magnitudes of depolarizations eliciting APs were estimated from $V_m$ integrals following digital AP extraction (Section 3.6.2). During SNEs, the $V_m$ displayed prolonged (6.1 ±

0.8 s, N = 187) depolarizations carrying on average 4 APs (Fig. 5.2.1. C). These depolarizations were a hallmark of network synchrony, as they reliably mapped to the $Ca^{2+}$-detected SNEs. In contrast, non-SNE membrane events comprised brief (3.3 ± 0.2 s, N = 965) depolarizations eliciting, on average, 2 APs. While there was a significant difference between APs number in SNE and non-SNE events (Fig. 5.2.1. C, $p < 10^{-4}$, Kruskal-Wallis), the most striking difference was in magnitude of membrane depolarizations eliciting APs. Specifically, the integrals of SNE-associated membrane events (Fig. 5.2.1. B) were almost 4x higher than outside-SNE ($p < 10^{-4}$, Kruskal-Wallis). These suggested that spontaneous $V_m$ dynamics may better reflect the $Ca^{2+}$ signal, and function as a mediator between the local network activity, the firing code and $Ca^{2+}$ dynamics.

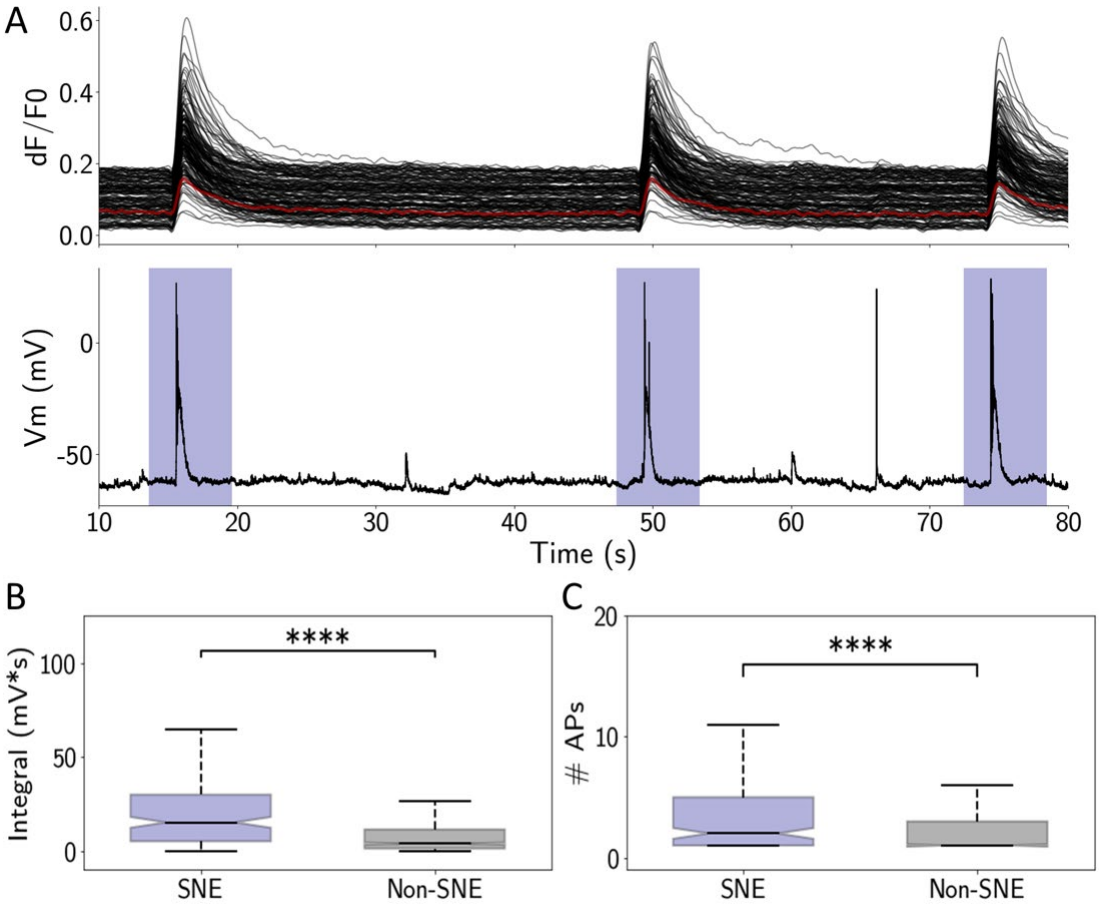


**Figure 5.2.1. Membrane potential changes in context of network synchronicity.** A. Simultaneous whole-cell patch-clamp and calcium imaging for ground truth of spontaneous activity. Top: $Ca^{2+}$ traces from neurons in ca. 0.2mm$^2$; red is the trace of the target neuron. Bottom: membrane potential detected by whole-cell current-clamp. SNE-associated membrane events are shaded in blue. B. Integrals of subthreshold membrane potential events within (blue) and outside of SNEs (gray). C. Number of APs

$Ca^{2+}$ fluorescence was then evaluated with respect to the firing, to assess whether the contextual dependency of the $Ca^{2+}$ spike magnitude arose from proportionally high AP frequency or firing-unrelated processes. To calibrate the whole-cell estimates to the existing on-cell[36, 171, 303] and juxtacellular,[304] benchmarking from other groups, clusters of APs corresponding to a given $Ca^{2+}$

spike were determined from the binned AP rate code (Fig. 5.2.2.A, red line). Accordingly, a firing event comprised of APs within a 0.5 s window preceded > 2 s of voltage silence, and the corresponding $Ca^{2+}$ transients were aligned according to the first AP. This raster windowing sporadically isolated the late APs from the cluster sharing the depolarization and $Ca^{2+}$ event (Fig. 5.2.2. A, blue rectangles), emphasizing the limitations of this approach on neurons with late-burst APs. The average $Ca^{2+}$ magnitude increased with the number of APs, however with insufficient resolution to determine the #APs from the $Ca^{2+}$ events. For instance, 2AP $Ca^{2+}$ spikes are easily distinguished from 1-AP events but have similar magnitude to 3AP spikes. Similarly, there was not a significant magnitude difference between 4-, 5- and 6-AP $Ca^{2+}$ spikes (Fig. 5.2.2.B-C). The within-range deviation from linearity may be physiological, however the late-burst AP exclusion from raster windowing is an additional contributor. The latter, frequent in adaptive multispikers, exerts a stronger flattening effect on $Ca^{2+}$ magnitudes.

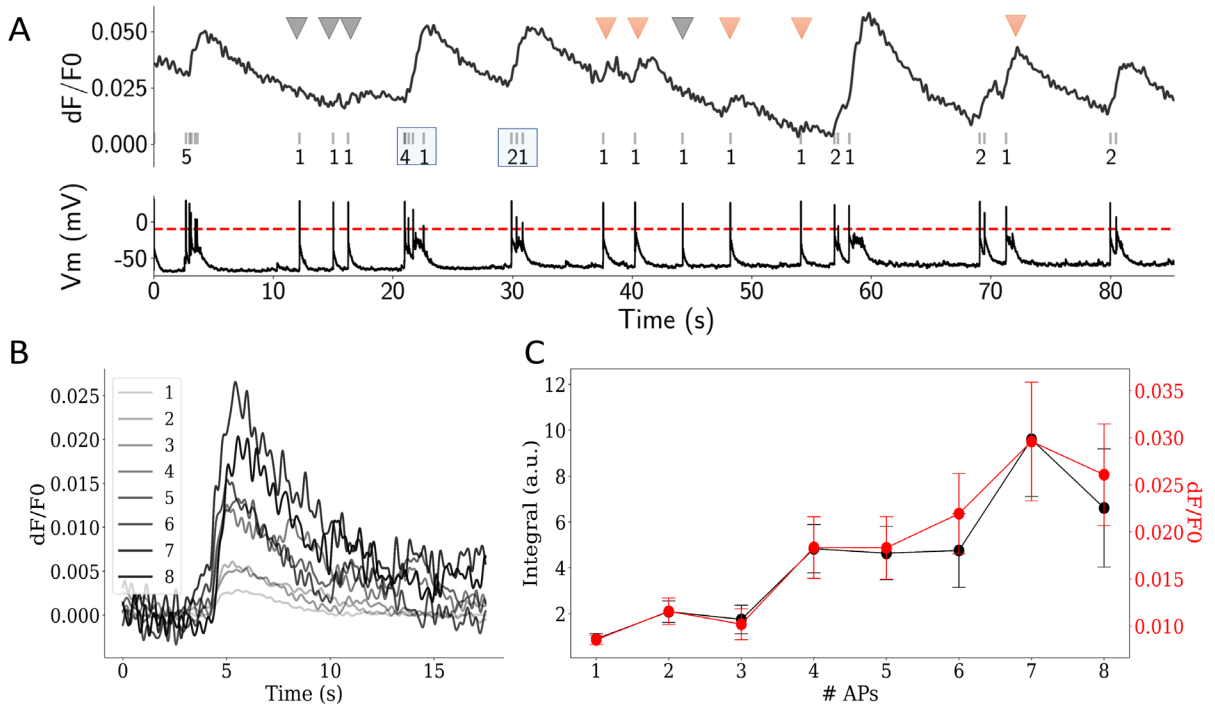


**Figure 5.2.2. The relationship between the calcium fluorescence and firing dynamics.** A. Simultaneously detected $Ca^{2+}$ signal (top) and membrane potential in whole-cell mode (bottom). Horizontal red line accounts for the information content obtained with targeted extracellular measures from the publicly available datasets. Rasters below the $Ca^{2+}$ trace denote each spiking event, and numbers indicate APs for each $Ca^{2+}$event. B. Average $Ca^{2+}$ windows corresponding to 1 (N = 851), 2 (N = 273), 3 (N = 125), 4 (N = 52), 5 (N = 44), 6 (N = 16), 7 (N = 13) and 8 APs (N = 12). >8 AP $Ca^{2+}$ spikes were omitted from comparisons due to the low sample size. Average waveforms were computed from all windows, irrespective of the threshold crossing. C. Calcium integral (black) and amplitude (red) vs. #APs.

Figure 5.2.2. A also shows that the neuronal UP states coincided with well-defined $Ca^{2+}$ spikes, while the non-SNE membrane events bearing only a few APs did not always match visible $Ca^{2+}$ signals. Accordingly, 1AP $Ca^{2+}$ spikes were occasionally visible (Fig. 5.2.2. A, orange arrows) and sometimes not (Fig. 5.2.2A, gray arrows). The sensitivity of the jRCaMP1b to isolated AP

events was then investigated to estimate how reliably $Ca^{2+}$ traces translate into neuronal firing. Single APs were identified per depolarization to exclude biased assignments from raster windowing (Section 3.6.2). At a 1% false positive rate, 1AP detection probability was 27 ± 5% per neuron, and it rose to 47 ± 6% and 53 ± 6% for the 5% and 10% incidence of false positives, respectively (Fig. 5.2.3. B). The reduced sensitivity matches the previous reports from *in vivo* benchmarking in broad-network imaging.[36] A 5% false positive incidence was chosen as a $Ca^{2+}$ detection threshold, as this rate universally showed the optimal accuracy (Fig. C3, Appendix C2). At this false error rate, only 32% of the pooled 1AP $Ca^{2+}$ spikes were detected. The overall reduced $Ca^{2+}$ signal sensitivity to 1APs contradicts previous hypotheses that all prevalent small-amplitude $Ca^{2+}$ spikes in spontaneous $Ca^{2+}$ traces corresponded to 1APs.[302]

At a 5% false positive rate, 1AP $Ca^{2+}$ spike detection incidence ranged from 0% to 100% (Fig. C3, Appendix C2). That technical aspects, such as variable jRCaMP1b expression levels or $Ca^{2+}$ buffering, were not a primary determinant of variable 1AP $Ca^{2+}$ spike detection, was strongly suggested by negligible and insignificant difference of total $SNR_{avg}$ in neurons that showed at least one 1AP $Ca^{2+}$ spike and those that did not (Fig. C4, Appendix C2). Further, there were no significant differences in holding $V_m$ across the two groups (Fig. 5.2.3. Ci), suggesting that inter-cellular 1AP $Ca^{2+}$ magnitude differences did not arise from various pre-potentiation of $Ca_V$s. Importantly, neurons with at least one suprathreshold 1AP $Ca^{2+}$ spike had, on average, 3x lower firing rates and showed higher firing thresholds than neurons with all below-threshold 1AP $Ca^{2+}$ spikes (Fig. 5.2.3. Cii-Ciii). Accordingly, the neurons with at least 1AP $Ca^{2+}$ spike above-threshold required stronger inputs to produce an AP. Thus, the primary source of inconsistencies in 1AP $Ca^{2+}$ visibility may be input-related.

The detection of 1AP $Ca^{2+}$ spikes varied within the same cell, since on average, less than half of 1AP events were detected per trace. Whole-cell benchmarking further revealed that supra-threshold 1AP $Ca^{2+}$ spikes corresponded to greater 1AP-evoking depolarizations (Fig. 5.2.3. A). In addition, 1AP-evoking depolarizations coinciding with suprathreshold 1AP $Ca^{2+}$ spikes occasionally carried one or more spikelets with an average height 5.2 ± 0.9 mV (Fig. 5.2.3. A). Accordingly, the absolute voltage value at the peak of the spikelet was -39.8 ± 1.8 mV, which is below the threshold for the full HVA activation. Spikelets represent a somatic failure to produce an AP upon receiving regenerative events from other compartments.[305] While their magnitude does not suffice to solely produce significant $Ca^{2+}$ influxes, spikelets indicate various inputs soma receives during network synchrony. As a measure of magnitude, the integrals of 1AP depolarizing events were estimated from voltage trace following the AP removal by digital filtering (Fig. 5.2.3. Di). The integrals of 1AP-evoking depolarizations matching to suprathreshold 1AP $Ca^{2+}$ spikes were 2x larger ($p < 10^{-4}$, Kruskal-Wallis, Fig. 5.2.3. Dii) than those coinciding with subthreshold 1AP $Ca^{2+}$ spikes. In either case, the AP-evoking depolarizations had integrals ca. 100 x higher than those of 1 APs (0.089 ± 0.001 mVs).

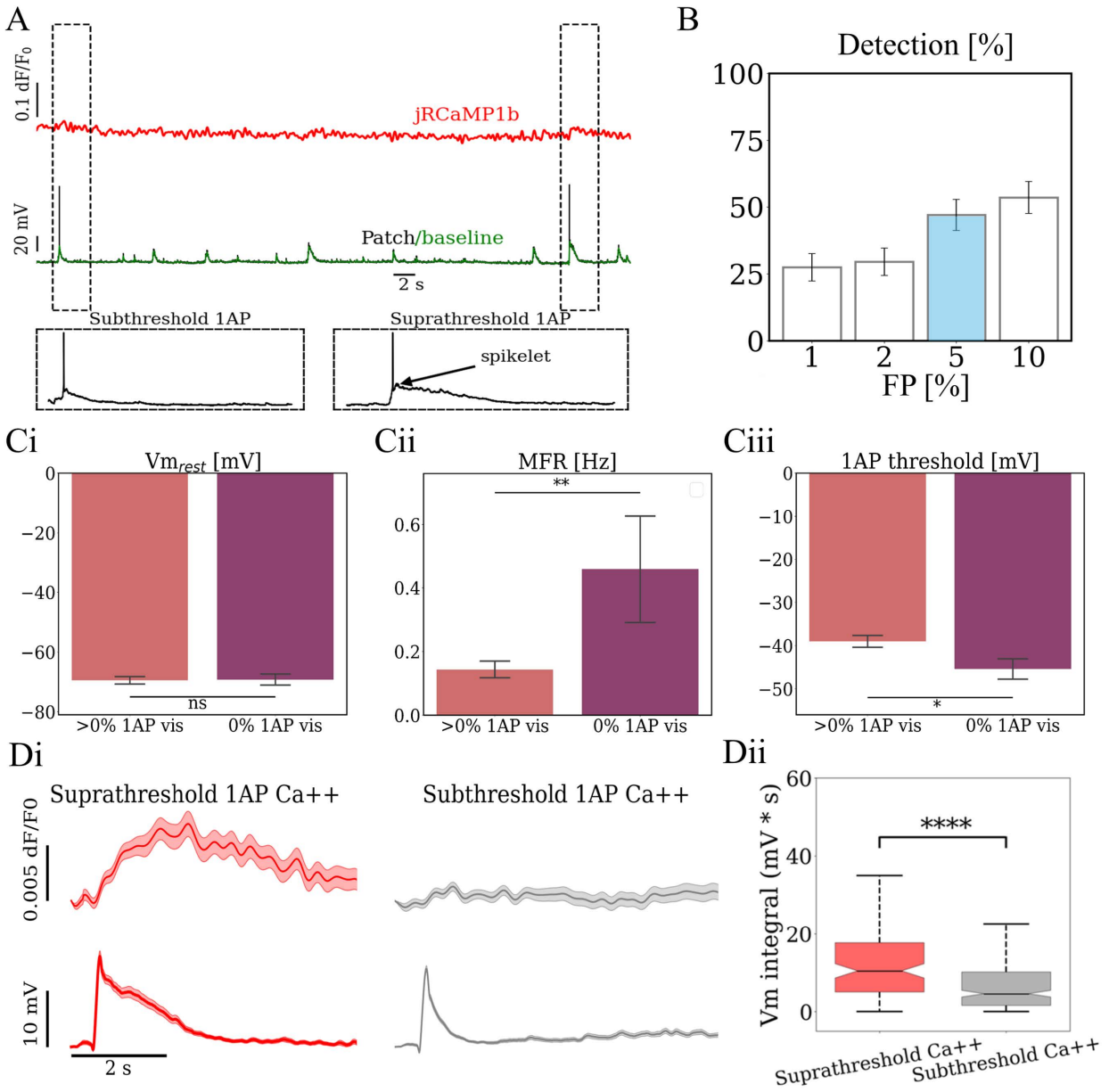


**Figure 5.2.3. Sensitivity to 1APs depends on the magnitude of subthreshold depolarizations.** A. Paired $Ca^{2+}$ fluorescence (top) and voltage traces (bottom) depicting two 1 AP events (*-ed), carried by UP-state (left) or isolated PSP (right). Blue lines denote the membrane depolarization after the AP removal by filtering. B. Detection probability of 1AP $Ca^{2+}$ spikes at different false detection incidences. Blue highlights 5% false positive incidence used as a threshold. C. Electrophysiological profiles of neurons with at least one (>0% 1AP vis) and with none (0% 1AP vis) detectable 1AP $Ca^{2+}$ spikes. Ci. Holding membrane potential. Cii. Mean firing rate. Ciii. AP threshold. Statistical annotation: **: $p < 10^{-2}$, *: $p < 0.05$, t-test. D. Separation of suprathreshold and subthreshold 1AP $Ca^{2+}$ transients. Di. Suprathreshold and subthreshold 1AP $Ca^{2+}$ transients (top) and corresponding membrane depolarizations that evoked an AP (bottom). Isolated APs were removed by filtering to focus on the subthreshold voltage changes for integral calculation. Thick lines represent the mean and shaded areas denote SEM. Dii. Membrane depolarization integrals for suprathreshold and subthreshold 1AP $Ca^{2+}$ transients. Statistical annotation: ****: $p<10^{-4}$, Kruskal-Wallis.

In summary, combined whole-cell patch-clamp and local network calcium imaging revealed the context dependency of membrane potential. Although SNE-related membrane events elicited on

average twice as many APs, magnitude differences of the underlying membrane depolarizations showed a larger effect size. The inconsistent magnitude and visibility of 1AP $Ca^{2+}$ signals in a single neuron's jRCaMP1b trace suggested a biological contribution to the variable $Ca^{2+}$ signal – firing relation. An investigation of the underlying membrane potential showed a significantly larger membrane depolarization corresponding to above-threshold 1AP $Ca^{2+}$ signals. Accordingly, the inconsistent 1AP $Ca^{2+}$ spike visiblity may arise from differences in input strength and firing properties of the neuron. The findings are relevant for two reasons. First, they suggest that the processes that ultimately evoke firing contribute to somatic $Ca^{2+}$ signal, causing inconsistent magnitudes and detectability of 1AP $Ca^{2+}$ spikes in a neuron. Since the subthreshold membrane potential dynamics reliably reports the input strength, the findings also indicate that the $Ca^{2+}$ trace could more reliably predict the underlying depolarizing events than the firing sequence. In the following section, I further explored the calcium signal – membrane potential relation in the context of spontaneous and evoked activity.

# 5.3. Calcium traces are a reliable predictor of membrane depolarizations

To evaluate to what extent firing events influence the magnitude and visibility of somatic $Ca^{2+}$ signals, $Ca^{2+}$ responses to current injections were detected when APs were pharmacologically blocked. Neurons were stimulated either by 1 s or 100 ms current injections at 1 s intervals. Stimulating neurons resulted in well-defined stimulus-triggered averages (STAs) for individual current pulses and plateau elevations from steady $Ca^{2+}$ build-up (Fig. 5.3.1. Ai).[306] Block of APs by TTX induced $Ca^{2+}$ responses similar to the control (Fig. 5.3.1. Aii), suggesting that AP-evoked $Ca^{2+}$ influxes are not required to produce comparable $Ca^{2+}$ signals. Since current-evoked responses were below the potential required for full HVA channel activation (-23 ± 7 mV), HVA $Ca_V$s are likely not the primary contributors to evoked somatic $Ca^{2+}$ signals.

In addition, neurons that spontaneously participated in SNEs but showed SNE-associated depolarizations below the firing threshold had visible $Ca^{2+}$ signals despite the lack of APs (Fig. 5.3.1. B). These spontaneous activity observations indicated that the synchrony-related background events, leading to strong somatic depolarizations, suffice for generating suprathreshold $Ca^{2+}$ signals at the soma. In contrast, two putative interneurons[307] spontaneously fired a train of APs without a requirement for strong depolarizations. Despite a high firing rate, $Ca^{2+}$ traces of these neurons had most frequently no discernible signals, except when the strong depolarizations occurred (Fig. 5.3.1. B). These suggested that the background events causing strong membrane depolarizations are necessary for robust $Ca^{2+}$ spikes.

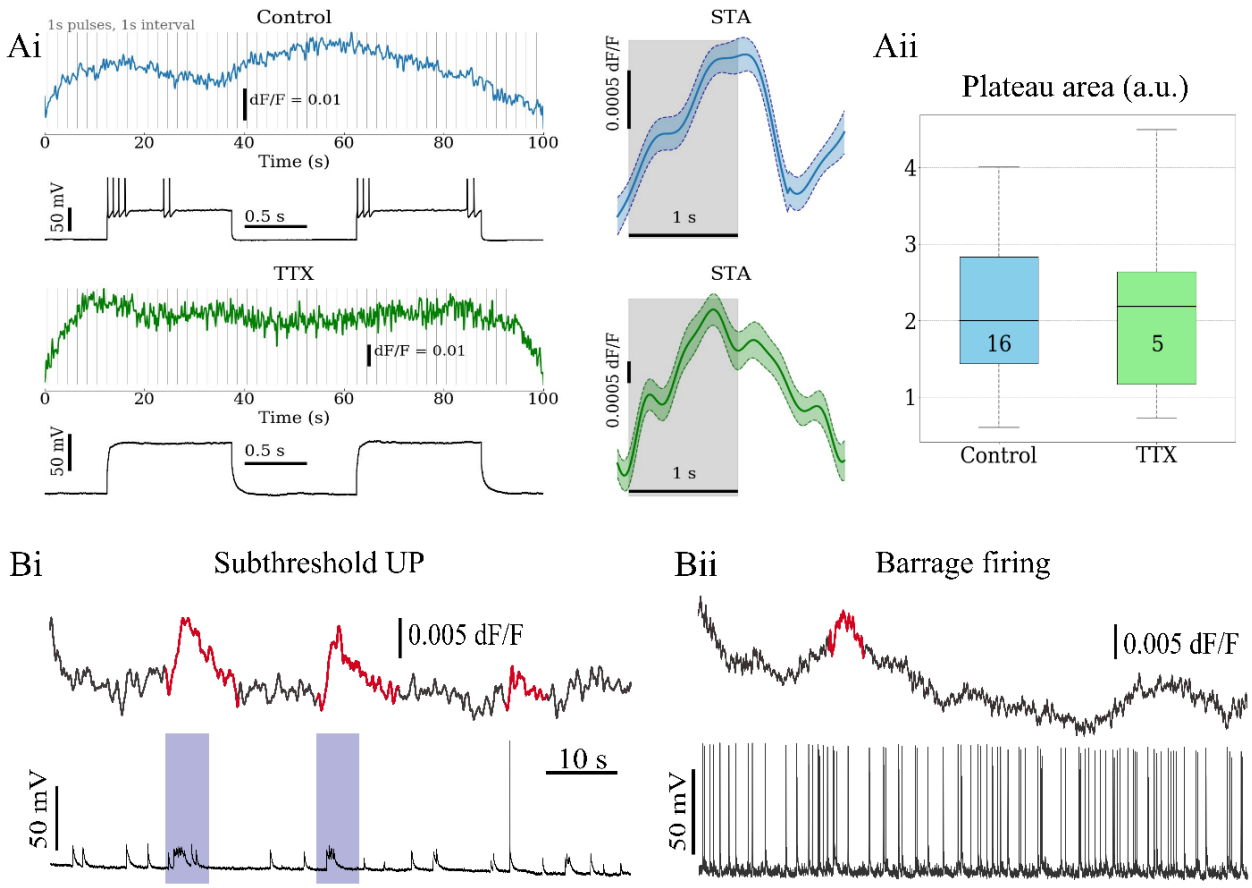


**Figure 5.3.1. Depolarizations are sufficient and necessary for calcium spike development.** A. Neuron's responses to current injections. Ai. Representative traces showing calcium responses to 1s current pulses in native conditions (blue) and TTX treatment (green); vertical lines represent the onset of individual current pulses. Black traces denote membrane potential to the first two pulses. Right panels represent the stimulus-triggered averages; shaded areas denote SEM. Gray rectangles indicate duration of current pulses. Aii. Areas under the curve for control and TTX-treatment. The numbers below the median lines indicate sample size. Bi. SNE-coinciding subthreshold membrane depolarizations (blue rectangles) correspond to discernible calcium spikes in absence of APs. Bii. Putative interneuron with a train of APs. Above-threshold calcium events marked in red.

$Ca^{2+}$ fluorescence was then evaluated with respect to the slow membrane depolarizing events only. APs were filtered from the voltage trace, and depolarizing events were isolated via thresholding (details in Section 3.6.2). This approach found 1297 depolarizations in 54 neurons. Similar to the previously described pipeline for 1APs (previous Section), corresponding $Ca^{2+}$ trace windows were aligned by the depolarizations' onsets, and projected to the unitary template vector to obtain scalar values. Depolarizations related to suprathreshold $Ca^{2+}$ signals (26.7 mVs, IQR = 40.9 mVs, N = 470) were about 4x stronger than those corresponding to subthreshold $Ca^{2+}$ events (6.3 mVs, IQR = 10.6 mVs, N = 827, $p < 10^{-3}$, two-tailed Mann-Whitney; Fig. 5.3.2. A). Importantly, magnitudes of the underlying depolarizations showed a strong and significant linear correlation with the magnitudes of $Ca^{2+}$ fluorescence ($R^2 = 0.74$, $p < 10^{-4}$, Pearson's, Fig. 5.3.2. B).

In addition, about 1/5 of membrane depolarizations corresponding to a suprathreshold $Ca^{2+}$ spike were without APs (Fig. 5.3.2. C). That suprathreshold $Ca^{2+}$ events most frequently corresponded to membrane depolarizations eliciting multiple APs (53%) is unsurprising, as the number of firing events correlates with the magnitude of the underlying membrane depolarizations (Pearson's; $R^2 = 0.46$, $p < 10^{-4}$).

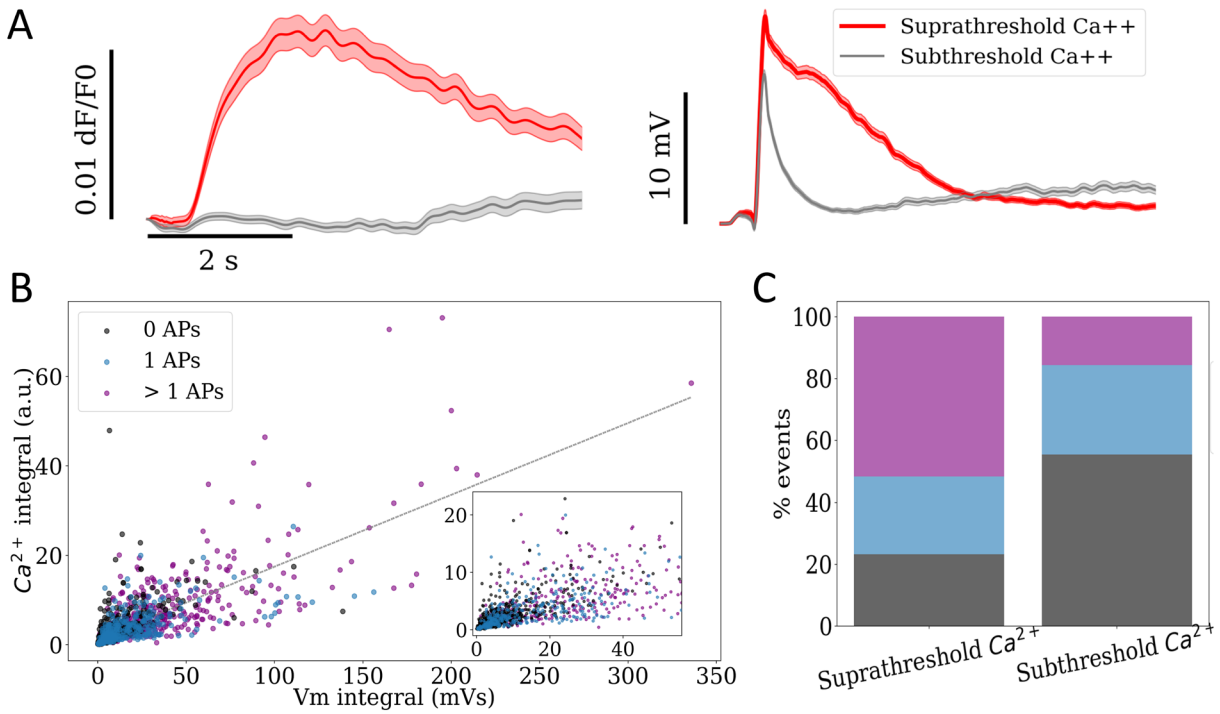


**Figure 5.3.2. Membrane depolarization – calcium signal magnitude relationship.** A. Average membrane depolarizations corresponding to suprathreshold (orange) and subthreshold (blue) calcium spikes. Right. Calcium waveforms separated by thresholded projections onto unitary template vector. Orange represents averaged suprathreshold calcium and blue denotes average below threshold calcium windows. Shaded areas in both plots denote SEM. B. Magnitude of membrane depolarizations correlates with the magnitude of calcium signals. Color code relates to the number of elicited APs per depolarizing event. Bottom right is the zoomed in inset of the main figure. C. Distribution of AP numbers per depolarization corresponding to and suprathreshold (left) and subthreshold (right) calcium events.

Relatively low sampling rate and reduced spatial resolution due to the network-level measurements affected the visibility of the membrane events in jRCaMP1b traces. I next investigated which membrane depolarizations could be reliably recognized in the $Ca^{2+}$ trace under these conditions. Starting from AP filtering and depolarization detection, the found membrane depolarizations were classified according to their kinetics and magnitude via dimensionality reduction by a single-value decomposition (SVD) followed by K-means clustering and curation (details in Section 3.6.2). Among the membrane depolarizations, 69% (N = 894) were somatic PSPs (Fig. 5.3.3. A, green), 18% (N = 236) were GDPs (Fig. 5.3.3. A, blue), and 13% (N = 167) were UP states (Fig. 5.3.3. A, red). Table 5.3.1 contains average properties of the membrane events found. In individual neurons' $Ca^{2+}$ traces, the most frequently visible membrane depolarizations were the UP states (detection probability: 0.91), followed by

GDPs (0.79), and PSPs (0.15) (Fig. 5.3.3. B). Among the somatic PSPs that manifested as visible $Ca^{2+}$ signals, only a third were isolated events, with 6.1 ± 0.6 mVs average integral (N = 62); the rest were coinciding, superimposed PSPs from temporally close synaptic inputs. Thus, the jRCaMP1b signal in broad-network imaging shows the highest visibility for membrane events associated with network synchrony.

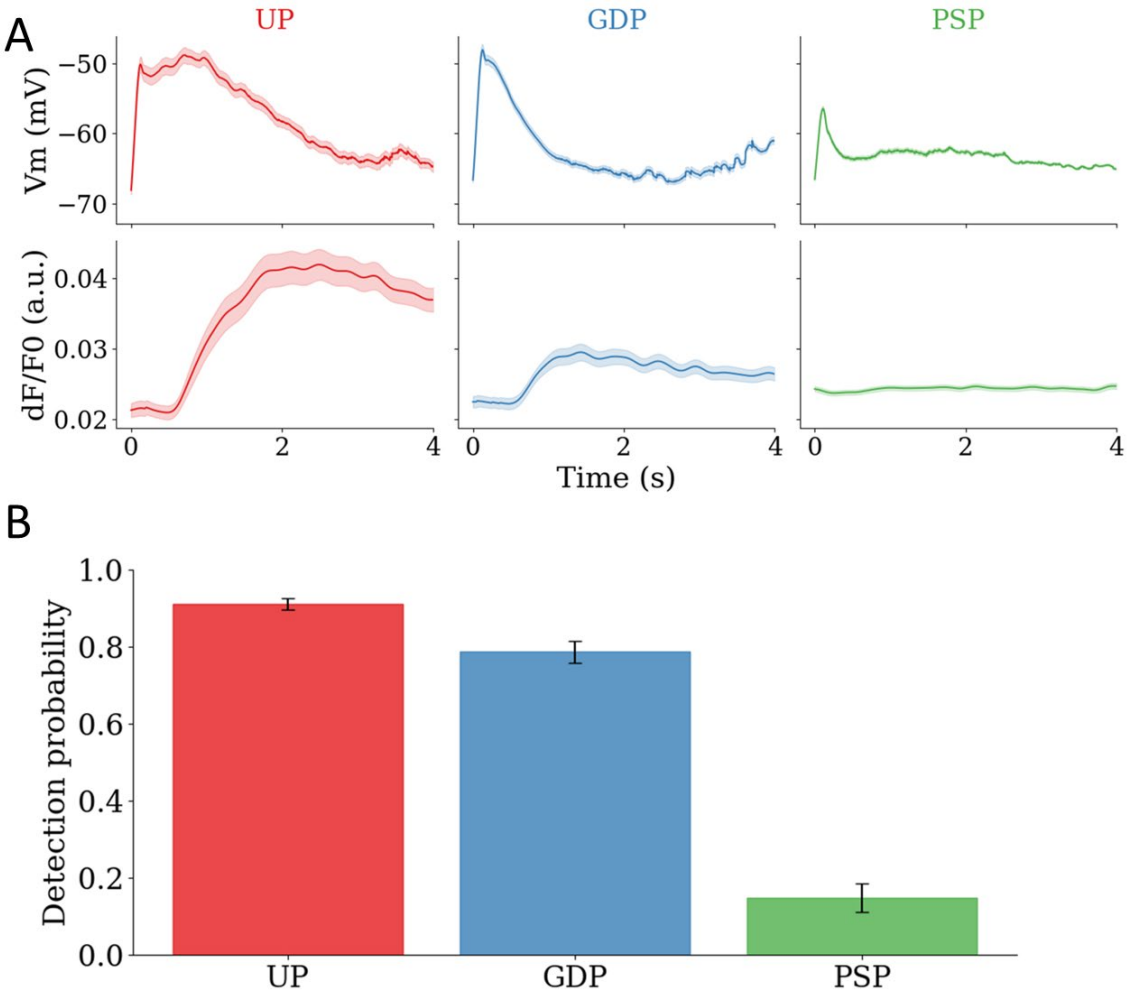


**Figure 5.3.3. Classification of the membrane depolarizations by their kinetics and magnitude.** A. Average waveforms for all UP-states (N = 167, red), GDPs (N = 236, blue) and PSPs (N = 894, green) and corresponding calcium windows. Shaded areas represent SEM in all cases. Corresponding calcium signals are shifted by a 2-frame lag for visible representation of magnitude. The average PSP waveform's tail is due to overlaid and superimposed PSPs. B. Visibility of calcium signals classified by the membrane depolarizations, per calcium trace.

Table 5.3.1. Properties of membrane depolarizing events

| Properties | UP events (N = 167) | GDPs (N = 236) | PSPs (N = 894) |
|---|---|---|---|
| Integral (avg ± SEM) | 30.6 ± 3.4 mV s | 26.0 ± 2.1 mV s | 16.4 ± 0.8 mV s |
| Amplitude (avg ± SEM) | 32.8 ± 0.7 mV | 23.2 ± 0.5 mV | 12.8 ± 0.2 mV |
| # APs (avg ± SEM) | 4.87 ± 0.36 | 2.72 ± 0.21 | 1.80± 0.08 |
| Fraction evoking APs | 89.22% | 71.61% | 44.41% |

The findings suggest a more direct relation between $Ca^{2+}$ signals and underlying depolarizing events than $Ca^{2+}$ signals and firing dynamics. First, the pharmacological removal of APs by TTX treatment did not abolish evoked $Ca^{2+}$ responses (Fig. 5.3.1. A). In addition, about 20% of the spontaneous $Ca^{2+}$ spikes matched the membrane depolarizations that did not elicit an AP (Fig. 5.3.1. B and Fig. 5.3.2. C), while there were no discernible $Ca^{2+}$ spikes for AP trains in barrage-firing neurons (Fig. 5.3.1 B). $Ca^{2+}$ magnitude strongly correlated with the membrane depolarizations irrespective of the firing outcome (Fig. 5.3.2. B), suggesting the $Ca^{2+}$ traces could be more accurately translated into the membrane depolarizing events. The most often visible membrane events were synchrony-related UP states and GDPs, while the PSPs were rarely detected. The more prolonged and robust depolarizations associated with network synchrony were most frequently recognized in $Ca^{2+}$ traces. In contrast, the isolated synaptic events were hardly visible during the network-level imaging conditions.

# 5.4. Discussion and conclusions

Calcium imaging is commonly used to sample neuronal activity with excellent spatial information content. Assuming the direct and causal relation between intracellular $Ca^{2+}$ and firing,[31] current models directly estimate the neuronal activity from $Ca^{2+}$ traces.[35, 223, 308] However, several lines of evidence suggest that somatic $Ca^{2+}$ increases are also supported by non-firing processes,[309] while recent work in broad-network settings indicated inconsistent detectability of $Ca^{2+}$ signals matching to isolated APs.[36] This chapter investigated if the cause of such inconsistent $Ca^{2+}$ signal-firing relation is biologically grounded and contextually dependent, and which information about the network activity and network connections could be reliably extracted from $Ca^{2+}$ traces.

## The calcium signal's magnitude is context-defined

Calcium imaging of the local neuronal network (Section 5.1) revealed network synchrony at incidences similar to *in vitro* cultures grown on MEAs, screened in about 10x larger area (Section 4.1). These demonstrated that $Ca^{2+}$ signals accurately reflect the network synchrony, enabling spatially precise estimates of the network-wide oscillations. Similar wide-network activity profiles at different space scales also suggested that the local circuitry represents the global network activity during the synchronous regime. Interestingly, the same neuron's $Ca^{2+}$ spikes participating in SNEs had significantly higher magnitudes than those outside SNEs (Fig. 5.1. D). This difference could be due to increased neuronal firing rates in network bursts, or additional contribution from synchronous synaptic inputs to somatic $Ca^{2+}$ signals. Combined whole-cell and calcium imaging confirmed that SNEs were indeed accompanied by stronger depolarizations, eliciting more APs than non-SNE events. The context-dependency of the $Ca^{2+}$ signals is in accordance with previous benchmarking studies.[309] However, the magnitude difference between SNE and non-SNE depolarizing events showed a larger effect size than the firing frequency (Fig. 5.2.1). These observations suggested that the membrane depolarizations may be a more accurate representation of $Ca^{2+}$ signal, especially when the broad-network imaging of oscillating networks is involved.

## Biological influence for single-neuron inconsistent 1AP $Ca^{2+}$ spike visibility

Unlike the targeted extracellular benchmarking, which is prone to errors when assigning APs to separate inputs (Fig. 5.2.2), the whole-cell's sensitivity allowed the unbiased isolation of APs belonging to the same depolarizing event. Whole-cell benchmarking of the spontaneous jRCaMP1b $Ca^{2+}$ signals demonstrated low sensitivity to isolated APs (Fig. 5.2.2. and 5.2.3), akin to observations from *in vivo* benchmarking of several GECIs.[36] The reduced detection of strongly attenuated 1AP $Ca^{2+}$ signals emphasizes the limitations of always interpreting highly prevalent, smaller $Ca^{2+}$ spikes as 1AP events in *in vitro* network calcium screening.[302]

Further, the between-neuron differences in 1AP $Ca^{2+}$ spike detection correlated with the firing type and firing threshold. Specifically, the neurons with at least one above-threshold 1AP $Ca^{2+}$

spike required stronger inputs to evoke an AP. In contrast, those with all 1AP $Ca^{2+}$ spikes below the threshold more readily fired an AP in responses to weaker inputs. These suggested that between-neuron differences in 1AP $Ca^{2+}$ signal visibility are deepened by the neurons' predisposition to fire, and thus in magnitudes of inputs that evoked an AP.

The first demonstration of inconsistent $Ca^{2+}$ signal–firing relation was the variable magnitude and detectability of 1AP $Ca^{2+}$ spikes in the same neuron. The rapid and reversible detectability of 1AP $Ca^{2+}$ spikes (Fig. 5.2.3) supported the biological contribution via processes not caused by firing. Given the robustness of APs,[59] a sole contribution of AP-evoked $Ca^{2+}$ influxes to $Ca^{2+}$ signals is expected to manifest in consistent 1AP $Ca^{2+}$ detection within a neuron. In contrast, less than half of 1AP $Ca^{2+}$ spikes per neuron crossed the threshold. Moreover, there was a strong correlation between the magnitudes of membrane depolarizing events and corresponding 1AP $Ca^{2+}$ signals (Fig. 5.4. A). In particular, single APs were more likely to be manifested as threshold-crossing $Ca^{2+}$ spikes if stronger inputs, such as the synchrony-related UP state or GDP, caused an AP. The findings suggest that aside from external influences, intrinsic factors, such as the strength of inputs driving the $Ca^{2+}$ influxes and slow membrane depolarizations, influence the magnitude and visibility of 1AP $Ca^{2+}$ signals in the same cell.

## Somatic firing is not the only source of detected $Ca^{2+}$ signals

Electrical stimulation produced similar $Ca^{2+}$ responses when APs were abolished (Fig. 5.3.1), suggesting that firing is not necessary to produce significant $Ca^{2+}$ increases. This is in agreement with the previous study showcasing that prolonged (1 s) stimulation pulses evoke $Ca^{2+}$ elevations in TTX.[310] However, the findings contrast the previous benchmarking showing attenuation of $Ca^{2+}$ responses [311, 312] or their complete absence in TTX.[313] The partial or full attenuation in these studies may be due to relatively short stimulus durations (1 – 10 ms), along with very high spatial resolution,[311, 312] which produces excellent 1AP sensitivity.[36] With stimulation pulses this brief, baseline depolarizing events represent only a small fraction of total depolarization, and AP-driven $Ca^{2+}$ influxes, which are well-captured due to an optimal spatial resolution,[36] likely predominated detected $Ca^{2+}$ signals. Indeed, in studies demonstrating TTX attenuation, the least effect was reported for the longest current injection pulses (10 ms).[311]

Further, these brief pulses hardly reflect the spontaneous membrane depolarizations, as even the isolated PSPs are in tens of ms ranges, while the network-burst-associated UP states last for seconds (Section 5.3). In such cases, prolonged subthreshold depolarizations may suffice for visible $Ca^{2+}$ signals and even overpower the electrical effects of an AP.[310] First, nearly a 100x higher depolarization integral (Section 5.2) sustains $Ca^{2+}$ influxes through low-threshold $Ca_V$s.[227-229] Second, the prolonged subthreshold depolarization can trigger $Ca^{2+}$ mobilization from endoplasmic reticulum, even in reduced external $Ca^{2+}$.[310] In the light of spontaneous communication, coincident synaptic inputs trigger global regenerative $Ca^{2+}$ events,[156] while network-level synchrony further promotes $Ca^{2+}$ mobilization from internal depoes,[230-232] which can further elevate somatic calcium.

Accordingly, spontaneous SNE-associated depolarizations coincided with suprathreshold $Ca^{2+}$ signals even in the absence of APs required for full HVA activations (Fig. 5.3.1 B). Specifically, about a fifth of all above-threshold $Ca^{2+}$ spikes corresponded to SNE-associated depolarizations without any AP (Fig. 5.3.2). Thus, in broad-network calcium imaging, where reduced photon fluxes per neuron also reduce the AP sensitivity, the deciding factor affecting the $Ca^{2+}$ signal magnitude is not related to firing. On the same token, $Ca^{2+}$ traces of the putative interneurons, which did not require strong depolarizations to fire, lacked distinct $Ca^{2+}$ spikes despite a high frequency of APs. While these interneuron-specific inconsistencies were often attributed to differential $Ca^{2+}$ buffering extent,[31] the finding of this study suggest that the infrequent strong depolarizing events in conjunction with low firing threshold in these neurons are likely the primary cause of inconsistent translation of the $Ca^{2+}$ signal into the neuronal firing. Therefore, broad-network imaging faces several challenges for neuronal activity translation, from rendering SNE-related no-firing events as multiple APs, to interpreting barrage-firing neurons as inactive.

## Calcium traces are reliable predictors of membrane depolarizing events

A strong linear correlation between the membrane depolarization magnitudes and the fluorescence intensity and clear separation of the membrane events corresponding to sub- and suprathreshold $Ca^{2+}$ signals showed that the $Ca^{2+}$ trace predicts slow membrane depolarizations better than it predicts the evoked firing sequence. As previously discussed, this correlation can be attributed to steady $Ca^{2+}$ influxes via LVA, depolarization-evoked $Ca^{2+}$ mobilization from internal depoes, and additional input-specific $Ca^{2+}$ sources.

Due to its low specific capacitance,[48] the membrane acts as a reliable sensor to inputs since the small ion fluxes or charge re-distributions are required for eliciting a membrane depolarization. Although the firing probability is correlated with the depolarization's magnitude (Section 5.3), how many APs are evoked depends on the neuron's ion channel constitution that predisposes it to a single-spiker, adaptive, or constitutive multi-spiker, as well as on the membrane state.[59, 153] Thus, spontaneous synchrony-related inputs that consistently drive strong membrane depolarizations may evoke different numbers of APs. These differences between neuronal types and the input-related membrane state could further confound direct firing estimates from $Ca^{2+}$ traces.

Accordingly, suprathreshold $Ca^{2+}$ signals were most often related to synchrony-mediated strong membrane depolarizations (UP states and GDPs, Section 5.3), whereas isolated PSPs were hardly visible in the $Ca^{2+}$ trace. Therefore, calcium imaging is robust for identifying SNEs and SNE-participating neurons. The inconsistent $Ca^{2+}$ trace-firing relation shown in this study, along with the highest visibility of SNE-associated events, suggest that special care should be taken when operating with inferred firing rates to map the functional connectome, particularly in oscillating networks.[314] First, not all detected $Ca^{2+}$ signals directly relate to the firing activity. Second, the degree of translation errors depends on the neuron's firing type, with more consistent $Ca^{2+}$ signal-firing relation for constitutive multi-spikers, and larger deviations in $Ca^{2+}$-firing

relationship for single-spikers. Specifically, constitutive multi-spikers are expected to have proportionally higher $Ca^{2+}$ magnitudes for increasing AP number since they fire without adaptation.[59] On the contrary, single-spikers may produce single or zero APs during relatively strong, synchrony-related depolarizing events, causing overestimates of firing predictions from $Ca^{2+}$ traces. Moreover, a strong relation between the $Ca^{2+}$ events and membrane post-synaptic responses suggests that calcium imaging could be a good strategy for identifying the strengths of inputs at the imaged neuron. Yet, the sensitivity of the broad-network calcium imaging limits these observations mainly to SNE-related membrane events. Thus, correlating $Ca^{2+}$ traces as a work-around solution[236] may yield false positive connections, since the most-detected activity features SNEs that also recruit non-directly connected neurons (see Section 6.5).[14]

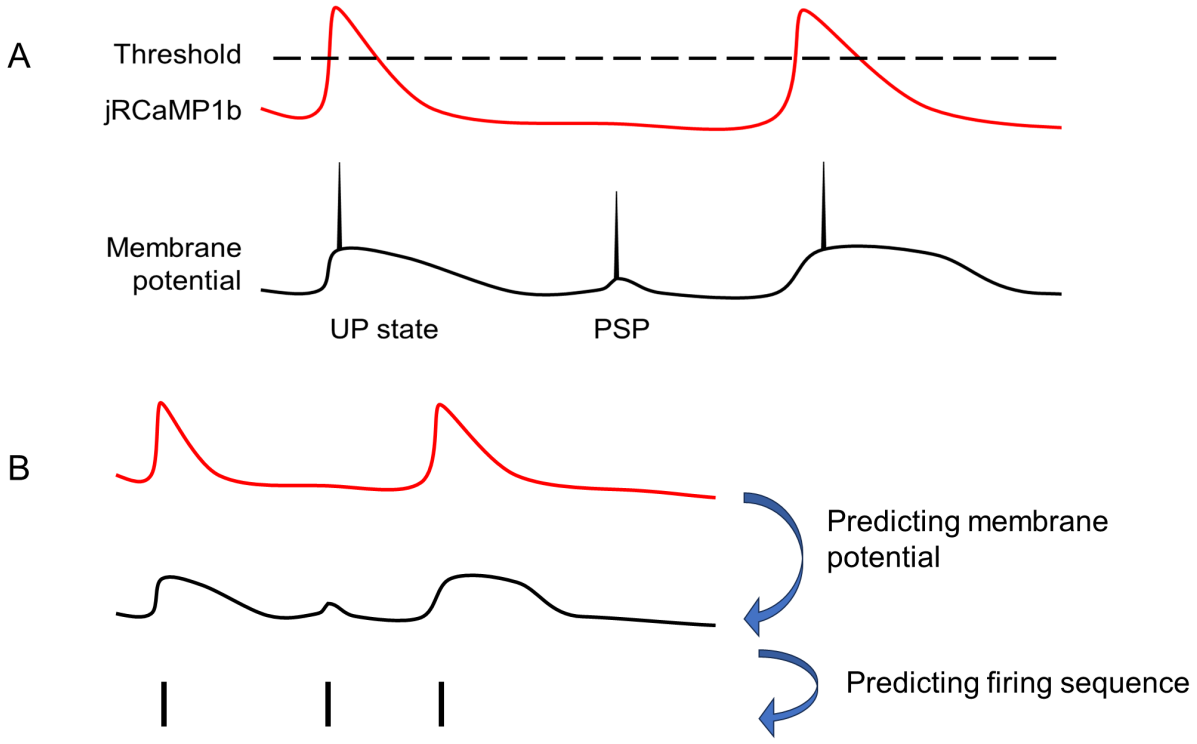


**Figure 5.4. Calcium traces are a reliable predictor of the membrane baseline depolarizing events.** A. Calcium signal-firing code relation is mediated by membrane potential dynamics. B. Proposed pipeline for estimating calcium firing dynamics.

## Implications and outlook for spiking inferences

The findings of this study suggest biologically rooted inconsistencies in $Ca^{2+}$ signal-firing relation, caused by strong $Ca^{2+}$ trace sensitivity to various input processes. In particular, they emphasize that different strength of inputs and the neuron's firing types introduce errors in direct firing estimates from calcium imaging. One of the future goals is to accurately correlate firing predictions to the morphology- or calcium-informed classification of the neuron's firing types for more accurate connectivity estimates.

Another key consideration in the neuron's firing rate predictions is strong correlation of the membrane depolarizing events with the $Ca^{2+}$ signals. The current biophysical model, which considers how the internal $Ca^{2+}$ increases reflect on the membrane potential and the elicited firing dynamics, suffers from excessive free parameters that require careful tweaking when a new, unseen dataset is introduced. Since the membrane depolarizations show direct relations to the calcium fluorescence, a direct prediction of membrane potential from $Ca^{2+}$ signals could be a preliminary step toward the firing rate predictions (Fig. 5.4. B). One of the future goals should be combining the information on the membrane depolarizations with the neuronal firing type classifier, informed by morphology and calcium dynamics, to improve the firing rate predictions further.

## Study limitations and outlook

In the scope of this work, I benchmarked $Ca^{2+}$ signals from cortical neurons by pairing calcium imaging with somatic whole-cell patch-clamp. While this benchmarking showed a strong relation between the jRCaMP1b signals and membrane depolarizations and an inconsistent $Ca^{2+}$ magnitude-firing relation, only a single GECI was characterized. Pursuing this relation in the light of other GECIs is relevant for finding universal trends across calcium reporters and tackling the reporter's contribution to calcium event–membrane potential relations. Furthermore, the neurons were benchmarked without prior knowing of their firing type. The sample was likely biased toward the cortical excitatory neurons, given their high prevalence *in vitro*.[126] This is evidenced by only two putative interneuron, barrage-firing phenotypes from the benchmarked dataset (Section 5.3). Finally, the findings of inconsistent $Ca^{2+}$ signal – firing relation should be interpreted in the light of strongly synchronized network states, widespread *in vitro* and also in some brain states *in vivo*. One of the future goals is to investigate the extent of inconsistencies in systems with different extents of synchrony.

# 6. Single-neuron perturbation excites the target and the surrounding network

From individual neurons[39, 41] to network-level deformations[37, 40, 43, 104], imaging techniques and particularly calcium imaging[38] demonstrated that neurons respond robustly to a mechanical stimulus. Among various mechanical neurostimulation strategies, ultrasound stimulation (US) stands out as a promising modality to manipulate brain activity for clinical purposes, as it does not necessitate opening the skull or altering the neuron's DNA.[38] The ultrasound advances allow temporally precise targeting at a specific depth and a lateral spatial precision of a mm.[315] While the key players mediating the mechanoresponses have been identified,[37, 39-41, 107, 316] it is unknown if there's a biological limit to spatial resolution. Specifically, it is unknown whether mechanically deformed neurons disperse the information to the non-deformed neighbors, which may result in broadening of the excitation. It is accepted that mechanical stimulus excites each neuron individually,[37] as the block of synaptic transmission does not attenuate network responses in multi-neuron deformations.[37, 104] Nevertheless, previous studies on cell types other than neurons demonstrated the ability of mechanoresponses to disperse via non-synaptic mechanisms involving gap-junctions or paracrine communication.[317-319] As neurons can communicate via either means,[97, 320] it is necessary to re-evaluate if mechanical responses spread into the network of neurons.

Investigating if a single-neuron deformation induces network-level detectable responses among the subpopulation of connected neurons is also relevant for advancing strategies for mapping of neuronal ensembles. Expanding the knowledge about mechanisms of neuronal ensemble development and maturation requires reconciling functional topology from the correlation of detected spontaneous activity with causal connections.[15, 22] While the previous studies demonstrated that the neurons whose detected spontaneous activity is highly correlated are more likely to be synaptically connected,[321] network-wide bursts may also recruit non-connected neurons, giving false positive estimates of synaptic connections.[14] Tracking the networks' responses to a single-neuron stimulation provides more accurate estimates, as the connected neighbors' responses are time-locked to the stimuli. While this approach has been used to map the local circuitry, the outcome of a single-neuron electrical stimulation also depends on the strength of synaptic connections, the target neurons' type, and the amplitude sensitivity of readout.[19, 20] Since multi-neuron deformation produces responses readily visible at the broad-network level,[37] this study also aimed to evaluate if mechanical response propagation was within a community of morphologically and synaptically coupled neurons.

To assess if mechanical responses disperse from the initiation site into the network, I investigated the network's responses to a single-neuron deformation during the giga-seal in the patch-clamp technique. Giga-seal is obligatory for any patch-clamp recording configuration[179] and consists of several membrane-deforming steps. Since patch-clamp is widely used to study

the native activity and excitability, it is important to evaluate if and how the pre-recording conditions affects the target, the network, or both.

In accordance with this, the primary objectives of this chapter are:

- investigate if membrane deformation during the giga-seal excites the target;
- investigate if a single-neuron deformation responses disperse through the network;
- evaluate if response dispersion targets interconnected neurons;
- estimate if a single-neuron deformation imposes neuromodulatory effects.

The chapter opens with the characterization of calcium responses upon membrane deformation. Section 6.2. investigates the molecular basis of calcium plateau initiation and its manifestation on the target neuron's membrane potential. Section 6.3. explores the extent and mechanism of mechanoresponse dispersion to the non-targeted neurons. Pharmacological interventions demonstrated that responses propagate via the gap junctions (Section 6.4), while paired electrophysiology and network activity assessments indicated the responding neurons belonged to a subpopulation of synaptically and morphologically interconnected neurons (Section 6.5), with the capacity to evoke firing in the coupled neurons (Section 6.6). A comparison between the extents of giga-seal and electrical stimulation is made in Section 6.6. This chapter closes with an investigation of the neuromodulation of the responding ensemble by a single-neuron deformation (Section 6.7).

Parts of this Chapter have been published in:

**Bogdana Cepkenovic**, Florian Friedland, Erik Noetzel, Vanessa Maybeck, Andreas Offenhäusser. Single-neuron mechanical perturbation evokes calcium plateaus that excite and modulate the network. *Scientific Reports* (2023). DOI: 10.1038/s41598-023-47090-z

# 6.1. Acute membrane deformation evokes calcium plateaus

During the giga-seal, the membrane undergoes several mechanically perturbing steps.[179] When the pipette nears the neuron under a 60-80 mmHg overpressure, the liquid flow imposes a shear stress onto the target. Further lowering induces membrane indentation underneath the pipette tip as the pipette passes one pipette radius above the cell (Fig. 6.1.1. A). Finally, the pressure release and the following suction favor the membrane protrusion inside the pipette tip and the generation of a tight contact between the membrane and the glass. Calcium imaging during giga-seal revealed that the target robustly responds with prolonged calcium responses, further noted as calcium plateaus. Plateaus were ca. 5x slower (Fig. 6.1.1 B-C) than spontaneous $Ca^{2+}$ events (41.7 ± 0.5 s, N = 1291 plateaus vs. 9.2 ± 0.1 s, N = 4345 spikes), and were more similar to the synapse-driven[163, 322, 323] and synapse-independent[85] $Ca^{2+}$ waves of neurons. Compared to electrically-evoked plateaus (Fig. 5.3.1. A) that arise from $Ca^{2+}$ accumulation due to slower buffering, giga-seal associated plateaus had 2x faster onset kinetics (slope: 0.02 $s^{-1}$, electrical slope: 0.01 $s^{-1}$, $p < 10^{-2}$ paired t-test) and 3x higher magnitudes ($dF/F_0$: 0.10 ± 0.01, electrical plateau $dF/F_0$: 0.03 ± 0.01, $p < 10^{-4}$ paired t-test).

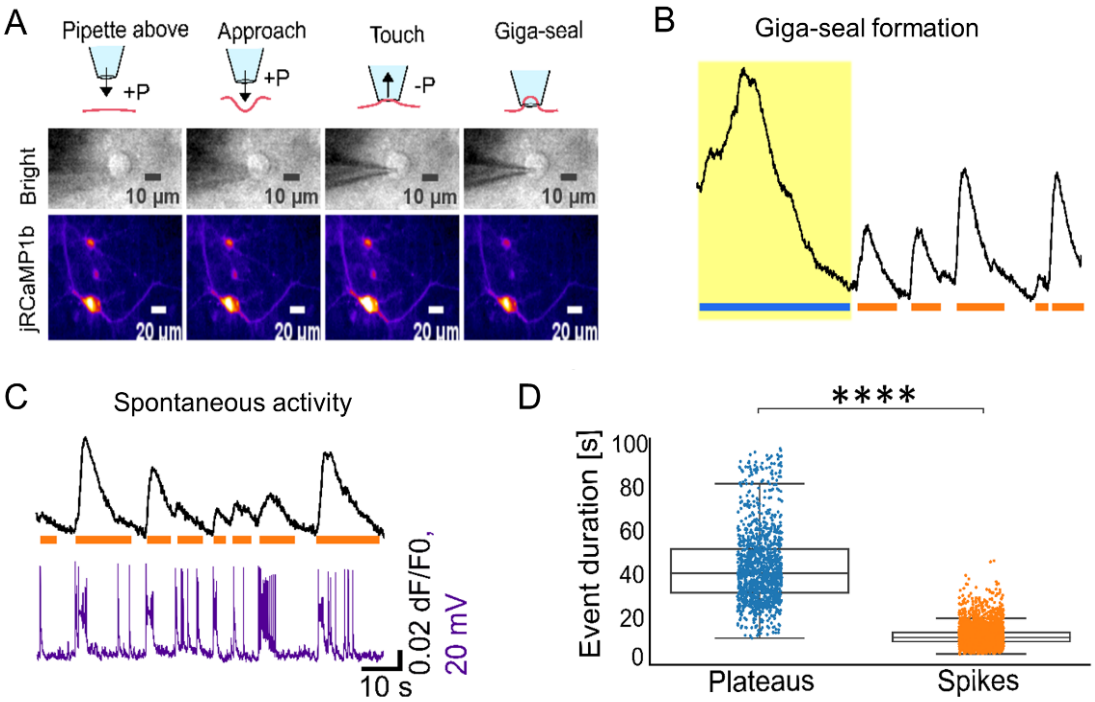


**Figure 6.1.1. Target neurons respond with calcium plateau during the giga-seal formation.** A. Pipette-neuron interaction during the giga-seal. Top: Schematics of different membrane-deforming steps preceding the giga-seal. Middle: brightfield images for each membrane-perturbing step. Bottom: jRCaMP1 micrographs of the target during various stages of giga-seal formation. B. Calcium trace of the target during the giga-seal formation (yellow). Horizontal lines denote the durations of calcium plateaus (blue) and AP-associated calcium spikes (orange). C. Spontaneous activity of the same neuron in C after the giga-seal formation. Calcium imaging was paired with whole-cell patch-clamp (purple trace). D. Widths of calcium plateaus and spontaneous $Ca^{2+}$ spikes.

Are the responses biologically grounded, or are they due to light interference? Calcium imaging during the pipette Z-axis movement ca. 10 µm above the cell layer showed calcium spikes associated with spontaneous activity (Fig. C1, Appendix C3). These suggest that calcium plateaus arise from cellular responses.

Since the pipette solution matched the ionic constitution of the cytosol, two experiments were designed to estimate if plateaus originate through diffusion of the pipette constituents. Firstly, the internal pipette solution was allowed to diffuse ca. 5 µm above the neuron under the +80 mmHg positive pressure (Fig. 6.1.2. A). The lack of plateaus when the internal solution containing pipette was above the neuron suggests that the target excitation was not due to diffusion of the internal solution. Secondly, responses were also observed when the pipette solution was switched to the bath solution (Fig. 6.1.2. B), favoring the pipette-membrane engagement over diffusion.

Unlike sharp-pipette intracellular records, where the pipette penetrates the cell membrane, giga-seal formation includes a series of membrane-perturbing steps without membrane injury.[179] When the pipette adversely penetrates the cell prior to giga-seal, the pipette responses to 5 mV, 5 ms electrical pulses display a sharp resistance drop and slow capacitive transients, akin to the whole-cell configuration (Fig. 6.1.2. C). In the case of the pipette penetration, the ion leakage around the injury site depolarizes the membrane and produces sustained $Ca^{2+}$ elevations (Fig. 6.1.2. C).[324] To avoid any confounding effects, calcium imaging focused on giga-seals without the immature intracellular access. It was also postulated that the shear stress, in combination with acute membrane deformation, might induce pores at the membrane. To rule out the creation of smaller pores in the membrane due to shear stress or membrane tension,[325] giga-seal formation was performed on trypan-blue-treated neurons under the brightfield. Trypan blue is a small (960 Da) hydrophilic dye that stains exclusively the cells with compromised membrane integrity.[326] If intact, the membrane is non-permeant to the dye and the neurons remain translucent. As a positive control, I used the cell whose soma was damaged by pipette penetration. In Figure 6.1.2. D, I demonstrate that neurons remain transparent 10 min after the giga-seal, while the neurons with injured membranes acquire weak staining (Fig. C2, Appendix C3).

So far, the experiments concerning the mechanisms of $Ca^{2+}$ plateau generation have shown that giga-seal evokes responses regardless of solution constituents, and that the membrane integrity remains intact throughout. Another possibility is that 5 mV voltage pulses generate an electrical field that might have excited the neurons. However, the magnitude of test pulses is about 400x smaller than that required for extracellular stimulation,[327] and even there, only the slight deviations in membrane potential, not greater than 1 mV, were reported.[327] Given a good correlation of the jRCaMP1b signal with the magnitude of membrane depolarization (Chapter 5), it is unlikely that the subtle fluctuations in the electrical field from pipette test-pulses could have caused strong $Ca^{2+}$ responses. Having also ruled out the electrical component of the pipette-induced perturbation as a plausible cause of plateau generation, the main trigger comes from the mechanical component of the pipette-membrane engagement.

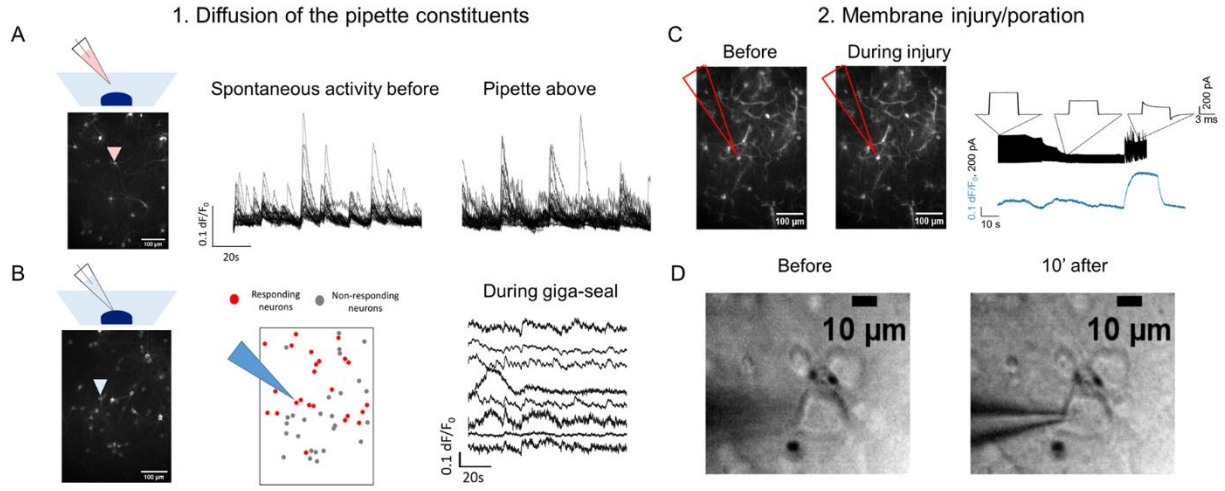


**Figure 6.1.2. Mechanisms of calcium plateau generation.** A. Pipette solution is not the main trigger of plateaus. A pipette containing the internal solution was placed above the target (pink), allowing the constituents to diffuse under overpressure. Plateaus were absent before and during the diffusion. B. Replacing internal with the bath solution (blue triangle) evoked responses during giga-seal. C. Investigating membrane injury or poration as a plausible mechanism. Left: jRCaMP1b micrograph depicting the neuron before and during the membrane injury. Right: Simultaneous pipette responses to the 5 mV, 5 ms test pulses (black) and calcium trace of the target neuron (blue). The initial contact point is followed by a slight current drop due to increased pipette resistance. Concurrently with the poration during the giga-seal establishment, current responses gain slow capacitive transients indicative of intracellular access. D. Giga-seal formation in trypan-blue. Left: Brightfield micrograph depicting a healthy neuron incubated in trypan blue before the giga-seal. Right: Brightfield micrograph of the same neuron 10 minutes after forming the giga-seal.

Which of these different, even opposing, membrane-deforming steps acts as a trigger of plateaus? As switching between the brightfield and fluorescence filter reduces the sampling rate and temporal resolution, I opted for the pipette responses to electrical 5 mV, 5 ms test pulses as an indicator of pipette-membrane interaction, while concurrently tracking the target's responses via calcium imaging (Fig. 6.1.3. A). At the start of the video, while the pipette is above the cell layer, the current responses are proportional to the pipette resistance, and the calcium trace is at a baseline (Fig. 6.1.3. A, 1). A 0.1-0.6 MΩ increase marks the initial pipette-membrane engagement, or about 6% of the current drop, (Fig. 6.1.3. A, red arrow); under the brightfield, this event coincides with an onset of dimple formation under the pipette tip, and $Ca^{2+}$ plateau development under the jRCaMP1b filter. Calcium plateaus rise as the pipette advances towards the cell, reaching the maximum around the pressure release (Fig. 6.1.3. A, blue arrow). The sharp drop in the current response with the pressure release and suction coincides with membrane protrusion inside the pipette tip, where the resistance advances until the giga-seal is formed. These combined measurements revealed that the calcium plateau onset precedes the pipette-membrane engagement by 4.4 ± 1.3 s (N = 13), when the pipette tip is positioned about 1µm above the cell. The response starts declining after the pressure release and returns to the baseline before the giga-seal was established (Fig. 6.1.3. A, 4). These suggest that membrane indentation, rather than protrusion, mediates the development of calcium plateaus.

As the plateau onset precedes the physical contact the shear stress likely represents the primary trigger of calcium plateaus. To estimate the role of the shear stress from the liquid flow, the same neuron was approached under no and increasing overpressures. Figure 6.1.3. B shows that, under no pressure, calcium plateaus are masked by spontaneous AP-associated calcium spikes and only fully developed when the neuron was approached under overpressure. As shown in Figure 6.1.3.C, plateau amplitude scales with the shear stress applied, indicating that neurons also sense the extent of mechanical stimulus. In conclusion, shear stress and the following membrane indentation are the main stimuli that promote the onset and development of calcium plateaus.

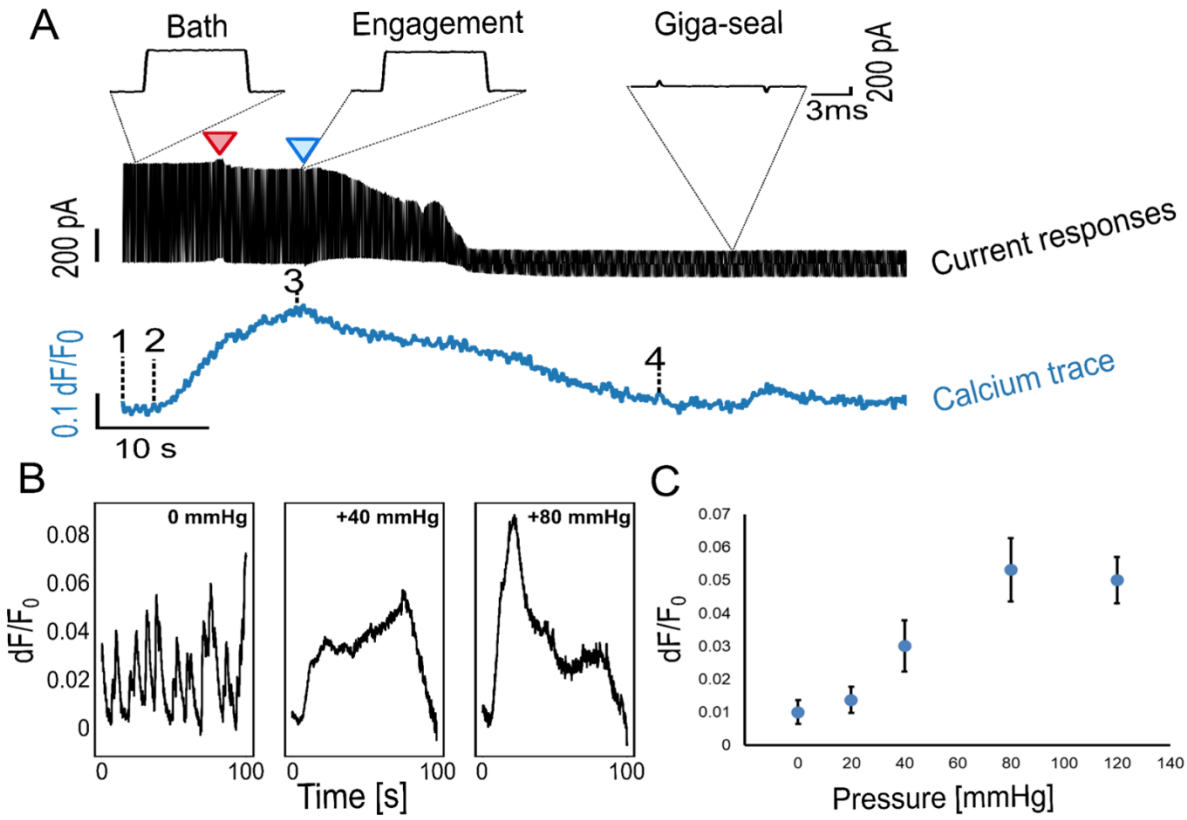


**6.1.3. Shear stress and membrane indentation evoke calcium plateaus.** A. Correlating the calcium plateau development with various stages of membrane deformation preceding the giga-seal. Black trace: pipette responses to 5 mV, 5 ms electrical test-pulses. Depicted above are zoomed-in pipette responses to individual pulses at (L to R): pipette in the bath, pipette-membrane engagement, and giga-seal formation. The red arrow marks the time point of the initial pipette-membrane engagement; the blue arrow depicts the time point of the pressure release. B. Calcium responses of the same neuron during the approaches under different overpressures. C. Calcium response amplitude as a function of overpressure magnitude (N=6); whiskers denote SEM

For 60-80 mmHg overpressure, canonically used for *in vitro* patch-clamp,[327] shear stress was experimentally determined from the effective mass loss during the long-term positive-pressure applied to the pipette in the bath. For a 45 min overpressure, the pipette flow (G) was: $G = 0.74\ \frac{nL}{s}$. The maximum exit velocity at the pipette tip is inversely proportional to pipette radius (r) and calculated as: $v = G / r^2\pi = 23.56$ cm/s. The maximum shear stress is at one pipette diameter above the perpendicular surface, and scales with velocity gradient ($dv/dz$).[328]

Assuming the water viscosity $\eta$ = 1 mPas, the shear stress is calculated as: $dv/dz \times \eta$ = 230 pN/µm. As plateaus further develop during the pipette advancement towards the cell membrane and dimple development, this estimated stress is the lower boundary. The estimated force is about 10-20x higher than localized mechanical deformations at the membrane.[41]

In summary, target neurons respond with internal calcium increases during the giga-seal formation. Calcium plateaus arise because of mechanical stimulation of the neuron during the pipette-membrane engagement. Shear stress from the liquid exiting the pipette and the following membrane indentation are the main triggers of the target's mechanoresponses. Neurons respond to deformation and sense the magnitude of the forces applied, indicating that mechanical stimulation could be precisely tuned to modulate the neuronal responses.

## 6.2. Molecular mechanisms of calcium plateau generation and development

At the cellular level, what initiates calcium plateaus? The neuronal membrane is exceptionally equipped to respond promptly to mechanical stimuli due to the expression of several species of mechanically gated ion channels. In addition to evolutionary-shaped mechanosensitive specialists,[244] many non-mechanically gated channels are shown to have mechanosensitive properties as a by-product of gating kinetics susceptible to mechanical stimulus (for review, see Morris 2011 [329], and Sukharev et al. 2012 [330]). Since different species of mechanically gated channels and mechanosensitive conductivities collectively participate in mechanical responses,[37] I first screened the calcium activity in a universal blocker of mechanosensation, gadolinium.

$Gd^{3+}$ reduces the lateral diffusion and membrane tension under mechanical stress due to strong electrostatic interactions with negatively charged phospholipid heads.[331] $Gd^{3+}$ acts as an indirect universal antagonist of mechanically gated and mechanosensitive conductivities. In 50 µM, $Gd^{3+}$ effectively reduced the plateau amplitude (Fig. 6.2.1. A, 0.05 ± 0.01, N = 20), pointing to the membrane as the first responder, and MS channels as the main initiators of responses. Notably, the attenuation was without gadolinium's interference with the target's intrinsic and synaptic excitability,[246] as both evoked and spontaneous APs were detected in $Gd^{3+}$-treated neurons. A treatment with 1 µM of Piezo-1 antagonist GsMTx4, [332] failed to reduce the plateau's amplitude (median = 0.09, IQR = 0.19, N = 31), suggesting that plateaus do not initiate via these channels.

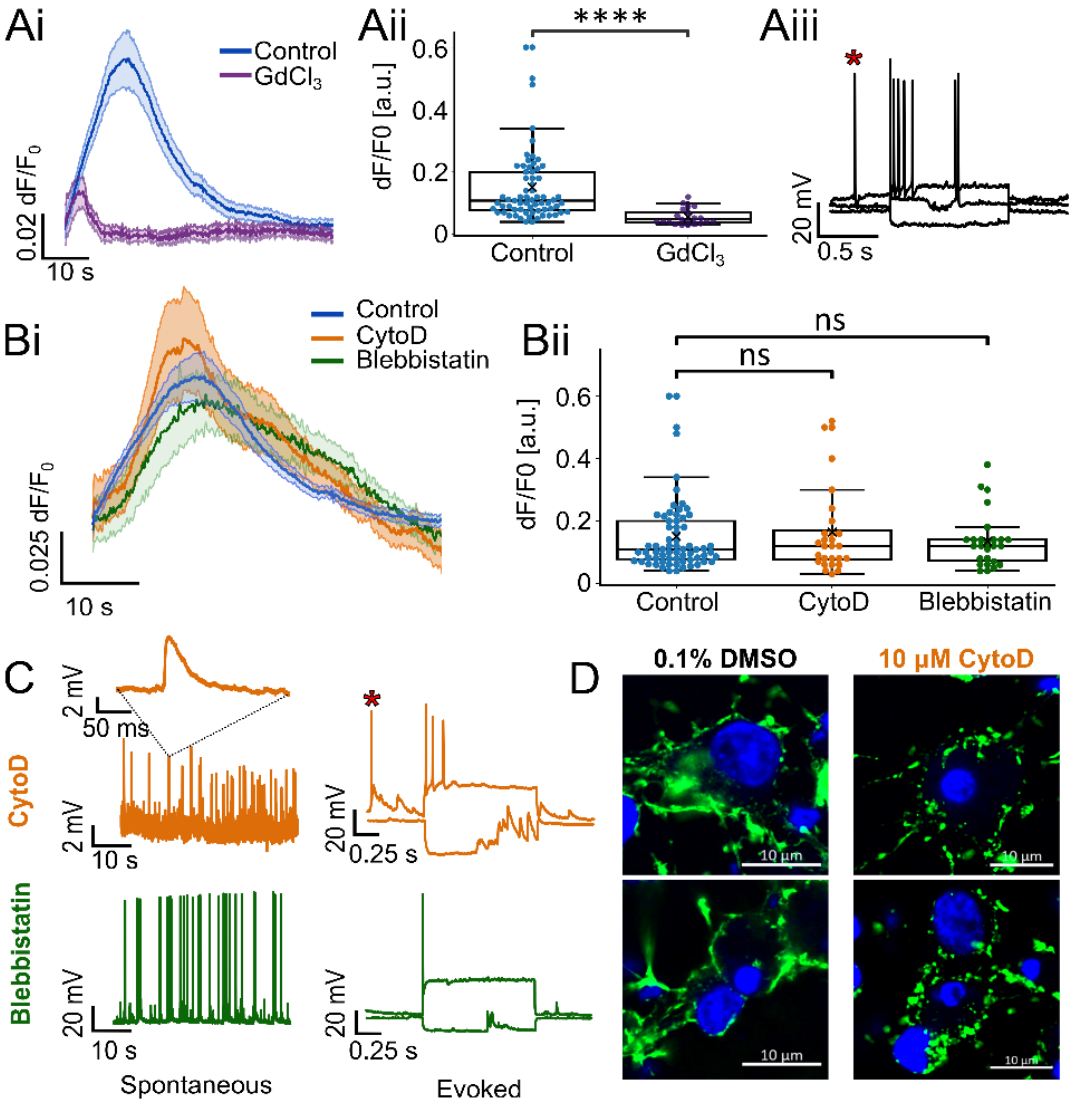


**Figure 6.2.1. The role of the membrane and cytoskeleton in calcium plateau generation.** A. Universal block of MS channels via 50 µM $GdCl_3$. Ai: averaged plateaus in control (blue) and $GdCl_3$-treated neurons (purple). Aii: plateau amplitudes in the control and treated group. Aiii. $GdCl_3$ did not interfere with spontaneous (*-ed) or evoked firing. B. Plateaus persist upon cytoskeleton disruption. Bi: averaged plateaus in control (blue), cytoD (orange), and blebbistatin (green). Shaded areas represent standard errors. Bii: Target neuron amplitudes in control, cytoD, and blebbistatin. C. Pharmacological disruption of the cytoskeleton affected neither neuronal excitability nor synaptic communication. Intracellular recordings of neurons in cytoD and blebbistatin show intact synaptic communication and excitability; spontaneous APs preceding the stimulus and post-synaptic potentials are also present (*-ed). D. CytoD treatment disrupted the actin cytoskeleton. Green: phalloidin actin staining of 0.1% DMSO control (left) and CytoD group (right); blue: counterstaining of nuclei with DAPI. Phalloidin staining was performed by Florian Friedland from IBI-2.

Since MS channels, through interaction with the actin cytoskeleton, may transduce the responses deeper into the cell,[333] I tested whether the cytoskeleton acts as a signaling scaffold in plateau development. Actin was disrupted by a long-term (> 5 h) incubation in cytochalasin D (CytoD), an actin uncoupling agent (Fig. 6.2.1. B). To confirm the actin-depolymerizing action of CytoD, actin was labeled via Phalloidin-488 and imaged by Florian Friedland from IBI-2 (details in

Section 3.2.3). Unlike the vehicle control (0.1% DMSO), CytoD-treated neurons had a disrupted actin cortex that manifested as focal fluorescence accumulations (Fig.6.2.1. D). Importantly, CytoD did not affect the neuron's ability to fire an AP (Fig. 6.2.1. C). In addition, neurons were treated with 50 μM blebbistatin (-), a non-muscle MHC II ATPase inhibitor, to test if active actin reorganization participates in plateau generation (Fig.6.2.1. B). Blebbistatin also failed to alter the neuron's excitability and spontaneous firing (Fig. 6.2.1. C). The amplitudes in treated groups were comparable to those of the control (Fig. 6.2.1. C): 0.12 (median, IQR: 0.10, N = 28) for CytoD, and 0.12 (median, IQR: 0.07, N = 26) for blebbistatin; control (median: 0.11, IQR: 0.12, N = 67). These suggest that the actin cytoskeleton is not a primary transducer of giga-seal-associated membrane deformation since it is not required for calcium plateau generation.

As discussed in Chapter 5.2, the detected $Ca^{2+}$ signal correlate strongly with the membrane depolarizing events. I first examined whether acute membrane deformation triggers APs. MEA measurements of the target neuron during the deformation showed bursting activity coinciding with the giga-seal (Fig. 6.2.2. A). Next, two consecutive contacts separated by 10 min were done to detect the target's membrane potential changes at a subthreshold resolution: the first pipette detected subthreshold changes upon deformation via a second pipette. These indicated slow depolarization associated with the mechanical stimulus, which in 2 out of 5 recordings led to the firing activity (Fig. 6.2.2. B). In voltage-clamp mode, slow inward currents were superimposed with the AP-associated fast currents. These suggest that APs are not required to develop mechanical responses, although they can be associated with acute membrane deformation. Instead, the persistent depolarization may induce firing activity upon a threshold crossing, and APs could arise due to the giga-seal formation.

The concurrent membrane depolarization suggests that responses develop through the $Ca^{2+}$ influx since the immediate charging could only be explained by the flux-mediated accumulation of cations along the cytosolic leaflet. However, MS channels interact directly with $Ca^{2+}$ leak channels from the endoplasmic reticulum,[333, 334] so I asked whether plateaus arose solely from $Ca^{2+}$ influx, mobilization from internal depoes, or both. Neurons were perturbed in nominally 0 mM $Ca^{2+}$ solution containing 2 mM EGTA to bind the residual $Ca^{2+}$ (details in Section 3.5.2). Mechanostimulation evoked plateaus in only 30% of treated neurons, and the rest had a non-significant SNR. Among the fully developed $Ca^{2+}$ plateaus, there was about an 80% amplitude decrease compared to the control (Fig. 6.2.2. C, $dF/F_0 = 0.03$, N = 15, $p < 10^{-4}$). These suggest that the plateaus are evoked by extracellular $Ca^{2+}$ entering the cell. Since previous findings report incomplete chelation of $Ca^{2+}$ bound to transmembrane proteins by 2 mM EGTA,[249] a weak signal in about a third of perturbed neurons is not surprising. However, higher concentrations of EGTA led to an abrupt $Ca^{2+}$ baseline loss, presumably due to internalization and intracellular $Ca^{2+}$ chelation. Thus, neurons were perturbed in $Cd^{2+}$ to further confirm the extracellular origin of plateaus. Cadmium is a pore-acting, universal $Ca^{2+}$ channel antagonist with a competitive binding mechanism. Due to longer pore-retention times at depolarized $V_m$, $Cd^{2+}$ displays only a partial (60%) block at the resting potential and a full block at +20 mV.[251] In 200 μM $Cd^{2+}$,

plateau amplitude reduced to 70% that of the control group (Fig. 6.2.2. C, $dF/F_0 = 0.04 \pm 0.02$, N = 19; $p < 10^{-4}$). The weak signals could be explained by an incomplete block at the resting membrane potential advancing further as the weakened plateau develops. Moreover, to test if $Ca^{2+}$ influxes were from store-operated $Ca^{2+}$ entry (SOCE), neurons were deformed in 100 µM 2-APB, a potent SOCE inhibitor. Since 2-APB did not attenuate plateau amplitudes (Fig. 6.2.2. C, median $dF/F_0$: 0.10, IQR: 0.07, N = 26; $p > 0.05$, Mann-Whitney), $Ca^{2+}$ influx is likely unrelated to internal stores.

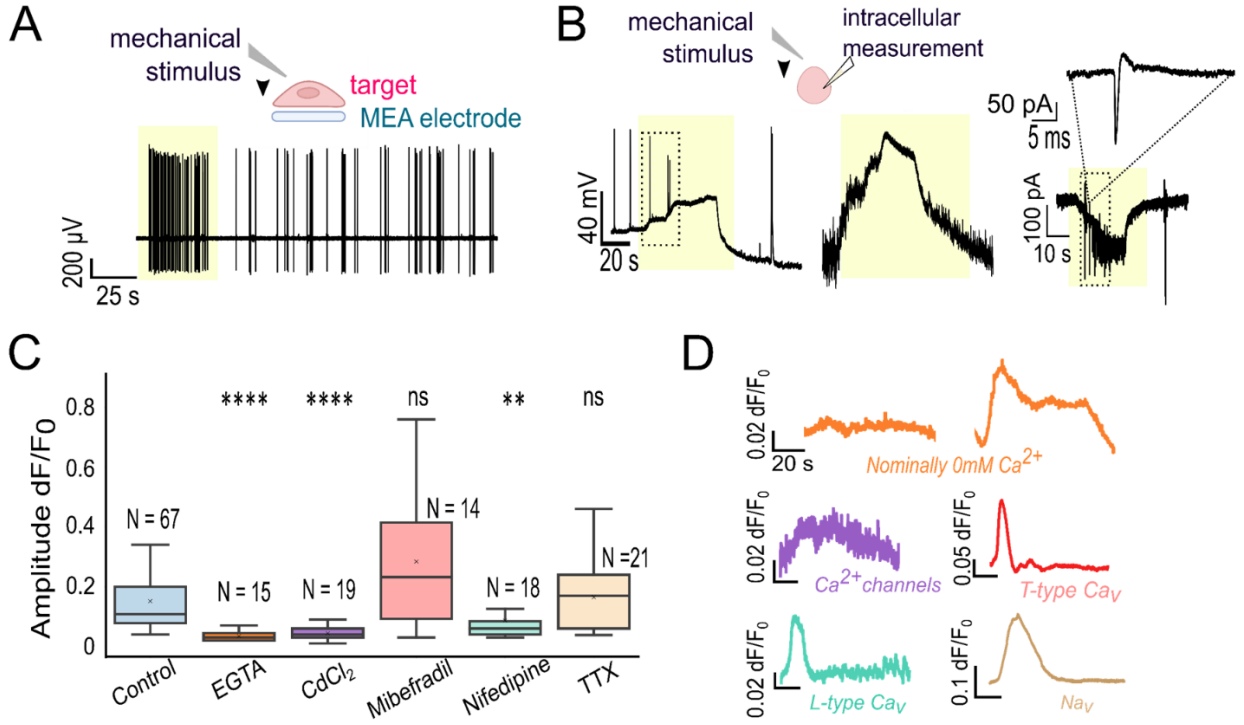


**Figure 6.2.2. Generation mechanism of calcium plateaus and ground-truth.** A. Ground-truth of mechanical responses at the target. Yellow rectangles emphasize potential changes associated with deformation. A. On-chip patch-clamp during giga-seal shows bursts of EAPs during deformation of the coupled neuron. B. Intracellular detection of responses. Current- and voltage-clamp traces showing slow depolarizations and inward currents during the mechanical stimulus, capable of inducing APs. C. Pharmacological investigations of the calcium plateau generation. Ci. Boxplots summarize plateau amplitudes of the target in control and treated groups. N denotes # of fields of view. Cii. Exemplary target traces under pharmacological treatments.

Finally, I investigated if rectifying channels participate in plateau generation and development. $Na_V$s do not transduce the signal, as $Na_V$ antagonist failed to attenuate plateaus (Fig. 6.2.2. C, $dF/F_0 = 0.16 \pm 0.02$, N = 21; $p > 0.05$, Mann-Whitney). TTX inhibited APs (Fig. 5.3.1. A) but not plateaus, confirming that these mechanoresponses do not rely on APs for a generation. Rather, mechanical responses trigger slow events whose depolarizing effect on the resting membrane potential may elicit APs. Application of Nifedipine, an L-type $Ca_V$s antagonist, reduced the amplitudes of plateaus by almost 50% (Fig. 6.2.2. C, $dF/F_0 = 0.09 \pm 0.02$, N = 18; $p < 0.05$, Mann-Whitney). These suggest that although not essential for plateau development, L-type $Ca_V$s, jointly with MS channels, participate in plateau development. Neurons were treated with mibefradil to test if T-type $Ca_V$s are required for plateau development. As this treatment did

not abolish plateaus (Fig. 6.2.2. C, $dF/F_0 = 0.28 \pm 0.06$, N = 14; $p > 0.05$, Mann-Whitney), T-type $Ca_V$s are not required for their initiation.

To conclude, neuronal membrane, but not cortical actin, is the first transducer of signaling cascades during the pipette-mediated deformation. At the membrane, calcium influx through MS and L-type (but not T-type) $Ca_V$ channels initiates the development of calcium plateaus. Plateaus develop independently of electrical signaling but manifest as slow depolarizations capable of eliciting APs.

# 6.3. Regenerative propagation of calcium plateaus

Calcium imaging in 0.2 $mm^2$ revealed about a third of 52 ± 2 neighboring somas responded to a nearby neuron patching with plateaus (Fig. 6.3.1. A, N = 67 regions, 3473 neurons). Although the responsiveness ratio varied between the trials (responders' fraction: 6-100% of the cells; Fig. 6.3.1. A), always at least some of the neighbors responded to the mechanical deformation of the target. Plateaus were detected in the neighbors a few hundred microns from the target. As the triggering stimulus for the target's plateau is shear stress, I first tested if the neighbors' plateaus are from the direct influence of the liquid flow. To estimate the extent to which the liquid flow disperses into the surroundings, individual neurons were approached by a pipette containing 0.01% FITC, which covalently binds to the primary amine groups of amino acids. If the liquid flow also affected the surrounding neurons with the magnitude that suffices for the full development of plateaus, a FITC signal in the surrounding neurons would be expected. From the micrographs of the pipette in the bath (Fig. 6.3.1. B), one can appreciate that the liquid flow under the +80 mmHg overpressure resembles the sphere of only a few µm radius. At the cell layer and under the jRCaMP1b, the neighboring somas also responded with calcium plateaus during the giga-seal of the target, however, only the target showed the FITC staining post-giga-seal. These suggest that the neighbors are not directly affected by the liquid flow and that the signal is rather propagated from the target to the neighbors.

How do plateaus propagate? The underlying mechanisms of plateau propagation could be purely passive (i.e., diffusion), characterized by signal attenuation and information loss with increasing distance from the target. Alternatively, plateaus could re-initiate within the neighbors and disperse regeneratively through the network. In either case, the dispersion of mechanoresponses could be via the extracellular route (e.g., paracrine means) or purely internal (via intracellular signaling cascades). Calcium plateaus propagated as a wave. Therefore, I extracted the propagation metrics from concentric circles around the target, with a radius corresponding to a multiplier of 30 px (46 µm), which matches the peaks in the collective inter-soma distance histogram (Fig.C3, Appendix C3). For every circle around the target, the fraction of responders, plateau propagation velocity, and plateau amplitude distribution were investigated.

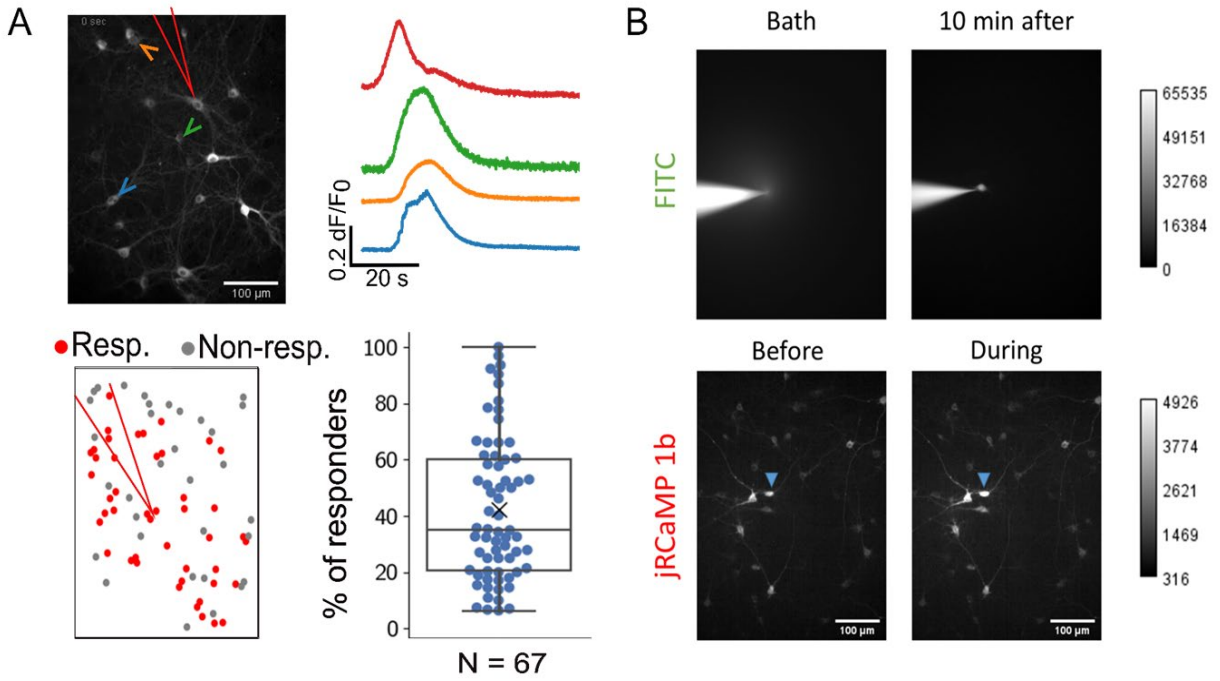


**Figure 6.3.1. Calcium plateaus propagate through the network.** A. Somatic plateaus in 0.2 mm$^2$ during the giga-seal at the target (red triangle). Top: jRCaMP1b signal and example ROIs marked with colored arrows. Bottom: a schematic of responding ROIs and fraction of responding neurons in 0.2 mm$^2$. B. Extent of flow vs. extent of plateaus. Top: Pipette flow under +80 mmHg, labeled with FITC – with pipette above the cell layer (left) and post-giga-seal. Bottom: jRCaMP1b signal from the same region, before and during the giga-seal. The calibration bars on the right depict the pixel intensities. Scale bars are universal to bottom and top micrographs.

Although the responders' ratio fell with increased distance from the patched neuron ($p<10^{-3}$, N = 67, Kruskal-Wallis), even the closest circle contained about 20% of non-responders (Fig. 6.3.2. Aii). Responding neighbors did not follow a simple radial distribution around the target, and it is unlikely that propagation follows a gradient of a soluble molecule. The average propagation velocity of 50 µm/s was several orders of magnitude slower than that of AP-associated events and comparable the neurons' slow calcium waves[301] or mechanically induced calcium waves in astrocytes.[319] There was no significant difference in velocities across the successive concentric circles: 51.9 ± 11.5 µm/s (1$^{st}$ circle), 56.3 ± 10 µm/s (2$^{nd}$), 53.3 ± 8.8 µm/s (3$^{rd}$), 47.3 ± 6.4 µm/s (4$^{th}$), 54.7 ± 12.1 µm/s (5$^{th}$) (Fig. 6.3.2. Aiii, $p > 0.05$, N = 67, Kruskal-Wallis). This perseverance in velocity favors the regenerative dispersion over passive diffusion since, in the latter, it is also dictated by the concentration gradient. Calcium plateau amplitude declined as the calcium wave propagated away from the target (Fig. 6.3.2. Aiv, $p < 10^{-2}$, N = 67, ANOVA), with $\Delta F/F_0 = 0.11$ within the first circle to $\Delta F/F_0 = 0.08$ in the fifth. However, the amplitude drop was not steep but rather asymptotic, as the amplitudes of the last two regions remained consistent (Fig. 6.3.2. Aiv).

Since some responders were on the edges of a 0.2 mm$^2$ field of view, I determined the plateau propagation extent in a larger (3 mm$^2$) area (Fig. 6.3.2. B). Both the technical and computing limitations affected the temporal resolution in 3 mm$^2$. Firstly, an air objective was used to scan

the larger fields of view; due to light dissipation, more prolonged exposure is necessary to obtain the fluorescence signal. A higher number of pixels per frame consumed more RAM, already loaded by simultaneous electrophysiology and imaging measurements. Both were accommodated by an increase in exposure time, resulting in a 25-33 Hz sampling rate. The lower temporal resolution of larger field-of-view recordings allowed only accurate estimates of the calcium plateau propagation extents and amplitude trends. As with the local area recordings, the fraction of responding neurons dropped further from the target, with an average end-boundary of about 730 µm (Fig. 6.3.2. Biii). As with 0.2 $mm^2$ fields of view recordings, the amplitude asymptotically dropped and remained consistent from the fourth circle (Fig. 6.3.2. Biv). The last responding circle contained neighbors that either responded or did not respond with fully developed calcium plateaus (Fig. 6.3.2. Bii). In summary, these observations favor regenerative propagation over passive diffusion since: (1) there was a spatially specific distribution of responding neighbors, unlike the simple radial distribution typical for the diffusion of a generic messenger; (2) plateau amplitude did not exponentially drop with increased distance from the target, which would indicate a gradient-dependent passive propagation; (3) propagation velocity persisted across different distances from the target.

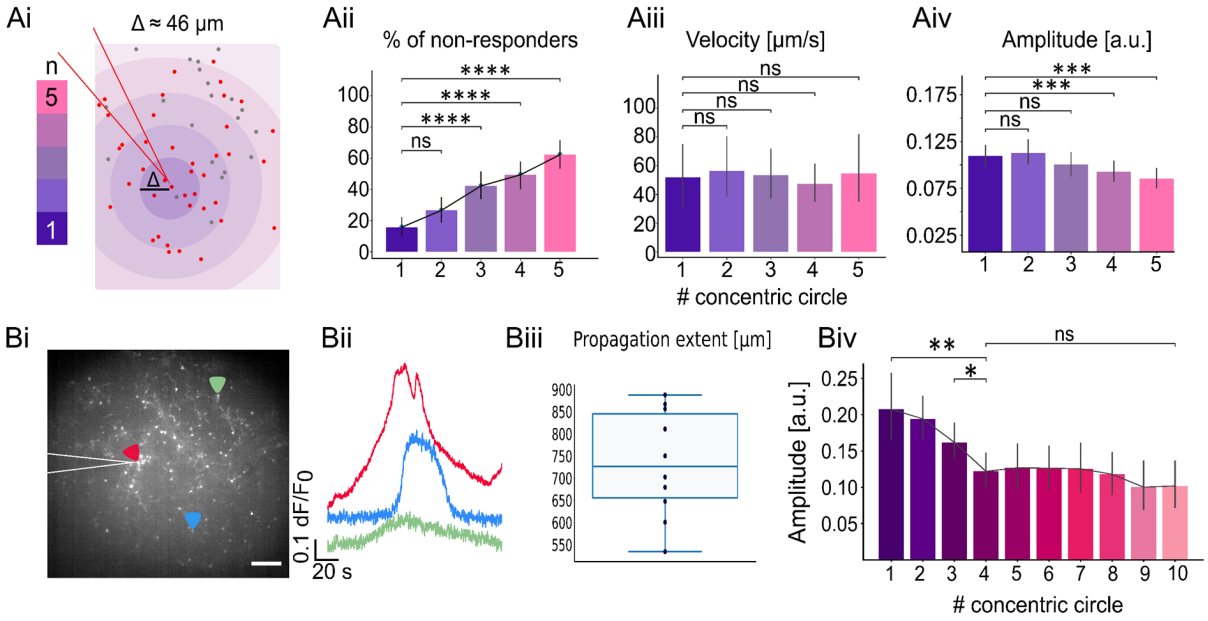


**Figure 6.3.2. Plateaus propagate regeneratively through the network.** Long triangles point to the target in all plots. A. Somatic plateaus in 0.2 $mm^2$ during the single-neuron deformation. Ai. Schematics of the network responses (red) around the target. Propagation parameters were extracted from concentric circles of a common multiplier radius (Δ). Aii. Non-responding fraction vs. distance. Aiii. The velocity of the waves crossing successive concentric circles. Aiv. Amplitude distribution around the target. B. Propagation parameters extracted from a 3 $mm^2$ network. Bi. jRCaMP1b micrograph with marked ROIs, including the target (red) and neighbors near the edges of the propagation extent (green, blue). Scale bar: 200 µm. Bii. Exemplary traces of the ROIs in Bi. Biii. A combined box and swarm plot summarizing the maximum propagation extent in 3 $mm^2$. Biv. Amplitude distributions with increased distances from the target.

Although the functional imaging was performed with spatial resolution lower than conventionally used for detection of the neuritic signals (0.645 px/µm), in ¼ of trials (18 of 67), the calcium signal from the neurites of the target was distinct and well-isolated from the background. In these recordings, the target neuron's plateaus initiated at the soma but persevered through the neurites and propagated to the neighbors (Fig. 6.3.3. A). While the plateaus at the neighbor's somas were comparable to those of the target, the target's neuritic signals were 26 ± 3% of the somatic plateaus (N=18). The apparent drop could be attributed to a reduced reporter expression in the neurites.[335] The precise estimation of intra-neurite propagation velocity was prevented by a low time resolution and reduced SNR.

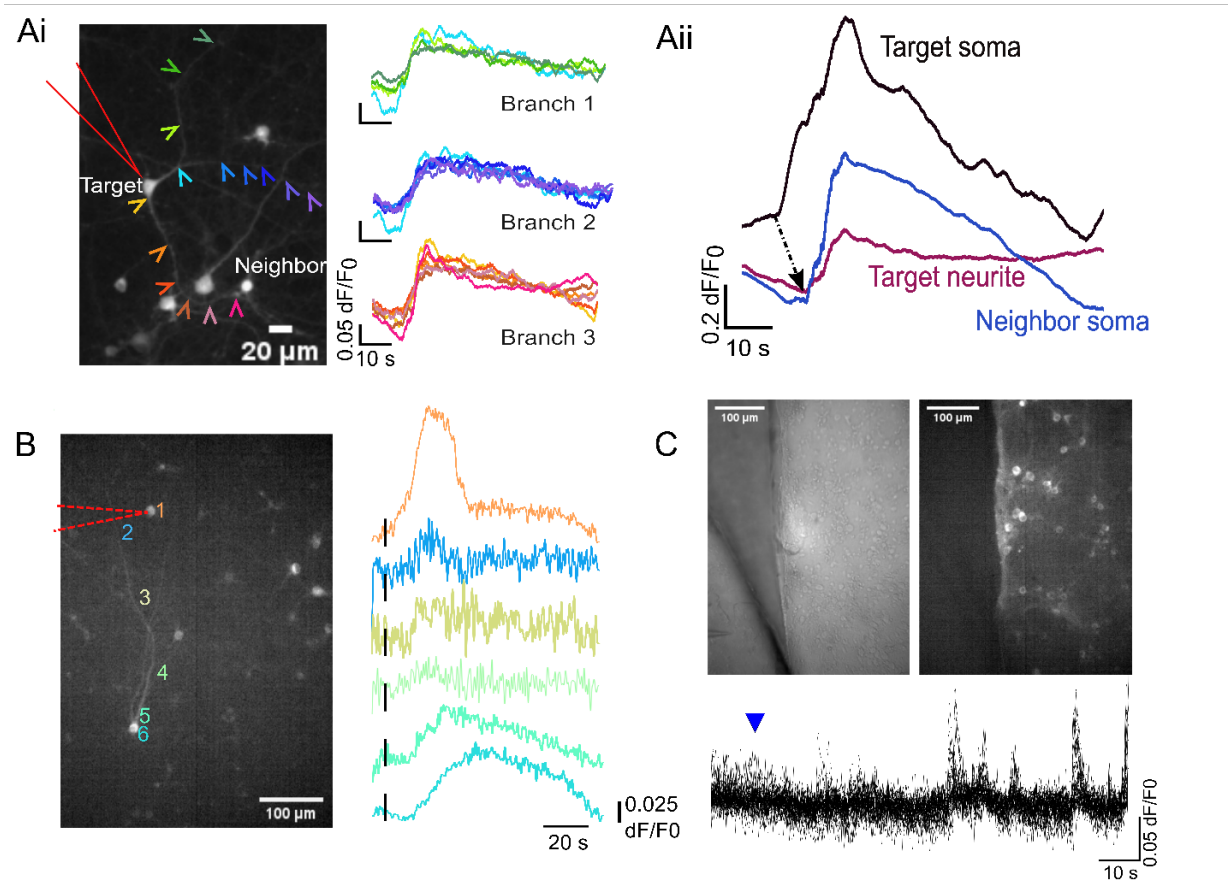


**Figure 6.3.3. The propagation route is via physical connections.** A. Plateaus persist through the neurites of the target. Ai. Neurite calcium signals. Left: Target soma (red triangle), neurite branches (arrows), and responding neighbors. Bottom scale: 20 µm. Right: Plateaus from three neurite branches of the target. Aii. Plateau propagation from the soma through the neurites to the visibly connected neighbor. Somatic (black) and neuritic (purple) responses of the target and somatic response of the neighbor (blue); arrow marks onsets. B. Plateau propagation from the target's soma (red triangle) through the neurite and the soma of the neighbor. Left: jRCaMP1b micrograph. Numbers denote positions of ROIs whose traces are on the right. The dashed line marks the target's plateau's onset. C. Two-coverslip experiments. Top: brightfield and jRCaMP1b micrograph. Coverslips were in different focal planes. The left coverslip contained the mechanically stimulated neuron, while the calcium imaging was focused on the right coverslip. Bottom: $Ca^{2+}$ traces during the mechanical stimulation of the neuron on the top left. The blue arrow marks the time point of the stimulation.

Nonetheless, the somatic signals always preceded the neuritic ones. The rough estimations of intra-neuron propagation velocity could be inferred from delays of somatic calcium plateaus and at the farthest point in neurites led to estimates of 44.3 ± 9.1 μm/s (N = 18). Likewise, in neighbors with distinct neurite signals, calcium plateau propagated through the neighbor's neurites and to the soma (Fig. 6.3.3. B), with similar velocity: 46.1 ± 9.9 μm/s (N = 18). These suggest that calcium plateaus take the intracellular route, defined by morphological connections. To confirm that paracrine communication is not involved in the process, I performed a two-coverslip experiment in which two morphologically separated neuronal networks were positioned within a 0.2 $mm^2$ field of view. If plateaus propagated exclusively via intrinsic pathways, the responders would distribute only across the morphologically coupled network but not within a network on another glass coverslip connected only by the medium. Otherwise, the diffusion of a soluble agent within reach of the second network would induce the responses on another coverslip. The absence of responses in proximal but non-connected networks confirms that mechanical responses propagate through morphological connections (Fig. 6.3.3.C).

In summary, mechanical deformation of individual neurons during the giga-seal affected the target and about a third of the surrounding neurons, hundreds of microns away. Excitation of the local network was not due to simultaneous mechanical stimulation of the nearby neurons since the liquid flow from the pipette was exclusively limited to the target neuron. Instead, plateaus persist within the neurites and propagate through the target to the morphologically coupled neurons, where they re-initiate.

# 6.4. Gap junctions propagate plateaus

Considering the morphologically-defined route of calcium plateaus, I investigated if synapses or APs mediate inter-neuronal propagation. Synapse involvement was first tested in an antagonist cocktail of ionotropic post-synaptic receptors, in the further text referred to as cocktail #1. Cocktail #1 contained (in μM): NBQX (20; blocks AMPARs), D-AP5 (80; blocks NMDARs), and bicuculine (20; blocks $GABA_A$Rs). Figure 6.4.1 shows that this treatment did not attenuate calcium plateaus nor reduce the number of responding neurons (fraction: 67 ± 4%, N = 26). Besides the ligand-gated ion channels, post-synapses are also equipped with neurotransmitter-sensitive metabotropic receptors, capable of transducing and amplifying the information within the recipient. To entirely eliminate synaptic transmission as a plausible mechanism for inter-neuron plateau propagation, neurons were treated by blockers of metabotropic receptors and the constituents of cocktail #1. Cocktail #2 also included (in μM): AIDA (200; blocks Type I mGluRs), CPPG (200; blocks Type II/III mGluRs), and CGP 55845 (10; blocks $GABA_B$R). Adding metabotropic receptor antagonists also failed to attenuate or reduce the fraction of plateauing neighbors (fraction: 66 ± 5%, N = 22), further confirming that synapses are not required for plateau propagation. Applying TTX to block APs also did not reduce the fraction of responding neurons (34 ± 4%, N = 21, $p > 0.05$). These confirm that neurons propagate plateaus independently of the AP generation and chemical synapses.

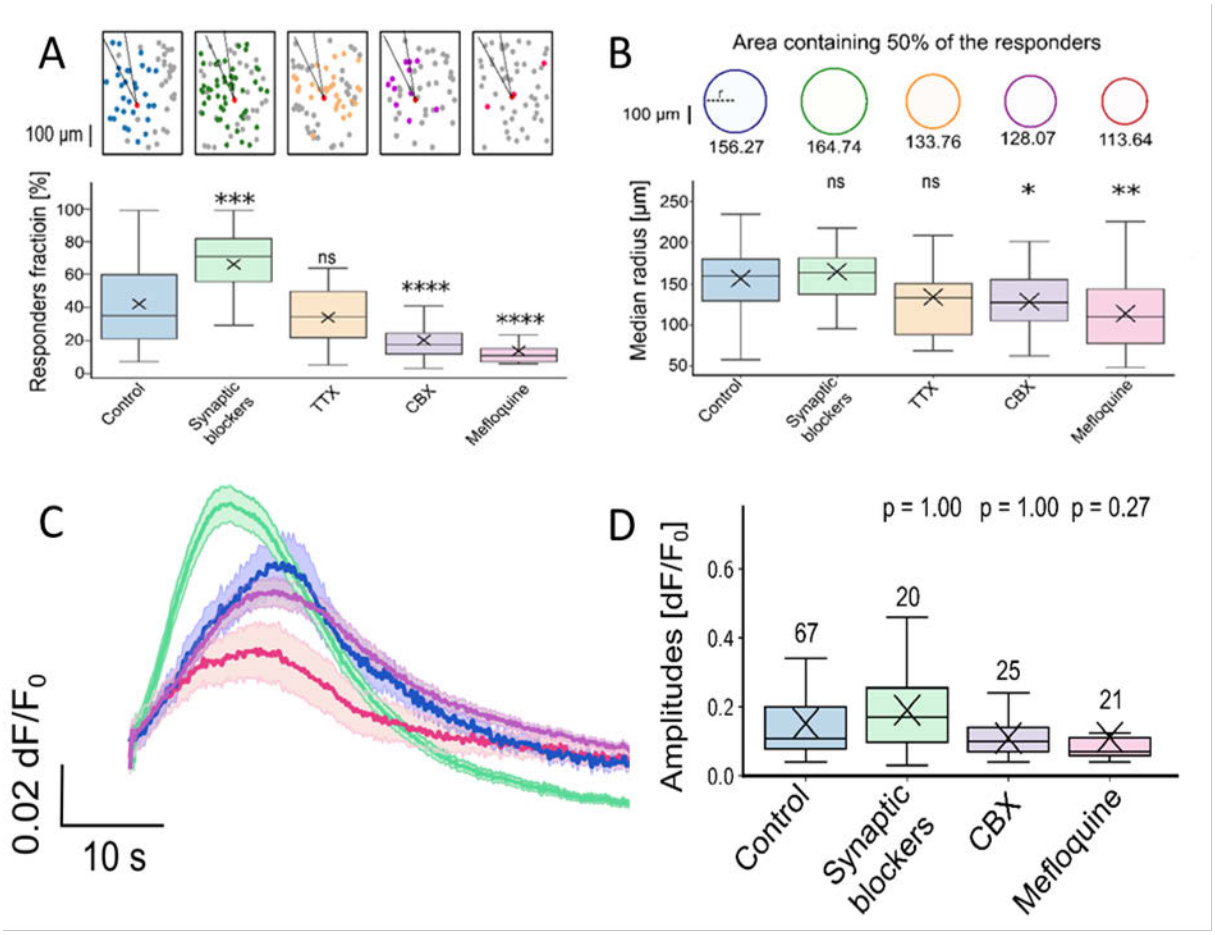


**Figure 6.4.1. Pharmacological treatments to investigate mediators of propagation**. A. Fraction of the responders in 0.2 $mm^2$ in control (blue), synaptic blockers (green), TTX (yellow), CBX (purple), and mefloquine (pink). Top: representative schematics of 0.2 $mm^2$ network depicting relative distributions of responding (color) and non-responding neighbor (gray) upon a target neuron (red) deformation. The color-code matches the boxplot below. Bottom: Fraction of responding neurons in 0.2 $mm^2$. B. Propagation extent upon different pharmacological treatments. Top: Areas around the target containing 50% of the responding assembly, colored to match the boxplot. Numbers depict the average circle radii in µm. C. Calcium plateau amplitude upon different pharmacological treatments. C. Mean plateaus aligned to onsets with a shaded area corresponding to SEM. The color code matches the box plots. D. Plateau amplitude distribution in control, synaptic, and gap junction blockers. The numbers above whiskers indicate the sample size, top: p-values from the two-tailed Mann-Whitney test with Bonferroni correction.

On a side note, both cocktail treatments significantly increased the fraction of responders compared to the control ($p < 10^{-3}$ for cocktail #1 and $p < 10^{-4}$ for cocktail #2). Since synapses represent the main route of information transfer, one plausible mechanism was that the increase in the local network's responsiveness was only apparent due to network silencing and de-masking of the weak calcium plateaus. An even higher fraction of weak plateaus in the control group suggests that synapse silencing impacted the mechanisms underlying the plateau propagation (Fig. 6.4.2. A). Alternatively, the superposition of inhibitory inputs with the plateau-associated membrane depolarization attenuates the neighbors' responses, and removing inhibition eliminates this superposition. However, treatment with bicuculine only failed to increase the fraction of responding neurons (median: 29%, IQR: 30%, N =15, $p > 0.05$), suggesting rather

that glutamatergic inputs and mechanical responses are temporally exclusive. This was further supported by the observation that, during the mechanical stimulation of individual neurons, AP-associated calcium spikes and SNEs were anti-correlated with plateaus (Fig. 6.4.2. B). A similar temporal exclusion was reported for spontaneous, non-synaptic plateauing events and synapse-driven calcium spikes in developing post-natal hippocampal slices.[85] Although yet to be characterized, the cascades underlying the mutual exclusion of SNEs and plateaus likely belong to synaptic homeostatic mechanisms that downregulate the internal calcium to prevent excitotoxicity and preserve input-specific scaling of synaptic weights.

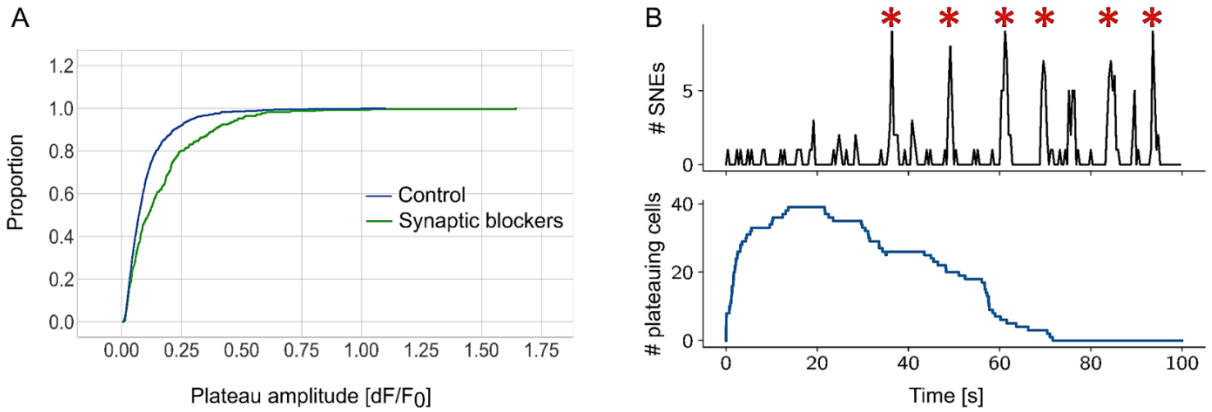


**Figure 6.4.2. Calcium plateaus and SNEs are temporally exclusive.** A. Amplitude distribution of calcium plateau amplitudes in control (blue) and synaptic blockers (green). B. Plateaus and SNEs are anti-correlated. Top black: A histogram of AP-associated calcium spikes. Bottom: A histogram of plateaus time aligned to calcium spikes. Red stars mark the occurrences of SNEs, whose onset overlaps with the end of calcium plateaus.

As recent findings point to the ubiquitous presence of constitutive[336] and activatable gap junctions [97] *in vitro* and *in vivo*, I tested if they mediate the propagation of mechanical responses. I first probed gap junctions via tracer injection and paired electrophysiology. Details of the tracer injection procedure are given in Chapter 3.2.4. Briefly, Neurobiotin was electrodiffusively administered through the pipette in the whole-cell through a 5-10 min injection of 500 ms current pulses at 1 Hz. Following a 1-2 h incubation to allow the diffusion into the neurites and electrically coupled neurons, cells were fixed and visualized by Streptavidin-Alexa 488 (1:300) conjugate. The fluorescence signal in the target and the neighbors demonstrated physical coupling, as the tracer diffuses to the neighboring neurons exclusively through open hemichannels (Fig. 6.4.3. A).

The intracellular measurements of proximal pairs of somas were made to test the presence of functional electrical synapses. Double whole-cell recordings were performed in antagonist cocktail #1 to silence the primary synaptic transmission. Although the work of A. Vogt [337] and others [76, 338] showed that APs also propagate to the electrically coupled neurons, in the neighboring soma, they often manifest as spikelets[337] that have several origins.[162, 305] Instead, the two neurons were regarded as GJC coupled only if a subthreshold voltage change propagated from the stimulated to the non-stimulated neurons and if propagation was bi-directional. In a

current-clamp mode, the current injection in the target evoked the same-sign, but attenuated voltage response in electrically coupled neuron, and vice versa (Fig. 6.4.3. Bi). Upon a voltage injection, the neighbor's currents were of opposite sign, reflecting the neighbor's charging when the stimulated neuron discharged, and vice versa (Fig. 6.4.3. Bii).

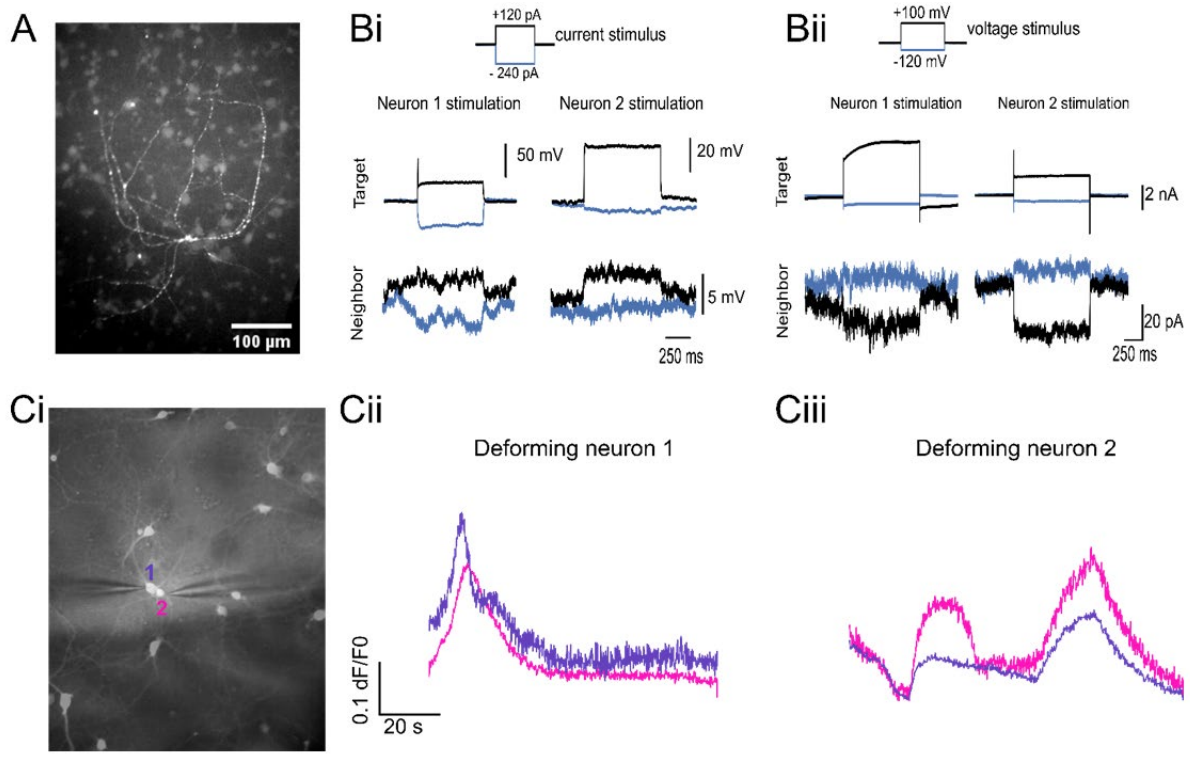


**Figure 6.4.3. Confirmation of the gap junctions in dissociated networks of cortical neurons.** A. Streptavidin-Alexa 488 signal following the Neurobiotin injection. B. Confirmation of electrical coupling by paired whole-cell. Bi. Current-clamp injections in neuron 1 produced attenuated, same-sign voltage deflections in neuron 2 (left) and vice versa (right). Bii. Voltage injection in neuron 1 evoked attenuated, but opposite sign current in neuron 2 (left), and vice-versa. C. Bidirectional responsiveness upon consecutive mechanostimulation. Successive stimulation of 1 neuron evoked calcium plateaus in the neighbor and vice versa.

There are several disadvantages in the approach above for quantifying the % of GJC-coupled neurons. Due to the space-clamp issue, paired whole-cell reliably confirms the GJC coupling within proximal pairs of neurons, for instance if neurons were GJC coupled at their somas.[339] First, electrotonic events that arise by current injection attenuate as they passively propagate from injected somas to the neurites. The space-clamp issue could be partially reduced by artificial increase of the membrane resistance, such as perfusion with CsCl,[340] however I avoided this approach to preserve the native state of the neurons. Nevertheless, I demonstrated functional GJCs in our *in vitro* system in a proof-of-concept fashion. Additionally, consecutive mechanical deformations of neuron pairs show cross-responsiveness and bi-directional propagation of mechanoresponses, pointing to reciprocity typical for gap junctions.

Neurons were treated with GJC uncoupling agents to test if previously confirmed GJCs mediate propagation of the mechanical responses. Without affecting the amplitude (Fig. 6.4.1 C-D),

connexin antagonist carbenoxolone (CBX) led to ca. 50% decrease in the responding neighbors (median: 17%, IQR = 13%, N = 29, $p < 10^{-4}$), while the more potent antagonist mefloquine reduced the fraction of responding neurons by 70% (median: 10%, IQR = 8%, N = 22, $p < 10^{-4}$) of the control. Among the treatments, only the block of gap junctions effectively reduced the propagation extent of calcium plateaus (Fig. 6.4.1. B). Accordingly, even the closest surrounding contained ca. 36% of the non-responders in CBX, and 40% in mefloquine.

Overall, pharmacological interventions showed that APs and synapses are not required to propagate calcium plateaus. A higher network's responsiveness following synaptic block and anti-correlation between synaptically-driven calcium spikes and calcium plateaus suggest that these events are temporally exclusive. Following confirmation of GJCs *in vitro*, pharmacological block of GJCs effectively reduced the local network's responsiveness and pointed to connexins as a main route for intercellular information transfer of mechanical responses. The current model proposes the exchange of secondary messengers, which propagate via the GJCs to re-initiate the plateau in the recipient.

# 6.5. Calcium plateaus propagate through the ensemble

Since giga-seal-associated plateaus are readily detected by local-network calcium imaging, the goal was to assess if responders belonged to a subpopulation of functionally connected neurons by examining whether they form a module within the local network. The second part compares the efficacy of single-neuron deformation vs. electrical stimulation for neuronal ensemble mapping via calcium imaging.

First, I tested how the spontaneous calcium activity of responders and non-responders correlates to the target prior to the mechanical stimulation. As shown in Figure 6.5.1. A, the average correlation coefficient between the target and plateauing neighbors (median: 0.10, IQR: 0.08, N = 24) was 10x higher than between the target and non-responders (median: 0.01, IQR: 0.03, N = 24; $p < 10^{-4}$, Mann-Whitney). The greatest level of activity overlap occurred during synchronous network events, with nearly half of the non-responders engaging in SNEs (Fig. C4, Appendix C3). Although a higher correlation of spontaneous calcium activity indicates a higher connection probability,[13] even non-coupled pairs of neurons synchronize during SNEs.[14]

To account for the spurious correlations from network synchrony, connectivity was directly probed via paired whole-cell recordings following the mechanical stimulation. Based on the membrane (Section 6.6) and calcium responses (Section 6.3) during the giga-seal deformation of the target, neighbors were classified as responding or non-responding. Details of the procedure and criteria for definition of synaptic coupling are given in Section 3.3.5. Briefly, the spontaneous activity of a neuron was monitored during the current injection of another neuron; using the criteria of Vogt 2003,[337] PSPs $\geq$ 0.1 mV in amplitude and with $\leq$ 10 ms latency were classified as monosynaptic connections. The procedure was repeated *vice-versa* to test if there was a connection in the other direction. In total, the pooled fraction of coupled neurons (53%, N

= 19)[10] is in the range of previous estimates of the network connectivity for *in vitro* cultures of dissociated cortical neurons.[147, 342]

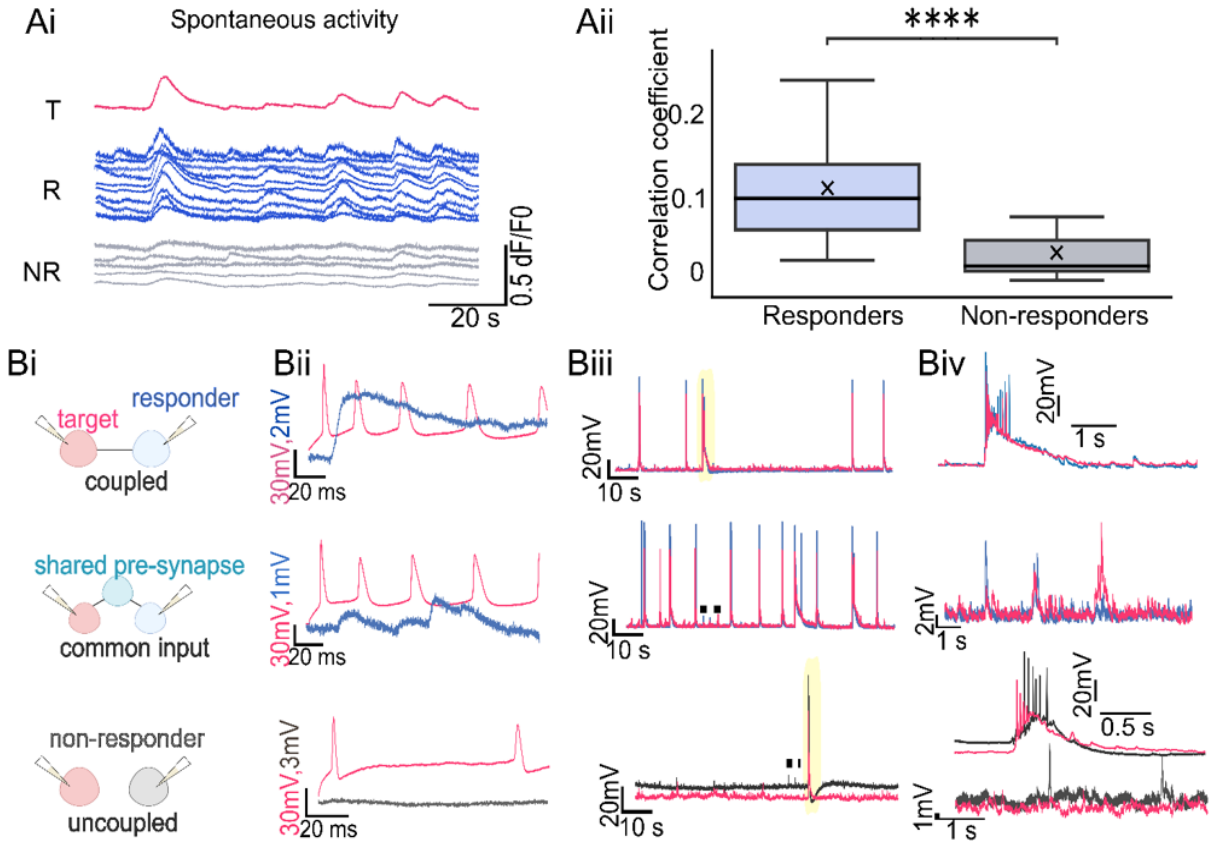


**Figure 6.5.1. Mechanical responses propagate through neuronal ensemble.** A. Functional connections from calcium imaging of spontaneous activity prior to giga-seal. Ai. $Ca^{2+}$ traces of the target (T), responders (R), and non-responders (NR) before the giga-seal. Neurons were categorized as R/NR after their responses to the target deformation. Aii. Cross-correlation coefficients from the pairwise correlation of the spontaneous $Ca^{2+}$ spikes. B. Direct connectivity estimates via paired whole-cell following the deformation of the target. Bi. Schematics of different recording configurations; neurons responding to a neighbor's deformation (top and middle) are in blue, and non-responders are in gray. Bii. Neighbor's responses to electrically evoked pre-synaptic APs. Rows match schematics depicted in Bi. Biii. Spontaneous activity detected intracellularly from two patched neurons. Biv. Focus on bursting events (yellow in Biii) or individual PSPs (dotted in Biii).

In monosynaptically connected neurons (N = 10), the firing of a pre-synaptic neuron evoked 0.7 ± 0.2 mV PSPs with a 3.9 ± 1.3 ms delay. As depicted in Figure 6.5.1. B, electrical stimulation of the target evoked time-locked PSPs but failed to produce APs. Among the benchmarked neuronal pairs, only the ones that responded to each other's mechanical deformations had monosynaptic connections. Of 13 pairs belonging to the responding assembly, 10 were bi- (N = 3) or unidirectionally coupled (N = 7) (Fig. 6.5.1. B, first row). The other three pairs lacked a direct connection (Fig. 6.5.1. B, middle row), but their spontaneous activity was highly synchronized. Figure 6.5.1. Biii-iv show synchronization not only at the level of individual

[10] The reported fractions consider the number of coupled neuron pairs, not connection probabilities.[341]

bursts but also at individual PSPs, indicating a shared pre-synaptic neighbor. In contrast, non-responders were neither monosynaptically coupled to the target, nor shared spontaneous events beyond bursts (N = 6, Fig. 6.5.1. B, bottom row).

As the target neuron electrical stimulation induced post-synaptic potentials that are seldom visible in calcium traces (Section 5.3.), I evaluated how reliably electrical stimulation identifies synaptically coupled neurons via calcium imaging. A subset of 5 out of 13 confirmed synaptic connections was complemented by calcium imaging during the current injection of the pre-synaptic neuron to benchmark the sensitivity of calcium imaging for connection mapping (Fig. 6.5.2. ). Target responded with plateau-like calcium elevation and showed well-defined STAs (Section 5.3). Unlike the mechanically evoked calcium plateaus, electrically-evoked calcium elevations did not propagate to neighbors (Fig. 6.5.2. Aii, Bii); coupled neurons otherwise showed distinct but attenuated calcium STAs.

Without the ground truth, a neighboring neuron is considered to be coupled to the target if its calcium STA crosses the soft threshold of 2.3 SEM, to discard spurious connections from noise averaging (Figure 3.6.6. A, details in Section 3.6.6). The same averaging on sham stimulation (Figure 3.6.6. A) showed only 0.7% of false positive connections, which was several-fold smaller than the fraction of connections estimated during the electrical stimulation of the target (12.4%, Fig. 6.5.3). However, paired benchmarking indicated that such criterium risks omitting weak synaptic connections, since three out of five post-synaptic neighbors had below-threshold STAs (Fig. 6.5.2. B). The magnitudes of calcium and membrane STAs correlated linearly (Fig. 6.5.2. C, $R^2 = 0.9$, $p < 0.05$, Pearson's), indicating that functional connection mapping by electrical stimulation was not only restricted to the out-connections of excitatory targets, but the threshold of detection depended on the coupling strength.

Although the calcium STAs for the other 11 connections were not benchmarked by joint calcium imaging during the current injection at the pre-synapse, the sensitivity of calcium imaging could be extrapolated as follows. Calcium STA magnitudes were estimated from post-synaptic neurons' membrane responses according to the linear membrane-calcium STA relation (Fig. 6.5.2. C). As a visibility criterium, a $90^{th}$ percentile of population-level calcium STA threshold was used instead of a cell-specific soft threshold (Fig. 6.5.2. D). Thus, the post-synaptic neuron's STA was considered as above-threshold if its magnitude was above the population-level STA threshold. Estimated this way, the only 6 out of 13 postsynaptic neurons showed supra-threshold STAs, indicating that over half of out-connections could not be reliably detected by calcium imaging and averaging of electrically-evoked post-synaptic responses.

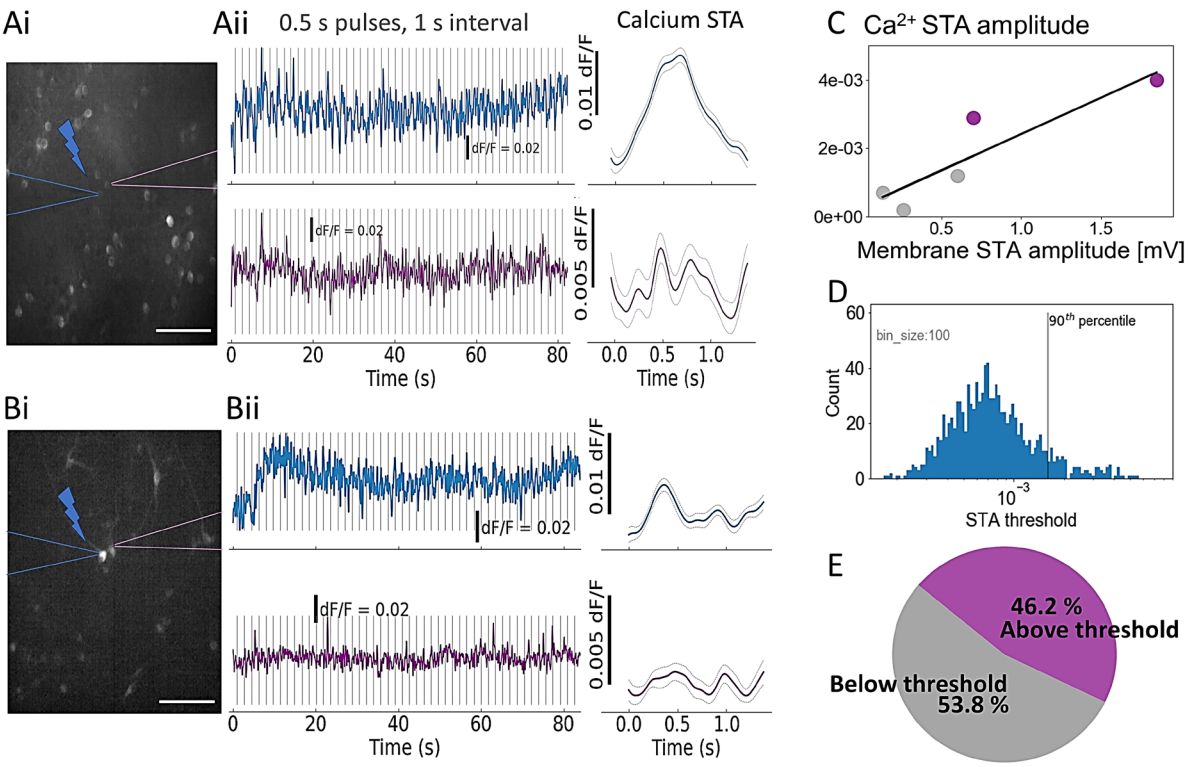


**Figure 6.5.2. Calcium and membrane responses to a coupled neighbor's electrical stimulation.** A. Strong synaptic connections give rise to above-threshold calcium STAs. B. Weak synaptic connections give rise to below-threshold STAs. Ai, Bi. jRCaMP1b micrograph of stimulated (blue) and coupled neuron (purple). Scale: 100 µm. Aii, Bii. $Ca^{2+}$ traces and STAs of the target and neighbor. C. Membrane vs. $Ca^{2+}$ STA magnitudes in post-synaptic neurons. Gray dots denote coupled neurons with below-threshold $Ca^{2+}$ STAs. D. Histogram of 2.3 SEM calcium STA thresholds. As a threshold, the 90$^{th}$ percentile was set as a universal boundary. E. Pie chart of above and below threshold $Ca^{2+}$ STAs of truly connected post-synaptic neurons (N = 13).

Network responses were investigated with calcium imaging during the single-neuron deformation, then electrical stimulation to estimate how the plateauing ensemble maps onto the electrically identified, putative out-connections. Neuronal ensembles during giga-seal were identified by single-time calcium plateaus in the neighbors, while current injection mapping was via comparison of averaged neighbors' responses to a cell-specific soft threshold (Section 3.6.6).

As shown in Figure 6.5.3. A, neighbors that showed significant calcium STAs during the electrical stimulation also responded to the target's deformation. On average, only 12.4% of the neighbors were identified to respond to a single-neuron electrical stimulation. This is ca. 4x less than the fraction of the neighbors responding to the deformation of the same target (Fig. 6.5.3. B, $p < 10^{-4}$, paired t-test). A reduced network's responsiveness to a single-neuron current injection arises from the joint effects of exclusively mapping the output connections and a high false negative incidence from STA thresholding. Unlike electrical stimulation, detectable calcium influxes from the neighbor's deformation show a higher spread (Fig. 6.5.3. B, $p < 10^{-2}$, paired t-test), indicating that mechanical stimulation of individual neurons could reliably map a broader boundary of the neuronal ensemble.

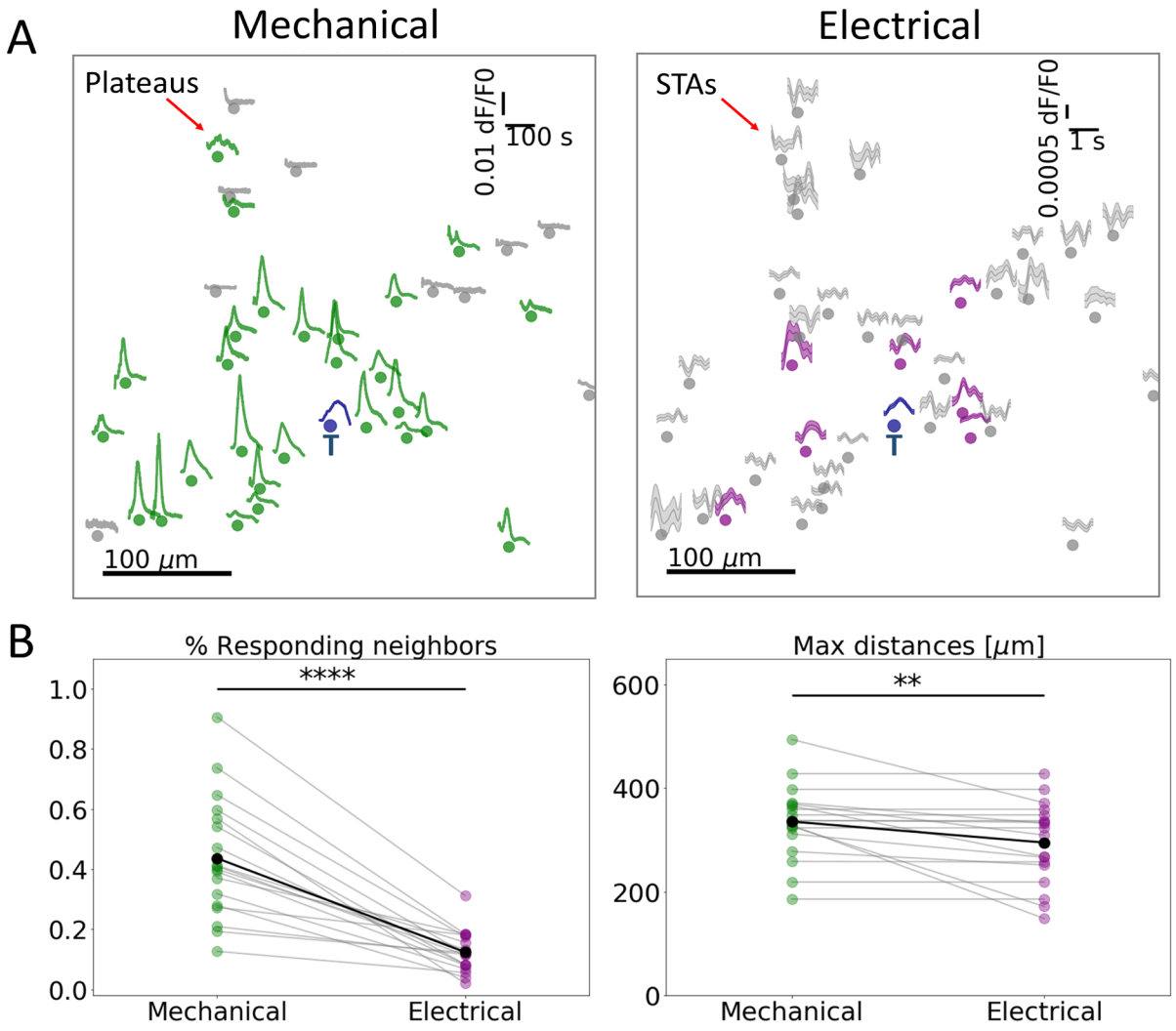


**Figure 6.5.3. The effects of single-neuron mechanical and electrical stimulation on network calcium.** A. Schematic of the local network's responses to giga-seal (left) and current injection (right) to the target (T). Dots denote the location of the target and neighbors, and waveforms denote full $Ca^{2+}$ traces (left) and $Ca^{2+}$ STAs (right). B. Fraction of responding neurons and maximal responding distances for each kind of stimulus.

Overall, recordings of spontaneous calcium activity and paired electrophysiology demonstrated that the neighbors responding to a target neuron's deformation are a part of the neuronal ensemble. Unlike mechanical deformation, electrical stimulation of single neurons produced isolated PSPs and required multiple stimulations and stimulus averaging to reach signal visibility. Benchmarking the neighbor's STAs demonstrated that less than ½ of post-synaptic neurons would be recognized in calcium traces from a single-neuron current injection. A high incidence of false negative connections and electrical stimulation preferences to map only the directly connected post-synaptic neurons coupled to excitatory pre-synapse reduced the fraction of calcium-detected responders to only 12%. The findings confirm that a single-neuron deformation has a broader effect on the calcium marking of functionally coupled neurons and that, due to its specificity, it could be used as a valuable tool to visualize neuronal ensembles.

# 6.6. Single-neuron deformation excites the ensemble

Calcium imaging during the single-neuron mechanical deformation showed distinct plateau responses that propagated to morphologically- and functionally-coupled neurons. Since the calcium fluorescence is a better predictor of the membrane potential dynamics than the firing sequence (Chapter 5), paired electrophysiology further estimated the capacity of a single-neuron deformation to elicit APs in plateauing neighbors. The goal was to quantify the efficacy of mechanical modality to evoke firing in the ensemble, while also exploring the consistency of neuronal ensemble mapping in combined single-neuron deformation and standard MEAs.

During the paired patch-clamp measurements, pairs of neurons were selected to observe the changes in a neuron's membrane potential during its neighbor's mechanical deformation. The network was concurrently imaged via the jRCaMP1b to assess the generation of a plateau within the randomly chosen neighbor. The membrane of the non-responders remained stable during the deformation of a nearby neuron and showed spontaneous membrane and $Ca^{2+}$ events unrelated to the mechanical stimulus (Fig. 6.6. Aii). In contrast, plateauing neurons had slow depolarizations similar to the target (Fig. 6.6. Ai). These $V_m$ changes matched the kinetics of calcium plateaus and induced APs in 45% of the investigated cells. The firing probability correlated with the initiation kinetics and magnitude of depolarization. Plateauing neurons that also responded with firing had 12x faster membrane depolarization (median: 61.7 mV/s, IQR: 53.2 mV/s, N = 10) than responding neurons who responded without firing (median: 4.9 mV/s, IQR: 4.2 mV/s, N = 12, $p < 10^{-4}$, two-tailed Mann-Whitney, Fig. 6.6. B). Thus, the maximum depolarization values exceeded the threshold exclusively in plateauing neighbors with APs (median: -33.5 mV, IQR: 10.9 mV for bursting, median: -47.7 mV, IQR: 7.0 mV for non-bursting; $p < 10^{-2}$, two-tailed Mann-Whitney, Fig. 6.6. Bii). The absence of firing was due to reduced driving force, as $Na_v$s inactivated at pre-depolarizations.

What factors control the depolarization and plateau kinetics in neighboring cells? The neighbor's response kinetics may depend on external or internal factors. Despite the consistent duration of the mechanical stimulation during the giga-seal, varying levels of 60-80 mmHg overpressures used in patch-clamp may have affected the development of mechanoresponse kinetics. Since the target's plateau amplitude and kinetics correlate with the shear stress amplitude (Fig. 6.1.3. C), responses at the initiation site were compared across the trials with different firing outcomes. The calcium plateau at the initiation site showed no variation in slope (Fig. 6.6. Ci) or amplitude (Fig. 6.6. Cii), suggesting that the firing outcomes were not tied to the strength of the mechanical stimulus. Although the responses propagate regeneratively, the partial reduction of the rising kinetics could be attributed to a cumulative decline of the messenger crossing through the gap junctions as plateaus propagate. The lack of statistically significant difference among the bursting and non-bursting responding neighbors (Fig. 6.6. Ciii) rules out the position as an external factor influencing the kinetics. Another factor influencing the depolarization kinetics and firing outcomes could be the passive properties of the membrane: with an increasing time

constant, the membrane requires more time to depolarize to the threshold point. The time constant was calculated from a single-exponential fit to the -20 pA hyperpolarizing current pulse to estimate the passive properties of the neurons. There was no difference in time constants (Fig. 6.6. Civ), indicating that rather subtle differences among the responders determine the firing outcomes, such as the availability of signaling cascades to regenerate the responses and depolarize the membrane.

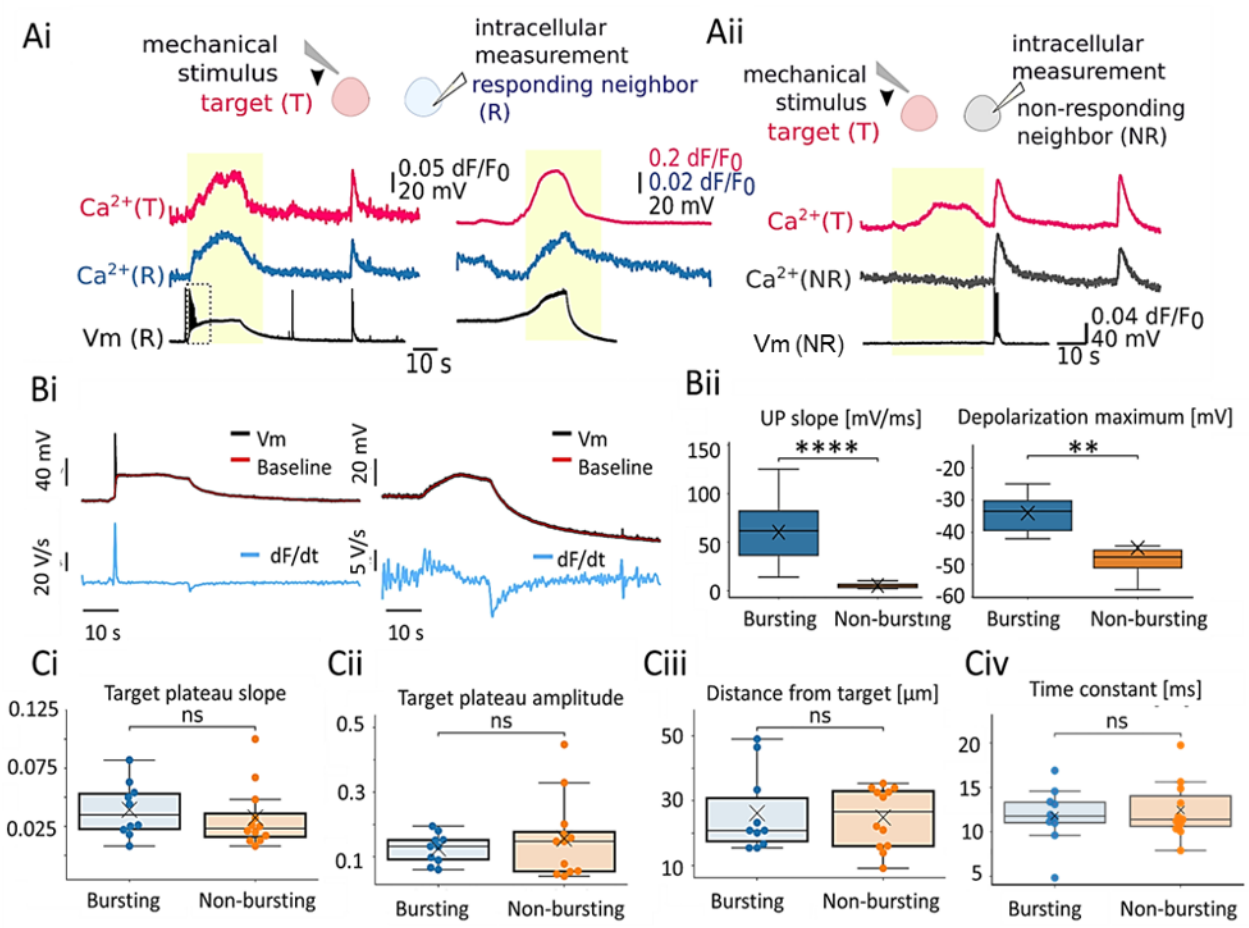


**Figure 6.6. Membrane responses of the responding ensemble.** A. Ground-truth of calcium plateaus during the deformation of a nearby cell. Ai. Responding neighbors (R) displayed depolarizations corresponding to calcium plateaus, capable of eliciting APs (left, rectangle). Aii. Non-responding neurons lacked the calcium responses and respective depolarizations and showed only spontaneous calcium spikes. B. Differences in depolarization kinetics among the plateauing neurons with evoked APs or depolarization only. Bi. Membrane potential (Vm) was filtered to obtain the baseline (red) cleared of APs. The temporal first derivative of the baseline (blue) was used to estimate the maximum of the UP slope of slow mechanoresponses. Bii. Boxplots depicting the UP slope distribution (left) and depolarization maxima (right) among bursting (N=10) and non-bursting neighbors (N=12). C. Factors defining depolarization kinetics and firing outcomes. Ci. Comparison of the calcium plateau UP slope at the initiation site. Cii. Calcium plateau amplitude at the target. Ciii. Distance of plateauing neuron from the stimulated neuron. Civ. Membrane's time constant extracted from the exponential fit of voltage response to -20 pA current pulse.

In summary, mechanical stimulation of individual neurons showed the capacity to evoke APs in the neighbors, as evidenced by paired electrophysiology measurements. Whole-cell measurements of the neighbor's responses during the mechanical stimulus allowed ground truth

of calcium plateaus without positional restrictions of the second pipette. These demonstrated reliable, time-locked, slow somatic depolarization with firing outcomes in 45% of the investigated calcium-responding neighbors. A reduced yield of evoked APs suggests that over half of the ensemble would be under-reported in single-neuron deformation assays coupled with conventional extracellular electrophysiology. Nevertheless, the ensemble more frequently responded with APs to a single-neuron deformation than the current injection, which reliably evoked only PSPs (Section 6.5.).

## 6.7. Single-neuron deformation increases the output gain of the responding neurons

As $Ca^{2+}$ is a secondary messenger, I investigated whether calcium plateaus evoke plasticity changes within the responding ensemble. The intrinsic excitability changes were evaluated in a whole-cell patch-clamp since it allowed the highest temporal and amplitude resolution and source specificity. Regenerative inter-neuronal propagation of the mechanical responses allowed probing the excitability changes associated with internal $Ca^{2+}$ increases within the ensemble.

Firstly, I investigated if prolonged $Ca^{2+}$ increases during the single-neuron deformation had a neuromodulatory effect on the responding ensemble. The intrinsic excitability was tested from membrane responses to the current injection. As a baseline, the excitability was probed 5 min before the deformation of a randomly chosen neighbor and compared to responses after. Based on their responses to a neighbor's deformation, the probed neurons were divided into plateauing or non-plateauing. Deforming a nearby neuron increased the firing frequency of the plateauing multispiking neighbors from 8 ± 1 Hz to 10 ± 1Hz ($N = 13$, $p < 10^{-3}$, paired t-test, Fig. 6.7. A). The firing frequency returned to the baseline 10 min after the neighbor's deformation (9±1 vs. 9 ± 1 Hz; $N = 10$, $p = 0.41$ paired t-test). In contrast, the firing frequency of the non-responders was not affected by the deformation of a nearby neuron (7 ± 1 vs. 8 ± 1, $N = 12$, $p > 0.05$, paired t-test). A similar firing frequency of the responding and non-responding multispikers ($p > 0.05$, two-sample t-test) suggests that the observed frequency changes are not pre-defined by the firing type. The absence of the effect among the non-responders indicates a response-specific potentiation of pre-synapses for further inputs.

The voltage responses to a -20 pA current pulse were used to estimate membrane resistance and capacitance. The responding and non-responding neurons did not differ in passive membrane properties (Fig. 6.7. B). Mechanical stimulation of a nearby neuron did not alter membrane resistance in the responding (236 ± 22 to 243 ± 17 MΩ, $N = 16$, $p > 0.05$, paired t-test) nor in the non-responding group (237 ± 37 to 250 ± 33 MΩ, $N = 13$, $p > 0.05$, paired t-test). Similarly, the membrane capacitance remained consistent in both groups after the stimulation (responders: 43 ± 7 – 30 ± 5, $p = 0.74$, Wilcoxon; non-responders: 34 ± 5 – 30 ± 4 pF, $p > 0.05$, Wilcoxon). These indicate the intrinsic excitability changes are not due to modulation of the constitutive membrane conductivities or effective membrane area. In plateauing neighbors, mechanical stimulation

reduced the firing threshold (-36.3 ± 1.5 to -38.3 ± 1.7 mV; N = 16, $p < 10^{-3}$, paired t-test; Fig. 6.7. C), while the firing of non-plateauing neurons was unaffected (-32.9 ± 2.4 to -33.2 ± 1.9 mV, N = 13, p > 0.05, paired t-test). This selective modulation of the neuron's onset was transient, as there was not a significant difference 10 minutes after the mechanostimulation of the neighbor (-36.7 ± 2.3 to -34.7 ± 1.7 mV, N = 10, p > 0.05, paired t-test). In addition, the firing threshold was similar between the firing and non-firing groups (p > 0.05, two-sample t-test), indicating that the neuromodulatory outcomes within responding and non-responding neighbors were not due to the different threshold distributions. These suggest that the increased gain of the responding ensemble post-stimulation is due to the modulation of sodium channel opening probability by the internal calcium increase.

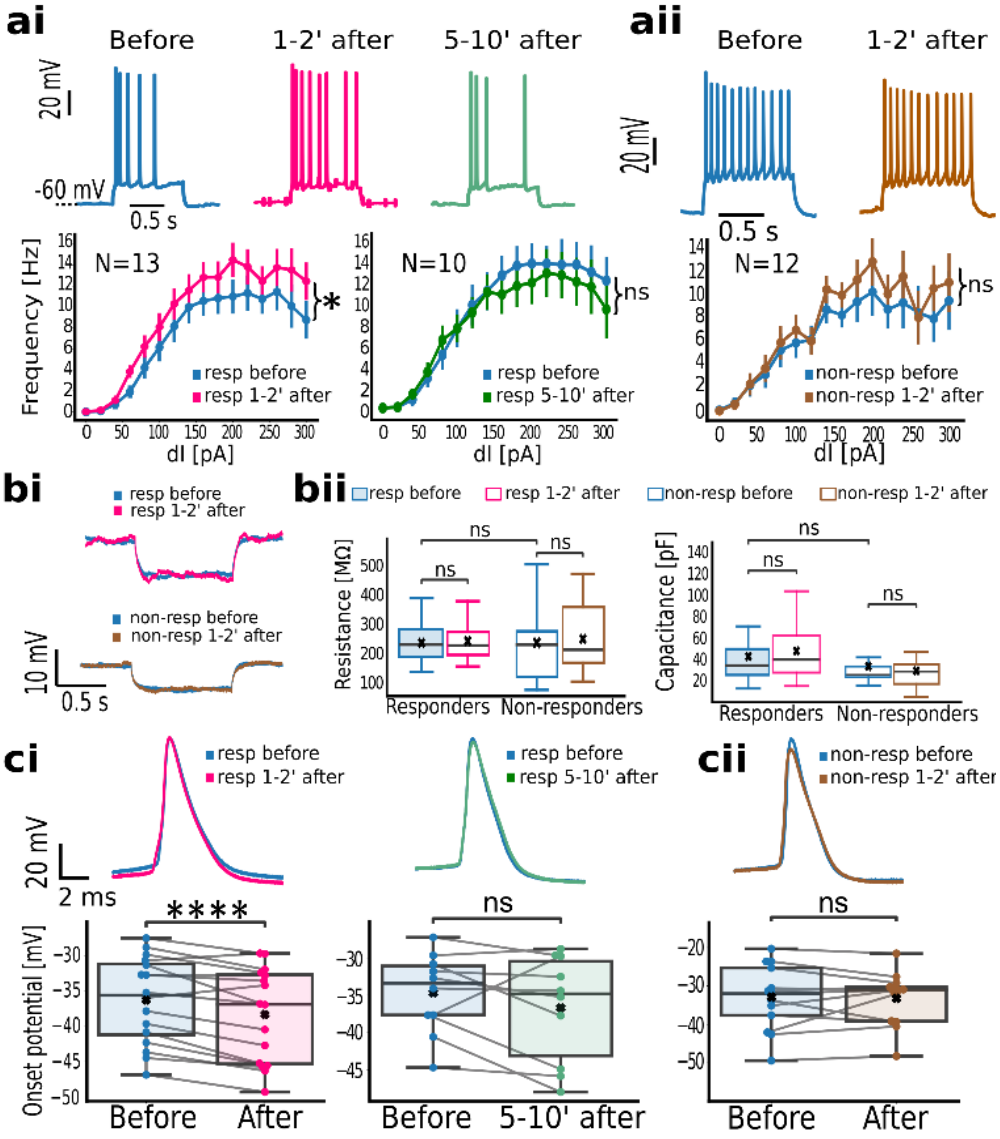


**Figure 6.7. Intrinsic excitability of neurons responding to the neighbor deformation.** A. Intrinsic excitability changes throughout the mechanical stimulation of a nearby neuron. Ai. The evoked firing of responding neuron before (blue), 1-2 min after (pink), and 5-10 min after (green) the neighbor deformation. Bottom: firing frequency

per applied current 1-2 min, and 5-10 min after the mechanical stimulus. Aii. The evoked firing of the non-responding neurons before (blue) and 1-2 min after the mechanical stimulus (brown). Bottom: firing frequency comparison before and 1-2 min after the stimulus. Whiskers denote standard errors. B. Passive membrane properties among responding and non-responding neurons during a nearby neuron stimulation. Bi. Exemplary voltage responses to a -20 pA pulse, detected for plateauing and non-plateauing neurons. Bii. Membrane resistance (left) and capacitance (right) for responding and non-responding neurons, before and after the mechanical stimulation. C: Comparison of active neuron properties before and after the mechanical stimulus. Ci. Action potential waveforms of plateauing neurons before (blue), 1-2 min after (pink) and 5-10 min after the mechanical stimulus (green) and firing thresholds. Cii. Action potential waveforms among non-plateauing neurons before (blue) and after (brown) the mechanical stimulus and threshold comparison on the bottom. Whiskers of the box plots span over 1.5 x IQR. Dependent samples were probed for significance via Wilcoxon or paired t-test; independent samples were tested via two-tailed, two-sample t-test: ns: $p > 0.05$, *: $0.01 < p \leq 0.05$, ****: $p \leq 10\text{-}4$.

To conclude, whole-cell screening of the neighbors following the single-neuron deformation provided insight into the modulatory effect of the calcium mechanoresponses dispersing into the network. The modulation was selective, as exclusively the neurons that responded to a neighboring deformation showed increased APs for the same input. The increase was transient, as the output gain of the responding ensemble returned to the baseline 5-10 min following the deformation and involved lowering the threshold for the APs.

# 6.8. Discussion and conclusions

## Deformation evokes calcium influxes via MS channels

The evoked responses could be assigned to several factors other than mechanical stimulation. Firstly, diffusion of the pipette solution could have excited the surrounding membranes, for instance, by local increases of $K^+$[343] or ATP.[344] Yet, the presence of responses when the solution was exchanged with the bath and their absence when pipette solution diffused above the neuron suggested that the solution is not the main trigger (Section 6.1). Secondly, the responses could have arisen from the membrane injury or shear-induced membrane poration,[325] leading to membrane depolarization via the influx of cations through the pores downstream of the electrochemical gradient. These were disputed by trypan blue assay, which demonstrated intact membranes of the target neurons following the giga-seal (Section 6.1). Thirdly, electrical test pulses used to navigate the pipette could have affected the target and surrounding neurons. The magnitude of test pulses for pipette navigation was 400-fold smaller than those required for excitation via electrical field modulations,[327] indicating that electrical pulses alone are unlikely to produce membrane responses matching calcium plateaus. Finally, a strong response attenuation in gadolinium, a universal antagonist of mechanosensation, (Section 6.2) further confirmed that giga-seal associated calcium plateaus are mechanical.

Responses developed via the calcium crossing the cell membrane, as the reduction of external calcium with EGTA and the broad-spectrum block of calcium conductivities attenuated plateaus. Deformation-evoked calcium influxes did not rely on internal store depletion, as the application of SOCE inhibitor 2-APB did not attenuate calcium plateaus. The initiation mechanism agrees with the ones previously found for other mechanical stimulation modalities, such as ultrasound [37] or membrane indentation,[40] suggesting that the ion channels act as a universal first responder to a mechanical stimulus. While Piezo1 inhibition failed to attenuate plateaus, several other mechanically gated ion channel family species, such as vanilloid receptors (TRPVs), TRPM7, or PRPP, could have contributed to the mechanical sensation.[37] The influence of these channels was not pharmacologically tested, either because of the lack of specific antagonists (TRPM7, PRPP)[37] or the pleiotropic effects of existing ones (TRPV). For example, capsazepine, initially found to antagonize TRPV1, also inhibits $Ca_V$s.[345] While future work involving molecular biology to down- and up-regulate the expression of mechanically gated ion channels should aim to dissect the origin of calcium influxes fully, it is likely that several species of mechanically gated channels jointly support the initiation of calcium plateaus. In addition, other mechanosensitive channels contribute to the development of calcium mechanoresponses.[107] Accordingly, L-type but not T-type $Ca_V$s act as an additional gateway for calcium.

Besides the MS channels, integrins have also been reported to mediate mechanical calcium influxes via several kinase pathways.[346-348] However, several lines of reasoning suggest integrin activation did not mediate calcium plateaus. Firstly, surface integrins require a trigger for their

pre-assembly, achieved by stimulant coating with integrin-activating agents.[348] In this work, the deforming agent was the patch pipette, and neither the glass nor pipette solution constituents could have triggered *de novo* integrin assembly. Another possibility is the activation of pre-assembled, substrate-interfacing integrins.[349] However, neurons also responded in the disrupted actin cortex, the main top-down force transducer.[349] On the same token, the PLL coating does not potentiate the assembly of substrate-interfacing integrins and is often used as a negative control for integrin-mediated signaling cascades.[350, 351] While the influence of a few pre-assembled, substrate-interfacing integrins could not be fully excluded, the several-fold slower kinetics and delayed onset of integrin-mediated calcium influxes[346, 348] suggest that calcium plateaus do not require integrin-mediated calcium influxes.

## Calcium plateaus spread regeneratively via the gap junctions

The previous multi-cell mechanostimulation indicated the neurons respond individually.[37] On the contrary, this work shows that mechanical excitation propagates within the target and up to a few hundred microns through the network (Section 6.3), without the requirement for synapses (Section 6.4). The previously demonstrated extensive fluidity of the membrane[233] suggested that signal transmission via propagating deformation was unlikely. Rather, the internal calcium increases trigger self-amplifying signaling cascades that sustain the calcium responses in the neurites. The underlying propagation cascades may involve the calcium-mediated amplification via internal calcium stores[232, 301], spanning both dendrites[352, 353]and axons.[354, 355] Although several morphological features can distinguish axons from dendrites,[356] this study did not attempt to directly evaluate if plateaus have a propagation preference. Firstly, brightfield reliably identifies the soma and, occasionally, thick neurites. Secondly, the non-uniform jRCaMP1b neuritic expression and low spatial resolution limited calcium signals to only some neurites (Section 6.3). Nevertheless, paired electrophysiology suggested that intra-neuronal plateau propagation can be both ortho- and antidromic since plateauing neurons were typically connected unidirectionally (Section 6.5), plateaus propagated bi-directionally (Section 6.4), and axo-dendritic synapses are the most prevalent type in the cortex.[357] That propagation of mechanical excitation is bi-directional is also supported by a two-fold higher network responsiveness than in electrical stimulation of the same target neuron, even when correcting for false negative connections from stringent amplitude thresholding (Section 6.5).

The absence of responses in proximal but disconnected networks demonstrated that propagation follows internal routes, while amplitude and velocity profiles indicated that plateaus propagate regeneratively. This contrasts the propagation of plateau-like calcium elevations from current injections, which failed to spread to the neighbors (Section 6.5). Since electrically-evoked calcium elevations arise from slow calcium buildup, the findings suggest that regenerative propagation of calcium signals depends on the kinetics and magnitude of calcium influxes. For instance, calcium-induced calcium release requires above-threshold calcium increases to evoke regenerative events.[230]

Following confirmation of gap junctions in *in vitro* cortical networks, pharmacology demonstrated the key mediators of the interneuronal spread were the gap junctions. Specifically, both less-potent broad-spectrum and highly potent narrow-spectrum Cx antagonists, carbenoxolone[255] and mefloquine[358], respectively, reduced the network's responsiveness to a single-neuron deformation (Section 6.4). While mefloquine also antagonizes L-type $Ca_Vs$,[359] preserved plateaus in mefloquine suggest the reduced network's responsiveness was from its antagonistic effect on Cxs.

Interestingly, mechanically evoked calcium plateaus and SNEs were anti-correlated, whereas the silencing of the synapses increased the fraction of the local network's responsiveness. While the mechanism of mutual exclusion is yet to be characterized, it is likely due to homeostatic synaptic mechanisms that promote input specificity and prevent calcium-induced excitotoxicity. These include, but are not limited to:

1. shunting inhibition due to a transient resistance drop at the recipient;
2. ion channel modulation by internal calcium: $Ca^{2+}$-sensitive $K^+$ channels that hyperpolarize the membrane,[360] down-regulating the calcium entry through L-type $Ca_Vs$;[361]
3. up-regulation of $Ca^{2+}$ clearance: $Ca^{2+}$ P-ATP-ase,[362] SERCA,[363] NCX, MCU.[364]

A similar propagation route was found for other calcium plateauing events in spontaneous activity of the developing retina,[83, 84] hippocampus,[85] [365] and cortex,[81, 82] suggesting a shared mechanism of calcium wave dispersion, irrespective of their origin. The mutual temporal exclusion of gap junctions and synaptic transmission was also found in these spontaneous co-existing propagation routes, indicating a universal transmission principle for both evoked and spontaneously occurring calcium waves. The findings suggest that the degree of mechanoresponse dispersion will depend not only on the morphological wiring, but also on the strengths of synaptic connections, and their co-activation.

Gap junctions are particularly suited to propagate slow membrane potential changes[78, 366] and exchange of secondary messengers (i.e., IP3, calcium, cAMP)[75] capable of re-initiating the responses in recipient neurons. Compared to synaptic transmission, gap junctions allow reliable, non-quantal transmission of depolarization irrespective of the relaying neuron's type.[42] It is thus unsurprising that mechanically evoked calcium plateaus propagate unaltered up to a few hundred microns. The findings demonstrate that the lateral resolution of wide-network mechanical stimulation could be reduced from mechanical excitation spread and propose gap junctions as the main target to limit the responses to the region of interest.

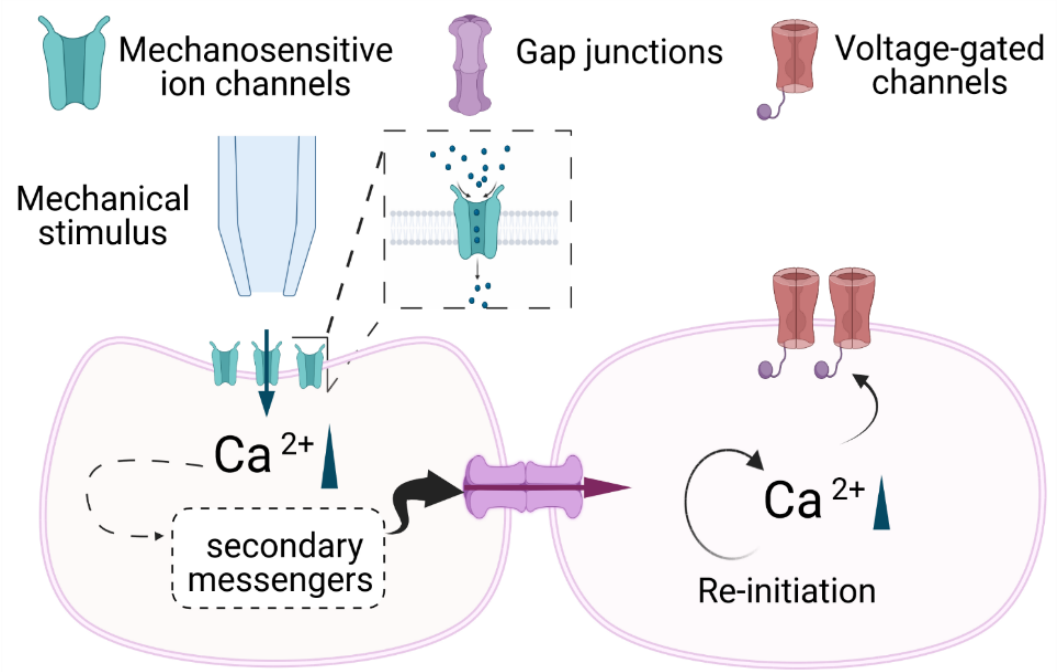


**Figure 6.8.1. Mechanisms of calcium plateau generation and propagation.** Pipette-mediated membrane indentation at the target activates MS channels. Calcium influx induces amplification of the secondary messengers that cross the gap-junctions and re-initiate the response in the morphologically coupled neuron. Prolonged calcium influxes transiently increase the excitability of the responding ensemble, likely via the potentiation of sodium-gated voltage channels. Created with BioRender.com.

## Mechanical stimulation (not always) induces firing in responding neurons

Previous investigations of mechanically evoked excitation employed imaging approaches[37, 39-41, 104] to circumvent confounding effects of the membrane deformation via the pipette. Functional imaging may not entirely portray the neuronal firing since $Ca^{2+}$ signals inconsistently translate into the firing code (Chapter 5). This work relied on the regenerative propagation of mechanical excitation to benchmark the neighbors' responses intracellularly. This benchmarking revealed that plateauing neurons consistently respond with slow membrane depolarization, which evoked APs in half of the responding neurons (Section 6.6). The findings emphasize that the firing outcome is only secondary, which should be considered particularly when mechanical stimulation is used to evoke neuronal firing. The absence of firing in half of the responders indicates that effective connectome mapping with conventional MEAs may yield false negative estimates (Chapter 4), even with mechanical stimulation. Further analyses revealed that the kinetics of the membrane depolarization determines if plateauing neurons respond with APs. The study remains inconclusive about the factors influencing the kinetics of membrane depolarization, as there were no significant differences in external factors nor the electrical properties among the responding neurons with different firing outcomes. Several other factors include the ion channel constitution, availability of GJCs to propagate the secondary messengers, as well as the availability of signaling cascades that re-initiate the responses.

## Bursting networks respond weakly to a single-neuron electrical stimulation

As demonstrated in Chapter 4 and Chapter 5, the primary mode of mature, densely interconnected *in vitro* networks is the bursting regime. Paired connectivity mapping with whole-cell patch-clamp demonstrated that SNEs also recruit non-connected neurons into synchrony, which aligns with the previous benchmarking.[14] In the context of connection mapping from correlation of detected activity, the findings emphasize that these not only risk omitting weak connections from reduced SNR, but also introduce spurious connections in highly synchronized states. Thus, correlative estimates suffer from context-dependent accuracy reduction. Since the oscillatory regime expands beyond the *in vitro* systems and organoids,[149] to native and pathological brain states *in vivo*,[85, 150] exploring other causal connection mapping strategies is crucial. One solution involves connection mapping by stimulation, where interconnected neurons are identified by their responses to single-neuron stimuli.

In all cases, electrical stimulation of the target produced isolated, subthreshold PSPs in recipients. This is expected, since densely interconnected neurons preferably form weak connections. Since single-neuron electrical stimulation failed to produce robust bursting responses in recipients (Section 6.5), the findings further suggest that SNEs in densely interconnected networks arise from collective actions, or that previously hypothesized burst-generators, whose mode of action is strictly by activating post-synapses, are sparse.[159] The findings point to several limitations in line with the causal connection mapping when single-cell electrical stimulation is combined with network readouts. First, conventional planar MEAs fail to register weak connections in dense networks, due to their inability to detect subthreshold events. Further, even state-of-the-art NS-NC electrodes accurately report connections only in < 20% of neurons (Section 4.3). Secondly, broad-network calcium imaging has a limited resolution for detecting PSPs (Chapter 5), although it displays a better correlation to the neuron's inputs. However, averaging the responses to the stimulus time stamps successfully marked about half of the recipient neurons by jRCaMP1b. Thus, the development of more sensitive calcium reporters could improve detection of weak connections and increase the yield of causal connectome mapping, even in dense networks.

## Single-neuron deformation for ensemble mapping

Besides the sensitivity-related limitations in neuronal ensemble mapping, the synaptic efficacy can limit connectivity detection even by averaging responses of recipient neurons. Moreover, calcium imaging is not expected to report responses to inhibition. Connection mapping by electrical stimulation is thus limited to output connections of excitatory targets. To that end, deforming single neurons may be advantageous to map interconnected neurons, especially when combined with functional imaging. Plateauing neighbors showed spontaneous calcium activity highly correlated to the target and were monosynaptically connected or shared a common synaptic input (Section 6.5). Plateau marking of functionally coupled neurons is unsurprising, given a strong co-localization of the gap-junctions with synaptic contacts.[98, 99] Moreover, this

approach could be favorable over electrical stimulation, since the latter maps the connections effectively when the target is excitatory, and the synapse is directed from the target,[20] which limits the pool of detected connections. Even when the conditions are met, the connection strength and calcium SNR determine the visibility of STAs in the recipients. In particular, benchmarking of the neighbors' calcium responses to a current injection in the target demonstrated that less than half of all output connections produce significantly high STAs. As a result, less than a ¼ of the neuronal ensemble is mapped by a single-neuron electrical stimulation and calcium imaging. In contrast, calcium plateaus were easily distinguished from spontaneous calcium activity by their magnitude and kinetics and did not require repetitive stimulation (Fig. 6.8.2). Because the prolonged calcium influxes propagate regeneratively via the gap junctions and consistently manifest as excitation, coupled neighbors are easily distinguished from the non-coupled ones, irrespective of the connection directionality (Fig. 6.8.2).

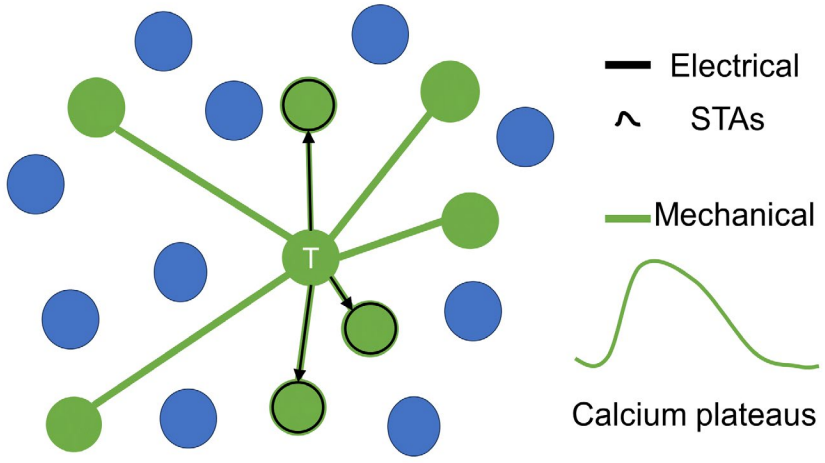


**Figure 6.8.2. Single-neuron deformation has a broader effect on the local circuitry.** Deforming a target (T) induces plateau-like calcium elevations (green) in morphologically and functionally coupled neighbors (green circles). Electrical stimulation at T produced a few detectable calcium STAs in recipient neurons (black circles and arrows).

## Giga-sealing transiently modulates the responding ensemble

Paired electrophysiology before and after the mechanical stimulus demonstrated a transient increase of intrinsic excitability, specifically in the neurons that responded to the deformation of a target (Section 6.7). The increased firing frequency was accompanied by a threshold shift towards hyperpolarizing potentials, suggesting that the single-neuron deformation increases the output gain of the responding ensemble. This narrow window, where local-circuitry-level excitability changes happen, imposes a time restriction post-giga seal, mainly when the intent is to study the native neuronal behavior or local circuitry activity upon a stimulus receipt. Moreover, an increased neuronal firing during the probe insertion in *ex vivo* retina preparations[368] suggests that the effect may be universal to more native systems and to any stimulation and measuring approach that requires physical contact with the neuron(s).

In contrast to optogenetic or electrical stimulation, which required prolonged and multi-neuron co-activation to exert the ensemble-wide effect,[14] a single, single-neuron deformation suffices for a transient modulation. The findings support a non-Hebbian pattern completion mechanism and propose ion channel modulation by prolonged calcium increases (Fig. 6.8.1). While the effect was transient, it suggests an avenue for exploring if repeated deformations could be effectively used to re-program the network by promoting specific connections or introducing new members.

## Implications in acute brain injury

On a broader scale, the excitation and excitability modulation of the neighboring neurons upon a single-neuron deformation indicates interneuronal cross-talk during adverse mechanical perturbations, such as traumatic brain injury (TBI).[369] While the effect of a single-neuron fine membrane manipulation should not be confused with long-term and direct neurodegeneration promoting mechanisms of TBI, such as complex neuron-glia interactions,[370] they indicate yet another pathway that amplifies the internal calcium increases associated with the early-stage signaling cascades. Interestingly, the gap junctions, here found to mediate the dispersion of single-neuron mechanical responses, are up-regulated following the TBI: on the shorter time-scales, physical stress upon TBI promotes the opening of connexins; long-term, the expression of connexins is increased following TBI.[92] The extent of early calcium signaling following the TBI may be further amplified by the positive feedback involving the interplay between the mechanically-induced internal calcium increases and mechanically-induced increased availability of functional gap junctions.

## Study limitations

There are several aspects that limit the conclusions of this study. Perturbation experiments were done at room temperature, and the effect's extent and velocity may be even higher at physiological temperatures. Neurons were cultured in 2D on glass coverslips, with a young's modulus orders of magnitudes higher than the brain. It could be that the effect is more pronounced in *in vitro* systems due to the lack of amortizing forces. Thus, one of the future goals is to investigate whether the broad-network effect exists beyond the *in vitro* systems. Besides neurons, astrocytes are mechanosensitive, extensively communicate through the gap junctions, and participate in cross-talks through tri-partite synapses.[371] However, culturing conditions aimed for astrocyte reduction for MEA measurement reliability, and the culturing protocols remained consistent for comparisons between the MEA and calcium imaging network screening. It would be interesting to estimate the extent of the single-neuron mechanical stress on cultures containing physiological amounts of astrocytes and further investigate how neuron-glia interactions shape the mechanotransduction and dispersion of mechanical excitation.

# 7. Summary and outlook

Understanding the neural network functional topology is essential for advancing our understanding of information processing, refining the computational network models, and developing targeted brain modulation strategies. Direct mapping of neuronal connections motivates technological advances to improve the detection sensitivity of the network readouts[25, 27, 171, 172, 186, 191, 192, 274] with the end goal of inferring causal connections from spontaneous activity. However, reliable estimates of connections require a full grasp of the current network readout limitations, and analysis advances to circumvent them.[30, 33, 34, 36, 62] Connectivity-from-perturbation emerges as a promising strategy in connectome mapping, as stimulus time-locked responses in the neighbors provide another basis for connection distinction.[15, 20, 22] This work investigated single-neuron stimulation as a potential tool for mesoscale connectivity mapping in bursting *in vitro* networks of cortical neurons.

The first aim was to determine which information about the network activity and connections could be reliably extracted from the current network readouts, including state-of-the-art MEA electrodes (Chapter 4) and local-network jRcaMP1b calcium imaging (Chapter 5). Using patch-clamp as a gold standard, this benchmarking aimed to obtain further insight into the detected signal representations and quantify errors associated with connectivity estimates derived from correlations of detected activity in oscillating networks.

2D+ electrodes, such as NS-NC MEAs,[26] show promise in network activity screening, given their improved amplitude sensitivity. The prevalence of positive spikes in high SNR NS-NC traces initially suggested the possibility of intracellular access.[26] However, benchmarking against the patch-clamp indicated a direct signal transfer across the intact membrane, akin to loose-patch configurations. This work further demonstrated that a tight engulfment expands sensitivity to the lower frequencies and subthreshold detection. This non-invasive PSP detection offers direct assessments of synaptic strengths and could allow long-term and multi-site causal connection estimates from observed activity. Nevertheless, this goal requires further interface and geometry refinement to promote a strong coupling yield and higher electrode density for better spatial resolution. To this end, connection mapping using MEAs relies on statistical inferences on detected EAP trains.

Another key challenge persisting in MEAs is uncertain source identification of detected signals. While SNR advances are expected to improve source designation accuracy,[199] this work revealed that increased amplitude sensitivity introduces higher variations in single-neuron EAPs. This variability, particularly during bursts, reduces source identification accuracy by 30%. Alongside IAP variations, this work identified inconsistent IAP-EAP coupling as another source of EAP variability in high SNR traces. Transfer function changes were reversible and short-term, suggesting modulation of the signal transfer at the coupling. Besides being relevant for

addressing extensive EAP variations, the findings emphasize the eventual errors of IAP analog predictions using models that assume consistent coupling.[189]

Uncertainty in identifying how many neurons are detected by an electrode adds subjectivity to EAP source designation.[62] This work investigated the effect of signal misclassification and curation decisions on network metrics in bursting networks. Results emphasize the sensitivity of functional connectome estimates to EAP misclassifications. Retaining smaller units of misclassified EAPs halves the estimated connection strengths, while discarding them preserves the unit landscape and maintains more accurate correlative estimates. The findings support discarding smaller units of EAPs in oscillating networks to achieve more accurate correlative estimates in high SNR traces. However, this approach reduces the pool of analyzed signals, akin to spike omission in low SNR traces.[265] Since vertical electrodes[372] and oscillatory regimes extend beyond *in vitro* systems, future refinements in spike-sorters are crucial to fully benefiting from improved amplitude sensitivity. Recent advances in spike sorters include modulated template-matching[198] or data-driven burst recognition[373] to account for burst-associated EAP variations that arise from IAP changes. A higher misclassification incidence from inconsistent IAP-EAP relation could guide the development of less-stringent spike sorting pipelines that consider EAP variability from variable coupling in high SNR traces.

Calcium imaging provides accurate signal source identification but faces challenges in extracting neural activity due to its limited temporal precision and sensitivity. Chapter 5 demonstrates further inconsistencies in the relationship between $Ca^{2+}$ signals and neuronal firing, which are biologically grounded. Even within a single neuron's trace, the magnitude and detection of the 1AP $Ca^{2+}$ signal vary proportionally to the strength of inputs. The predominant source of detected $Ca^{2+}$ signals is thus not always related to firing, and the background processes arising from various inputs imprint onto the $Ca^{2+}$ signal. The inconsistencies extend beyond 1AP events since a strong correlation exists between the magnitudes of $Ca^{2+}$ signals and input strength across all firing outcomes. Accordingly, network-level calcium imaging most reliably detected strong inputs associated with network synchrony. Thus, the network-state dynamics should be considered when developing spike inferences. Given that the $Ca^{2+}$ signal reliably correlates with membrane depolarization magnitudes, one potential solution lies in predicting baseline membrane potential dynamics from $Ca^{2+}$ signals, followed by firing estimates using a biophysical model or trained NN network.[224] Such estimates would reduce the free parameters required for inferring the firing frequency, potentially reducing overfitting.[35]

Chapter 6 explored single-neuron perturbation as a strategy for mapping causal connections in oscillatory networks. Whole-cell confirmed that most inputs in dense cortical networks comprise isolated PSPs, aligning with previous findings.[367] The findings emphasize the setbacks of combining single-cell electrical stimulation with MEAs to map causal connections, as even the novel 2D+ electrodes would accurately detect a monosynaptic connection in < 20% of neurons. Despite the inability of a single-neuron electrical stimulation to produce robust $Ca^{2+}$ responses, trace averaging by the stimulus timings accurately recognized about half of the verified

recipients. While advances in the calcium reporters[374] hold promise for reliable connection mapping with targeted electrical stimulation, future studies should quantify their sensitivity in detecting weak, less efficient connections.

However, the finding that a single-neuron perturbation during the giga-seal excites the target and the surrounding network suggests another strategy to map interconnected neurons with calcium imaging. Plateaus initiate and develop through the $Ca^{2+}$ influx via MS and L-type Cav channels, independently of the neuronal firing. At the membrane, the $Ca^{2+}$ influx induced slow depolarizations capable of eliciting APs. Plateaus persist through the neurites and propagate at 50 µm/s to the morphologically and functionally coupled neurons. Propagation is regenerative, and responses re-initiate as they propagate to the neighbors. The gap junctions mediate propagation, without a requirement for synaptic transmission. Unlike electrical stimulation, deforming a single neuron marks a broader ensemble, irrespective of the connection directionality and the target neuron type. The findings further indicate that the spatial resolution could be limited by biological dispersion and suggest gap junction blockers to improve the spatial precision of mechanostimulation. Finally, any approach that acutely interfaces neurons may impose excitation and modulation of the network, with implications for bi-directional communication approaches that require proximity to the neurons, even in *in vivo* systems.

A primary limitation of these findings is the focus on dense, bursting *in vitro* networks. While bursting dynamics is also connected to various brain states and pathologies, the translation of investigated approaches to *in vivo* systems requires further exploration. Further, context- and state-dependent solutions for activity inferences from 2D+ electrodes and calcium imaging are likely needed. Several directions hold promise.

1) The inconsistency in IAP-EAP coupling and high EAP variability in oscillating regimes requires refining spike-sorting algorithms that specifically address extensive single-neuron EAP variation. Such algorithms will be essential for extracting accurate source information and single-neuron spike trains from high-SNR traces during highly active, bursting states.

2) Developing a classifier that allows integration of the neuronal firing properties with membrane potential prediction could be one solution to resolve firing rate-calcium signal inconsistencies. The spiking inference could be refined by classifying algorithms that use the neuron's morphology, participation in collective network activity, or both. While this model would benefit from cell type identification on a larger dataset, recent collective initiatives within the calcium benchmarking community and neuronal firing type characterization provide a promising framework to pursue these questions further.[34]

3) Combining the strengths of MEA electrophysiology for output readouts with refined calcium imaging that allows input and source resolution could offer a good strategy for high-throughput cross-validation. This approach, especially in combination with high-density MEAs[182] and sensitive calcium reporters,[374] could enable accurate mapping of both input

strengths and firing outputs in oscillating networks, improving the yield and accuracy of network topology estimates from spontaneous activity.

4) While further investigation is needed to translate the effects of single-neuron deformation to more native networks, it can potentially expand our understanding of neural circuit dynamics. Targeted mechanical modulation could probe circuit-level topology and dynamics and even modify aberrant activity patterns in a therapeutic context. One central goal is to evaluate the long-term, neuromodulatory potential of mechanostimulation in the context of native systems.

# Acknowledgements

I would like to thank **Prof. Andreas Offenhäusser** for supervising and supporting my PhD work, for giving me the freedom to pursue my research interests and for always asking good questions. Most of all, thank you for fostering a supportive and collaborative atmosphere which I genuinely enjoyed being a part of. I also thank **Prof. Marc Spehr** for agreeing to supervise this PhD work.

I'd like to thank my master's mentors, **Prof. Miroslav Živić** and **Nataša Todorović**, for their guidance during my first venture into science. *Hvala Vam na ukazanom poverenju, podeljenom znanju u oblasti elektrofiziologije i svesrdnom mentorstvu!*

I'd like to thank **Vanessa Maybeck**, for the opportunity to be a part of the Cell Engineering group. Thank you for the project-related discussions, and for the feedback on thesis and manuscripts. Thanks to all CellEng members – **Timm**, **Jiali**, **Ekaterina**, **Dominik, Ruoyan** for all the great times I had working with you. To **Ekaterina**, thank you for helping me with getting comfortable with the BioMAS readouts, for the cell culture troubleshooting, and for the hallway small talks. To **Dominik**, thank you for introducing me to the IBI's patching ways, dos and don'ts in the lab service, and for your help with setting Zyla. To **Jiali**, thank you for prompting the patch-clamp discussions, for sharing the tips on LCI calcium imaging, and for having an open ear to all lab-related questions. Special thanks to **Bettina Breuer (Tina)**, for her great support inside and outside of cell culture, for celebrating all little victories, and for being the awesomest!

I further thank **Timm** and **Justus** for having the patience and insightful feedback on coding-related questions.

I thank **Florian Friedland** and **Erik Nötzel** from Mechanobiology Institute for the help with actin cytoskeleton imaging and for discussions on cell deformations.

I'd like to thank **Prof. Simon Mussall** for recommending SpikeInterface for spike-sorter benchmarking. Many thanks to **Alina Bazarova** and **Stefan Kesselheim** from Helmholtz AI Center for all the fruitful discussions and help with NN models for MEA spike predictions. **Nikola Pejić**, thank you for questioning my interpretations of "black box" model outputs, and for being such a great friend. I further thank **Csaba Forro** for the help and discussions on transfer functions.

Special gratitude goes to my less-official supervisors from whom I learned a lot.

To **Pegah Shokoohimehr** – thank you for being such a great internship mentor and for introducing me to the bioelectronics and NS-NC MEA project. Thank you for sharing your expertise on MEA fabrication and measurements, and for all your support I received throughout.

Most of all, thank you for all the discussions we had on the NS-NC MEA project, which showed me the beauty of interdisciplinary collaboration. I'm truly proud of our work!

Many thanks to **Timm Hondrich** for convincing me to look beyond a single neuron and for establishing solid foundations in calcium imaging and network analyses at IBI-3. Most of all, thank you for your mentorship and guidance, especially at the beginning, and your encouragements to pursue Python coding. Your curiosity inspired me to ask all kinds of questions, and you always inspired me to learn more.

To **Katarina Stevanović** – thank you for introducing me to the arts of patch-clamp and for your "big sister" energy. *Hvala ti na pečerskim danima ispunjenim muzikom kojih se vrlo rado prisećam, kontinuiranom mentorstvu koje je preraslo u dragoceno prijateljstvo, ali i na podsticaju da se drznem u nepoznato. Hvala ti i za Stivena Vilsona.*

I further thank the **IT** support, for their help with all computers-related bugs, and for patiently responding to my bugging.

Thanks to all **IBI-3** members for creating such an interdisciplinary and multicultural atmosphere. Thank you for all the nice gatherings, virtual and in-person Christmas parties, which I will fondly remember!

*Juliškim frajlama, **Katarini**, **Jeleni** i **Medi**, hvala na druženjima i šetnjama. Katarini zahvaljujem na zdravoj dozi optimizma, karaoke žurkama i temeljnom uvodu u život u Julihu. Jeleni hvala na domaćinskoj atmosferi i na neiscrpnom izvoru (fenomenalnih!) domaćih kolača! Medi posebno hvala na svim ushićenim dočecima i što je najmilije stvorenje.*

*Svojim saborcima iz fakultetskih dana, **Ivani** i **Nemanji**, hvala na svim podeljenim kuknjavama i dragocenim trenucima uprkos udaljenosti!*

***Goci** i **Milanu**, pored neizmerne zahvalnosti koju osećam zbog Đileta, tople atmosfere i roditeljske podrške, zahvalnost dugujem i za donaciju aparata za pritisak, čiji su delovi našli primenu u izradi završnih eksperimenata ove teze.*

***Mami** i **tati** – hvala na bezuslovnoj ljubavi i podstreku. Tati – hvala za svu podršku i prenesenu ljubav prema elektronici. Počivaj u miru, a tvoja načela i vedrina živeće večno sa mnom!*

***Điletu** – hvala na svim prethodnim i trenucima koji slede. Hvala ti na svemu.*

# Appendix A: Analysis details

## 1. SpykeClick GUI for manual curation of detected spikes

The GUI was written in Tkinter to manually correct for the automatic detection of spike onsets, peaks, and ends. The GUI operates on 1D vectors that could either be electrophysiological or calcium imaging traces. The GUI description is below, and it can be downloaded from: https://fz-juelich.sciebo.de/s/n5qBIIzPrsbynIW.

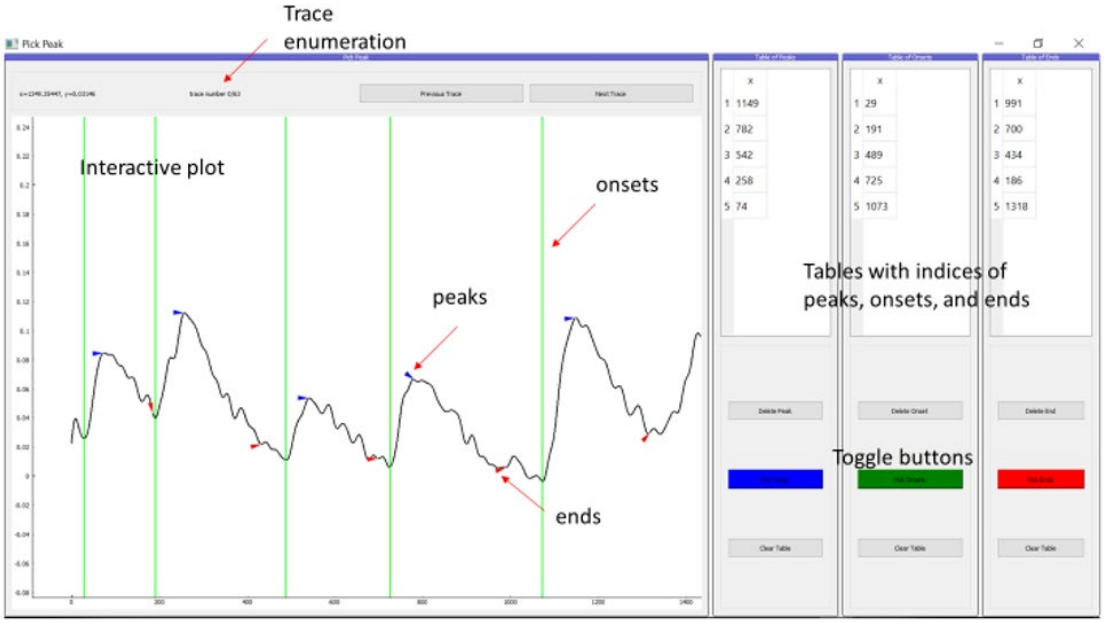


**Figure A1. SpykeClick GUI for manual curation of spike onsets, peaks and ends.**

## 2. VC check and CC check protocols

Protocols described below were used for:

1) estimation of passive membrane properties at least hyperpolarizing pulses, if recordings were acquired without membrane capacitance compensation;
2) estimation of the neuron's intrinsic excitability/firing properties.

Either in voltage-clamp or current-clamp mode, the membrane was clamped at a resting -60mV potential. From there, 0.5-1s- long voltage (VC check) or current (CC check) pulses were applied in increments of 20 mV/20 pA, starting from the strongest hyperpolarization, followed by a 250-500 ms recovery at a resting potential. In voltage-clamp mode, the range of injected voltage was from -120 mV to +100 mV; in current-clamp, the injected current ranged from -200pA to + 400pA. Exemplary CC and VC check recordings are presented below.

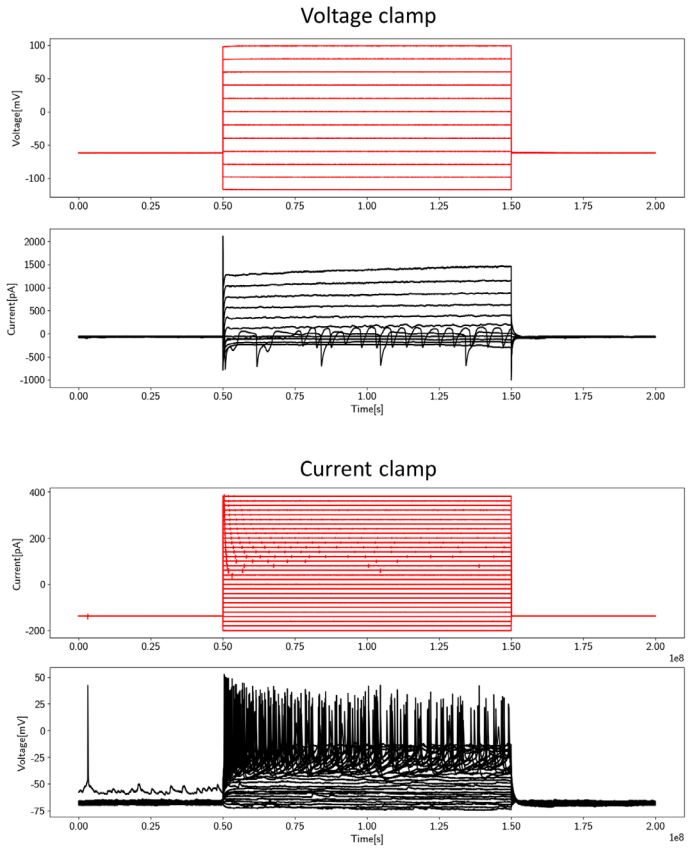


**Figure A2. VC and CC-check protocols performed in whole-cell configuration.** Red traces depict the stimulation pulses (voltage in VC, current in CC-check). Black traces represent the whole-current or whole-voltage membrane responses. Incremental stimulations and corresponding responses are stacked. Upon threshold crossing, the neuron fires a single or multiple action potentials, depicted as fast sodium currents (VC-check, top) or positive voltage deflections > 60 mV (CC-check, bottom).

## 3. Spike sorting parameters

Below tables describe parameters used in SpikeInterface, for each spike sorter. While many of the listed sorters have over 20 parameters, only adjustable ones are listed below. Color code depicts spike sorting step for which a given parameter applies: spike detection (green), feature extraction (blue), clustering (yellow), template-matching (red). Among different parameters, only the spike detection was changed from default, to match the high SNR of NS-NC MEAs.

Table A3-1. Parameters for sorting with MountainSort

| Sorter | Threshold[1] | Width [ms][2] | [3]Sign |
|---|---|---|---|
| MountainSort | 2.8 – 5 | 12-15 | +/- |

*[1]Threshold in units of standard deviation from the mean*
*[2]Width of spikes in ms*
*[3]Sign: + for positive, - for negative local extrema*

Table A3-2. Parameters for sorting with Tridesclous

| Sorter | Threshold[1] | Width [ms][2] | [3]Sign |
|---|---|---|---|
| Tridesclous | 10-12 | 12-16 | +/- |

*[1]Threshold in units of standard deviation from the mean*
*[2]Width of spikes in ms*
*[3]Sign: + for positive, - for negative local extrema*

Table A3-3. Parameters for sorting with Klusta

| Sorter | Threshold[1] | Width [ms][2] | Sign[3] | n_features_per_channel[4] | num_starting_clusters[5] |
|---|---|---|---|---|---|
| Klusta | weak: 6-8<br>strong: 10-13 | 8 | +/- | 3 | 50 |

*[1]Threshold in units of standard deviation from the mean; [2]Width of spikes in ms*
*[3]Sign: + for positive, - for negative local extrema; [4] n_features_per_channel: # of PCA features;*
*[5] num_starting_clusters: number of initial clusters*

Table A3-4. Parameters for sorting with Combinato

| Sorter | Threshold[1] | Width [ms][2] | Sign[3] | MaxClusters PerTemp[4] | MaxDist MatchGrouping[5] | Match Factor[6] |
|---|---|---|---|---|---|---|
| Combinato | 5-8 | 15-18 | +/- | 5 | 1.8 | First: 0.75<br>Second: 3 |

*[1]Threshold in units of standard deviation from the mean; [2]Width of spikes in ms*
*[3]Sign: + for positive, - for negative local extrema; [4] MaxClustersPerTemp: How many clusters can be selected at one temperature; [5] MaxDistMatchGrouping: At what cluster distance does grouping stop; [6] MatchFactor: How close do spikes have to be in the first/second template matching step*

Table A3-5. Waveclus sorting parameters

| Sorter | Threshold[1] | Width [ms][2] | Sign[3] | Scales[4] | Maxtemp[5] | Min_clus[6] | template_sdnum[7] |
|---|---|---|---|---|---|---|---|
| Waveclus | 8-12 | 12.8 | +/- | 4 | 0.251 | 20 | 10 |

*[1]Threshold in units of standard deviation from the mean; [2]Width of spikes in ms*
*[3]Sign: + for positive, - for negative local extrema; [4] Scales: Levels of the wavelet decomposition used as features; [5] MaxTemp: Maximum temperature calculated by the SPC method; [6] Min_clus: minimum number of spikes per cluster; [7] template_sdnum: Maximum distance (in total variance of the cluster) from the mean waveform to force a spike into a cluster*

Table A3-6. Spyking circus sorting parameters

| Sorter | Threshold[1] | Width [ms][2] | Sign[3] | Sub_dim | Sensitivity | auto_merge |
|---|---|---|---|---|---|---|
| Spyking Circus | 10-16 | 16-18 | +/- | 10 | 3 | 0.75 |

*[1]Threshold in units of standard deviation from the mean; [2]Width of spikes in ms*
*[3]Sign: + for positive, - for negative local extrema; [4] Sub_dim: Number of dimensions to keep for local PCA per electrode; 5 Sensitivity: Single parameter for clustering sensitivity; lower values correspond to a higher sensitivity; 6 Auto-merge: CC threshold between two templates; if it is higher, the two templates are merged.*

## 4. Network simulation parameters: Iszhikevich model of bursting network

**Table A4.1. Parameters used for construction of bursting *in silico* network**

| Parameter | Value [Unit]* | Description |
|---|---|---|
| $N$ | 100 | Number of neurons |
| $P_{ex}$ | 80 | Fraction of excitatory neurons |
| $P_{inh}$ | 20 | Fraction of inhibitory neurons |
| $Iext_{max}$ | 80 mV/ms | Maximal current injected to neurons throughout the measurement; randomly scaled for each neuron |
| $a$ | 0.001 $ms^{-1}$ | Defines recovery kinetics of $V_m$ after the reset; lower a increases chances of burst |
| $b$ | 0.6 $ms^{-1}$ | Defines sensitivity of recovery to fluctuations in $V_m$; higher values lead to bursts; $b>>a$ or $b<<a$ induce Hopf bifurcations |
| $c$ | -55 mV | $V_m$ value to which the neuron re-sets after the spike. |
| $d$ | 120 mV/ms | Determines the rate of the neuron's recovery after the spike |
| $k$ | 0.4 | Influences $dV_m/dt$ as a function of time and $V_m$. |
| $V_r$ | -60 mV | Resting membrane potential |
| $V_t$ | -55 mV | Threshold potential |
| $V_{peak}$ | 35 mV | Membrane potential that triggers re-setting |

*Note that the central parameters are dimension-less.

# Appendix B: Protocols

## MEA substrate cleaning and coating

### Materials

- MEA chips
- 70% EtOH
- autoclaved MilliQ
- 3-4 ml HBSS per sample
- 10 µl concentrated PLL solution per sample
- 2 autoclaved glass beakers
- 2 falcon tubes
- well plate

### Procedure

1. Using 70% EtOH, sterilize the bench surface and materials introduced into the bench.
2. In one falcon tube, dilute the stock solution in HBSS to obtain 0.01 mg/ml working PLL solution.
3. In another falcon tube, separate only HBSS for substrate washing (2-3 ml per sample).
4. Pour the autoclaved MilliQ into one beaker under the bench.
5. Pour 70% EtOH into another beaker; the liquid level should be high enough to cover the substrate fully.
6. Submerge the samples in 70% EtOH for a few minutes, then wash them in a MilliQ beaker.
7. Place the substrates in the well-plate and carefully aspirate the leftover liquid.
8. Optionally, sterilize the samples under the UV light for 1 h.
9. Pipette 1ml of the working PLL solution on each substrate and incubate at RT for 1 h.
10. Rinse the substrates 2-3 times with 1 ml HBSS and store the samples at $4^{o}$ C for up to a week before plating.

## jRCaMP1b AAV transduction

### Materials

- Neurobasal medium (0.25 ml per sample)
- AAV stock solution (ca. $10^{13}$ viral particles/ml)
- A 24-well plate with cells to be transduced
- 2 falcon tubes

**Procedure**

1. Prepare the medium under the sterile bench according to the recipe in Section 3.1.2, and heat at 37° C.
2. Calculate the volume of AAV stock solution for transduction:

$$V_{AAV,stock} = \frac{MOI * N_{cells} \times N_{samples}}{C_{AAV,stock}}$$

   MOI denotes the final amount of viral particles per cell, $N_{cells}$ – number of cells per sample, $N_{sample}$ – number of samples to be transduced, and $C_{AAV,stock}$ – initial concentration of viral particles.
3. Under the sterile bench, mix the desired volume of AAV stock solution into the pre-warmed NB medium.
4. Draw 0.75 ml of the old medium and add 0.25 ml of AAV-containing NB medium.
5. Incubate the cells at 37 ° C and 5% $CO_2$ at least 7 days before calcium imaging. Change the medium bi-weekly.
6. Gloves, pipette tips, tubes, and old medium are disposed of in a separate container and autoclaved. After the work, the surfaces are treated with UV light for 1 h.

## Standard whole-cell patch-clamp measurement

For details on patch-clamp combinations with MEA electrophysiology or calcium imaging, refer to Section 3.3.4 and 3.3.2, respectively.

## Materials

- Tweezers and pipette tips for coverslip extraction
- Plastic petri dish lids
- Superglue or vacuum grease for coverslip adhesion
- Pellet Ag/AgCl electrode
- Bath electrode connecting wire
- 2x10 ml and 2x20 ml syringes for pressure control and patch solutions
- Borosilicate glass (1.5 mm with filament, fire-polished, Sutter Instrument)

## Solutions

- E-patch solution (Table B2) – ca. 4 ml per sample
- I-patch solution (Table B3 or B4) – 1 ml per session

## Instruments

- Pipette puller (P-2000, Sutter Instrument)
- Upright microscope (AxioVision, Carl Zeiss AG)

- Light source (100 W HBO lamp, Zeiss or LED light source, Thorlabs)
- Water-immersive 20x objective (Olympus, UMPlanFl)
- Camera (sCMOS camera Zyla, Andor)
- Patch arm micromanipulator (Luigs & Neumann, SM I)
- Focus control (Luigs & Neumann, SM IV)
- HEKA EPC 10 dual USB amplifier (HEKA Electronics GmbH)
- Optional, but preferable: anti-vibrational table (Thorlabs)
- Faraday cage

## Software

- PatchMaster Software (HEKA Electronics GmbH) for acquisition
- Self-written Python code for ASCII file opening and analysis
- Andor Solis (Oxford instruments) software for the brightfield snapshots

## Acquisition parameters

| | |
|---|---|
| Sampling frequency: | 10 kHz |
| Low-pass filter: | 3 kHz Bessel filter |
| Gain: | 5 mV/pA |
| Gentle CC switch: | ON |

## Procedure

### I Preparation

1. Regularly observe the fitness of the culture under the inverted brightfield microscope. Healthy cells show well-defined somas adhered to the surface; older (+7 DIV) cultures also have some primary neurites visible under the brightfield.
2. Turn on the instruments.
3. Thaw the E-patch in a water bath at 37 ºC, and I-patch at RT.
4. Check the medium and E-patch osmolarity and adjust the osmolarity of E-patch with glucose, if necessary.
5. Pull the pipettes from borosilicate glass using a pipette puller. The pipette resistance should be in the 5–10 MΩ range.
6. Draw the pre-heated E-patch using a 20 ml syringe and place it on the heating plate pre-set to 37 ºC.

### II Preparing the sample

1. Under the sterile bench, isolate the lid of a sterile petri dish; the coverslip will be adhered to the inside of the lid.
2. Using the 1000 µl pipette tip, place a small amount of glue/grease on the center of the lid and spread it evenly.

3. Under the sterile bench, discard about 0.5 ml of the medium for easier access. With the pipette tip, leverage the coverslip on one side. Using tweezers, pick the coverslip and adhere it to the center of the lid. Place ca. 0.1 ml of the medium on the cell layer to slow dehydration and osmotic stress. Return the well-plate to the incubator.
4. Place the sample on the heating plate and add ca. 3 ml of pre-heated E-patch solution.
    - CRITICAL STEP: Minimize the time from coverslip isolation to E-patch addition to reduce the dehydration/osmotic shock.
5. Mount the sample on the stage and immerse the bath electrode in the bath.

## III Obtaining the giga-seal

1. Relying on the oculars or camera, locate and center the target. Move the focus away from the cell layer to allow pipette insertion.
2. Fill the pipette using a 1 ml syringe coupled to the pipette filler. The liquid level should only contact the measuring Ag/AgCl electrode to minimize the pipette capacitance.
3. Mount the pipette on the holder while touching any metal part of the Faraday cage.
4. Apply + 60-80 mmHg positive pressure and immerse the pipette into the bath.
5. In acquisition software, cancel the pipette offset and apply 5 mV, 5ms test pulses to read the pipette resistance. Optionally, correct for the liquid junction potential (point VI).
6. Localize the pipette tip. Lower the microscope focus and the pipette toward the cell layer using the patch-arm microcontroller and focus control.
7. With the first signs of the cell layer, switch the focus and microcontroller options to establish finer movements. Focus on the target and re-center the pipette tip if necessary.
8. Approach the target cell until the resistance increases by a few 0.1 MΩ. This step also manifests as a dimple forming under the tip (Fig. 6.1.1. A).
9. Release the positive pressure and track the pipette resistance. The resistance should steadily increase by 10s of MΩ. Apply a steady suction until GΩ is reached.
10. Cancel the fast transients using auto C-FAST mode.
11. Wait for a few minutes until the seal (and the cell) is stabilized.

## IV Obtaining the whole-cell

1. Set the command potential to -60 mV.
2. Switch to the 1 ml syringe for the finer pressure control. Apply brief suction pulses to open the membrane. Slow capacitive transients are a sign of the membrane opening.
3. Switch to the current-clamp mode with the Gentle CC switch turned on to maintain the same holding potential.
4. After the recording session, take a brightfield micrograph of the patched neuron to capture its soma morphology or relative position.

## VI Additional: Experimental estimates of the liquid junction potential

1. Have the reference electrode in a salt bridge containing 3M KCl.
2. Both the bath and pipette should contain pipette solution with the offset cancellation.
3. After the cancellation, the bath is exchanged with extracellular patch solution.
4. The potential difference at 0pA applied current accounts for the LJP.

## Calcium imaging

### Materials

- Tweezers and pipette tips for coverslip extraction
- Plastic petri dish lids
- Superglue or vacuum grease for coverslip adhesion
- 21+ DIV neurons expressing jRCaMP1b
- Containers for waste collection
- Dismozon (if necessary)

### Solutions

- E-patch solution (Table B2) – ca. 4 ml per sample

### Instruments

- Upright microscope (AxioVision, Carl Zeiss AG)
- Light source (100 W HBO lamp, Zeiss)
- Water-immersive 20x objective (Olympus, UMPlanFl) or 10x objective (Zeiss)
- Fluorescence filter set (for jRCaMP1b: BP 546/12 excitation and LP 590 emission filter)
- Camera (sCMOS camera Zyla, Andor)
- Focus control (Luigs & Neumann, SM IV)
- Portable UV light for sterilization

### Software

- Andor Solis (Oxford instruments) software for acquisition
- ImageJ, open-source or custom-made Python code for video processing
- Self-made Python script for calcium signal analysis

### Acquisition settings

| | |
|---|---|
| Binning: | 4x4 |
| Pixel readout rate: | 560MHz – fastest readout |
| Electronic shutter mode: | global |

| | |
|---|---|
| Sensitivity and dynamic range: | 16 (high well capacity and low noise) |
| Orientation: | anti-clockwise (to match with the oculars) |
| Sampling frequency: | 50 Hz |
| Exposure time: | 0.02 s |
| Trigger: | internal, otherwise external start for combined measurements |
| Recording time (# of frames): | 100s (5000) |

## Procedure

1. Under the inverted microscope, observe the culture's overall fitness either under the brightfield, using fluorescence filters, or both. Healthy neurons produce relatively weak basal $Ca^{2+}$ signals compartmentalized to the cytosol.
2. Turn on the instruments.
    - CRITICAL STEP: Switch the HBO lamp at least 30 min before the imaging to reach thermal equilibrium.
3. Separate and immobilize the sample as described in Section I in the whole-cell patch-clamp standard protocol.
    - AAV waste is disposed of in a separate container and autoclaved. The surfaces are treated by UV light for 1 h.
4. Place the sample under the microscope and locate the cell layer under the brightfield.
5. Switch to the filter and move the stage along the X-Y axis to find the region of interest.
6. Record the spontaneous calcium activity. Long-term records should be obtained in shorter blocks separated by a period (minutes) of dark to prevent phototoxicity from prolonged light exposure.
7. After the measurement, dispose of the samples in GMO-designated container to be autoclaved and sterilize the working surfaces with UV/ Dismoson.

## MEA measurements

Below is the standard protocol for MEA measurement of spontaneous neuronal activity. Refer to Section 3.3.4 for combined MEA and patch-clamp measurements.

## Materials

- MEA samples with mature primary cortical neuronal culture (+14 DIV)
- Sterile tweezers for sample extraction
- Plastic petri dish for transport
- Pellet Ag/AgCl electrode
- Bath electrode connector
- MilliQ water, wipes, and Q-tips for treating eventual spillage

- 2x Glass beakers and plastic Pasteur pipettes (for sample cleaning)

## Solutions

- E-patch solution (Table B2) – ca. 1 ml per sample (alternatively, measure in the medium)
- Optional – 24 mM caffeine in E-patch stock solution – ca. 0.3 ml per sample
- Optionally, if the samples are to be cleaned on the same day:
    1. 0.05% Trypsin-EDTA (Sigma-Aldrich) – ca. 2 ml per sample;
    2. 1% Tergazyme (Alconox)

## Instruments

- MEA headstage (home-built MEA III.1)
- MEA amplifier (home-built BioMAS)
- Digitizer (USB-6255 DAQ (National Instruments))
- Faraday cage
- Heating plate
- Optional:
    - Upright microscope (AxioVision, Carl Zeiss AG)
    - Light source (100 W HBO lamp, Zeiss)
    - Non-immersive 10x objective (Zeiss)
    - Camera (sCMOS camera Zyla, Andor)
    - Focus control (Luigs & Neumann, SM IV)
    - anti-vibrational table (Thorlabs)

## Software

- Home-built LabView software for acquisition (or commercially available)
- Home-built Python code (BioMAS viewer) for data extraction
- Self-written Python code for .csv file opening and analysis
- Andor Solis (Oxford instruments) software for the brightfield snapshots

## Acquisition parameters

| | |
|---|---|
| Sampling frequency: | 10 kHz |
| High-pass filter: | 10-72 Hz |
| Amplifier gain: | 10-100* |
| Offset correction: | ON |
| ADC range: | ±10 V |
| Coupling | AC |

*The final gain is amplifier gain x headstage gain (10.1)

## Procedure

### I Preparation

1. If the samples are transparent, regularly observe the fitness of the culture under the inverted brightfield microscope. Healthy cells show well-defined somas adhered to the surface. Optionally, capture the brightfield snapshots of the culture. For non-transparent samples, observe the medium turbidity and color.
2. If measurements are in E-patch, thaw it in a water bath at 37 ºC, and heat on the heating plate pre-set to 37 ºC. Thaw the stock caffeine solution at 37 ºC if caffeine is to be added.
3. If the samples are to be cleaned after the recording session, thaw 0.015% trypsin in the water bath at 37 ºC.
4. Connect the MEA headstage to the amplifier.
    - CRITICAL STEP: Regularly observe the state of the headstage pins. To maintain the good state of the pins, headstage should be stored with leverage lifting the top from its base.
5. Connect the bath Ag/AgCl electrode to the headstage.
6. Turn on the instruments. Run acquisition software (home-built in LabView) and:
    - specify if the sample comes with a carrier;
    - define the electrode layout;
    - specify the acquisition parameters (shown above).

### II Measurement

1. Carefully transfer the sample onto the hot plate. Observe for any spillage. If necessary, carefully wipe the medium with wipes, clean any remaining salts using MilliQ and Q-tips, and dry the contact edges with wipes.
    - OPTIONAL: Replace the old medium with the E-patch.
2. Position the chip on the headstage base so that the numbered edge of the chip matches the bottom left corner of the layout. Consistent positioning is essential when recording the same culture over days. Any re-positioning should be documented.
3. Align and lower the headstage top to contact the pads. Apply even but light pressure during lowering.
4. Prior to measurement, observe the spontaneous neuronal activity in TimeSeries.
    - OPTIONAL: If the culture shows sparse activity, add 8 mM caffeine to induce and recruit more neurons to the network bursts (Section 4.1).
5. Press “Record” to start the measurement. Because of the large memory consumption, individual measures over all 64 channels should not exceed 100 s. The software creates .dat and .xml files for recording and metadata, respectively.
6. Optionally, focus the upright microscope and capture the brightfield micrograph.

7. TimeSeries and Record buttons are unticked before lifting the headstage top. Remove the bath electrode and place the sample on the Petri dish.
8. Should the measurement be repeated the next day, return the sample to the incubator designated for the non-sterile ("outside") samples.
9. Otherwise, start sample preparation for cleaning.

## III MEA sample cleaning

1. Remove the medium and add the pre-heated and vortexed trypsin (ca. 1 ml per sample) with plastic Pasteur pipette.
2. Incubate the samples on a hot plate at 37 ºC for 15 min. Replace the old with the fresh trypsin solution and repeat the process.
3. Pour 1% Tergazyme into a glass beaker and immerse the trypsin-treated samples for 30 minutes. The solution level should fully cover the samples.
4. Wash the samples for 24 h under de-ionized water.
5. $N_2$ dry and store the samples in a closed container until further use.

## Table B1. Pharmacological agents used in this thesis

| Compound (supplier) | Target[a] | Final concentration [µM] | Incubation time |
|---|---|---|---|
| **$GdCl_3$ (Sigma-Aldrich)** | Mechanosensitive conductances (-) | 50 | 5-10 min |
| **GsMTx4 (HelloBio)** | Piezo1, TRPC1 (-) | 1-2.5 | 5-10 min |
| **Cytochalasin D (Sigma-Aldrich)** | Actin polymerization (-) | 10 (0.1%)* | 5h |
| **Blebbistatin (-) (Sigma-Aldrich)** | Non-muscle MHCII (-) | 50 | ≥30 min |
| **$CdCl_2$ (Sigma-Aldrich)** | Calcium conductances (-) | 200 | 5-10 min |
| **Mibefradil (Sigma-Aldrich)** | T-type $Ca_v$s (-) | 5 | 5-10 min |
| **Nifedipine (Sigma-Aldrich)** | L-type $Ca_v$s (-) | 10 (0.05%)* | 5-10 min |
| **2-APB (HelloBio)** | SOCE (-) | 100 (0.1%)* | ≥30 min |
| **TTX (Tocris)** | $Na_v$s (-) | 1 | 5-10 min |
| **NBQX (Tocris)** | AMPAR (-) | 20 | 5-10 min |
| **Bicuculine (Tocris)** | $GABA_AR$ (-) | 20 | 5-10 min |
| **D-AP5 (Sigma-Aldrich)** | NMDAR (-) | 80 | 5-10 min |
| **CPPG (Tocris)** | mGluRs (Type II/III) (-) | 200 (0.2 mM) ** | 5-10 min |
| **AIDA (Tocris)** | mGluRs (Type I) (-) | 200 (0.2 mM) ** | 5-10 min |
| **CGP 55845 (Tocris)** | $GABA_BR$ (-) | 10 (0.1%)* | 5-10 min |
| **CBX (Tocris)** | Connexins (-) (universal) | 100 | ≥30 min |
| **Mefloquine-hydrochloride (Sigma-Aldrich)** | Connexins (-) (Cx50 and Cx36) | 25-50 (0.05-0.1%)* | ≥30 min |
| **Caffeine (Sigma-Aldrich)** | RyRs (+), purinergic receptors (+), network bursts (+) | 8000 | 5-10 min |

[a] (-): antagonistic effect; (+): agonistic effect
* Diluted in DMSO (final v/v%)
** diluted in 1.1 eq NaOH (final concentration of $Na^+$)

Table B2. Extracellular patch solution

| Substance (Supplier) | Concentration [mM] |
|---|---|
| NaCl (Sigma-Aldrich) | 120 |
| KCl (Sigma-Aldrich) | 3 |
| $MgCl_2$ (Sigma-Aldrich) | 1 |
| $CaCl_2$ (Sigma-Aldrich) | 2 |
| HEPES (Sigma-Aldrich) | 10 |

pH = 7.3, adjusted with NaOH; osmolarity adjusted with glucose

Table B3. K-gluconate internal solution

| Substance (Supplier) | Concentration [mM] |
|---|---|
| K-gluconate (Sigma-Aldrich) | 135 |
| KCl (Sigma-Aldrich) | 20 |
| $MgCl_2$ (Sigma-Aldrich) | 2 |
| $CaCl_2$ (Sigma-Aldrich) | 2 |
| HEPES (Sigma-Aldrich) | 10 |
| EGTA (Sigma-Aldrich) | 0.1 |
| $Na_2ATP$ (Sigma-Aldrich) | 2 |

pH = 7.3, adjusted with KOH; osmolarity adjusted with glucose.

Table B4. Symmetric Cl- pipette solution

| Substance (Supplier) | Concentration [mM] |
|---|---|
| KCl (Sigma-Aldrich) | 120 |
| $MgCl_2$ (Sigma-Aldrich) | 4 |
| HEPES (Sigma-Aldrich) | 10 |
| EGTA (Sigma-Aldrich) | 0.2 |
| MgATP (Sigma-Aldrich) | 0.2028 |
| NaCl (Sigma-Aldrich) | 2 |

pH = 7.3, adjusted with KOH; osmolarity adjusted with glucose

# Appendix C: Additional figures and tables

## C1. Benchmarking neural activity on NS-NC MEAs

### *Estimating chip coverage by cell material*

FITC staining was performed to calculate % of covered chip area. Following the image acquisition, a mask was set to exclude background fluorescence and calculate the coverage ratio by the cell material, as shown below.

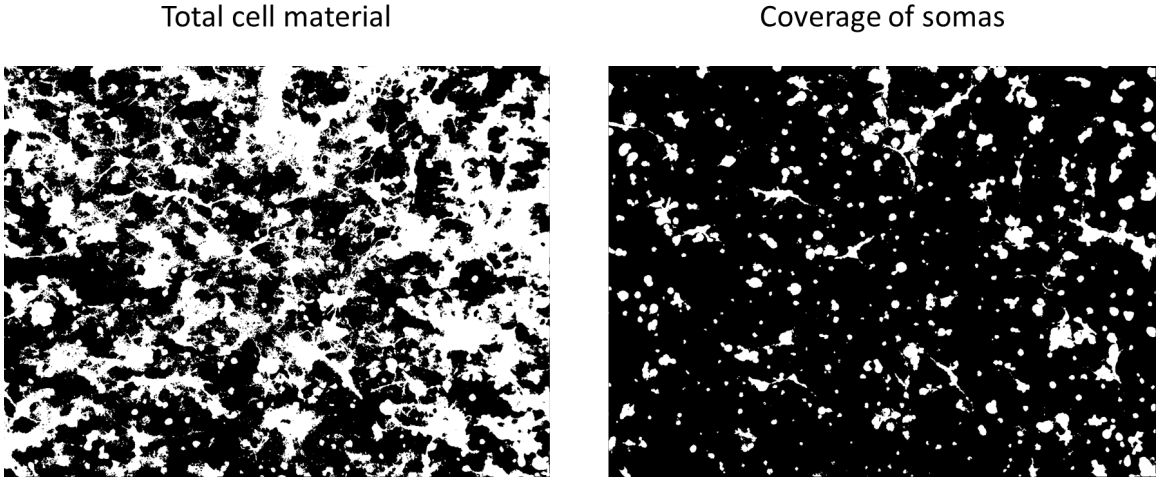


**Figure C1. Estimation of chip coverage % by selective masking of FITC signals.** Left: Mask threshold was set to include both somas and neurites. Right: Mask was set to include only somas. Coverage ratio was estimated as (# of bright pixels) / (total # of pixels).

## *Long-term IN-CELL EAPs*

The figure below shows IN-CELL EAPs, detected ca. 0.5 h before and during simultaneous patch-clamp measurement. Note the visibility of subthreshold pre-depolarizations in spontaneous IN-CELL EAPs prior to the patch-clamp measurement, indicating that IN-CELL configuration arises from stable neuron-electrode coupling.

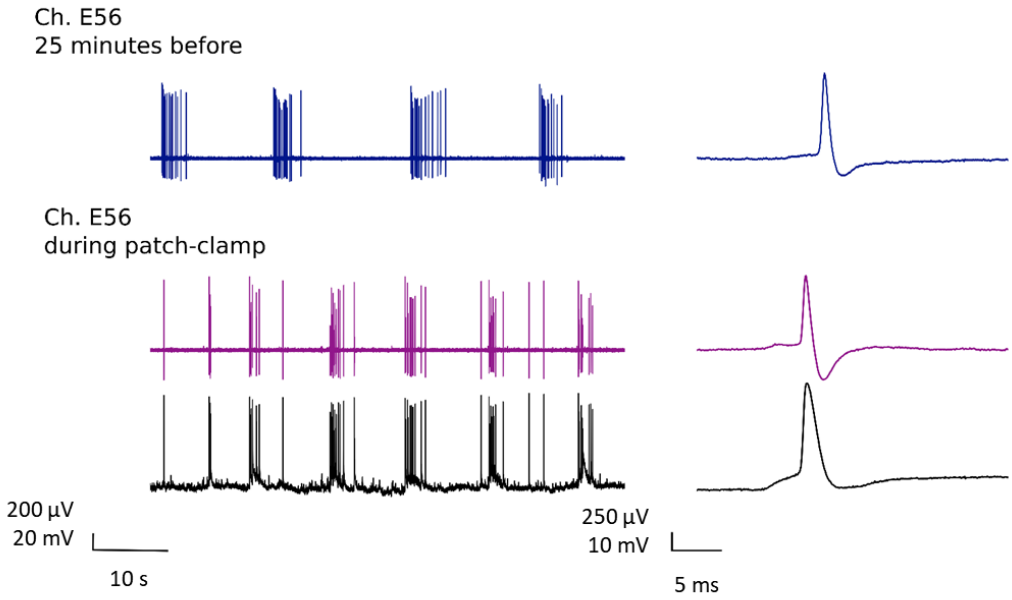


**Figure C2. IN-CELL configuration is stable throughout the recording.** Top: Activity on channel 56 25 min prior to the on-chip patch-clamp measurement. Bottom: paired patch-clamp and MEA measurements of the same neuron. Zoomed-in micrographs depict EAP's preservation throughout the whole measurement. Figure shows the results published in: [27]

## *EAP amplitude does not decrease with distance from the soma*

The figure below shows exponential decay fit on SNR-soma distance relation, performed in Origin. Electrode distances were obtained from brightfield micrographs reporting the patched soma and electrode position using ImageJ. The exponential decay fit failed to converge. Thus, EAPs arise from signal transfer at coupled compartment, rather than from long-range electrical fields.

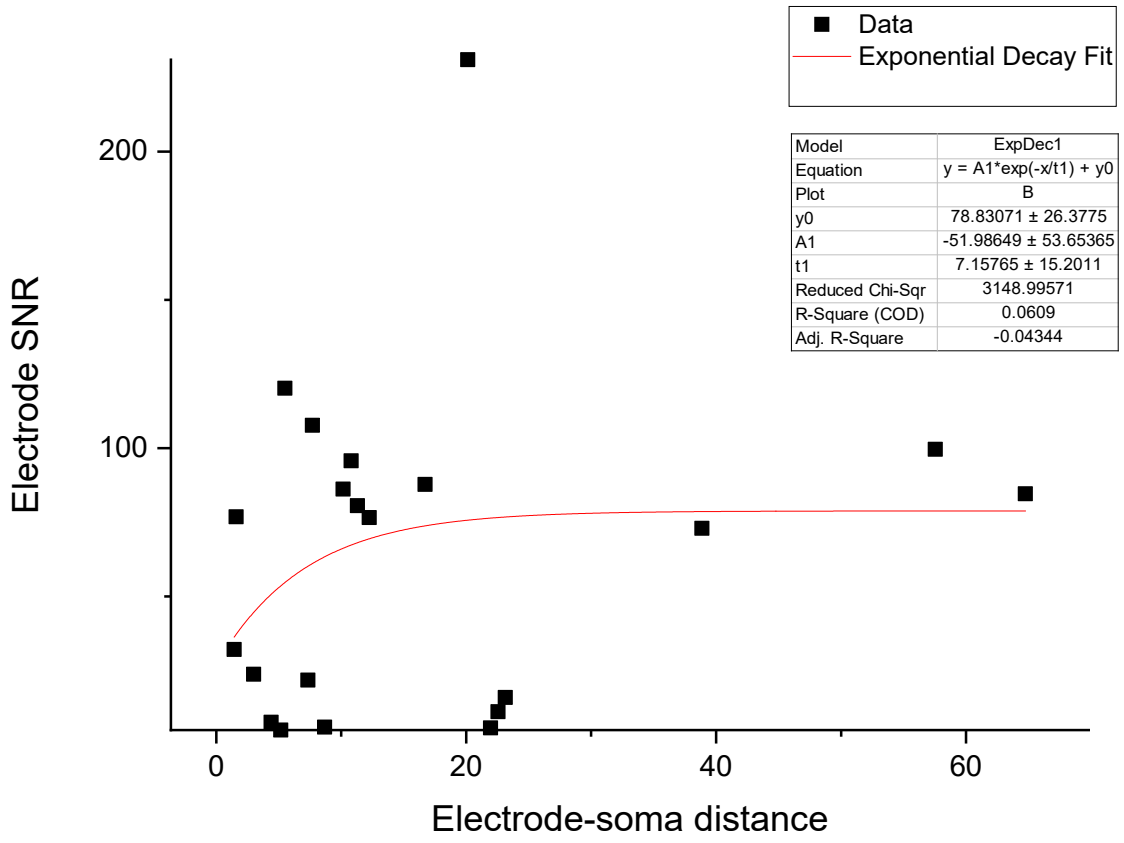


**Figure C3. Non-linear fit of SNR vs. electrode-soma distance failed to converge.** Y-axis represents maximum SNR for a given paired recording, calculated as the ratio of a maximum signal peak-to-peak amplitude and RMS of the trace. X-axis depicts the measured distance between the soma and recording electrode in microns. The table on the top right corner displays all the fit parameters, including the metrics of the fit quality.

### *EAP-IAP delays depend on the IAP dynamics*

As IN-CELL EAPs fall between the first IAP time derivative and IAP waveform, they show positive and negative delays to the IAP time derivative and IAP peaks, respectively. The figure below demonstrates another layer of variation of the delays, related to the UP slope of IAP waveform. In particular, faster IAPs experience larger absolute IAP-EAP delays, whereas there are larger delays for slower IAPs.

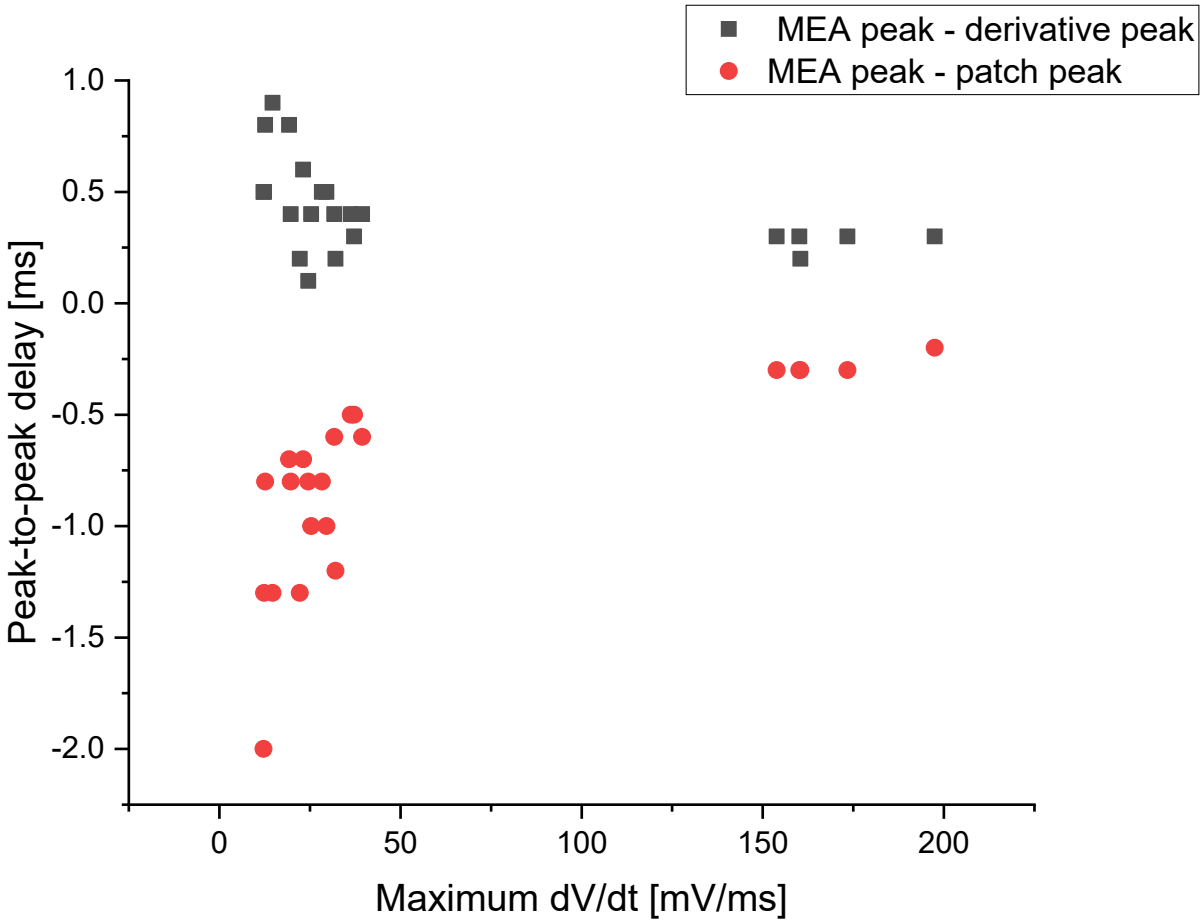


**Figure C4. Exemplary IAP-EAP peak delays as a function the UP slope of an IAP.** Depicted are EAP – IAP derivative (black) and EAP-IAP latencies (red) as a function of IAP UP-slope.

## *Summary of IAP-EAP relation from on-chip patch-clamp benchmarking*

Below are presented all benchmarked NS-NC electrode – neuron couplings with paired electrophysiology (Section 4.2).

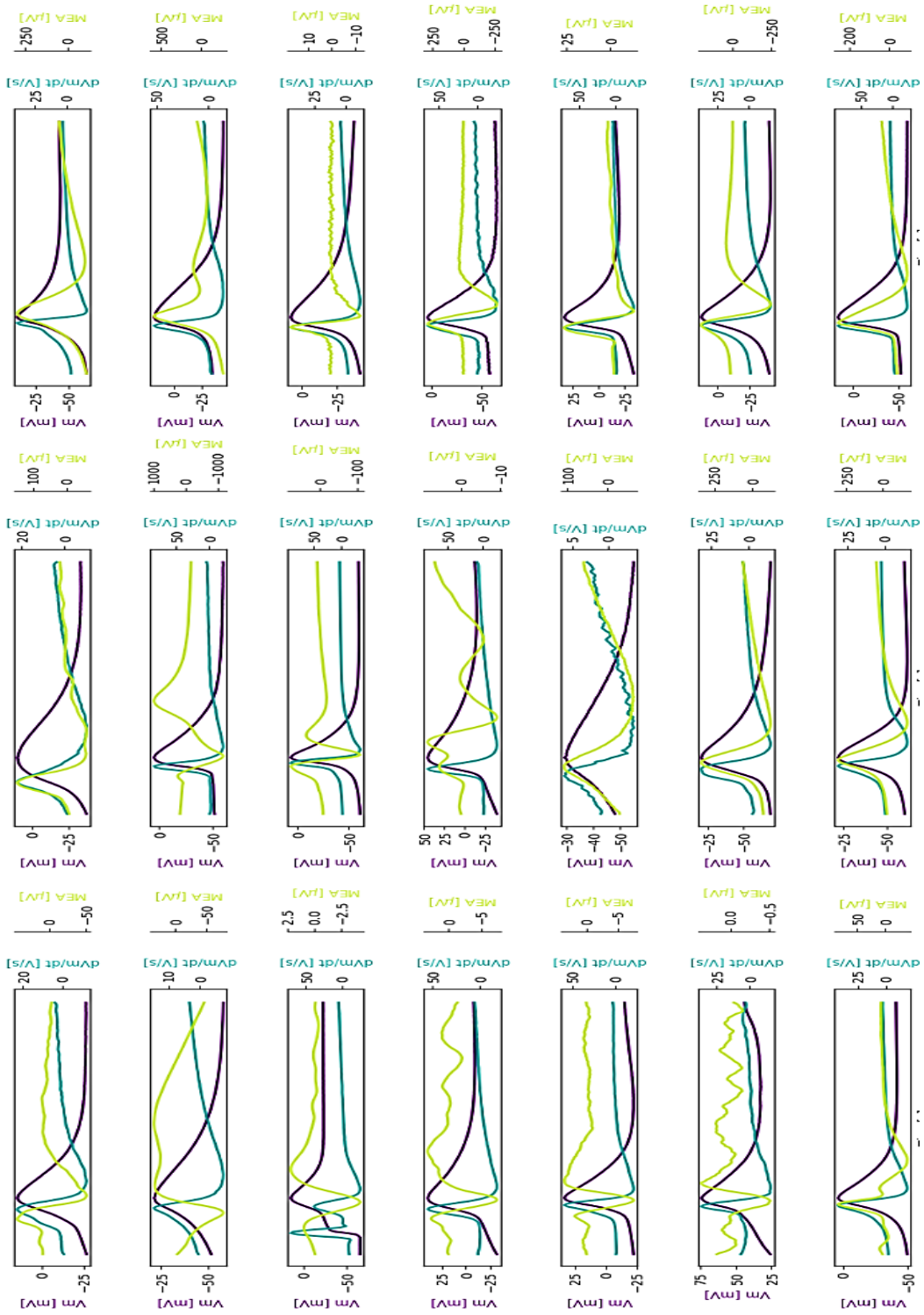

**Figure C5. Summary of all on-chip patch-clamp measurements in electrode-coupled neurons.** Depicted are averaged IAPs (dark purple), their first temporal derivatives (turquoise) and corresponding EAPs (yellow). All windows were centered on IAP maxima. For measurements with only evoked APs (i.e., 1st column, 3rd row), the first temporal derivative shows peaks matching the step-wise membrane depolarization due to the current injection.

## *High SNR neuron-electrode coupling excluded from spike-sorter benchmarking*

Automatic spike sorters were benchmarked on long-term measurements of spontaneous, high SNR activity. One paired recording involved pharmacological intervention by 8 mM caffeine, which resulted in abrupt EAP waveform change. Not to confound this waveform change by spontaneous EAP variations, this set was excluded although it satisfied all other criteria.

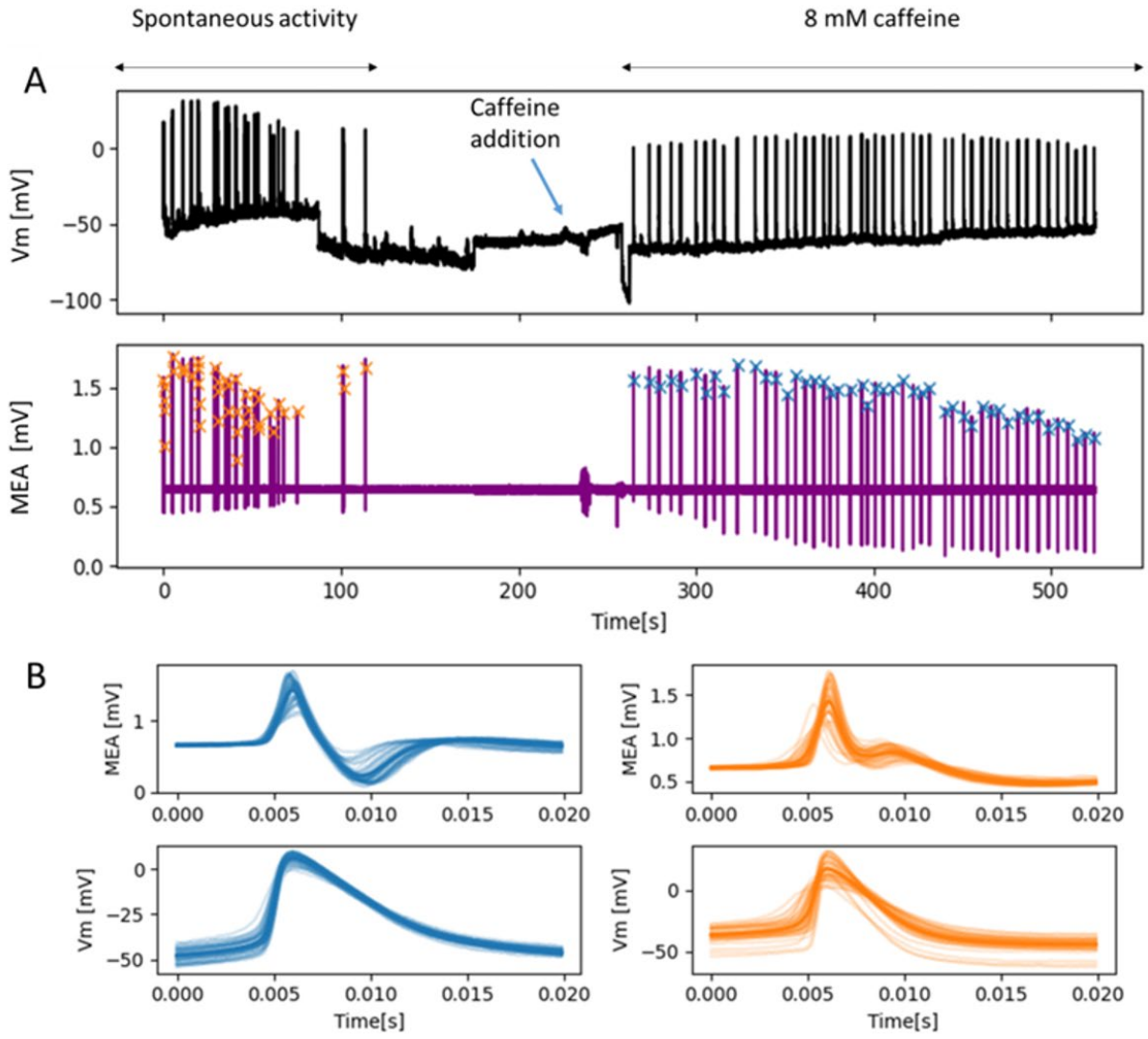


**Figure C6. Recording excluded from sorter benchmarking on high SNR recordings with spontaneous activity.** A. Simultaneous patch-clamp (black) and MEA measurement (purple) of spontaneous activity excluded from benchmarking despite the SNR = 51. Following the 100 s measurement of native activity, caffeine was applied to the bath at about 280 s. A transient hyperpolarization following caffeine addition is manifested as a dimple in both traces. Spike-sorter found two EAP clusters, separated by caffeine application (colors of x-es indicate spike indices belonging to different clusters). B. Top: superimposed EAPs before (orange) and after the caffeine addition (blue). Bottom: corresponding IAPs.

**Table C1. Performance of spike sorters**

| Accuracy | | | | | | |
|---|---|---|---|---|---|---|
| Recording | MS4 | TDC | KL | SC | WC | CO |
| *151020_E56* | 0.351662 | 0.5 | 0.430946 | 0.751918 | 0.704739 | 0.535623 |
| *151020_E59* | 0.626016 | 0.3357 | 0.345274 | 0.613868 | 0.783534 | 0.552174 |
| *091020_E55* | 0.983607 | 0.819672 | 0.9375 | 0.983607 | 0.870968 | 0.57377 |
| *020221_E44* | 0.530864 | 0.54321 | 0.51087 | 0.300699 | 0.506173 | 0.463415 |
| *310320_E55* | 0.655738 | 0.376238 | 0.288636 | 0.184375 | 0.540541 | 0.57622 |
| *310320_E62* | 0.475783 | 0.410256 | 0.817664 | 0.478992 | 0.407407 | 0.348525 |
| *030420_E56* | 0.527027 | 0.691892 | 0.776882 | 0.55832 | 0.759459 | 0.551867 |
| *030420_E34* | 0.407925 | 0.260918 | 0.577023 | 0.584842 | 0.220418 | 0.558939 |
| *060320_E43* | 0.804878 | 0.515152 | 0.846154 | 0.478261 | 0.697674 | 0.648649 |
| *260520_E55* | 0.544041 | 0.571066 | 0.412602 | 0.592593 | 0.544041 | 0.668904 |

| Recall | | | | | | |
|---|---|---|---|---|---|---|
| Recording | MS4 | TDC | KL | SC | WC | CO |
| *151020_E56* | 0.351662 | 0.5 | 0.430946 | 0.751918 | 0.741688 | 0.538363 |
| *151020_E59* | 0.627931 | 0.337411 | 0.353721 | 0.98369 | 0.863405 | 0.647299 |
| *091020_E55* | 0.983607 | 0.819672 | 0.983607 | 0.983607 | 0.885246 | 0.57377 |
| *020221_E44* | 0.5375 | 0.55 | 0.5875 | 0.5375 | 0.5125 | 0.475 |
| *310320_E55* | 0.660066 | 0.376238 | 0.419142 | 0.194719 | 0.660066 | 0.623762 |
| *310320_E62* | 0.475783 | 0.410256 | 0.817664 | 0.487179 | 0.407407 | 0.37037 |
| *030420_E56* | 0.527027 | 0.691892 | 0.781081 | 0.97027 | 0.759459 | 0.718919 |
| *030420_E34* | 0.407925 | 0.271562 | 0.772727 | 0.602564 | 0.221445 | 0.66317 |
| *060320_E43* | 1 | 0.515152 | 1 | 1 | 0.909091 | 0.727273 |
| *260520_E55* | 0.544041 | 0.582902 | 0.525907 | 0.704663 | 0.544041 | 0.774611 |

| Precision | | | | | | |
|---|---|---|---|---|---|---|
| Recording | MS4 | TDC | KL | SC | WC | CO |
| *151020_E56* | 1 | 1 | 1 | 1 | 0.933977 | 0.990588 |
| *151020_E59* | 0.995153 | 0.985119 | 0.93531 | 0.62018 | 0.894403 | 0.789801 |
| *091020_E55* | 1 | 1 | 0.952381 | 1 | 0.981818 | 1 |
| *020221_E44* | 0.977273 | 0.977778 | 0.79661 | 0.40566 | 0.97619 | 0.95 |
| *310320_E55* | 0.990099 | 1 | 0.481061 | 0.776316 | 0.749064 | 0.883178 |
| *310320_E62* | 1 | 1 | 1 | 0.966102 | 1 | 0.855263 |
| *030420_E56* | 1 | 1 | 0.993127 | 0.568038 | 1 | 0.703704 |
| *030420_E34* | 1 | 0.869403 | 0.694969 | 0.952118 | 0.979381 | 0.780521 |
| *060320_E43* | 0.804878 | 1 | 0.846154 | 0.478261 | 0.75 | 0.857143 |
| *260520_E55* | 1 | 0.965665 | 0.656958 | 0.788406 | 1 | 0.830556 |

*MS4- MountainSort 4, TDC – Tridesclous, KL – Klusta, SC – Spyking Circus, WC – Waveclus, CO – Combinato*

**Table C2. Miss rate during the spike finding, estimated on 7 recordings with >8 SNR.**

| Miss rate | | | | | | |
|---|---|---|---|---|---|---|
| **Recording** | **MS4** | **TDC** | **KL** | **SC** | **WC** | **CO** |
| *151020_E56* | 0.021739 | 0.258312 | 0.021739 | 0.035806 | 0.02046 | 0.103581 |
| *151020_E59* | 0.033639 | 0.491335 | 0.01631 | 0.01631 | 0.062181 | 0.147808 |
| *091020_E55* | 0.011364 | 0.090909 | 0.011364 | 0.011364 | 0.011364 | 0.045455 |
| *020221_E44* | Nan | Nan | Nan | Nan | Nan | Nan |
| *310320_E55* | 0.141914 | 0.623762 | 0.623762 | 0.270627 | 0.392739 | 0.267327 |
| *310320_E62* | 0.108262 | 0.2849 | 0.17094 | 0.122507 | 0.168091 | 0.22792 |
| *030420_E56* | 0.010811 | 0.208108 | 0.010811 | 0.013514 | 0.027027 | 0.027027 |
| *030420_E34* | Nan | Nan | Nan | Nan | Nan | Nan |
| *060320_E43* | 0 | 0.484848 | 0 | 0 | 0.090909 | 0.272727 |
| *260520_E55* | Nan | Nan | Nan | Nan | Nan | Nan |

MS4- MountainSort 4, TDC – Tridesclous, KL – Klusta, SC – Spyking Circus, WC – Waveclus, CO – Combinato. Nan denotes recordings excluded from these estimations due to electrode detection of the signals from multiple neurons.

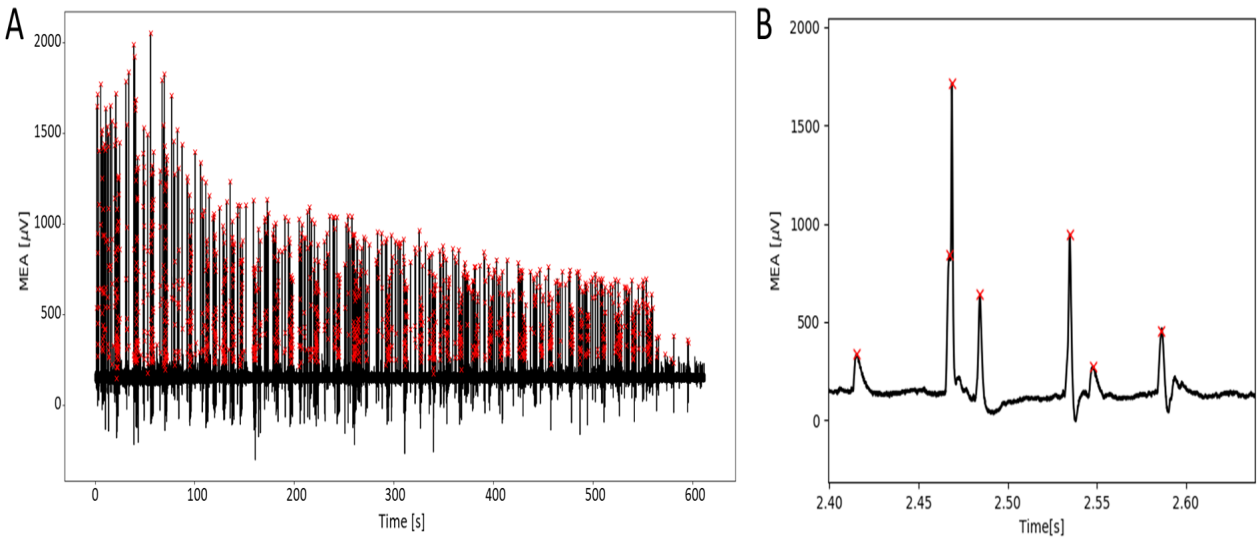


**Figure C7. False positives detected by Spyking Circus.** In high SNR MEA traces that also showed sensitivity for subthreshold events, SC found and clustered patched neurons' predepolarizations and ecPSPs into the best-matching unit. Thus, false positives mainly arose from assigning non-firing events of the same neuron to the EAP unit. A. A 10 min MEA trace with marked spikes found by Spyking Circus. B. Zoom-in showing recognition of EAPs, subthreshold pre-depolarizations, and individual ecPSPs.

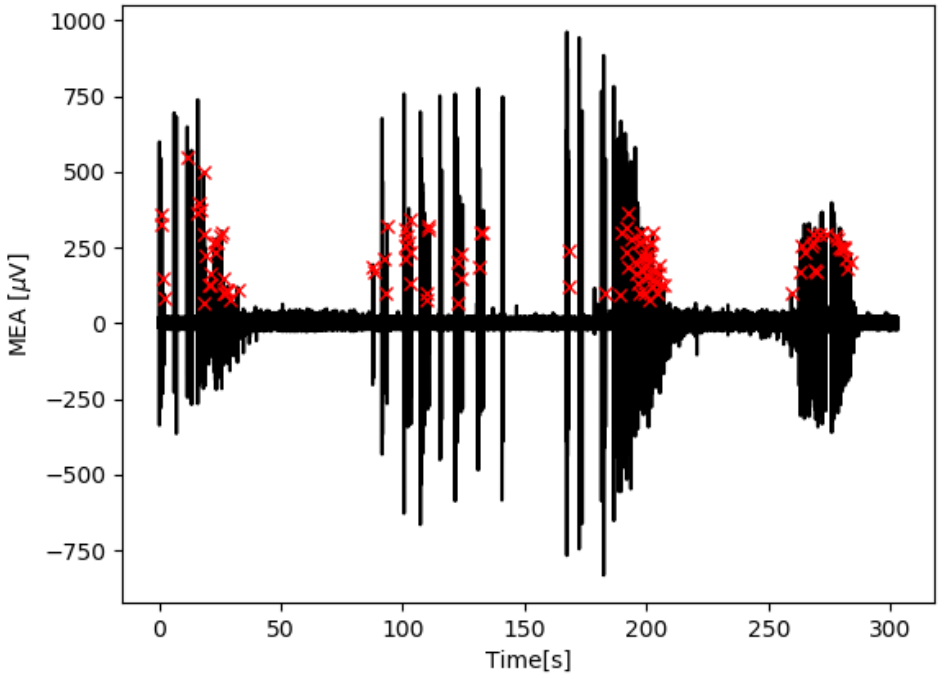


**Figure C8. High-amplitude EAPs omitted by Tridesclous.** An exemplary MEA trace showing omission of high-amplitude EAPs due to a hard-recognition of high-voltage events as artefacts.

## *Clustering errors estimated by WaveClus*

NS-NC MEA electrode sporadically coupled with more than one neuron, leading to true multi-source activity. In three benchmarked sets, the coupled neighbor's EAPs were detected alongside the target neuron's EAPs. Sporadically, the EAPs from the two sources merged to produce complex waveform. The first two instances (Fig. C9 A-B), with other neuron's EAPs comparable in magnitude to the target's EAPs, had clustering affected by EAP collision. The third instance (Fig. C9 C), with other neuron's EAPs significantly smaller than the target, shows clustering unaffected by the spike collision.

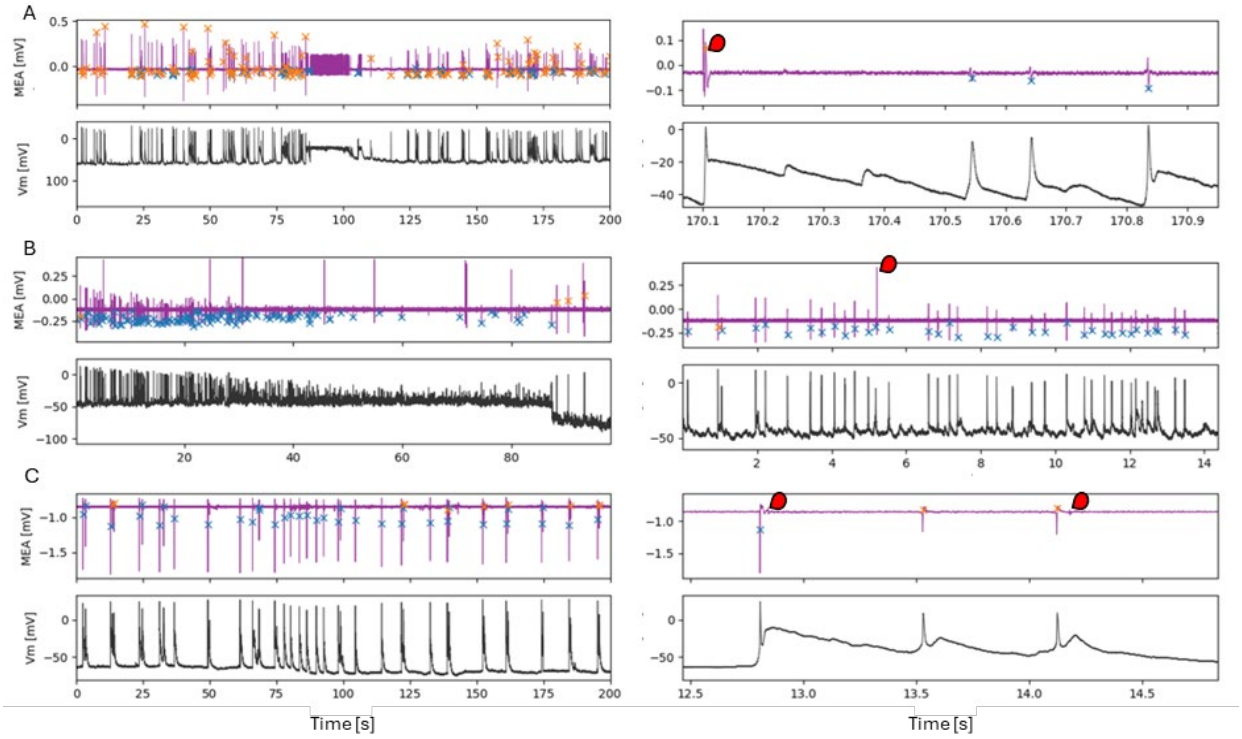


**Figure C9. Misclassifications as a consequence of spike collision in multi-spiking trains.** Simultaneous patch-clamp (black) and corresponding MEA signal (purple) containing spikes from the target and the coupled neighbor (red marks). A-B: Collisions of similar amplitude EAPs from various sources led to EAP misclassifications non-related to the intrinsic factors. C. An almost 100x higher amplitude of the target's EAPs led to classifications with respect to the target neuron's EAPs, despite sporadic spike collisions.

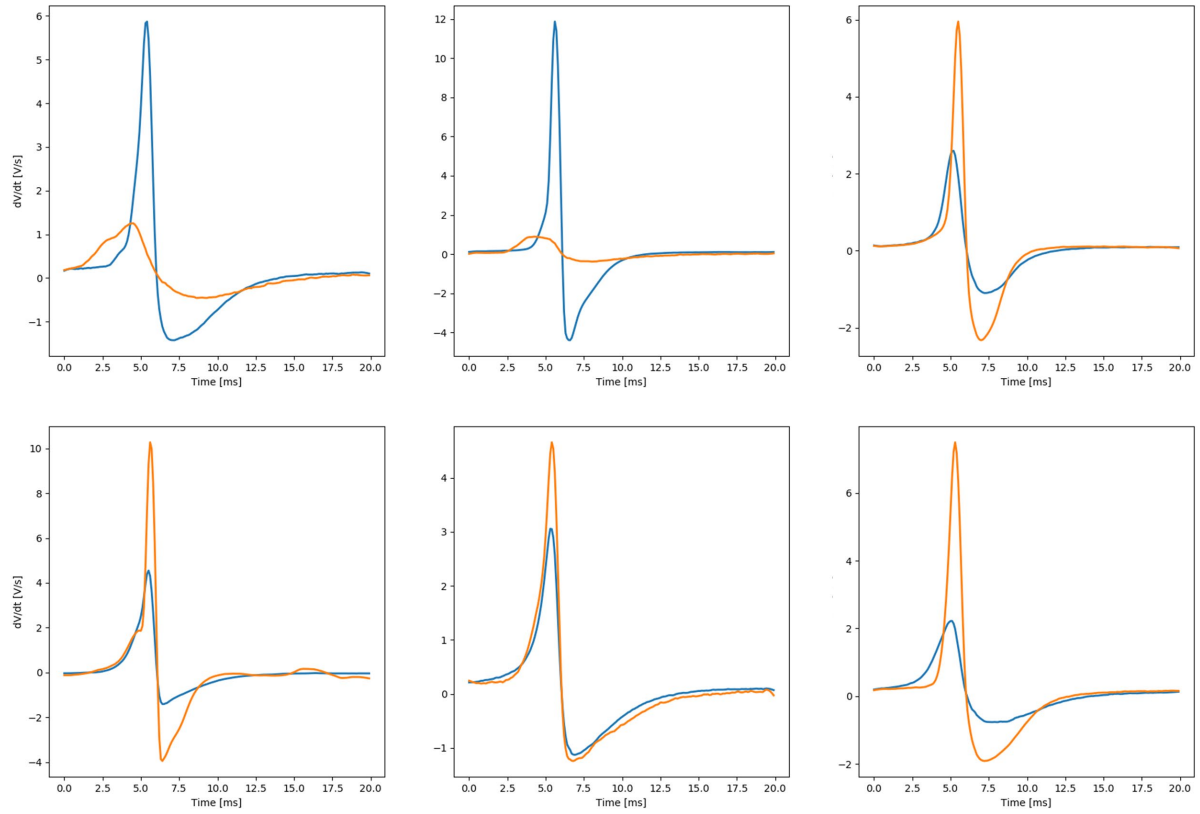


**Figure C10. First temporal IAP derivatives for different spike-sorter units.** Every plot represents the 1st temporal derivatives for the best (blue) and other (orange) spike-sorter units presented in Fig. 3.1.4.4.

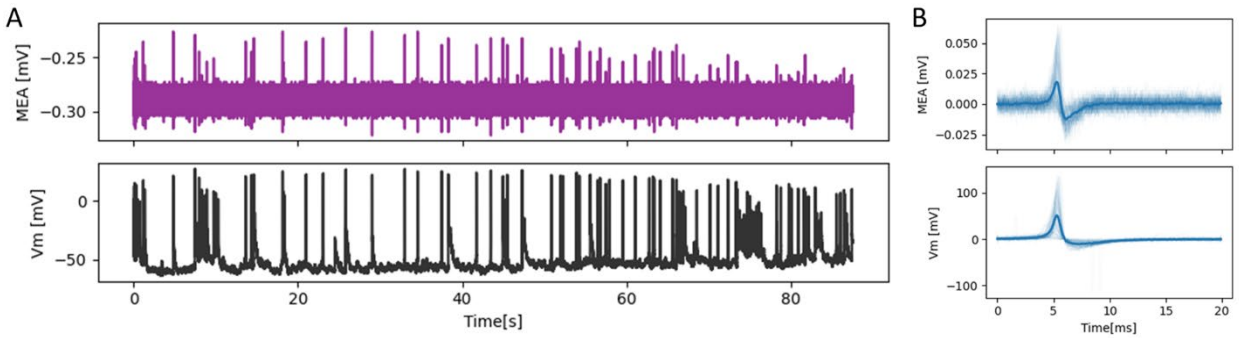


**Figure C11. Low SNR traces show no misclassifications, despite the bursting regime.** A. Inset of spontaneous activity detected by simultaneous MEA (purple) and patch-clamp (black) measurements. B. Zoom in on EAPs (top) and IAPs (bottom) after the SPC clustering via WaveClus.

## *IAP-EAP transfer function consistency evaluated by NN models*

Several NN models were trained, validated and tested on a subset of IAP-EAP pairs of the spike unit containing the most EAPs (BU). The trained model was then tested on the spike unit

containing fewer EAPs (OU). Table C3 denotes the number of IAP-EAP pairs for each step of the EAP prediction, and Table C4 reports each model's performances.

**Table C3. Number of spikes for NN training, validation, and testing**

| Recording # | BU training | BU validation | BU test | OU test |
|---|---|---|---|---|
| 1 | **154** | **77** | **76** | **63** |
| 2 | **262** | **131** | **131** | **260** |
| 3 | **358** | **179** | **179** | **265** |
| 4 | **131** | **65** | **65** | **42** |
| 5 | **97** | **48** | **49** | **88** |

*BU – Best Unit, OU – Other Unit*

**Table C4. Comparisons of the models' prediction of EAPs from corresponding IAPs**

| **MSE** | | | | | | | | | | |
|---|---|---|---|---|---|---|---|---|---|---|
| | Lin_reg | | Conv1d | | Conv1d_2l | | LSTM | | Dense_ReLU | |
| Rec # | BU | OU | BU | OU | BU | OU | BU | OU | BU | OU |
| 1 | **933** (874) | **1881** (1774) | **1289** (832) | **1575** (1574) | **744** (809) | **1534** (1628) | **364** (454) | **5958** (1964) | **307** (568) | **933** (815) |
| 2 | **412** (498) | **2349** (3884) | **681** (728) | **5925** (8780) | **410** (574) | **2144** (3313) | **407** (586) | **5303** (7672) | **350** (366) | **3280** (5636) |
| 3 | **1948** (2851) | **12317** (24150) | **3297** (3763) | **17980** (30051) | **2365** (3213) | **11468** (22854) | **2807** (5054) | **20693** (30201) | **1916** (4121) | **11996** (27646) |
| 4 | **3688** (3727) | **10118** (7202) | **2016** (2702) | **9444** (3646) | **3350** (3124) | **9748** (6218) | **2326** (4231) | **6997** (7724) | **1661** (1992) | **8380** (5291) |
| 5 | **78** (71) | **450** (490) | **86** (63) | **803** (731) | **80** (62) | **610** (545) | **86** (87) | **1426** (1522) | **77** (68) | **723** (479) |

| **MAE** | | | | | | | | | | |
|---|---|---|---|---|---|---|---|---|---|---|
| | Lin_reg | | Conv1d | | Conv1d_2l | | LSTM | | Dense_ReLU | |
| Rec # | BU | OU | BU | OU | BU | OU | BU | OU | BU | OU |
| 1 | **24** (11) | **35** (16) | **25** (10) | **31** (11) | **21** (13) | **32** (15) | **14** (8) | **50** (12) | **13** (9) | **23** (9) |
| 2 | **17** (9) | **38** (27) | **21** (12) | **61** (32) | **16** (10) | **37** (23) | **16** (11) | **52** (31) | **15** (9) | **47** (31) |
| 3 | **37** (25) | **87** (68) | **48** (27) | **108** (71) | **42** (26) | **84** (59) | **44** (34) | **107** (64) | **36** (36) | **85** (72) |
| 4 | **48** (23) | **81** (37) | **37** (20) | **82** (23) | **45** (24) | **79** (37) | **39** (32) | **74** (32) | **33** (19) | **74** (30) |
| 5 | **7** (3) | **16** (9) | **7** (3) | **23** (11) | **7** (3) | **20** (9) | **8** (4) | **28** (16) | **7** (3) | **21** (8) |

*Lin_reg: linear regression; Conv1d: 1-dimensional convolutional layer; Conv1d_2l: 1-dimensional convolutional model comprised of 2 layers; LSTM – long short-term memory; Dense_ReLU: model comprised of multiple densely connected layers with ReLU activation; BU: best unit; OU – other unit; presented are median MAE values (IQR).*

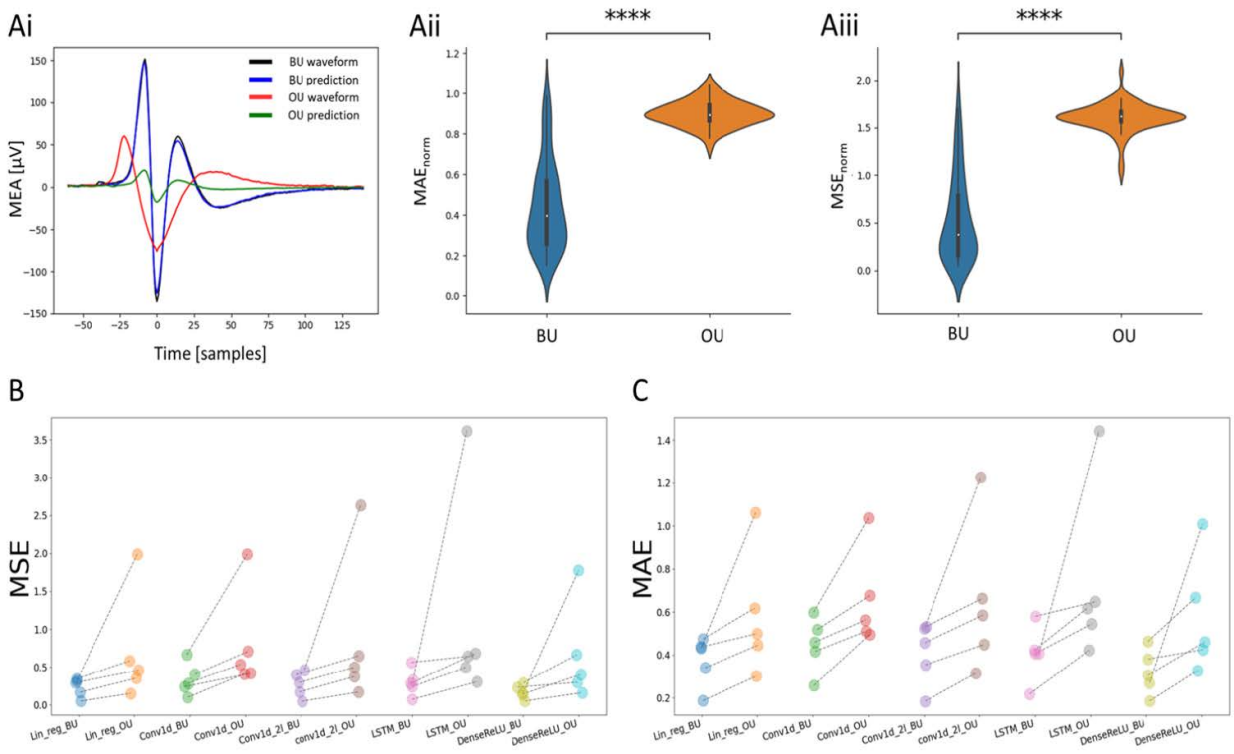


**Figure C12. Performance of NN models predicting EAPs from the first time IAP derivatives.** Models were trained on the subset of IAP-EAP pairs from unit with most spike pairs, the best unit (BU). Trained models were tested on BU and another spike-sorter unit (OU). Here, performances were estimated by comparison of EAP waveforms and predictions, both normalized to the mean and standard variation of corresponding EAP. A. Model prediction vs. the actual output from conv1d network on an exemplary recording. Ai. Comparisons of averaged traces and predictions for BU and OU. Figures on the right depict normalized MSE (Aii) and MAE (Aiii) on all spikes for the model in Ai. B. MSEs for BU and OU of each model. C. Normalized MAEs for each model.

## *IAP and EAP pre-processing prior to transfer function estimates*

Prior to explicit transfer function estimates (Section 4.5), both IAPs and EAPs were filtered with a 10 – 4000 Hz Butterworth filter. The figure below shows that this pre-processing step did not alter the waveforms.

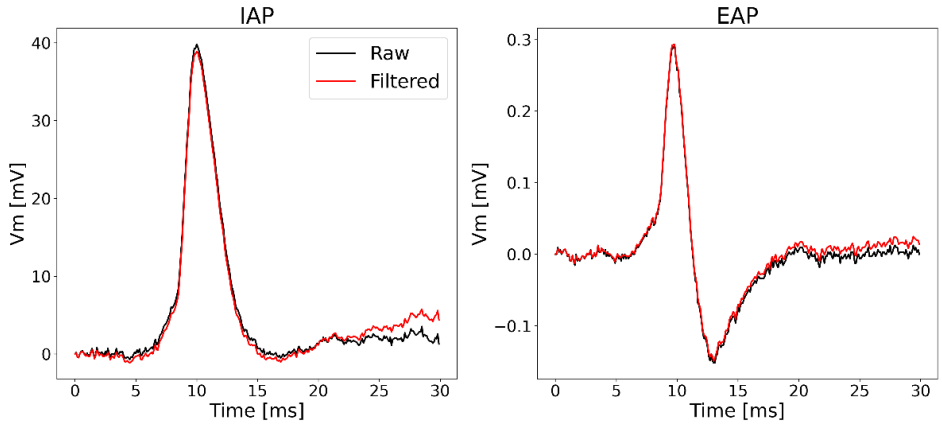


**Figure C13. Band-pass filtering has minimal effect on the waveform.** Left figure depicts raw trace of the of IAP (black) and bandpass filtered signal (red). The right figure corresponds to the raw and filtered EAP.

### *Direct IAP-EAP transfer function estimates*

Transfer function can be directly estimated for each IAP-EAP pair as $H = FFT(EAP) / FFT(IAP)$. These direct estimates are biased by noise, introducing large uncertainties in magnitude and phase plots. Large uncertainties were introduced by intrinsically noisier EAPs and spectral peaks at unmatching frequencies, especially above 1 kHz (Fig. C14 B). Similar peaks were also reported for EAPs detected by nanocavity-only MEAs,[193] and likely stem from acquisition, but this remains to be further elucidated. The large uncertainties denoted in explicitly estimated transfer functions from individual IAP-EAP pairs (Fig. C14 C-D) inspired the batch-fitting procedure both in 200 and 5- node NN models (Section 4.5).

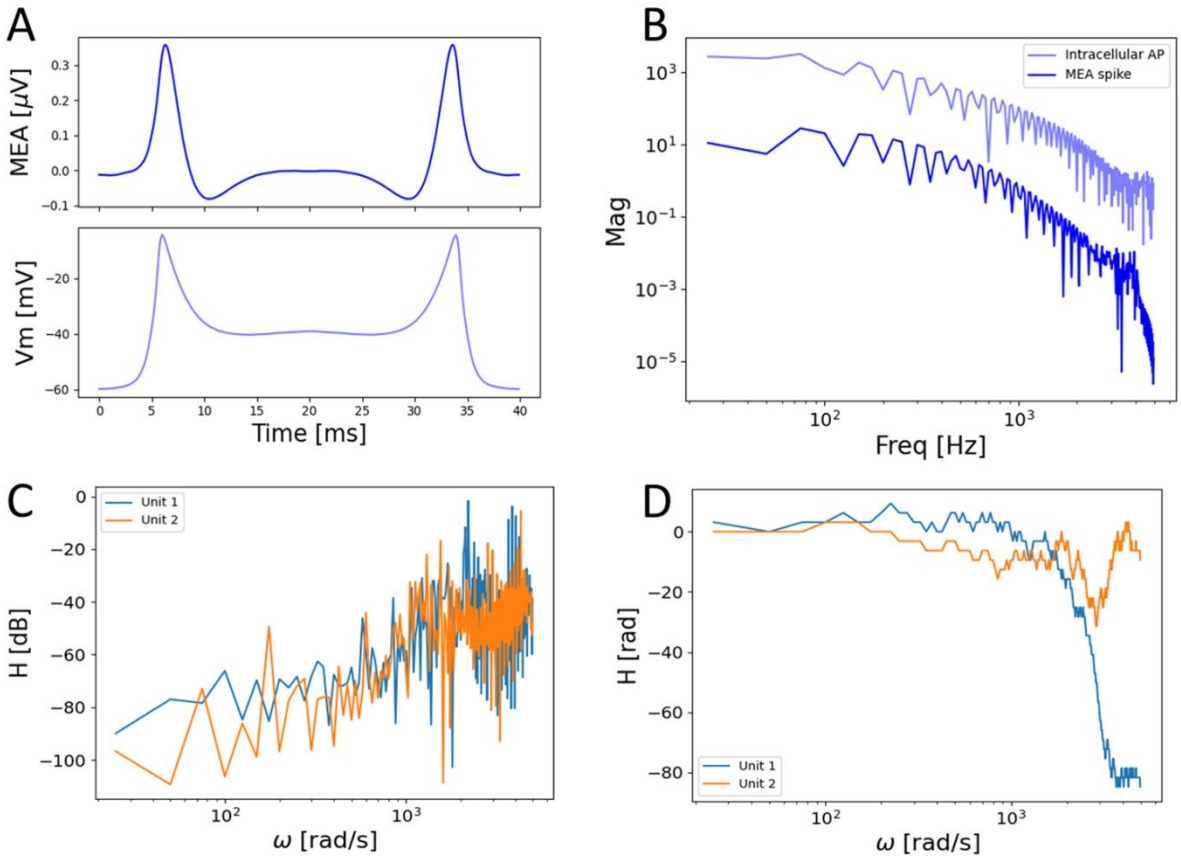


**Figure C14. Explicit estimations of IAP-EAP transfer functions from the spike relations in Fourier domain.** A. Averaged EAP (top) and IAP (bottom), mirrored to account for a false periodicity at the edges. B. FFT spectra of IAPs (light blue) and EAPs (dark blue), calculated from the discrete FFT on spikes in A. Non-matching frequency peaks in EAP FFT, especially for the high frequency ranges, introduced uncertainties in explicit transfer function estimates. C. Magnitude Bode plot for explicitly calculated TFs, from FFT of averaged EAPs and IAPs for different spike-sorter units. D. Phase Bode plot for explicitly calculated TFs.

Scaling one of the two transfer functions to mimic the purely Ohmic changes in the coupling did not produce a full overlap. Therefore, the found transfer function inconsistencies are not solely due to Ohmic coupling changes.

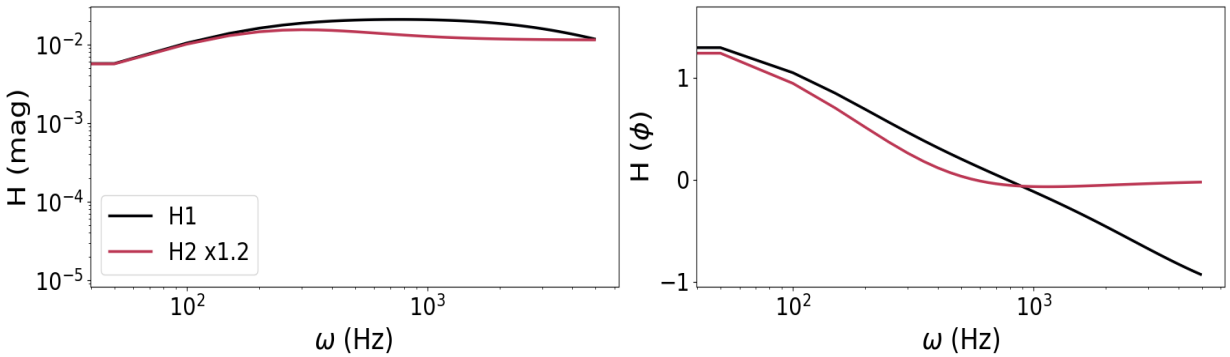


**Figure C15. Differences in transfer functions are not uniform across frequency ranges.** Bode magnitude(left) and phase (right) plots of the two transfer function found for coupling with positive monophasic signals. The second transfer function (H2) was scaled by 1.2 to elucidate if magnitude differences were universal and consistent for given frequency ranges.

Both 200-node and reduced NN model produced $H(j\omega)$ with apparent band-pass filtering profiles, with rising magnitude until 1 kHz and a magnitude drop at > 1 kHz (Section 4.2 and 4.5). Since noise predominates high-frequency ranges, a bias in transfer function estimates is expected. It is also expected that > 1 kHz ranges are less critical for EAP-from-IAP predictions. To evaluate whether the low-pass profiles at >1 kHz arise from physical process or fitting artefact from less parameter sensitivity, the found $H(j\omega)$ were altered to be either consistent or rising above 1 kHz. Fitting was not affected by either alternation.

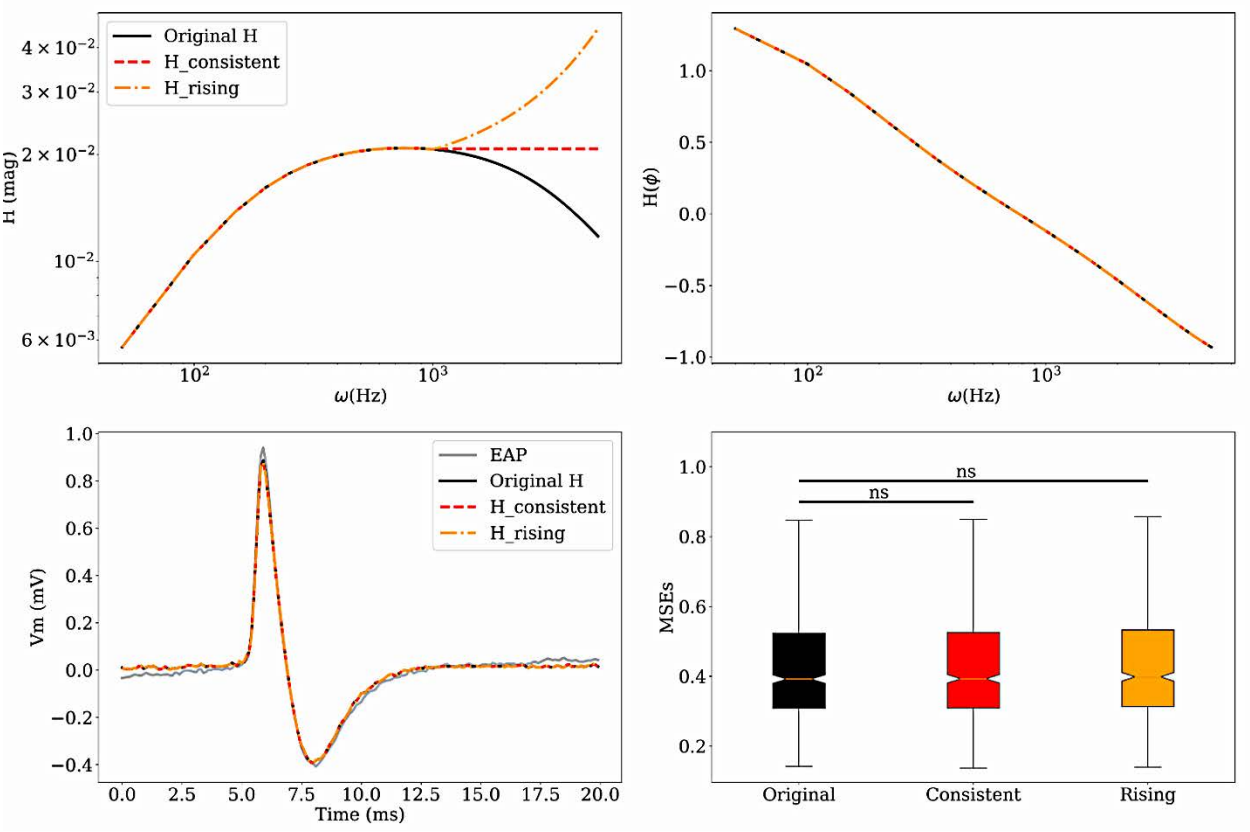


**Figure C16. Apparent low-pass effect above 1 kHz stems from reduced parameter sensitivity.** Top: Bode magnitude(left) and phase (right) plots of original and modified transfer functions to be consistent or rising at > 1 kHz. Bottom: exemplary EAP and corresponding EAP predictions, as well as pooled MSEs indicate the same prediction outcome for modified transfer functions.

Figure C17 indicates the fitting performance of 4 found transfer functions for IAP-triphasic EAP spike pairs. The notch feature, specific for sharp triphasic EAPs, could be obtained by fitting the transfer function with the 2nd order complex polynomial.

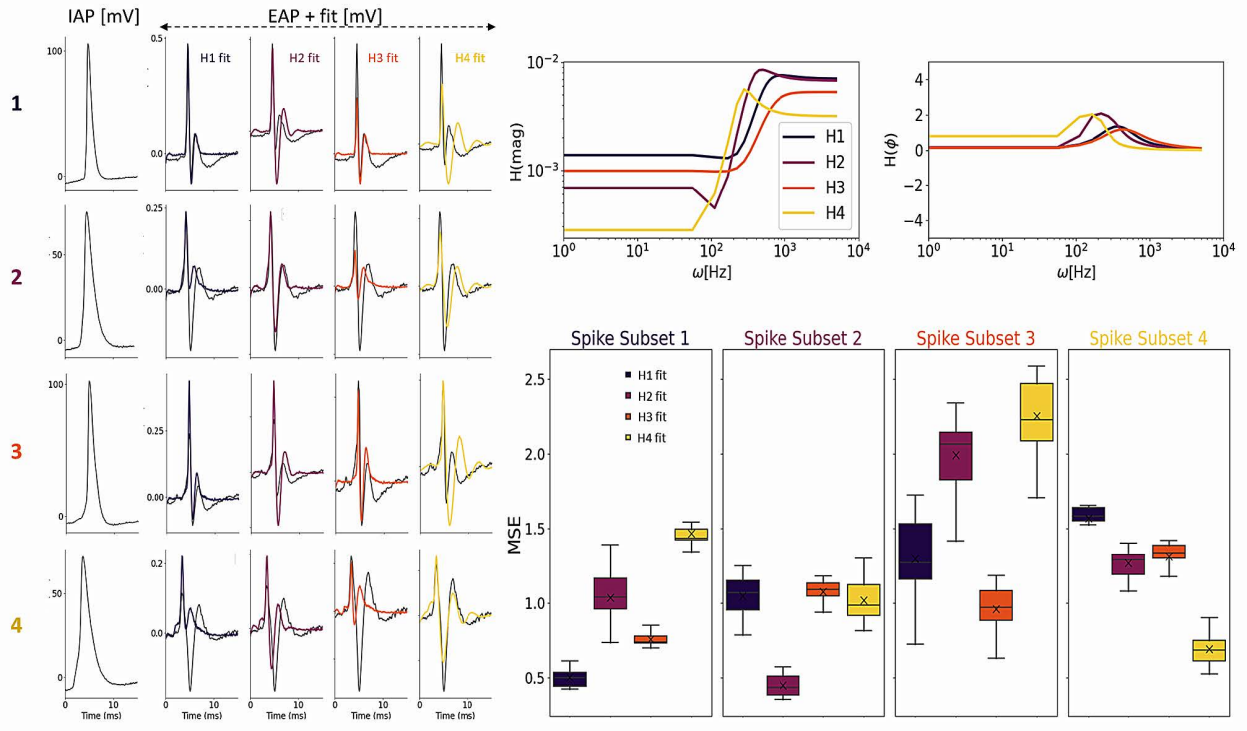


**Figure C17. IAP-EAP transfer functions for coupling with tri-phasic EAPs.** Left: fitting quality for all found transfer functions. Each row represents an IAP-EAP pair belonging to a H cluster marked by number. The first column illustrates a representative IAP. Every other column represents the corresponding EAP (black) overlaid by fit with different Hs. The color code of the fit matches the Hs on the right. Top right: Bode plots illustrating different Hs used for fitting. Bottom: MSEs of the H fits and corresponding EAPs for every H cluster.

Transfer function inconsistencies were found in bursting, but not sparsely firing neurons. The same fitting procedure serving to obtain transfer functions from 200-node convolutional layer produced similar transfer function profiles. Further inspection of fitting quality by cross-transfer function predictions indicated that all IAP-EAP spike subsets could be comparably well explained by either of the found transfer functions.

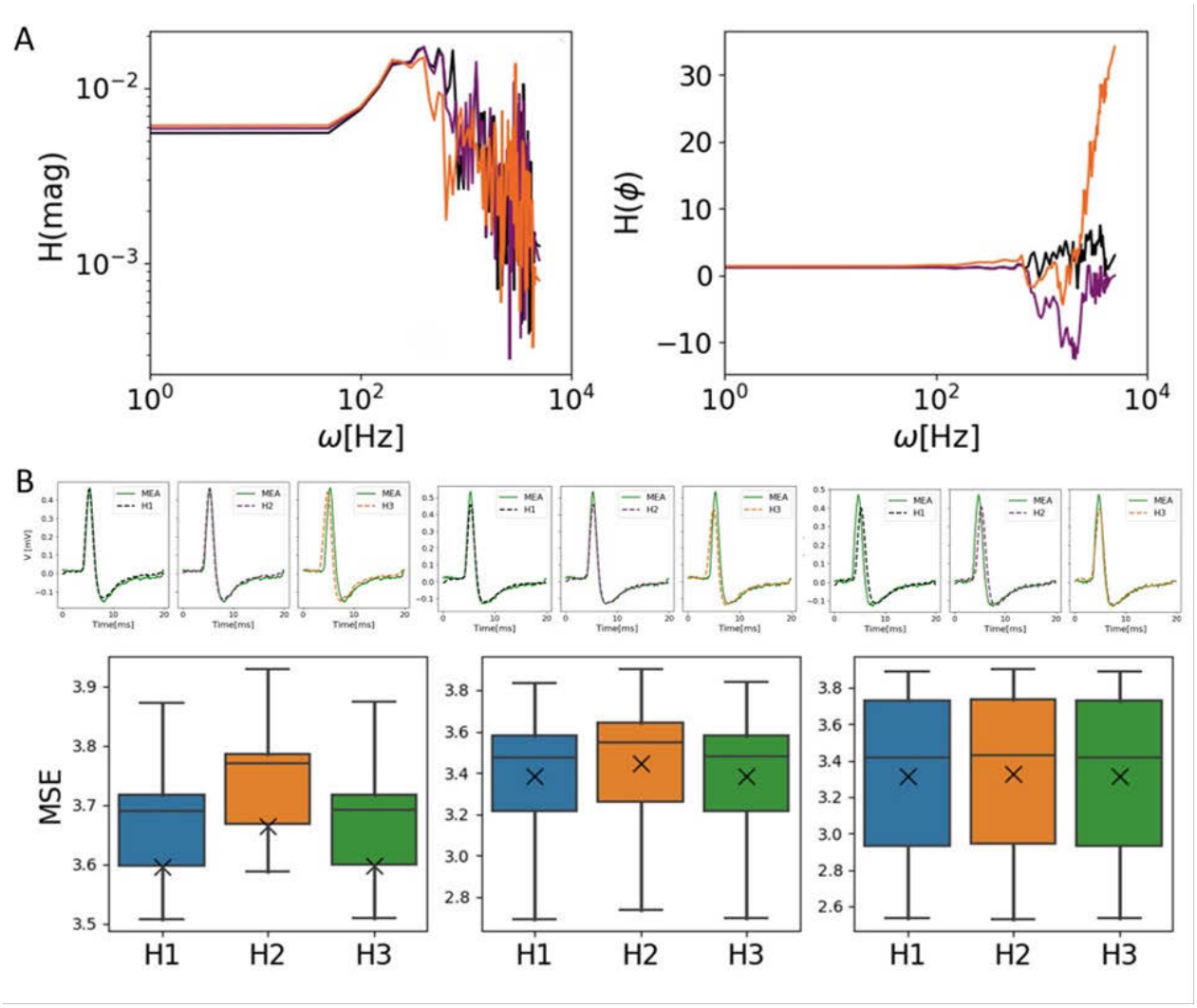


**Figure C18. Transfer functions found for sparsely firing neuron** A. Magnitude (left) and phase (right) Bode plots of IAP-EAP transfer functions. B. Different Hs fitted equally well spike pairs of each subset. Top: exemplary trace of EAP and fit with each found transfer function. Bottom: MSE estimates of every spike pair subset for given found H.

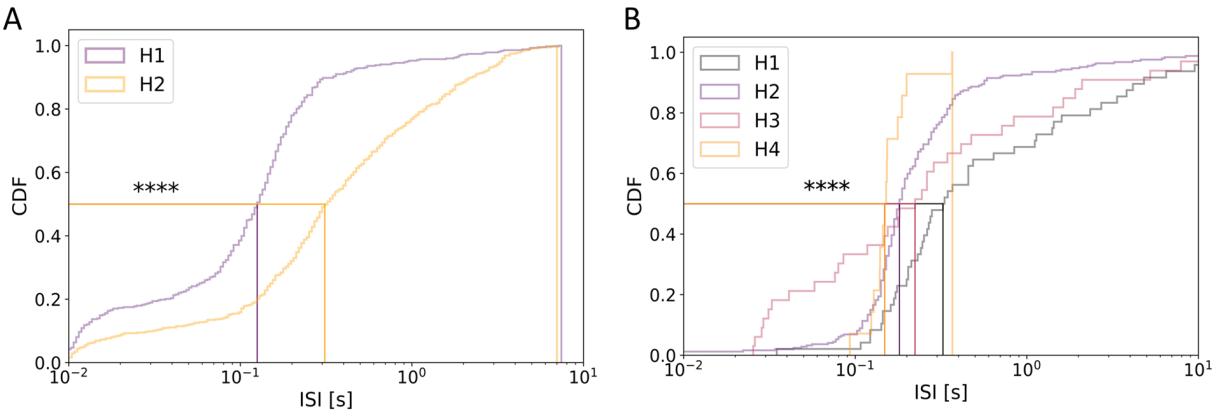


**Figure C19. ISI distributions across different transfer function subsets.** Depicted are cumulative density functions of preceding interspike intervals for transfer function subsets in IN-CELL like (A) and triphasic MEA couplings (B). Vertical lines denote median values. Statistical annotation: Kruskal-Wallis, ****: $p<10^{-4}$.

# C2. Ground truth of calcium signals

## *Excess $Ca^{2+}$ spiking arises from asynchronous inputs*

The figure below shows a strong inverse relation between the $Ca^{2+}$ spiking frequency and fractions of SNE-participating $Ca^{2+}$ spikes, suggesting that higher $Ca^{2+}$ spiking rates arose from asynchronous inputs.

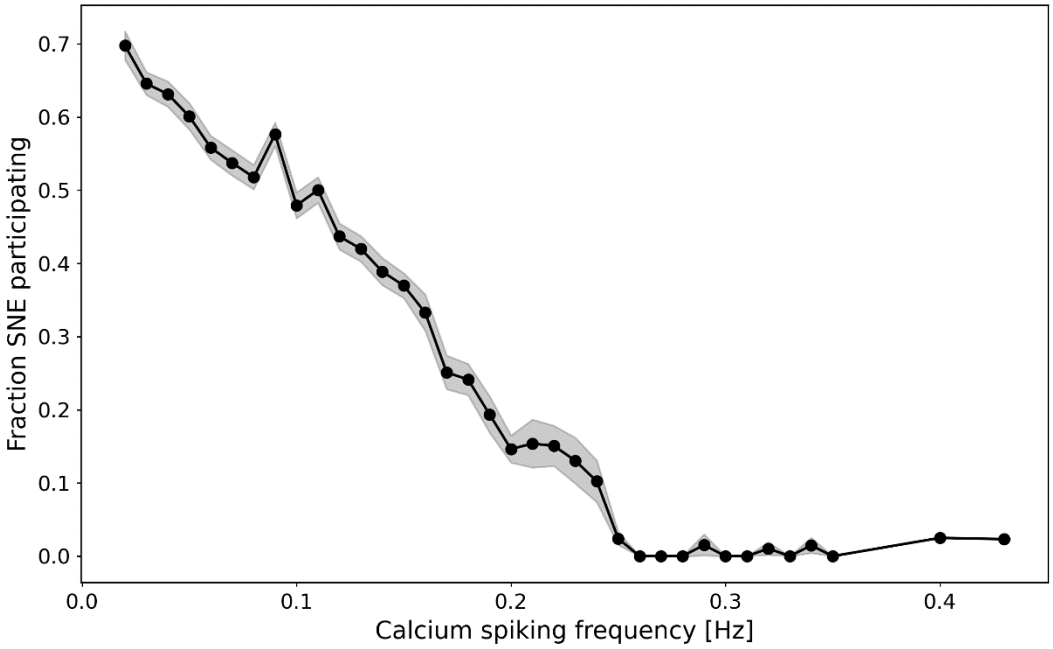


**Figure C1. Fraction of SNE-participating $Ca^{2+}$spikes vs. $Ca^{2+}$ spiking frequency.** The points denote mean, and shaded areas indicate standard error for each spiking rate.

## *SNE vs. non-SNE $Ca^{2+}$ spike amplitudes in paired dataset*

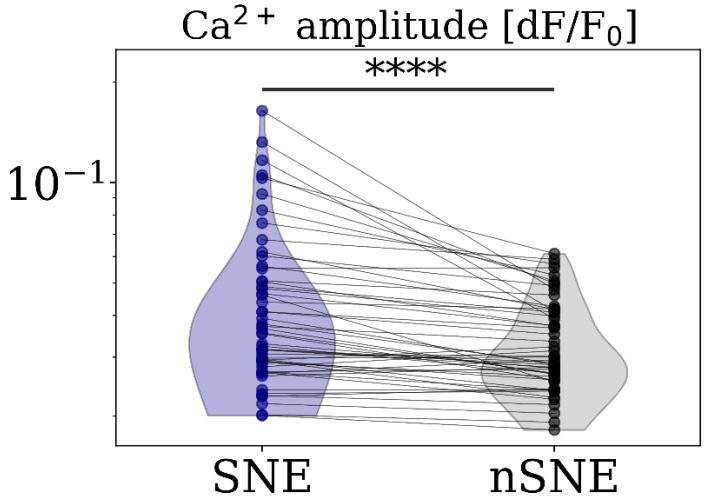


**Figure C2. SNE vs. non-SNE $Ca^{2+}$ signal amplitudes from paired dataset.** Violin plots denote distributions of SNE and non-SNE $Ca^{2+}$ spike amplitudes. Each point denotes amplitude average for a field of view. Statistics: Wilcoxon test, ****: $p < 10^{-4}$.

## *ROC curve for visibility of depolarization-centered $Ca^{2+}$ signals*

To obtain a holistic overview of $Ca^{2+}$ visibility and estimate appropriate projection threshold, ROC curve was evaluated on all $Ca^{2+}$ windows extracted by the membrane depolarizing events.

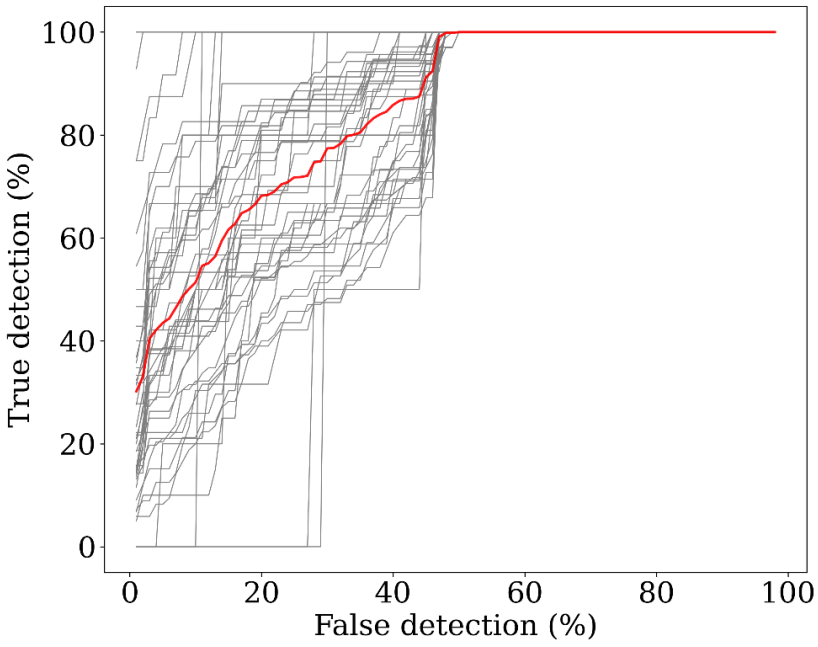


**Figure C3. ROC curve of all-AP $Ca^{2+}$ events.** Grey lines denote the ROC curve for all calcium events found in a single neuron's calcium trace. Red line denotes mean.

## *Detectability of 1AP $Ca^{2+}$ spikes at 5% false positive rates*

Figure below demonstrates the incidence of suprathreshold 1AP $Ca^{2+}$ events at 5% false positive rate. The right figure shows that between-neuron variations in 1AP $Ca^{2+}$ event detection was not due to differences in calcium SNR.

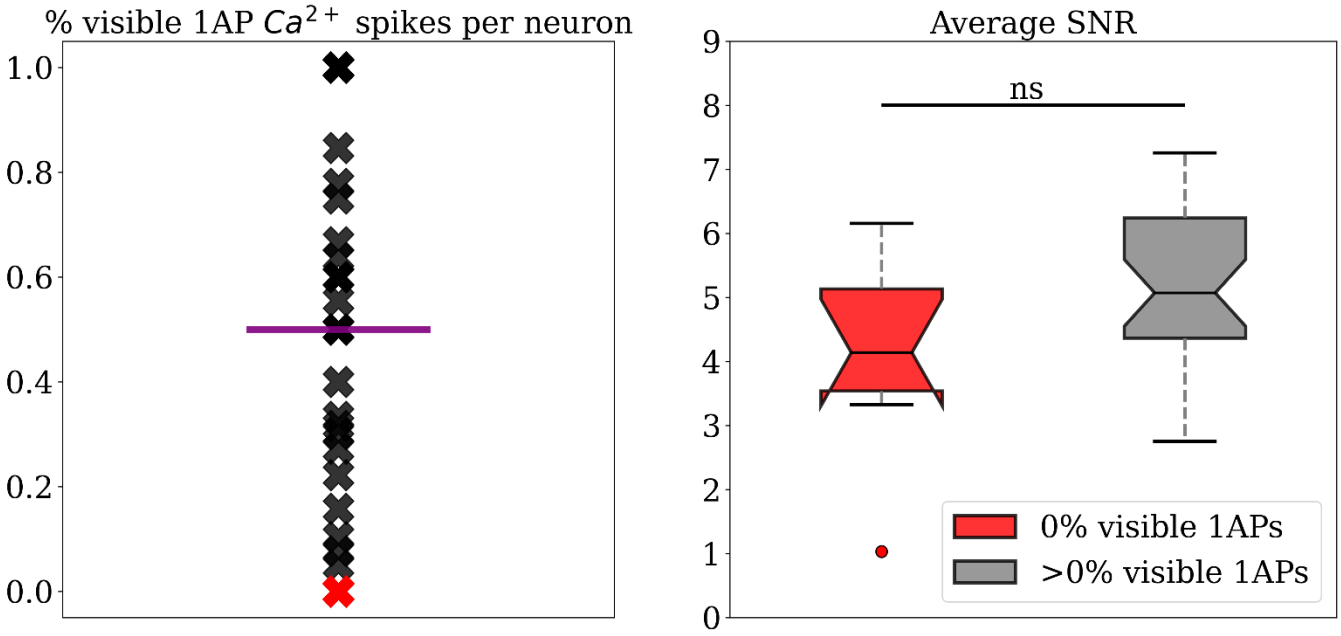


**Figure C4. Average 1AP discovery rate at 5% false positive incidence in relation to the SNR.** Left: Detection rate of 1AP $Ca^{2+}$ signals for individual neurons. Purple line denotes median, red marks neurons with all below-threshold 1AP $Ca^{2+}$ spikes. Right: Overall SNR for cells showing no visible 1AP $Ca^{2+}$ spikes and those that had at least one above-threshold signal.

# C3. Calcium responses during giga-seal formation

## *Giga-seal associated calcium plateaus are not from the light interference*

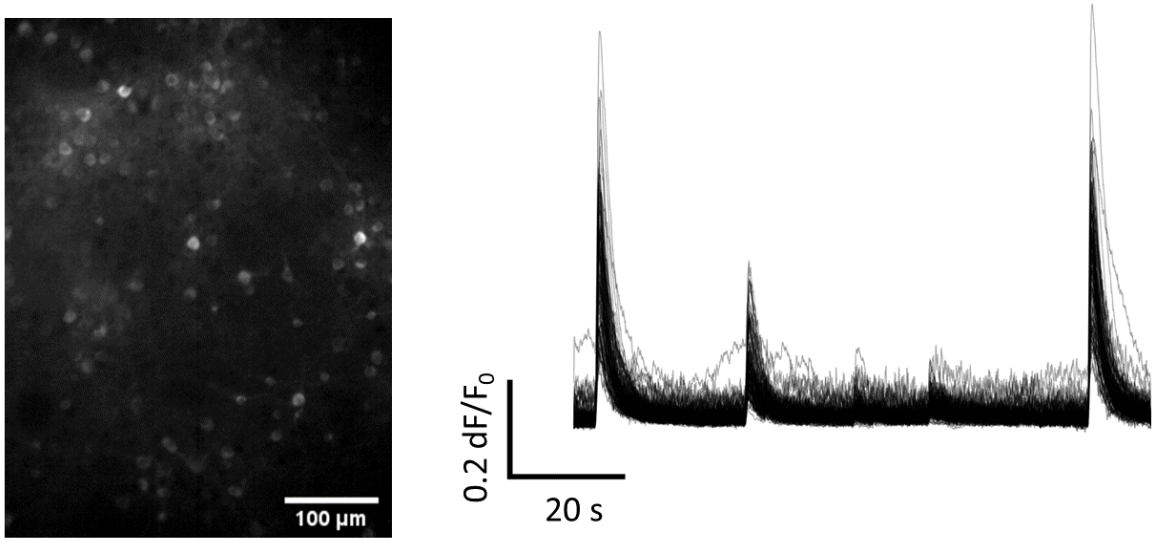


**Figure C1. Calcium responses during the pipette movement along the Z-axis.** Left: jRCaMP1b micrograph of the local network whose calcium responses are overlaid on the right.

## *Trypan blue shows positive stain for disrupted cells*

In Section 6.1., the absence of trypan blue staining following the giga-seal formation indicated no membrane poration during the procedure. As a positive control, the cell was penetrated by the pipette in trypan blue solution; after 5-10 minutes, the target was positive for trypan blue signal.

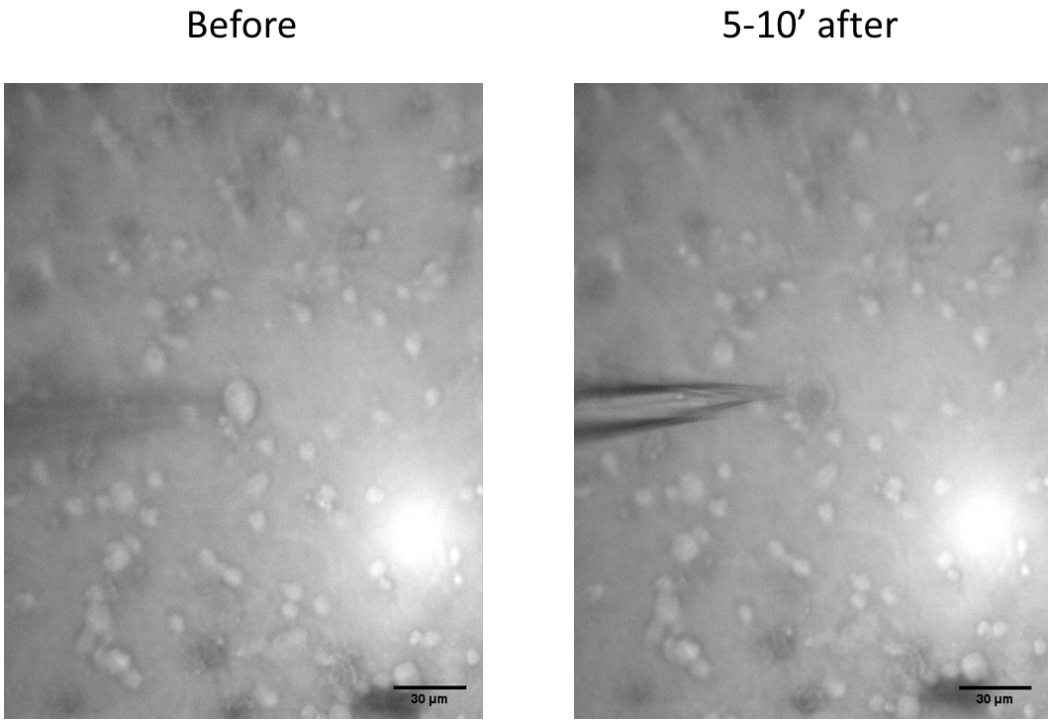


**Figure C2. Trypan blue assay upon the pipette-induced membrane injury.** Left: a brightfield micrograph of the target prior to injury. Right: a brightfield micrograph of the target after the membrane injury.

## *Distribution of inter-soma distances in in vitro networks*

To evaluate dispersion of the neighboring somas to the target, ROI centers [X,Y] were extracted for each neuron. This was followed by estimates of Euclidean distances of all the neighboring somas from the target in a 0.2 $mm^2$ FOV. The histogram below demonstrates that frequency response peaks are concentrated around multiplies of 46 µm. This distance was used as a radius for drawing concentric rings in propagation estimates.

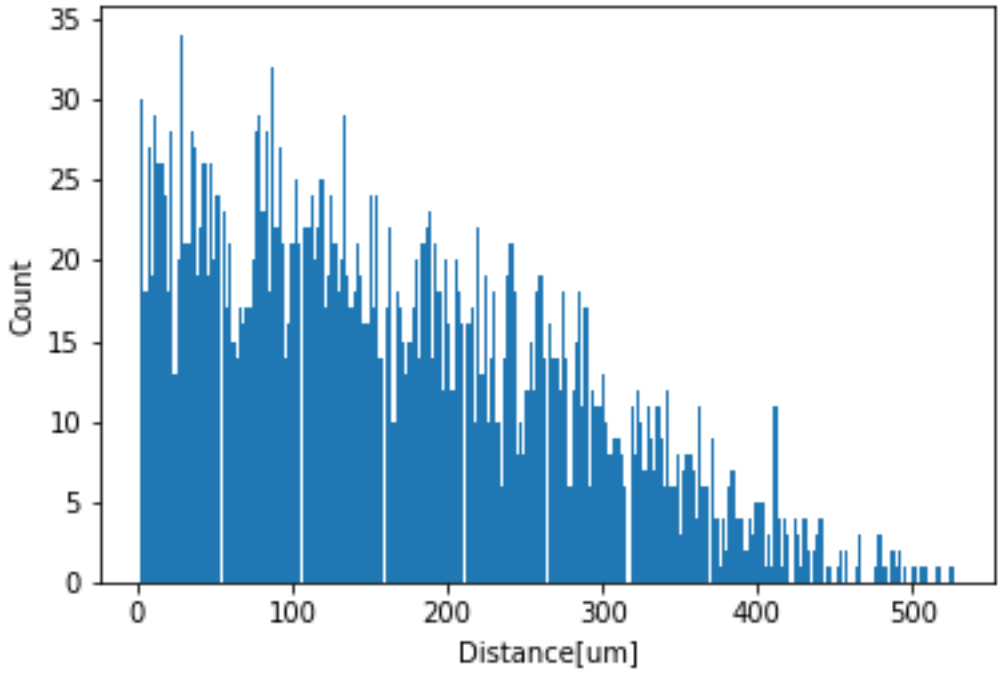


**Figure C3. Inter-soma distance histogram.** Frequency response peaks are concentrated around multiplies of 46 µm.

## *Network bursts engage the non-responding neurons*

Spontaneous activity prior to the giga-seal was imaged using jRCaMP1b calcium imaging. Major bursting events were estimated from the peaks of the convolved sum of calcium peaks. The neighbors were separated into responding or non-responding depending on calcium plateaus presence during the giga-seal formation. As shown on Figure C4.B, non-responding neighbors are also co-activated during the network-level bursts.

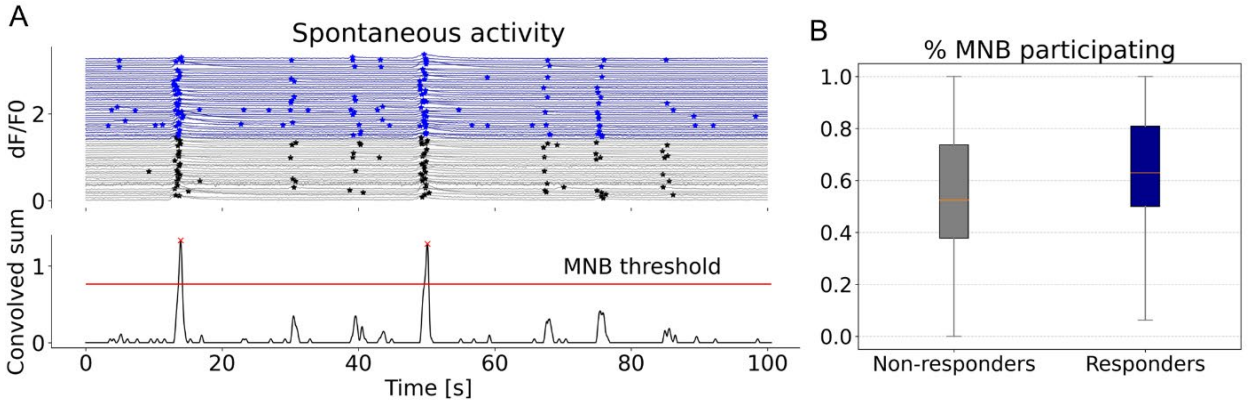


**Figure C4. Major network bursts also engage non-responding neurons.** A. Calcium traces of spontaneous activity and population dynamics, for representative field of view. Top plot depicts traces and peaks (*-ed) of responding (blue) and non-responding neurons (gray). Bottom plot depicts the population dynamics and major network bursts (MNB) detected by soft threshold. B. Fractions of MNB participating neurons among non-responders and responders.

# Appendix D: Origin of targeted EAPs

Targeted extracellular measures isolate single neurons and even a single neuron's compartment. Understanding how EAPs originate in targeted extracellular records is useful when modeling cell-electrode interfaces because the recording location, distance, and sealing extent can be easily controlled. This appendix displays how different extracellular targeted configurations transform IAPs into various EAP waveforms.

In **loose-patch (LoP)** measures, often with suction, the pipette establishes some extent of contact with the membrane (5-100 MΩ). [270-272] Detected EAPs are predominantly positive, in the mV range, and match the 1st IAP time derivative. LoP EAPs are positive for all neuronal compartments, indicating that detected signals arise from IAP at the detection site. Detected EAPs arise from capacitive currents, with the exemptions of negative EAPs at the AIS, and complex waveforms arising from somatic measures close to AIS. The latter is often attributed to a higher Ohmic sensing due to a higher $Na_v$ density at the AIS.

In **cell-attached (CA)** measures, the pipette fully isolates the membrane patch with $R_{seal}$ in the GΩ range. Unlike the LoP measures that high-pass filter the IAPs, CA current-clamp (CA/CC) low-pass filters the IAPs.[178] It is counter-intuitive how similar recording configurations which differ only in the sealing extent, LoP/CC and CA/CC, perform opposite IAP transformations: the former high-pass (HP) filters the IAPs, and the latter sets a low-pass (LP) filter. The model of the pipette-membrane interface was constructed in LTSpice XVII to address how similar configurations, with only differing contact strengths, yield opposing effects.

The model of Vazetdinova et al. was implemented[178] to approximate giga-seal contact in CA/CC. It comprises the membrane resistance ($R_{membrane}$), RC circuit representing the patch membrane capacitance and resistance ($C_{patch}$ and $R_{patch}$), serially connected with the pipette resistor ($R_{pip}$). Additionally, there is a seal resistor connected to the bath ($R_{seal}$), and patch pipette capacitor ($C_{pip}$), also connected to the bath and positioned above the $R_{pip}$ (Fig. D1, also Fig. 2.2.1.2.). Optionally, the high-impedance patch-clamp amplifier is involved ($R_{amp}$). In CA, the pipette capacitance is equal or higher than membrane patch capacitance ($C_{pip} \geq C_{patch}$), providing the basis for the LP effect. The formal interpretation is as follows.

The CA/CC circuit in Figure D1 has two signal-altering components: HP and LP filter. HP filter comprises the RC membrane patch ($R_{patch}$, $C_{patch}$) and bath-connecting $R_{seal}$ that behaves as a voltage divider. Here, $C_{patch}$ provides a low-impedance path for high-frequency signals, thus attenuating the slow frequency components. As previously stated, $C_{pip}$ and $R_{pip}$ set a LP filter, where $C_{pip}$ acts as a frequency-dependent voltage divider. Given the high amplifier impedance and $R_{pip} << R_{patch}$, the CA/CC transfer function can be approximated as:

$$H(s) = \frac{R_{seal}(C_{patch}R_{patch}s+1)}{C_{patch}R_{patch}R_{seal}s+C_{pip}R_{patch}R_{seal}s+R_{patch}+R_{seal}}$$

To obtain the time-constant of each component, fast analytical techniques (FACTs) were employed. Briefly, for each capacitive element of the circuit, a capacitive branch would be considered open, and the time constant expression was derived from the total resistance at terminals. Accordingly, HP time constant was evaluated as:

$$\tau_{HP} = (R_{patch} \,||\, R_{seal})\, C_{patch} = \frac{R_{patch} R_{seal}}{R_{patch} + R_{seal}} C_{patch}$$

Similarly, LP time constant can be derived as:

$$\tau_{LP} = (R_{patch} \,||\, R_{seal})\, C_{pip} = \frac{R_{patch} R_{seal}}{R_{patch} + R_{seal}} C_{pip}$$

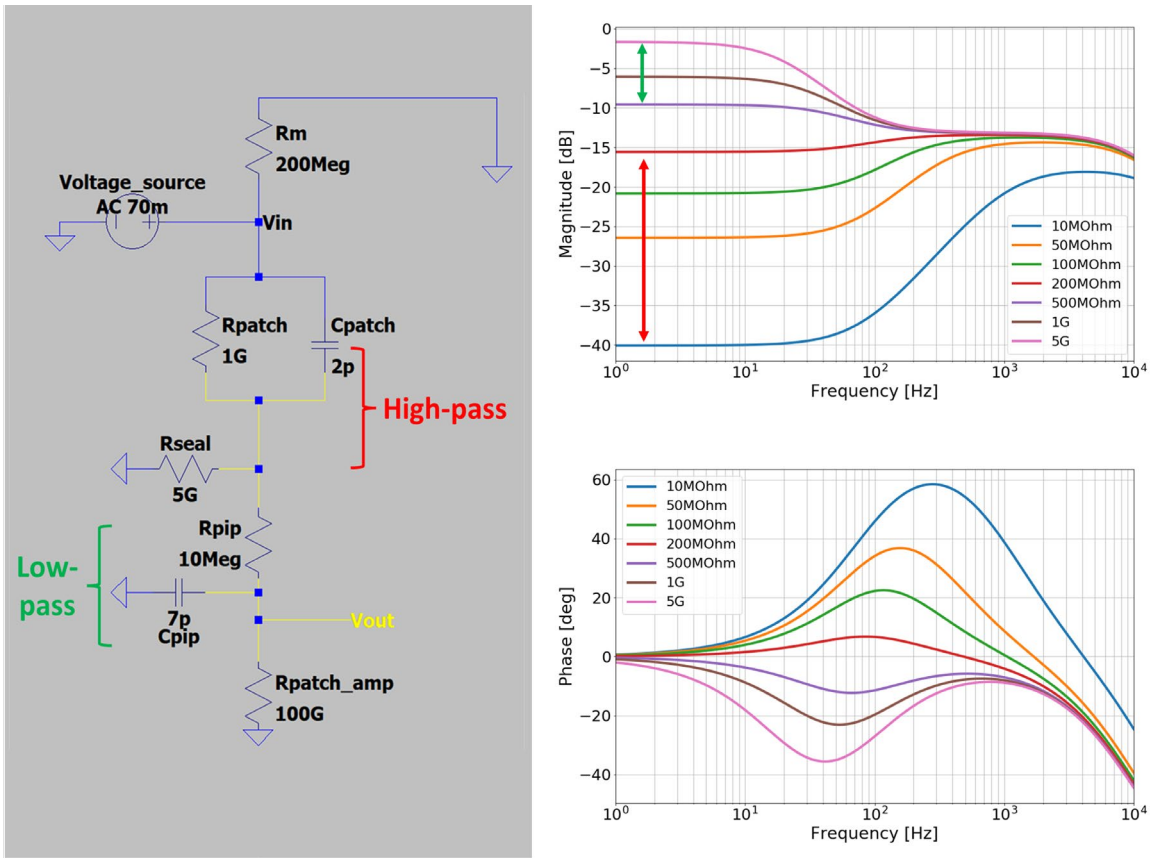


**Figure D1. Extracellular patch circuit has opposite filtering effect depending on the sealing.** LTSpice XVII simulation of the circuit representing CA configuration, composed of: voltage source, free membrane resistor (Rm), membrane patch component (Rpatch and C patch), sealing resistor (Rseal), pipette resistor (Rpip) and capacitor (Cpip), and patch amplifier resistor (which is often omitted due to an exceedingly high impedance). Highlighted are components contributing to high-pass (red) and low-pass filtering (green). The circuit is adaptation of Vazetdinova et al. 2022 CA/CC model [178]; the exception is Cpip placed higher than Rpip, since the liquid separation effect takes place after the resistive component. The voltage source was set to AC mode to directly obtain transfer function from frequency analysis in LTSpice. Right: circuit transfer function magnitude (top) and phase (bottom) plots for different Rseal values. Arrows in magnitude plot mark H subsets having low-pass or high-pass filtering effect.

From both expressions, it can be appreciated how both time constants scale directly with $R_{seal}$: high $R_{seal}$ yields larger time constants and correspondingly smaller cut-off frequencies. HP derives all signals below the cut-off. Analogously, LP integrates all the frequencies above the

cut-off. Thus, cut-off frequencies in 100 Hz range exert a minimal deviation by HP and integrate IAP-associated frequencies above the cut-off via LP. LTSpice simulation demonstrates a strong LP effect for relatively high $R_{seal}$, typical for CA/CC (Fig. D1). With very loose coupling, as in LoP/CC, most of the signal is lost to the ground at low $R_{seal}$ (10 and 50 MΩ examples in Fig. D1). Here, relatively small time constants increase cut-off frequencies by an order of magnitude, producing an opposite effect. Accordingly, HP differentiates all IAP-associated frequencies, while LP exerts little to no deviating effect. As a result, IAPs are high-pass filtered in LoP/CC (Fig. D1). To summarize, IAPs are low-pass filtered in strong-seal CA/CC mode due to non-negligible $C_{pip}$ and high $R_{seal}$. With reduced $R_{seal}$, such in LC/CC, EAPs are attenuated and derived IAPs due to predominant HP effect.

Given the effect of $C_{pip}$ on loose-patch measures, the question arises whether it has any effect on the IAPs detected in WC/CC mode. In WC, the membrane patch is torn to obtain an intracellular access. With intracellular access, the membrane resistance and capacitance go through a several-fold decrease and increase, respectively. Accordingly, $C_{mem} >> C_{pip}$, and $C_{pip}$ has no filtering effect across biologically relevant frequencies (1Hz – 1 kHz).[25] Thus, whole-cell measures IAPs unaltered, even in lack of fast capacitance compensation. Similar transfer function profiles are also expected for active porating 2D+ electrodes with demonstrated intracellular access.[294]

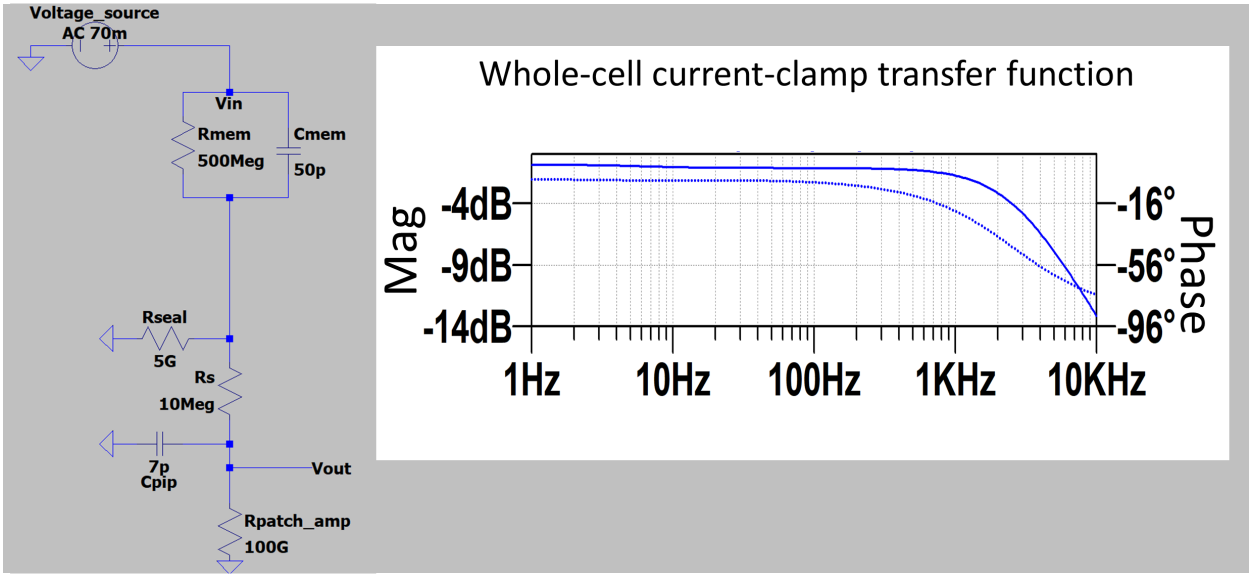


**Figure D2. Whole-cell current-clamp circuitry.** LTSpice XVII simulation of the circuitry corresponding to whole-cell configuration, composed of: voltage source, membrane resistor (Rmem) and capacitor (Cmem), sealing resistor (Rseal), series resistor (Rs) and patch amplifier resistor. Voltage source was in AC mode for direct transfer function inferences from frequency analysis in LTSpice. Despite uncompensated pipette capacitance (Cpip), signal transfer preserves across relevant frequency ranges (1 Hz-10 kHz).

# List of abbreviations and IUPAC names

**2-APB** – 2-Aminoethoxydiphenylborane

**AHP** – After-hyperpolarization

**AIDA** – 1-amino-2,3-dihydroindene-1,5-dicarboxylic acid

**AMPA** – α-amino-3-hydroxy-5-methyl-4-isoxazole propionic acid

**APs** – Action potentials

**ATP** – Adenosine triphosphate

**bAPs** – back-propagating action potentials

**Bicuculine** – [R-(R*,S*)]-6-(5,6,7,8-Tetrahydro-6-methyl-1,3-dioxolo[4,5-g]isoquinolin-5-yl)furo[3,4-e]-1,3-benzodioxol-8(6H)-one

**Blebbistatin** – 3a-hydroxy-6-methyl-1-phenyl-2,3-dihydropyrrolo[2,3-b]quinolin-4-one

**BMU** – Best-matching unit, the spike-sorter unit with a highest temporal correlation with the ground truth

**BU** – Best unit, containing the majority of the spikes corresponding to the ground-truth

**Caffeine –** 1,3,7-Trimethylpurine-2,6-dione

**$Ca_V$s** – Calcium voltage-gated channels

**CB** – Cytoskeleton Buffer

**CBX** – Carbenoxolone, IUPAC: (2S,4aS,6aR,6aS,6bR,8aR,10S,12aS,14bR)-10-(3-carboxypropanoyloxy)-2,4a,6a,6b,9,9,12a-heptamethyl-13-oxo-3,4,5,6,6a,7,8,8a,10,11,12,14b-dodecahydro-1H-picene-2-carboxylic acid

**CGP 55845** – (2S)-3-[[(1S)-1-(3,4-Dichlorophenyl)ethyl]amino-2-hydroxypropyl](phenylmethyl)phosphinic acid hydrochloride

**Conv1D** – 1-dimensional convolutional layer

**CPPG** – (RS)-α-Cyclopropyl-4-phosphonophenylglycine

**CV** – Coefficient of variation

**Cxs –** Connexins

**CytoD** – Cytochalasin D, IUPAC:[(1R,2R,3E,5R,7S,9E,11R,12S,14S,15R,16S)-16-benzyl-5,12-dihydroxy-5,7,14-trimethyl-13-methylidene-6,18-dioxo-17-azatricyclo[9.7.0.01,15]octadeca-3,9-dien-2-yl] acetate

**D-AP5** – D-(-)-2-Amino-5-phosphonopentanoic acid

**DBSCAN** – Density-based spatial clustering of applications with noise

**DMSO** – Dimethyl-sulfoxide

**EAP** – Extracellularly detected Action Potential

**ecPSP –** Extracellularly detected Post-synaptic Potential

**EDTA** – 2,2',2",2"'-(Ethane-1,2-diyldinitrilo)tetraacetic acid

**EGTA** – Ethylene glycol-bis-(2-amin-o-ethyl-)-N,-N,-N',-N'-tetraacetic acid

**EM** – Expectation maximization

**EPSP** – Excitatory Post-synaptic Potential

**FOV** – Field of view

**GABA** – Gamma-aminobutyric acid

**GDPs –** Giant depolarizing potentials

**GJC** – Gap junction channels

**GMM** – Gaussian mixture model

**GsMTx4** – Mechanotoxin 4

**GTP** – Guanosine triphosphate

**GUI** – Graphical user interface

**HBSS** – Hank's Balanced Salt Solution

**HEPES** – 2-[4-(2-hydroxyethyl)piperazin-1-yl]ethanesulfonic acid

**IAP** – Intracellularly detected Action Potential

**icPSP** – Intracellularly detected Post-synaptic Potential

**IPSP** Inhibitory Post-synaptic Potential

**$K_v$s** – Potassium (K) voltage-gated channels

**LSTM** – Long Short-Term Memory

**LTP** – Long-term potentiation

**MAD** – Mean absolute deviation

**MAE** – Mean absolute error

**MEA** – Microelectrode (syn. Multielectrode) arrays

**Mefloquine** – [2,8-bis(trifluoromethyl)quinolin-4-yl]-piperidin-2-ylmethanol

**MES** – 2-(N-Morpholino)ethanesulfonic acid

**mGluRs** – Metabotropic Glutamate Receptors

**MHCII** – Myosin Heavy Chain II

**Mibefradil** – [(1S,2S)-2-[2-[3-(1H-benzimidazol-2-yl)propyl-methylamino]ethyl]-6-fluoro-1-propan-2-yl-3,4-dihydro-1H-naphthalen-2-yl] 2-methoxyacetate

**MSE** – Mean squared error

**MUA** – Multi-unit activity

**$Na_v$s** – Sodium (Na) voltage-gated channels

**NBQX** – disodium;6-nitro-7-sulfamoylbenzo[f]quinoxaline-2,3-diolate

**NC** – Nanocavity

**Nifedipine** – dimethyl 2,6-dimethyl-4-(2-nitrophenyl)-1,4-dihydropyridine-3,5-dicarboxylate

**NMDA** – N-methyl-D-aspartate

**NN** – Neural network

**NS** – Nanostraws

**OU** – Other unit

**PCA** – Principal component analysis

**PSPs** – Post-synaptic potentials

**ReLU** – Rectified linear unit

**RMSE** – Root mean squared error

**ROC** – Receiver Operating Characteristic

**ROI** – Region of interest

**RyR** – Ryanodine Receptors

**SNEs** – Synchronous network events

**SNR** – Signal-to-noise-ratio

**SOCE** – Store operated calcium entry

**SPC** – Superparamagnetic clustering

**STA –** Stimulus-triggered average

**STDP** – Spike-timing dependent plasticity

**SUA** – Single-unit activity

**SVD** – Single-value decomposition

**TEA** – Tetraethyl ammonium

**TMS** – Transcranial Magnetic Stimulation

**TTX** – Tetrodotoxin, IUPAC: 4R,4aR,5R,6S,7S,8S,8aR,10S,12S)-2-azaniumylidene-4,6,8,12-tetrahydroxy-6-(hydroximethyl)-2,3,4,4a,5,6,7,8-octahydro-1H-8a,10-methano-5,7-(epoxymethanooxy)quinazolin-10-olate

**US** – Ultrasound Stimulation

# List of figures

## Supplementary figures

# List of tables



## Supplementary tables

# References


[1] Antonello, P.C., T.F. Varley, J. Beggs, M. Porcionatto, O. Sporns,J. Faber, *Self-organization of in vitro neuronal assemblies drives to complex network topology* eLife **2022**, *11*.

[2] Larkum, M.E., J. Wu, S.A. Duverdin,A. Gidon, *The Guide to Dendritic Spikes of the Mammalian Cortex In Vitro and In Vivo* Neuroscience **2022**, *489*.

[3] Mok, S.Y., Z. Nadasdy, Y.M. Lim,S.Y. Goh, *Ultra-slow oscillations in cortical networks in vitro* Neuroscience **2012**, *206*.

[4] van Pelt, J., I. Vajda, P.S. Wolters, M.A. Corner,G.J.A. Ramakers, *Dynamics and plasticity in developing neuronal networks in vitro*, in *Progress in Brain Research*. 2005, Elsevier. p. 171-188.

[5] Buzsaki, G., *Neural syntax: Cell assemblies, synapsembles, and readers. Neuron 68*. 2010.

[6] Cossart, R., D. Aronov,R. Yuste, *Attractor dynamics of network UP states in the neocortex* Nature **2003**, *423*.

[7] Yuste, R., *From the neuron doctrine to neural networks* Nature reviews neuroscience **2015**, *16*.

[8] Carrillo-Reid, L. *Neuronal ensembles in memory processes*. in *Seminars in Cell & Developmental Biology*. 2022. Elsevier.

[9] Carrillo-Reid, L., S. Han, W. Yang, A. Akrouh,R. Yuste, *Controlling visually guided behavior by holographic recalling of cortical ensembles* Cell **2019**, *178*.

[10] Buzsáki, G., *Large-scale recording of neuronal ensembles* Nature Neuroscience **2004**, *7*.

[11] Okujeni, S.,U. Egert, *Self-organization of modular network architecture by activity-dependent neuronal migration and outgrowth* eLife **2019**, *8*.

[12] Samora, O., K. Steffen,E. Ulrich, *Mesoscale Architecture Shapes Initiation and Richness of Spontaneous Network Activity* The Journal of Neuroscience **2017**, *37*.

[13] Cossell, L., M.F. Iacaruso, D.R. Muir, R. Houlton, E.N. Sader, H. Ko, S.B. Hofer,T.D. Mrsic-Flogel, *Functional organization of excitatory synaptic strength in primary visual cortex* Nature **2015**, *518*.

[14] Alejandre-García, T., S. Kim, J. Pérez-Ortega,R. Yuste, *Intrinsic excitability mechanisms of neuronal ensemble formation* eLife **2022**, *11*.

[15] Jiang, X., S. Shen, C.R. Cadwell, P. Berens, F. Sinz, A.S. Ecker, S. Patel,A.S. Tolias, *Principles of connectivity among morphologically defined cell types in adult neocortex* Science **2015**, *350*.

[16] Lee, A.K.,M. Brecht, *Elucidating Neuronal Mechanisms Using Intracellular Recordings during Behavior* Trends Neurosci **2018**, *41*.

[17] Wang, G., D.R. Wyskiel, W. Yang, Y. Wang, L.C. Milbern, T. Lalanne, X. Jiang, Y. Shen, Q.Q. Sun,J.J. Zhu, *An optogenetics- and imaging-assisted simultaneous multiple patch-clamp recording system for decoding complex neural circuits* Nat Protoc **2015**, *10*.

[18] Gerhard, F., G. Pipa, B. Lima, S. Neuenschwander,W. Gerstner, *Extraction of Network Topology From Multi-Electrode Recordings: Is there a Small-World Effect?* Front Comput Neurosci **2011**, *5*.

[19] Rickgauer, J.P., K. Deisseroth,D.W. Tank, *Simultaneous cellular-resolution optical perturbation and imaging of place cell firing fields* Nat Neurosci **2014**, *17*.

[20] Kwan, A.C.,Y. Dan, *Dissection of cortical microcircuits by single-neuron stimulation in vivo* Curr Biol **2012**, *22*.

[21] Randi, F., A.K. Sharma, S. Dvali,A.M. Leifer, *Neural signal propagation atlas of Caenorhabditis elegans* Nature **2023**, *623*.

[22] Franconville, R., C. Beron,V. Jayaraman, *Building a functional connectome of the Drosophila central complex* Elife **2018**, *7*.

[23] Okujeni, S.,U. Egert, *Inhomogeneities in network structure and excitability govern initiation and propagation of spontaneous burst activity* Frontiers in Neuroscience **2019**.

[24] Penn, Y., M. Segal,E. Moses, *Network synchronization in hippocampal neurons* Proceedings of the National Academy of Sciences **2016**, *113*.

[25] Spira, M.E.,A. Hai, *Multi-electrode array technologies for neuroscience and cardiology* Nature nanotechnology **2013**, *8*.

[26] Shokoohimehr, P., *Nanostraw- Nanocavity MEAs as a new tool for long-term and high sensitive recording of neuronal signals*. 2021, RWTH Aachen Universität.

[27] Shokoohimehr, P., B. Cepkenovic, F. Milos, J. Bednár, H. Hassani, V. Maybeck,A. Offenhäusser, *High-Aspect-Ratio Nanoelectrodes Enable Long-Term Recordings of Neuronal Signals with Subthreshold Resolution* Small **2022**, *18*.

[28] Rey, H.G., C. Pedreira,R. Quian Quiroga, *Past, present and future of spike sorting techniques* Brain Research Bulletin **2015**, *119*.

[29] Buccino, A.P., C.L. Hurwitz, S. Garcia, J. Magland, J.H. Siegle, R. Hurwitz,M.H. Hennig, *SpikeInterface, a unified framework for spike sorting* eLife **2020**, *9*.

[30] Magland, J., J.J. Jun, E. Lovero, A.J. Morley, C.L. Hurwitz, A.P. Buccino, S. Garcia,A.H. Barnett, *SpikeForest, reproducible web-facing ground-truth validation of automated neural spike sorters* eLife **2020**, *9*.

[31] Ali, F.,A.C. Kwan, *Interpreting in vivo calcium signals from neuronal cell bodies, axons, and dendrites: a review* Neurophotonics **2019**, *7*.

[32] Grienberger, C.,A. Konnerth, *Imaging Calcium in Neurons* Neuron **2012**, *73*.

[33] Hires, S.A., L. Tian,L.L. Looger, *Reporting neural activity with genetically encoded calcium indicators* Brain Cell Biology **2008**, *36*.

[34] Theis, L., P. Berens, E. Froudarakis, J. Reimer, M.R. Rosón, T. Baden, T. Euler, A.S. Tolias,M. Bethge, *Benchmarking spike rate inference in population calcium imaging* Neuron **2016**, *90*.

[35] Rahmati, V., K. Kirmse, D. Marković, K. Holthoff,S.J. Kiebel, *Inferring Neuronal Dynamics from Calcium Imaging Data Using Biophysical Models and Bayesian Inference* PLOS Computational Biology **2016**, *12*.

[36] Huang, L., P. Ledochowitsch, U. Knoblich, J. Lecoq, G.J. Murphy, R.C. Reid, S.E.J. de Vries, C. Koch, H. Zeng, M.A. Buice, J. Waters,L. Li, *Relationship between simultaneously recorded spiking activity and fluorescence signal in GCaMP6 transgenic mice* eLife **2021**, *10*.

[37] Yoo, S., D.R. Mittelstein, R.C. Hurt, J. Lacroix,M.G. Shapiro, *Focused ultrasound excites cortical neurons via mechanosensitive calcium accumulation and ion channel amplification* Nature Communications **2022**, *13*.

[38] Rabut, C., S. Yoo, R.C. Hurt, Z. Jin, H. Li, H. Guo, B. Ling,M.G. Shapiro, *Ultrasound Technologies for Imaging and Modulating Neural Activity* Neuron **2020**, *108*.

[39] Falleroni, F., U. Bocchero, S. Mortal, Y. Li, Z. Ye, D. Cojoc,V. Torre, *Mechanotransduction in hippocampal neurons operates under localized low picoNewton forces* iScience **2022**, *25*.

[40] Gaub, B.M., K.C. Kasuba, E. Mace, T. Strittmatter, P.R. Laskowski, S.A. Geissler, A. Hierlemann, M. Fussenegger, B. Roska,D.J. Müller, *Neurons differentiate magnitude and location of mechanical stimuli* Proceedings of the National Academy of Sciences **2020**, *117*.

[41] Falleroni, F., V. Torre,D. Cojoc, *Cell Mechanotransduction With Piconewton Forces Applied by Optical Tweezers* Frontiers in Cellular Neuroscience **2018**, *12*.

[42] Faber, D.S.,A.E. Pereda, *Two Forms of Electrical Transmission Between Neurons* Frontiers in Molecular Neuroscience **2018**, *11*.

[43] Clennell, B., T.G.J. Steward, M. Elley, E. Shin, M. Weston, B.W. Drinkwater,D.J. Whitcomb, *Transient ultrasound stimulation has lasting effects on neuronal excitability* Brain Stimul **2021**, *14*.

[44] Ucar, H., S. Watanabe, J. Noguchi, Y. Morimoto, Y. Iino, S. Yagishita, N. Takahashi,H. Kasai, *Mechanical actions of dendritic-spine enlargement on presynaptic exocytosis* Nature **2021**, *600*.

[45] Arimura, N.,K. Kaibuchi, *Neuronal polarity: from extracellular signals to intracellular mechanisms* Nature Reviews Neuroscience **2007**, *8*.

[46] Harrill, J.A., H. Chen, K.M. Streifel, D. Yang, W.R. Mundy,P.J. Lein, *Ontogeny of biochemical, morphological and functional parameters of synaptogenesis in primary cultures of rat hippocampal and cortical neurons* Molecular Brain **2015**, *8*.

[47] Lesuisse, C.,L.J. Martin, *Long-term culture of mouse cortical neurons as a model for neuronal development, aging, and death* Journal of Neurobiology **2002**, *51*.

[48] Gentet, L.J., G.J. Stuart,J.D. Clements, *Direct Measurement of Specific Membrane Capacitance in Neurons* Biophysical Journal **2000**, *79*.

[49] Hille, B., *Ionic channels in excitable membranes. Current problems and biophysical approaches* Biophysical journal **1978**, *22*.

[50] Kandel, E.R., J.H. Schwartz, T.M. Jessell, S. Siegelbaum, A.J. Hudspeth,S. Mack, *Principles of neural science*. Vol. 4. 2000: McGraw-hill New York.

[51] Plotkin, M., E. Snyder, S. Hebert,E. Delpire, *Expression of the Na-K-2Cl cotransporter is developmentally regulated in postnatal rat brains: a possible mechanism underlying GABA's excitatory role in immature brain* Journal of neurobiology **1997**, *33*.

[52] Clayton, G.H., G.C. Owens, J.S. Wolff,R.L. Smith, *Ontogeny of cation–Cl− cotransporter expression in rat neocortex* Developmental Brain Research **1998**, *109*.

[53] Johnston, D.,S.M.-S. Wu, *Foundations of cellular neurophysiology*. 1994: MIT press.

[54] Wright, S.H., *Generation of resting membrane potential* Advances in Physiology Education **2004**, *28*.

[55] Anđus, R.K., *Opšta fiziologija i biofizika - Osnovi neurobiofizike*. 2002, Beograd: Centar za multidisciplinarne studije Univerziteta u Beogradu

[56] Hodgkin, A.L.,A.F. Huxley, *A quantitative description of membrane current and its application to conduction and excitation in nerve* J Physiol **1952**, *117*.

[57] Colbert, C.M.,D. Johnston, *Axonal action-potential initiation and Na+ channel densities in the soma and axon initial segment of subicular pyramidal neurons* Journal of Neuroscience **1996**, *16*.

[58] Hodgkin, A.L., A.F. Huxley,B. Katz, *Measurement of current-voltage relations in the membrane of the giant axon of Loligo* J Physiol **1952**, *116*.

[59] Bean, B.P., *The action potential in mammalian central neurons* Nature Reviews Neuroscience **2007**, *8*.

[60] Zhang, L.,C.J. McBain, *Potassium conductances underlying repolarization and after-hyperpolarization in rat CA1 hippocampal interneurones* The Journal of Physiology **1995**, *488*.

[61] Bielajew, C., M. Lapointe, I. Kiss,P. Shizgal, *Absolute and relative refractory periods of the substrates for lateral hypothalamic and ventral midbrain self-stimulation* Physiol Behav **1982**, *28*.

[62] Hill, D.N., S.B. Mehta,D. Kleinfeld, *Quality metrics to accompany spike sorting of extracellular signals* J Neurosci **2011**, *31*.

[63] Erisir, A., D. Lau, B. Rudy,C.S. Leonard, *Function of specific K+ channels in sustained high-frequency firing of fast-spiking neocortical interneurons* Journal of neurophysiology **1999**, *82*.

[64] Henze, D.A., Z. Borhegyi, J. Csicsvari, A. Mamiya, K.D. Harris,G. Buzsáki, *Intracellular features predicted by extracellular recordings in the hippocampus in vivo* J Neurophysiol **2000**, *84*.

[65] Ma, M.,J. Koester, *The role of K+ currents in frequency-dependent spike broadening in Aplysia R20 neurons: a dynamic-clamp analysis* Journal of Neuroscience **1996**, *16*.

[66] Debanne, D., A. Bialowas,S. Rama, *What are the mechanisms for analogue and digital signalling in the brain?* Nat Rev Neurosci **2013**, *14*.

[67] Zbili, M.,D. Debanne, *Past and Future of Analog-Digital Modulation of Synaptic Transmission* Front Cell Neurosci **2019**, *13*.

[68] Markram, H., J. Lübke, M. Frotscher,B. Sakmann, *Regulation of Synaptic Efficacy by Coincidence of Postsynaptic APs and EPSPs* Science **1997**, *275*.

[69] Kampa, B.M., J. Clements, P. Jonas,G.J. Stuart, *Kinetics of Mg2+ unblock of NMDA receptors: implications for spike-timing dependent synaptic plasticity* J Physiol **2004**, *556*.

[70] Kampa, B.M.,G.J. Stuart, *Calcium Spikes in Basal Dendrites of Layer 5 Pyramidal Neurons during Action Potential Bursts* The Journal of Neuroscience **2006**, *26*.

[71] Cover, K.K.,B.N. Mathur, *Axo-axonic synapses: Diversity in neural circuit function* J Comp Neurol **2021**, *529*.

[72] Rizo, J.,C. Rosenmund, *Synaptic vesicle fusion* Nat Struct Mol Biol **2008**, *15*.

[73] Yuste, R.,L.C. Katz, *Control of postsynaptic Ca2+ influx in developing neocortex by excitatory and inhibitory neurotransmitters* Neuron **1991**, *6*.

[74] Staley, K.J., B.L. Soldo,W.R. Proctor, *Ionic mechanisms of neuronal excitation by inhibitory GABAA receptors* Science **1995**, *269*.

[75] Niculescu, D.,C. Lohmann, *Gap Junctions in Developing Thalamic and Neocortical Neuronal Networks* Cerebral Cortex **2013**, *24*.

[76] Bennett, M.V.,R.S. Zukin, *Electrical coupling and neuronal synchronization in the mammalian brain* Neuron **2004**, *41*.

[77] Connors, B.W., *Synchrony and so much more: Diverse roles for electrical synapses in neural circuits* Dev Neurobiol **2017**, *77*.

[78] Pereda, A.E., S. Curti, G. Hoge, R. Cachope, C.E. Flores,J.E. Rash, *Gap junction-mediated electrical transmission: Regulatory mechanisms and plasticity* Biochimica et Biophysica Acta (BBA) - Biomembranes **2013**, *1828*.

[79] Bennett, M., *Physiology of electrotonic junctions* Annals of the New York Academy of Sciences **1966**, *137*.

[80] Gibson, J.R., M. Beierlein,B.W. Connors, *Functional properties of electrical synapses between inhibitory interneurons of neocortical layer 4* J Neurophysiol **2005**, *93*.

[81] Yuste, R., D.A. Nelson, W.W. Rubin,L.C. Katz, *Neuronal domains in developing neocortex: mechanisms of coactivation* Neuron **1995**, *14*.

[82] Kandler, K.,L.C. Katz, *Coordination of neuronal activity in developing visual cortex by gap junction-mediated biochemical communication* Journal of Neuroscience **1998**, *18*.

[83] Kähne, M., S. Rüdiger, A.H. Kihara,B. Lindner, *Gap junctions set the speed and nucleation rate of stage I retinal waves* PLOS Computational Biology **2019**, *15*.

[84] Wong, W.T., J.R. Sanes,R.O. Wong, *Developmentally regulated spontaneous activity in the embryonic chick retina* Journal of Neuroscience **1998**, *18*.

[85] Crépel, V., D. Aronov, I. Jorquera, A. Represa, Y. Ben-Ari,R. Cossart, *A parturition-associated nonsynaptic coherent activity pattern in the developing hippocampus* Neuron **2007**, *54*.

[86] Szabadics, J., A. Lorincz,G. Tamás, *β and γ frequency synchronization by dendritic GABAergic synapses and gap junctions in a network of cortical interneurons* Journal of Neuroscience **2001**, *21*.

[87] Curti, S., G. Hoge, J.I. Nagy,A.E. Pereda, *Synergy between electrical coupling and membrane properties promotes strong synchronization of neurons of the mesencephalic trigeminal nucleus* Journal of Neuroscience **2012**, *32*.

[88] Ostojic, S., N. Brunel,V. Hakim, *Synchronization properties of networks of electrically coupled neurons in the presence of noise and heterogeneities* Journal of computational neuroscience **2009**, *26*.

[89] Kunze, A., M.R. Congreso, C. Hartmann, A. Wallraff-Beck, K. Hüttmann, P. Bedner, R. Requardt, G. Seifert, C. Redecker,K. Willecke, *Connexin expression by radial glia-like cells is required for neurogenesis in the adult dentate gyrus* Proceedings of the National Academy of Sciences **2009**, *106*.

[90] Elias, L.A., D.D. Wang,A.R. Kriegstein, *Gap junction adhesion is necessary for radial migration in the neocortex* Nature **2007**, *448*.

[91] Haas, J.S., C.M. Greenwald,A.E. Pereda, *Activity-dependent plasticity of electrical synapses: increasing evidence for its presence and functional roles in the mammalian brain* BMC Cell Biol **2016**, *17 Suppl 1*.

[92] Belousov, A.B.,J.D. Fontes, *Neuronal gap junctions: making and breaking connections during development and injury* Trends Neurosci **2013**, *36*.

[93] Nadarajah, B., A.M. Jones, W.H. Evans,J.G. Parnavelas, *Differential expression of connexins during neocortical development and neuronal circuit formation* J Neurosci **1997**, *17*.

[94] Talukdar, S., L. Emdad, S.K. Das,P.B. Fisher, *GAP junctions: multifaceted regulators of neuronal differentiation* Tissue Barriers **2022**, *10*.

[95] Fukuda, T., T. Kosaka, W. Singer,R.A. Galuske, *Gap junctions among dendrites of cortical GABAergic neurons establish a dense and widespread intercolumnar network* J Neurosci **2006**, *26*.

[96] Hamzei-Sichani, F., N. Kamasawa, W.G. Janssen, T. Yasumura, K.G. Davidson, P.R. Hof, S.L. Wearne, M.G. Stewart, S.R. Young, M.A. Whittington, J.E. Rash,R.D. Traub, *Gap junctions on hippocampal mossy fiber axons demonstrated by thin-section electron microscopy and freeze fracture replica immunogold labeling* Proc Natl Acad Sci U S A **2007**, *104*.

[97] Ixmatlahua, D., B. Vizcarra, G. Gómez-Lira, I. Romero-Maldonado, F. Ortiz, G. Rojas-Piloni,R. Gutiérrez, *Neuronal Glutamatergic Network Electrically Wired with Silent But Activatable Gap Junctions* The Journal of Neuroscience **2020**, *40*.

[98] Nagy, J.I., *Evidence for connexin36 localization at hippocampal mossy fiber terminals suggesting mixed chemical/electrical transmission by granule cells* Brain Res **2012**, *1487*.

[99] Lee, E., S. Lee, J.J. Shin, W. Choi, C. Chung, S. Lee, J. Kim, S. Ha, R. Kim, T. Yoo, Y.-E. Yoo, J. Kim, Y.W. Noh, I. Rhim, S.Y. Lee, W. Kim, T. Lee, H. Shin, I.-J. Cho, K. Deisseroth, S.J. Kim, J.M. Park, M.W. Jung, S.-B. Paik,E. Kim, *Excitatory synapses and gap junctions cooperate to improve Pv neuronal burst firing and cortical social cognition in Shank2-mutant mice* Nature Communications **2021**, *12*.

[100] Pereda, A.E., *Electrical synapses and their functional interactions with chemical synapses* Nature Reviews Neuroscience **2014**, *15*.

[101] Kirichenko, E.Y., S.N. Skatchkov,A.M. Ermakov, *Structure and Functions of Gap Junctions and Their Constituent Connexins in the Mammalian CNS* Biochem (Mosc) Suppl Ser A Membr Cell Biol **2021**, *15*.
[102] Del Corsso, C., R. Iglesias, G. Zoidl, R. Dermietzel,D.C. Spray, *Calmodulin dependent protein kinase increases conductance at gap junctions formed by the neuronal gap junction protein connexin36* Brain research **2012**, *1487*.
[103] Vivar, C., R.D. Traub,R. Gutiérrez, *Mixed electrical–chemical transmission between hippocampal mossy fibers and pyramidal cells* European Journal of Neuroscience **2012**, *35*.
[104] Weinreb, E.,E. Moses, *Mechanistic insights into ultrasonic neurostimulation of disconnected neurons using single short pulses* Brain Stimulation **2022**, *15*.
[105] Lin, W., U. Laitko, P.F. Juranka,C.E. Morris, *Dual stretch responses of mHCN2 pacemaker channels: accelerated activation, accelerated deactivation* Biophysical journal **2007**, *92*.
[106] Christensen, A.P.,D.P. Corey, *TRP channels in mechanosensation: direct or indirect activation?* Nature Reviews Neuroscience **2007**, *8*.
[107] Ranade, S.S., R. Syeda,A. Patapoutian, *Mechanically Activated Ion Channels* Neuron **2015**, *87*.
[108] Zhao, Q., H. Zhou, S. Chi, Y. Wang, J. Wang, J. Geng, K. Wu, W. Liu, T. Zhang, M.-Q. Dong, J. Wang, X. Li,B. Xiao, *Structure and mechanogating mechanism of the Piezo1 channel* Nature **2018**, *554*.
[109] Wang, L., H. Zhou, M. Zhang, W. Liu, T. Deng, Q. Zhao, Y. Li, J. Lei, X. Li,B. Xiao, *Structure and mechanogating of the mammalian tactile channel PIEZO2* Nature **2019**, *573*.
[110] Kanda, H., J. Ling, S. Tonomura, K. Noguchi, S. Matalon,J.G. Gu, *TREK-1 and TRAAK Are Principal K(+) Channels at the Nodes of Ranvier for Rapid Action Potential Conduction on Mammalian Myelinated Afferent Nerves* Neuron **2019**, *104*.
[111] Brohawn, S.G., Z. Su,R. MacKinnon, *Mechanosensitivity is mediated directly by the lipid membrane in TRAAK and TREK1 K<sup>+</sup> channels* Proceedings of the National Academy of Sciences **2014**, *111*.
[112] Douguet, D.,E. Honoré, *Mammalian Mechanoelectrical Transduction: Structure and Function of Force-Gated Ion Channels* Cell **2019**, *179*.
[113] Morris, C.E.,P.F. Juranka, *Lipid stress at play: mechanosensitivity of voltage-gated channels* Curr Top Membr **2007**, *59*.
[114] Paoletti, P.,P. Ascher, *Mechanosensitivity of NMDA receptors in cultured mouse central neurons* Neuron **1994**, *13*.
[115] Xu, J., J. Mathur, E. Vessières, S. Hammack, K. Nonomura, J. Favre, L. Grimaud, M. Petrus, A. Francisco,J. Li, *GPR68 senses flow and is essential for vascular physiology* Cell **2018**, *173*.
[116] Chiang, L.-Y., K. Poole, B.E. Oliveira, N. Duarte, Y.A.B. Sierra, L. Bruckner-Tuderman, M. Koch, J. Hu,G.R. Lewin, *Laminin-332 coordinates mechanotransduction and growth cone bifurcation in sensory neurons* Nature neuroscience **2011**, *14*.
[117] Suter, D.M.,P. Forscher, *Substrate–cytoskeletal coupling as a mechanism for the regulation of growth cone motility and guidance* Journal of Neurobiology **2000**, *44*.
[118] Balaban, N.Q., U.S. Schwarz, D. Riveline, P. Goichberg, G. Tzur, I. Sabanay, D. Mahalu, S. Safran, A. Bershadsky, L. Addadi,B. Geiger, *Force and focal adhesion assembly: a close relationship studied using elastic micropatterned substrates* Nature Cell Biology **2001**, *3*.
[119] Matthews, B.D., C.K. Thodeti,D.E. Ingber, *Activation of mechanosensitive ion channels by forces transmitted through integrins and the cytoskeleton* Current Topics in Membranes **2007**, *58*.
[120] Martinac, B., *The ion channels to cytoskeleton connection as potential mechanism of mechanosensitivity* Biochimica et Biophysica Acta (BBA)-Biomembranes **2014**, *1838*.
[121] Matthews, B.D., C.K. Thodeti,D.E. Ingber, *Activation of Mechanosensitive Ion Channels by Forces Transmitted Through Integrins and the Cytoskeleton*, in *Current Topics in Membranes*. 2007, Academic Press. p. 59-85.
[122] Starostina, I., Y.-K. Jang, H.-S. Kim, J.-S. Suh, S.-H. Ahn, G.-H. Choi, M. Suk,T.-J. Kim, *Distinct calcium regulation of TRPM7 mechanosensitive channels at plasma membrane microdomains visualized by FRET-based single cell imaging* Scientific Reports **2021**, *11*.
[123] Milos, F., A. Belu, D. Mayer, V. Maybeck,A. Offenhäusser, *Polymer Nanopillars Induce Increased Paxillin Adhesion Assembly and Promote Axon Growth in Primary Cortical Neurons* Advanced Biology **2021**, *5*.
[124] Milos, F., M. Spehr,A. Offenhäusser, *Three-dimensional polymeric topographies for neural interfaces*. 2021, Fachgruppe Physik.

[125] Santoro, F., G. Panaitov,A. Offenhäusser, *Defined Patterns of Neuronal Networks on 3D Thiol-functionalized Microstructures* Nano Letters **2014**, *14*.
[126] Marom, S.,G. Shahaf, *Development, learning and memory in large random networks of cortical neurons: lessons beyond anatomy* Quarterly Reviews of Biophysics **2002**, *35*.
[127] Guan, C.-b., H.-t. Xu, M. Jin, X.-b. Yuan,M.-m. Poo, *Long-Range Ca<sup>2+</sup> Signaling from Growth Cone to Soma Mediates Reversal of Neuronal Migration Induced by Slit-2* Cell **2007**, *129*.
[128] Zheng, J.Q.,M.-m. Poo, *Calcium signaling in neuronal motility* Annu. Rev. Cell Dev. Biol. **2007**, *23*.
[129] Shepherd, G.M., A. Stepanyants, I. Bureau, D. Chklovskii,K. Svoboda, *Geometric and functional organization of cortical circuits* Nature neuroscience **2005**, *8*.
[130] Kole, A.J., R.P. Annis,M. Deshmukh, *Mature neurons: equipped for survival* Cell Death & Disease **2013**, *4*.
[131] Hanse, E., H. Seth,I. Riebe, *AMPA-silent synapses in brain development and pathology* Nature Reviews Neuroscience **2013**, *14*.
[132] Durand, G.M., Y. Kovalchuk,A. Konnerth, *Long-term potentiation and functional synapse induction in developing hippocampus* Nature **1996**, *381*.
[133] Soriano, J., M. Rodríguez Martínez, T. Tlusty,E. Moses, *Development of input connections in neural cultures* Proceedings of the National Academy of Sciences **2008**, *105*.
[134] Ivenshitz, M.,M. Segal, *Neuronal Density Determines Network Connectivity and Spontaneous Activity in Cultured Hippocampus* Journal of Neurophysiology **2010**, *104*.
[135] Blankenship, A.G.,M.B. Feller, *Mechanisms underlying spontaneous patterned activity in developing neural circuits* Nature Reviews Neuroscience **2010**, *11*.
[136] Spitzer, N.C., *Electrical activity in early neuronal development* Nature **2006**, *444*.
[137] Garaschuk, O., J. Linn, J. Eilers,A. Konnerth, *Large-scale oscillatory calcium waves in the immature cortex* Nature neuroscience **2000**, *3*.
[138] Corlew, R., M.M. Bosma,W.J. Moody, *Spontaneous, synchronous electrical activity in neonatal mouse cortical neurones* The Journal of physiology **2004**, *560*.
[139] Shefi, O., I. Golding, R. Segev, E. Ben-Jacob,A. Ayali, *Morphological characterization of in vitro neuronal networks* Physical Review E **2002**, *66*.
[140] de Santos-Sierra, D., I. Sendiña-Nadal, I. Leyva, J.A. Almendral, A. Ayali, S. Anava, C. Sánchez-Ávila,S. Boccaletti, *Graph-based unsupervised segmentation algorithm for cultured neuronal networks' structure characterization and modeling* Cytometry Part A **2015**, *87*.
[141] Woiterski, L., T. Claudepierre, R. Luxenhofer, R. Jordan,J. Käs, *Stages of neuronal network formation* New Journal of Physics **2013**, *15*.
[142] Teller, S., C. Granell, M. De Domenico, J. Soriano, S. Gomez,A. Arenas, *Emergence of assortative mixing between clusters of cultured neurons* PLoS computational biology **2014**, *10*.
[143] Downes, J.H., M.W. Hammond, D. Xydas, M.C. Spencer, V.M. Becerra, K. Warwick, B.J. Whalley,S.J. Nasuto, *Emergence of a small-world functional network in cultured neurons* PLoS computational biology **2012**, *8*.
[144] Takahashi, N., T. Sasaki, W. Matsumoto, N. Matsuki,Y. Ikegaya, *Circuit topology for synchronizing neurons in spontaneously active networks* Proceedings of the National Academy of Sciences **2010**, *107*.
[145] Song, S., P.J. Sjöström, M. Reigl, S. Nelson,D.B. Chklovskii, *Highly nonrandom features of synaptic connectivity in local cortical circuits* PLoS Biol **2005**, *3*.
[146] Wagenaar, D.A., J. Pine,S.M. Potter, *An extremely rich repertoire of bursting patterns during the development of cortical cultures* BMC Neuroscience **2006**, *7*.
[147] Nakanishi, K.,F. Kukita, *Functional synapses in synchronized bursting of neocortical neurons in culture* Brain Research **1998**, *795*.
[148] Buzsáki, G., *Rhythms of the Brain*. 2006: Oxford University Press.
[149] Trujillo, C.A., R. Gao, P.D. Negraes, J. Gu, J. Buchanan, S. Preissl, A. Wang, W. Wu, G.G. Haddad, I.A. Chaim, A. Domissy, M. Vandenberghe, A. Devor, G.W. Yeo, B. Voytek,A.R. Muotri, *Complex Oscillatory Waves Emerging from Cortical Organoids Model Early Human Brain Network Development* Cell Stem Cell **2019**, *25*.
[150] Camille, A., C. Adriano, B.A. James, B. Paolo, A. Laurent, B.-A. Yehezkel,C. Rosa, *Sequential Generation of Two Distinct Synapse-Driven Network Patterns in Developing Neocortex* The Journal of Neuroscience **2008**, *28*.

[151] Sanchez-Vives, M.V.,D.A. McCormick, *Cellular and network mechanisms of rhythmic recurrent activity in neocortex* Nature Neuroscience **2000**, *3*.
[152] Platkiewicz, J.,R. Brette, *Impact of fast sodium channel inactivation on spike threshold dynamics and synaptic integration* PLoS computational biology **2011**, *7*.
[153] Azouz, R.,C.M. Gray, *Dynamic spike threshold reveals a mechanism for synaptic coincidence detection in cortical neurons in vivo* Proceedings of the National Academy of Sciences **2000**, *97*.
[154] Harnett, M.T., J.K. Makara, N. Spruston, W.L. Kath,J.C. Magee, *Synaptic amplification by dendritic spines enhances input cooperativity* Nature **2012**, *491*.
[155] Roome, C.J.,B. Kuhn, *Dendritic coincidence detection in Purkinje neurons of awake mice* eLife **2020**, *9*.
[156] Antic, S.D., W.L. Zhou, A.R. Moore, S.M. Short,K.D. Ikonomu, *The decade of the dendritic NMDA spike* J Neurosci Res **2010**, *88*.
[157] Gao, P.P., J.W. Graham, W.L. Zhou, J. Jang, S. Angulo, S. Dura-Bernal, M. Hines, W.W. Lytton,S.D. Antic, *Local glutamate-mediated dendritic plateau potentials change the state of the cortical pyramidal neuron* J Neurophysiol **2021**, *125*.
[158] Larkum, M.E., J.J. Zhu,B. Sakmann, *A new cellular mechanism for coupling inputs arriving at different cortical layers* Nature **1999**, *398*.
[159] Bonifazi, P., M. Goldin, M.A. Picardo, I. Jorquera, A. Cattani, G. Bianconi, A. Represa, Y. Ben-Ari,R. Cossart, *GABAergic Hub Neurons Orchestrate Synchrony in Developing Hippocampal Networks* Science **2009**, *326*.
[160] Neher, E.,B. Sakmann, *Single-channel currents recorded from membrane of denervated frog muscle fibres* Nature **1976**, *260*.
[161] Peng, Y., F.X. Mittermaier, H. Planert, U.C. Schneider, H. Alle,J.R.P. Geiger, *High-throughput microcircuit analysis of individual human brains through next-generation multineuron patch-clamp* eLife **2019**, *8*.
[162] Michalikova, M., M.W.H. Remme,R. Kempter, *Spikelets in Pyramidal Neurons: Action Potentials Initiated in the Axon Initial Segment That Do Not Activate the Soma* PLOS Computational Biology **2017**, *13*.
[163] Larkum, M.E., S. Watanabe, T. Nakamura, N. Lasser-Ross,W.N. Ross, *Synaptically Activated Ca2+ Waves in Layer 2/3 and Layer 5 Rat Neocortical Pyramidal Neurons* The Journal of Physiology **2003**, *549*.
[164] Kole, M.H.P.,G.J. Stuart, *Is action potential threshold lowest in the axon?* Nature Neuroscience **2008**, *11*.
[165] Stuart, G.J.,B. Sakmann, *Active propagation of somatic action potentials into neocortical pyramidal cell dendrites* Nature **1994**, *367*.
[166] Cohen, I.,R. Miles, *Contributions of intrinsic and synaptic activities to the generation of neuronal discharges in in vitro hippocampus* J Physiol **2000**, *524 Pt 2*.
[167] Cohen, D.,M. Segal, *Homeostatic presynaptic suppression of neuronal network bursts* Journal of neurophysiology **2009**, *101*.
[168] Brown, S.P.,S. Hestrin, *Intracortical circuits of pyramidal neurons reflect their long-range axonal targets* Nature **2009**, *457*.
[169] Jouhanneau, J.-S., J. Kremkow,J.F. Poulet, *Single synaptic inputs drive high-precision action potentials in parvalbumin expressing GABA-ergic cortical neurons in vivo* Nature Communications **2018**, *9*.
[170] Yger, P., G.L.B. Spampinato, E. Esposito, B. Lefebvre, S. Deny, C. Gardella, M. Stimberg, F. Jetter, G. Zeck, S. Picaud, J. Duebel,O. Marre, *A spike sorting toolbox for up to thousands of electrodes validated with ground truth recordings in vitro and in vivo* eLife **2018**, *7*.
[171] Dana, H., B. Mohar, Y. Sun, S. Narayan, A. Gordus, J.P. Hasseman, G. Tsegaye, G.T. Holt, A. Hu, D. Walpita, R. Patel, J.J. Macklin, C.I. Bargmann, M.B. Ahrens, E.R. Schreiter, V. Jayaraman, L.L. Looger, K. Svoboda,D.S. Kim, *Sensitive red protein calcium indicators for imaging neural activity* Elife **2016**, *5*.
[172] Chen, T.-W., T.J. Wardill, Y. Sun, S.R. Pulver, S.L. Renninger, A. Baohan, E.R. Schreiter, R.A. Kerr, M.B. Orger,V. Jayaraman, *Ultrasensitive fluorescent proteins for imaging neuronal activity* Nature **2013**, *499*.
[173] Wei, Z., B.-J. Lin, T.-W. Chen, K. Daie, K. Svoboda,S. Druckmann, *A comparison of neuronal population dynamics measured with calcium imaging and electrophysiology* PLOS Computational Biology **2020**, *16*.
[174] Nilius, B., *Pflügers Archiv and the advent of modern electrophysiology. From the first action potential to patch clamp* Pflugers Arch **2003**, *447*.
[175] Hodgkin, A.L.,A.F. Huxley, *The components of membrane conductance in the giant axon of Loligo* J Physiol **1952**, *116*.
[176] Molleman, A., *Patch clamping: an introductory guide to patch clamp electrophysiology*. 2003: John Wiley & Sons.

[177] Suchyna, T.M., V.S. Markin,F. Sachs, *Biophysics and Structure of the Patch and the Gigaseal* Biophysical Journal **2009**, *97*.
[178] Vazetdinova, A., F. Valiullina-Rakhmatullina, A. Rozov, A. Evstifeev, R. Khazipov,A. Nasretdinov, *On the accuracy of cell-attached current-clamp recordings from cortical neurons* Frontiers in Molecular Neuroscience **2022**, *15*.
[179] Malboubi, M.,K. Jiang, *Gigaseal Formation*, in *Gigaseal Formation in Patch Clamping: With Applications of Nanotechnology*, M. Malboubi and K. Jiang, Editors. 2014, Springer Berlin Heidelberg: Berlin, Heidelberg. p. 17-28.
[180] Jouhanneau, J.-S., J. Kremkow, A.L. Dorrn,J.F. Poulet, *In vivo monosynaptic excitatory transmission between layer 2 cortical pyramidal neurons* Cell reports **2015**, *13*.
[181] Robert, C., V. Tseeb, C. Kordon,C. Hammond, *Patch-clamp-induced perturbations of [Ca(2+)](i) activity in somatotropes* Neuroendocrinology **1999**, *70*.
[182] Jäckel, D., D.J. Bakkum, T.L. Russell, J. Müller, M. Radivojevic, U. Frey, F. Franke,A. Hierlemann, *Combination of High-density Microelectrode Array and Patch Clamp Recordings to Enable Studies of Multisynaptic Integration* Scientific Reports **2017**, *7*.
[183] Guo, L., *Perspectives on electrical neural recording: a revisit to the fundamental concepts* Journal of Neural Engineering **2020**, *17*.
[184] Eick, S., *Extracellular stimulation of individual electrogenic cells with micro-scaled electrodes*, in *Aachen*. 2010, RWTH Aachen University.
[185] Joye, N., A. Schmid,Y. Leblebici. *An electrical model of the cell-electrode interface for high-density microelectrode arrays*. in *2008 30th Annual International Conference of the IEEE Engineering in Medicine and Biology Society*. 2008.
[186] Shmoel, N., N. Rabieh, S.M. Ojovan, H. Erez, E. Maydan,M.E. Spira, *Multisite electrophysiological recordings by self-assembled loose-patch-like junctions between cultured hippocampal neurons and mushroom-shaped microelectrodes* Scientific reports **2016**, *6*.
[187] Bove, M., M. Grattarola, S. Martinoia,G. Verreschi, *Interfacing cultured neurons to planar substrate microelectrodes: characterization of the neuron-to-microelectrode junction* Bioelectrochemistry and bioenergetics **1995**, *38*.
[188] Massobrio, P., G. Massobrio,S. Martinoia, *Interfacing Cultured Neurons to Microtransducers Arrays: A Review of the Neuro-Electronic Junction Models* Frontiers in Neuroscience **2016**, *10*.
[189] Joye, N., A. Schmid,Y. Leblebici, *An Electrical Model of the Cell-Electrode Interface for High-density Microelectrode Arrays* Conference proceedings : ... Annual International Conference of the IEEE Engineering in Medicine and Biology Society. IEEE Engineering in Medicine and Biology Society. Conference **2008**, *2008*.
[190] Wrobel, G., M. Höller, S. Ingebrandt, S. Dieluweit, F. Sommerhage, H.P. Bochem,A. Offenhäusser, *Transmission electron microscopy study of the cell-sensor interface* J R Soc Interface **2008**, *5*.
[191] Hai, A., J. Shappir,M.E. Spira, *Long-Term, Multisite, Parallel, In-Cell Recording and Stimulation by an Array of Extracellular Microelectrodes* Journal of Neurophysiology **2010**, *104*.
[192] Hai, A., J. Shappir,M.E. Spira, *In-cell recordings by extracellular microelectrodes* Nature methods **2010**, *7*.
[193] Lewen, J., *Quantification and Improvement of the Electric Coupling between Electrogenic Cells and Microelectrode Arrays by Nanocavities and Nanostructures*, in *Forschungszentrum Jülich*. 2019, RWTH Aachen University.
[194] Hofmann, B., E. Kätelhön, M. Schottdorf, A. Offenhäusser,B. Wolfrum, *Nanocavity electrode array for recording from electrogenic cells* Lab Chip **2011**, *11*.
[195] Chung, J.E., J.F. Magland, A.H. Barnett, V.M. Tolosa, A.C. Tooker, K.Y. Lee, K.G. Shah, S.H. Felix, L.M. Frank,L.F. Greengard, *A Fully Automated Approach to Spike Sorting* Neuron **2017**, *95*.
[196] Hilgen, G., M. Sorbaro, S. Pirmoradian, J.-O. Muthmann, I.E. Kepiro, S. Ullo, C.J. Ramirez, A. Puente Encinas, A. Maccione, L. Berdondini, V. Murino, D. Sona, F. Cella Zanacchi, E. Sernagor,M.H. Hennig, *Unsupervised Spike Sorting for Large-Scale, High-Density Multielectrode Arrays* Cell Reports **2017**, *18*.
[197] Rossant, C., S.N. Kadir, D.F.M. Goodman, J. Schulman, M.L.D. Hunter, A.B. Saleem, A. Grosmark, M. Belluscio, G.H. Denfield, A.S. Ecker, A.S. Tolias, S. Solomon, G. Buzsaki, M. Carandini,K.D. Harris, *Spike sorting for large, dense electrode arrays* Nat Neurosci **2016**, *19*.

[198] Shabestari, P.S., A.P. Buccino, S.S. Kumar, A. Pedrocchi,A. Hierlemann. *A modulated template-matching approach to improve spike sorting of bursting neurons*. in *2021 IEEE Biomedical Circuits and Systems Conference (BioCAS)*. 2021.

[199] Stratton, P., A. Cheung, J. Wiles, E. Kiyatkin, P. Sah,F. Windels, *Action potential waveform variability limits multi-unit separation in freely behaving rats* PloS one **2012**, *7*.

[200] Jurga, M., A.W. Lipkowski, B. Lukomska, L. Buzanska, K. Kurzepa, T. Sobanski, A. Habich, S. Coecke, B. Gajkowska,K. Domanska-Janik, *Generation of functional neural artificial tissue from human umbilical cord blood stem cells* Tissue Eng Part C Methods **2009**, *15*.

[201] Pelkonen, A., C. Pistono, P. Klecki, M. Gómez-Budia, A. Dougalis, H. Konttinen, I. Stanová, I. Fagerlund, V. Leinonen, P. Korhonen,T. Malm, *Functional Characterization of Human Pluripotent Stem Cell-Derived Models of the Brain with Microelectrode Arrays* Cells **2021**, *11*.

[202] Pouzat, C.G., Samuel, *Tridesclous*, https://github.com/tridesclous/tridesclous/blob/master/LICENSE, Editor. 2015, MIT License.

[203] Chaure, F.J., H.G. Rey,R.Q. Quiroga, *A novel and fully automatic spike-sorting implementation with variable number of features* Journal of Neurophysiology **2018**, *120*.

[204] Steinmetz, N.A., et al., *Neuropixels 2.0: A miniaturized high-density probe for stable, long-term brain recordings* Science **2021**, *372*.

[205] Jun, J.M., Jeremy, *IronClust*. 2018: https://github.com/flatironinstitute/ironclust.

[206] Svoboda, K., W. Denk, D. Kleinfeld,D.W. Tank, *In vivo dendritic calcium dynamics in neocortical pyramidal neurons* Nature **1997**, *385*.

[207] Matthew Evan, L., W. Jack, S. Bert,H. Fritjof, *Dendritic Spikes in Apical Dendrites of Neocortical Layer 2/3 Pyramidal Neurons* The Journal of Neuroscience **2007**, *27*.

[208] Jayant, K., J.J. Hirtz, I.J. Plante, D.M. Tsai, W.D. De Boer, A. Semonche, D.S. Peterka, J.S. Owen, O. Sahin, K.L. Shepard,R. Yuste, *Targeted intracellular voltage recordings from dendritic spines using quantum-dot-coated nanopipettes* Nat Nanotechnol **2017**, *12*.

[209] Bruton, J., A.J. Cheng,H. Westerblad, *Measuring Ca2+ in Living Cells*, in *Calcium Signaling*, M.S. Islam, Editor. 2020, Springer International Publishing: Cham. p. 7-26.

[210] Sabatini, B.L., T.G. Oertner,K. Svoboda, *The Life Cycle of Ca<sup>2+</sup> Ions in Dendritic Spines* Neuron **2002**, *33*.

[211] Icha, J., M. Weber, J.C. Waters,C. Norden, *Phototoxicity in live fluorescence microscopy, and how to avoid it* Bioessays **2017**, *39*.

[212] Stosiek, C., O. Garaschuk, K. Holthoff,A. Konnerth, *In vivo two-photon calcium imaging of neuronal networks* Proceedings of the National Academy of Sciences **2003**, *100*.

[213] Pologruto, T.A., R. Yasuda,K. Svoboda, *Monitoring neural activity and [Ca2+] with genetically encoded Ca2+ indicators* J Neurosci **2004**, *24*.

[214] Smith, N.A., B.T. Kress, Y. Lu, D. Chandler-Militello, A. Benraiss,M. Nedergaard, *Fluorescent Ca(2+) indicators directly inhibit the Na,K-ATPase and disrupt cellular functions* Sci Signal **2018**, *11*.

[215] Maes, M., G. Colombo, R. Schulz,S. Siegert, *Targeting microglia with lentivirus and AAV: Recent advances and remaining challenges* Neuroscience Letters **2019**, *707*.

[216] Tian, L., S.A. Hires, T. Mao, D. Huber, M.E. Chiappe, S.H. Chalasani, L. Petreanu, J. Akerboom, S.A. McKinney, E.R. Schreiter, C.I. Bargmann, V. Jayaraman, K. Svoboda,L.L. Looger, *Imaging neural activity in worms, flies and mice with improved GCaMP calcium indicators* Nature Methods **2009**, *6*.

[217] Hell, S.W., *Microscopy and its focal switch* Nature Methods **2009**, *6*.

[218] Rueckl, M., S.C. Lenzi, L. Moreno-Velasquez, D. Parthier, D. Schmitz, S. Ruediger,F.W. Johenning, *SamuROI, a Python-Based Software Tool for Visualization and Analysis of Dynamic Time Series Imaging at Multiple Spatial Scales* Front Neuroinform **2017**, *11*.

[219] Hanemaaijer, N.A.K., M.A. Popovic, X. Wilders, S. Grasman, O. Pavón Arocas,M.H.P. Kole, *Ca2+ entry through NaV channels generates submillisecond axonal Ca2+ signaling* eLife **2020**, *9*.

[220] Grewe, B.F., D. Langer, H. Kasper, B.M. Kampa,F. Helmchen, *High-speed in vivo calcium imaging reveals neuronal network activity with near-millisecond precision* Nature Methods **2010**, *7*.

[221] Greenberg, D.S., A.R. Houweling,J.N. Kerr, *Population imaging of ongoing neuronal activity in the visual cortex of awake rats* Nature neuroscience **2008**, *11*.

[222] Pnevmatikakis, E.A., D. Soudry, Y. Gao, T.A. Machado, J. Merel, D. Pfau, T. Reardon, Y. Mu, C. Lacefield,W. Yang, *Simultaneous denoising, deconvolution, and demixing of calcium imaging data* Neuron **2016**, *89*.
[223] Giovannucci, A., J. Friedrich, P. Gunn, J. Kalfon, B.L. Brown, S.A. Koay, J. Taxidis, F. Najafi, J.L. Gauthier, P. Zhou, B.S. Khakh, D.W. Tank, D.B. Chklovskii,E.A. Pnevmatikakis, *CaImAn an open source tool for scalable calcium imaging data analysis* eLife **2019**, *8*.
[224] Rupprecht, P., S. Carta, A. Hoffmann, M. Echizen, A. Blot, A.C. Kwan, Y. Dan, S.B. Hofer, K. Kitamura, F. Helmchen,R.W. Friedrich, *A database and deep learning toolbox for noise-optimized, generalized spike inference from calcium imaging* Nat Neurosci **2021**, *24*.
[225] Schiller, J., Y. Schiller, G. Stuart,B. Sakmann, *Calcium action potentials restricted to distal apical dendrites of rat neocortical pyramidal neurons* The Journal of physiology **1997**, *505*.
[226] Larkum, M.E.,J.J. Zhu, *Signaling of layer 1 and whisker-evoked Ca2+ and Na+ action potentials in distal and terminal dendrites of rat neocortical pyramidal neurons in vitro and in vivo* Journal of neuroscience **2002**, *22*.
[227] Lipscombe, D., T.D. Helton,W. Xu, *L-Type Calcium Channels: The Low Down* Journal of Neurophysiology **2004**, *92*.
[228] Almog, M.,A. Korngreen, *Characterization of Voltage-Gated Ca2+ Conductances in Layer 5 Neocortical Pyramidal Neurons from Rats* PLOS ONE **2009**, *4*.
[229] Iftinca, M.C., *Neuronal T-type calcium channels: what's new? Iftinca: T-type channel regulation* J Med Life **2011**, *4*.
[230] Usachev, Y.M.,S.A. Thayer, *All-or-none Ca2+ release from intracellular stores triggered by Ca2+ influx through voltage-gated Ca2+ channels in rat sensory neurons* J Neurosci **1997**, *17*.
[231] Verkhratsky, A., *Physiology and Pathophysiology of the Calcium Store in the Endoplasmic Reticulum of Neurons* Physiological Reviews **2005**, *85*.
[232] Verkhratsky, A.,A. Shmigol, *Calcium-induced calcium release in neurones* Cell Calcium **1996**, *19*.
[233] Shi, Z., Z.T. Graber, T. Baumgart, H.A. Stone,A.E. Cohen, *Cell Membranes Resist Flow* Cell **2018**, *175*.
[234] Zhang, T., N. Pan, Y. Wang, C. Liu,S. Hu, *Transcranial Focused Ultrasound Neuromodulation: A Review of the Excitatory and Inhibitory Effects on Brain Activity in Human and Animals* Front Hum Neurosci **2021**, *15*.
[235] Kamimura, H.A.S., A. Conti, N. Toschi,E.E. Konofagou, *Ultrasound neuromodulation: mechanisms and the potential of multimodal stimulation for neuronal function assessment* Front Phys **2020**, *8*.
[236] Hondrich, T.J.J., *Optogenetic and electrical investigation of network dynamics in patterned neuronal cultures*. 2021, RWTH Aachen University: Forschungszentrum Jülich GmbH Zentralbibliothek, Verlag. p. 177.
[237] Swietek, B., A. Gupta, A. Proddutur,V. Santhakumar, *Immunostaining of Biocytin-filled and Processed Sections for Neurochemical Markers* J Vis Exp **2016**.
[238] Peinado, A., R. Yuste,L.C. Katz, *Extensive dye coupling between rat neocortical neurons during the period of circuit formation* Neuron **1993**, *10*.
[239] Vogt-Eisele, A., G. Brewer, T. Decker, S. Meffert, V. Jacobsen, M. Kreiter, W. Knoll,A. Offenhäusser, *Independence of synaptic specificity from neuritic guidance* Neuroscience **2005**, *134*.
[240] Okada, Y., *Patch clamp techniques*. 2012: Springer.
[241] Lu, F.-M.,K. Kuba, *Synchronized Ca2+ signals mediated by Ca2+ action potentials in the hippocampal neuron network in vitro* Cell Calcium **2001**, *29*.
[242] Coulon, P., D. Herr, T. Kanyshkova, P. Meuth, T. Budde,H.-C. Pape, *Burst discharges in neurons of the thalamic reticular nucleus are shaped by calcium-induced calcium release* Cell calcium **2009**, *46*.
[243] Adding, L.C., G.L. Bannenberg,L.E. Gustafsson, *Basic experimental studies and clinical aspects of gadolinium salts and chelates* Cardiovascular drug reviews **2001**, *19*.
[244] Delmas, P.,B. Coste, *Mechano-Gated Ion Channels in Sensory Systems* Cell **2013**, *155*.
[245] Velasco, I.,R. Tapia, *Alterations of intracellular calcium homeostasis and mitochondrial function are involved in ruthenium red neurotoxicity in primary cortical cultures* J Neurosci Res **2000**, *60*.
[246] Sattler, R., Z. Xiong, W.-Y. Lu, J.F. MacDonald,M. Tymianski, *Distinct Roles of Synaptic and Extrasynaptic NMDA Receptors in Excitotoxicity* The Journal of Neuroscience **2000**, *20*.
[247] Kovács, M., J. Tóth, C. Hetényi, A. Málnási-Csizmadia,J.R. Sellers, *Mechanism of Blebbistatin Inhibition of Myosin II** Journal of Biological Chemistry **2004**, *279*.

[248] Patton, C., S. Thompson,D. Epel, *Some precautions in using chelators to buffer metals in biological solutions* Cell Calcium **2004**, *35*.
[249] Gebhardt, L.A., T.I. Kichko, M.J.M. Fischer,P.W. Reeh, *TRPA1-dependent calcium transients and CGRP release in DRG neurons require extracellular calcium* Journal of Cell Biology **2020**, *219*.
[250] Liu, B., M. Younus, S. Sun, Y. Li, Y. Wang, X. Wu, X. Sun, S. Shang, C. Wang, M.X. Zhu,Z. Zhou, *Reply to "TRPA1-dependent calcium transients and CGRP release in DRG neurons require extracellular calcium"* Journal of Cell Biology **2020**, *219*.
[251] Swandulla, D.,C.M. Armstrong, *Calcium channel block by cadmium in chicken sensory neurons* Proc Natl Acad Sci U S A **1989**, *86*.
[252] Abernethy, D.R., *Pharmacologic and Pharmacokinetic Profile of Mibefradil, a T- and L-type Calcium Channel Antagonist* The American Journal of Cardiology **1997**, *80*.
[253] Tang, F., E.W. Dent,K. Kalil, *Spontaneous Calcium Transients in Developing Cortical Neurons Regulate Axon Outgrowth* The Journal of Neuroscience **2003**, *23*.
[254] Tabarean, I.V.,T. Narahashi, *Potent modulation of tetrodotoxin-sensitive and tetrodotoxin-resistant sodium channels by the type II pyrethroid deltamethrin* J Pharmacol Exp Ther **1998**, *284*.
[255] Pan, F., S.L. Mills,S.C. Massey, *Screening of gap junction antagonists on dye coupling in the rabbit retina* Vis Neurosci **2007**, *24*.
[256] Alsarraf, H., K. Kelly, C. Anderson,J. Rhett, *Connexins in the Brain: Psychopharmaceutical Implications* Neuropsychiatry **2017**, *7*.
[257] Henze, D.A.,G. Buzsáki, *Action potential threshold of hippocampal pyramidal cells in vivo is increased by recent spiking activity* Neuroscience **2001**, *105*.
[258] Schuck, R., M. Go, S. Garasto, S. Reynolds, P. Dragotti,S. Schultz, *Multiphoton minimal inertia scanning for fast acquisition of neural activity signals* Journal of Neural Engineering **2017**, *15*.
[259] Quiroga, R.Q., Z. Nadasdy,Y. Ben-Shaul, *Unsupervised spike detection and sorting with wavelets and superparamagnetic clustering* Neural Comput **2004**, *16*.
[260] Niediek, J., J. Boström, C.E. Elger,F. Mormann, *Reliable Analysis of Single-Unit Recordings from the Human Brain under Noisy Conditions: Tracking Neurons over Hours* PLOS ONE **2016**, *11*.
[261] Maccione, A., M. Gandolfo, M. Tedesco, T. Nieus, K. Imfeld, S. Martinoia,L. Berdondini, *Experimental Investigation on Spontaneously Active Hippocampal Cultures Recorded by Means of High-Density MEAs: Analysis of the Spatial Resolution Effects* Front Neuroeng **2010**, *3*.
[262] Chen, L., Y. Deng, W. Luo, Z. Wang,S. Zeng, *Detection of bursts in neuronal spike trains by the mean inter-spike interval method* Progress in Natural Science **2009**, *19*.
[263] Ghaderi, P., H.R. Marateb,M.-S. Safari, *Electrophysiological Profiling of Neocortical Neural Subtypes: A Semi-Supervised Method Applied to in vivo Whole-Cell Patch-Clamp Data* Frontiers in Neuroscience **2018**, *12*.
[264] Stett, A., U. Egert, E. Guenther, F. Hofmann, T. Meyer, W. Nisch,H. Haemmerle, *Biological application of microelectrode arrays in drug discovery and basic research* Anal Bioanal Chem **2003**, *377*.
[265] Pazienti, A.,S. Grün, *Robustness of the significance of spike synchrony with respect to sorting errors* Journal of Computational Neuroscience **2006**, *21*.
[266] Quaglio, P., V. Rostami, E. Torre,S. Grün, *Methods for identification of spike patterns in massively parallel spike trains* Biological Cybernetics **2018**, *112*.
[267] Negri, J., V. Menon,T.L. Young-Pearse, *Assessment of Spontaneous Neuronal Activity In Vitro Using Multi-Well Multi-Electrode Arrays: Implications for Assay Development* eneuro **2020**, *7*.
[268] Compte, A., M.V. Sanchez-Vives, D.A. McCormick,X.-J. Wang, *Cellular and Network Mechanisms of Slow Oscillatory Activity (<1 Hz) and Wave Propagations in a Cortical Network Model* Journal of Neurophysiology **2003**, *89*.
[269] Weir, K., O. Blanquie, W. Kilb, H.J. Luhmann,A. Sinning, *Comparison of spike parameters from optically identified GABAergic and glutamatergic neurons in sparse cortical cultures* Frontiers in cellular neuroscience **2015**, *8*.
[270] Atherton, J.F., D.L. Wokosin, S. Ramanathan,M.D. Bevan, *Autonomous initiation and propagation of action potentials in neurons of the subthalamic nucleus* The Journal of Physiology **2008**, *586*.
[271] Meeks, J.P., X. Jiang,S. Mennerick, *Action potential fidelity during normal and epileptiform activity in paired soma–axon recordings from rat hippocampus* The Journal of Physiology **2005**, *566*.

[272] Teagarden, M., J.F. Atherton, M.D. Bevan,C.J. Wilson, *Accumulation of cytoplasmic calcium, but not apamin-sensitive afterhyperpolarization current, during high frequency firing in rat subthalamic nucleus cells* The Journal of Physiology **2008**, *586*.
[273] Berens, P., G. Keliris, A. Ecker, N. Logothetis,A. Tolias, *Feature selectivity of the gamma-band of the local field potential in primate primary visual cortex* Frontiers in Neuroscience **2008**, *2*.
[274] Abbott, J., T. Ye, K. Krenek, R.S. Gertner, S. Ban, Y. Kim, L. Qin, W. Wu, H. Park,D. Ham, *A nanoelectrode array for obtaining intracellular recordings from thousands of connected neurons* Nature Biomedical Engineering **2020**, *4*.
[275] Fromherz, P., *Three levels of neuroelectronic interfacing: silicon chips with ion channels, nerve cells, and brain tissue* Ann N Y Acad Sci **2006**, *1093*.
[276] Parnas, I., S. Hochstein,H. Parnas, *Theoretical analysis of parameters leading to frequency modulation along an inhomogeneous axon* Journal of Neurophysiology **1976**, *39*.
[277] Ling, T., K.C. Boyle, V. Zuckerman, T. Flores, C. Ramakrishnan, K. Deisseroth,D. Palanker, *High-speed interferometric imaging reveals dynamics of neuronal deformation during the action potential* Proceedings of the National Academy of Sciences **2020**, *117*.
[278] Nguyen, T.D., N. Deshmukh, J.M. Nagarah, T. Kramer, P.K. Purohit, M.J. Berry,M.C. McAlpine, *Piezoelectric nanoribbons for monitoring cellular deformations* Nature Nanotechnology **2012**, *7*.
[279] Fabiunke, S., C. Fillafer, A. Paeger,M.F. Schneider, *Optical studies of membrane state during action potential propagation* Progress in Biophysics and Molecular Biology **2021**, *162*.
[280] Alijevic, O., Z. Peng,S. Kellenberger, *Changes in H+, K+, and Ca2+ Concentrations, as Observed in Seizures, Induce Action Potential Signaling in Cortical Neurons by a Mechanism That Depends Partially on Acid-Sensing Ion Channels* Frontiers in Cellular Neuroscience **2021**, *15*.
[281] Barreto, E.,J.R. Cressman, *Ion concentration dynamics as a mechanism for neuronal bursting* Journal of Biological Physics **2011**, *37*.
[282] Clark, B.,M. Häusser, *Neural Coding: Hybrid Analog and Digital Signalling in Axons* Current Biology **2006**, *16*.
[283] Xu, G., R. Tianhe, Y. Chen,W. Che, *A One-Dimensional CNN-LSTM Model for Epileptic Seizure Recognition Using EEG Signal Analysis* Frontiers in Neuroscience **2020**, *14*.
[284] Jayant, K., J.J. Hirtz, I.J.-L. Plante, D.M. Tsai, W.D.A.M. De Boer, A. Semonche, D.S. Peterka, J.S. Owen, O. Sahin, K.L. Shepard,R. Yuste, *Targeted intracellular voltage recordings from dendritic spines using quantum-dot-coated nanopipettes* Nature Nanotechnology **2017**, *12*.
[285] Dipalo, M., H. Amin, L. Lovato, F. Moia, V. Caprettini, G. Messina, F. Tantussi, L. Berdondini,F. De angelis, *Intracellular and Extracellular Recording of Spontaneous Action Potentials in Mammalian Neurons and Cardiac Cells with 3D Plasmonic Nanoelectrodes* Nano letters **2017**, *17*.
[286] Nevian, T., M.E. Larkum, A. Polsky,J. Schiller, *Properties of basal dendrites of layer 5 pyramidal neurons: a direct patch-clamp recording study* Nature Neuroscience **2007**, *10*.
[287] Izhikevich, E.M., *Simple model of spiking neurons* IEEE Transactions on neural networks **2003**, *14*.
[288] Stimberg, M., R. Brette,D.F.M. Goodman, *Brian 2, an intuitive and efficient neural simulator* eLife **2019**, *8*.
[289] Eggermont, J., *Pair-Correlation in the Time and Frequency Domain*. 2010. p. 77-102.
[290] Denker, M., Köhler, Cristiano, Jurkus, Regimantas, Kramer, Maximilian, Kern, Moritz, Kurth, Anno Christopher, & Ito, Junji, *Elephant 0.12.0 (v0.12.0).* 2023: Zenodo.
[291] Leva, F., C. Verardo, P. Palestri,L. Selmi, *From Finite Element Simulations to Equivalent Circuit Models of Extracellular Neuronal Recording Systems based on Planar and Mushroom Electrodes*. 2023.
[292] Larkman, A.U., *Dendritic morphology of pyramidal neurones of the visual cortex of the rat: I. Branching patterns* Journal of Comparative Neurology **1991**, *306*.
[293] Gold, C., *Biophysics of extracellular action potentials*. 2007, California Institute of Technology.
[294] Jahed, Z., Y. Yang, C.-T. Tsai, E.P. Foster, A.F. McGuire, H. Yang, A. Liu, C. Forro, Z. Yan, X. Jiang, M.-T. Zhao, W. Zhang, X. Li, T. Li, A. Pawlosky, J.C. Wu,B. Cui, *Nanocrown electrodes for parallel and robust intracellular recording of cardiomyocytes* Nature Communications **2022**, *13*.
[295] Rusakov, D.A., L.P. Savtchenko,P.E. Latham, *Noisy synaptic conductance: bug or a feature?* Trends in Neurosciences **2020**, *43*.
[296] Liu, J., F. Li, Y. Wang, L. Pan, P. Lin, B. Zhang, Y. Zheng, Y. Xu, H. Liao, G. Ko, F. Fei, C. Xu, Y. Du, K. Shin, D. Kim, S.-S. Jang, H.J. Chung, H. Tian, Q. Wang, W. Guo, J.-M. Nam, Z. Chen, T. Hyeon,D. Ling, *A sensitive and*

*specific nanosensor for monitoring extracellular potassium levels in the brain* Nature Nanotechnology **2020**, *15*.

[297] Gopal, S., C. Chiappini, J. Penders, V. Leonardo, H. Seong, S. Rothery, Y. Korchev, A. Shevchuk,M.M. Stevens, *Porous Silicon Nanoneedles Modulate Endocytosis to Deliver Biological Payloads* Adv Mater **2019**, *31*.

[298] Lou, H.-Y., W. Zhao, X. Li, L. Duan, A. Powers, M. Akamatsu, F. Santoro, A.F. McGuire, Y. Cui, D.G. Drubin,B. Cui, *Membrane curvature underlies actin reorganization in response to nanoscale surface topography* Proceedings of the National Academy of Sciences **2019**, *116*.

[299] Yao, C.-K., Y.-T. Liu, I.C. Lee, Y.-T. Wang,P.-Y. Wu, *A Ca2+ channel differentially regulates Clathrin-mediated and activity-dependent bulk endocytosis* PLOS Biology **2017**, *15*.

[300] Octeau, J.C., M.R. Gangwani, S.L. Allam, D. Tran, S. Huang, T.M. Hoang-Trong, P. Golshani, T.H. Rumbell, J.R. Kozloski,B.S. Khakh, *Transient, Consequential Increases in Extracellular Potassium Ions Accompany Channelrhodopsin2 Excitation* Cell Reports **2019**, *27*.

[301] Ross, W.N., *Understanding calcium waves and sparks in central neurons* Nature Reviews Neuroscience **2012**, *13*.

[302] Tihaa, I., *Engineering neuronal networks in vitro: From single cells to population connectivity*. 2021, RWTH Aachen: Forschungszentrum Jülich GmbH Zentralbibliothek, Verlag. p. 242.

[303] Chen, T.W., T.J. Wardill, Y. Sun, S.R. Pulver, S.L. Renninger, A. Baohan, E.R. Schreiter, R.A. Kerr, M.B. Orger, V. Jayaraman, L.L. Looger, K. Svoboda,D.S. Kim, *Ultrasensitive fluorescent proteins for imaging neuronal activity* Nature **2013**, *499*.

[304] Schoenfeld, G., S. Carta, P. Rupprecht, A. Ayaz,F. Helmchen, *In Vivo Calcium Imaging of CA3 Pyramidal Neuron Populations in Adult Mouse Hippocampus* eneuro **2021**, *8*.

[305] Michalikova, M., M.W.H. Remme, D. Schmitz, S. Schreiber,R. Kempter, *Spikelets in pyramidal neurons: generating mechanisms, distinguishing properties, and functional implications* Reviews in the Neurosciences **2020**, *31*.

[306] Emery, E.C., A.P. Luiz, S. Sikandar, R. Magnúsdóttir, X. Dong,J.N. Wood, *In vivo characterization of distinct modality-specific subsets of somatosensory neurons using GCaMP* Science Advances, *2*.

[307] Sheffield, M.E., T.K. Best, B.D. Mensh, W.L. Kath,N. Spruston, *Slow integration leads to persistent action potential firing in distal axons of coupled interneurons* Nat Neurosci **2011**, *14*.

[308] Mukamel, E.A., A. Nimmerjahn,M.J. Schnitzer, *Automated analysis of cellular signals from large-scale calcium imaging data* Neuron **2009**, *63*.

[309] Sokolov, R.A.,I.V. Mukhina, *Spontaneous Ca2+ events are linked to the development of neuronal firing during maturation in mice primary hippocampal culture cells* Archives of Biochemistry and Biophysics **2022**, *727*.

[310] Ryglewski, S., H.J. Pflueger,C. Duch, *Expanding the Neuron's Calcium Signaling Repertoire: Intracellular Calcium Release via Voltage-Induced PLC and IP3R Activation* PLOS Biology **2007**, *5*.

[311] Tonini, R., T. Ferraro, M. Sampedro-Castañeda, A. Cavaccini, M. Stocker, C.D. Richards,P. Pedarzani, *Small-conductance Ca2+-activated K+ channels modulate action potential-induced Ca2+ transients in hippocampal neurons* Journal of Neurophysiology **2013**, *109*.

[312] Jonas, R., V. Prato, S.G. Lechner, G. Groen, O. Obreja, F. Werland, R. Rukwied, A. Klusch, M. Petersen, R.W. Carr,M. Schmelz, *TTX-Resistant Sodium Channels Functionally Separate Silent From Polymodal C-nociceptors* Frontiers in Cellular Neuroscience **2020**, *14*.

[313] Erika, K.H., B. Bruno,W.S. Michael, *Intracellular Calcium Responses Encode Action Potential Firing in Spinal Cord Lamina I Neurons* The Journal of Neuroscience **2020**, *40*.

[314] Eichler, M., R. Dahlhaus,J. Sandkühler, *Partial correlation analysis for the identification of synaptic connections* Biological Cybernetics **2003**, *89*.

[315] Rezayat, E.,I.G. Toostani, *A Review on Brain Stimulation Using Low Intensity Focused Ultrasound* Basic Clin Neurosci **2016**, *7*.

[316] Richardson, J., A. Kotevski,K. Poole, *From stretch to deflection: the importance of context in the activation of mammalian, mechanically activated ion channels* The FEBS Journal **2022**, *289*.

[317] D'Hondt, C., B. Himpens,G. Bultynck, *Mechanical stimulation-induced calcium wave propagation in cell monolayers: the example of bovine corneal endothelial cells* J Vis Exp **2013**.

[318] Moerenhout, M., J. Vereecke,B. Himpens, *Mechanism of intracellular Ca2+-wave propagation elicited by mechanical stimulation in cultured endothelial CPAE cells* Cell Calcium **2001**, *29*.
[319] Venance, L., N. Stella, J. Glowinski,C. Giaume, *Mechanism Involved in Initiation and Propagation of Receptor-Induced Intercellular Calcium Signaling in Cultured Rat Astrocytes* The Journal of Neuroscience **1997**, *17*.
[320] De-Miguel, F.F., C. Leon-Pinzon, S.G. Torres-Platas, V. del-Pozo, G.A. Hernández-Mendoza, D. Aguirre-Olivas, B. Méndez, S. Moore, C. Sánchez-Sugía, M.A. García-Aguilera, A. Martínez-Valencia, G. Ramírez-Santiago,J.M. Rubí, *Extrasynaptic Communication* Frontiers in Molecular Neuroscience **2021**, *14*.
[321] Bonifazi, P.,P. Massobrio, *Reconstruction of Functional Connectivity from Multielectrode Recordings and Calcium Imaging* Adv Neurobiol **2019**, *22*.
[322] Miller, L., J.J. Petrozzino, G. Golarai,J.A. Connor, *Ca2+ release from intracellular stores induced by afferent stimulation of CA3 pyramidal neurons in hippocampal slices* Journal of neurophysiology **1996**, *76*.
[323] Hagenston, A.M., J.S. Fitzpatrick,M.F. Yeckel, *MGluR-mediated calcium waves that invade the soma regulate firing in layer V medial prefrontal cortical pyramidal neurons* Cerebral cortex **2008**, *18*.
[324] Li, W.-C., S.R. Soffe,A. Roberts, *A Direct Comparison of Whole Cell Patch and Sharp Electrodes by Simultaneous Recording From Single Spinal Neurons in Frog Tadpoles* Journal of Neurophysiology **2004**, *92*.
[325] Tyler, W.J., *Noninvasive neuromodulation with ultrasound? A continuum mechanics hypothesis* The Neuroscientist **2011**, *17*.
[326] Strober, W., *Trypan Blue Exclusion Test of Cell Viability* Curr Protoc Immunol **2015**, *111*.
[327] Anastassiou, C.A., R. Perin, H. Markram,C. Koch, *Ephaptic coupling of cortical neurons* Nature Neuroscience **2011**, *14*.
[328] Sánchez, D., N. Johnson, C. Li, P. Novak, J. Rheinlaender, Y. Zhang, U. Anand, P. Anand, J. Gorelik, G.I. Frolenkov, C. Benham, M. Lab, V.P. Ostanin, T.E. Schäffer, D. Klenerman,Y.E. Korchev, *Noncontact measurement of the local mechanical properties of living cells using pressure applied via a pipette* Biophys J **2008**, *95*.
[329] Morris, C., *Voltage-Gated Channel Mechanosensitivity: Fact or Friction?* Frontiers in Physiology **2011**, *2*.
[330] Sukharev, S.,F. Sachs, *Molecular force transduction by ion channels – diversity and unifying principles* Journal of Cell Science **2012**, *125*.
[331] Ermakov, Y.A., K. Kamaraju, K. Sengupta,S. Sukharev, *Gadolinium ions block mechanosensitive channels by altering the packing and lateral pressure of anionic lipids* Biophys J **2010**, *98*.
[332] Suchyna, T.M., *Piezo channels and GsMTx4: Two milestones in our understanding of excitatory mechanosensitive channels and their role in pathology* Prog Biophys Mol Biol **2017**, *130*.
[333] Kim, T.J., C. Joo, J. Seong, R. Vafabakhsh, E.L. Botvinick, M.W. Berns, A.E. Palmer, N. Wang, T. Ha, E. Jakobsson, J. Sun,Y. Wang, *Distinct mechanisms regulating mechanical force-induced $Ca^{2+}$ signals at the plasma membrane and the ER in human MSCs* Elife **2015**, *4*.
[334] Wang, Y., J. Shi,X. Tong, *Cross-talk between mechanosensitive ion channels and calcium regulatory proteins in cardiovascular health and disease* International Journal of Molecular Sciences **2021**, *22*.
[335] Broussard, G.J., Y. Liang, M. Fridman, E.K. Unger, G. Meng, X. Xiao, N. Ji, L. Petreanu,L. Tian, *In vivo measurement of afferent activity with axon-specific calcium imaging* Nature Neuroscience **2018**, *21*.
[336] Yu, Y.-C., R.S. Bultje, X. Wang,S.-H. Shi, *Specific synapses develop preferentially among sister excitatory neurons in the neocortex* Nature **2009**, *458*.
[337] Vogt-Eisele, A., *Synaptic Connectivity in Micropatterned Networks of Neuronal Cells*. 2003, Johannes Gutenberg-Universität: Mainz.
[338] Furshpan, E.,D. Potter, *Mechanism of nerve-impulse transmission at a crayfish synapse* Nature **1957**, *180*.
[339] de Roos, A.D.G., E.J.J. van Zoelen,A.P.R. Theuvenet, *Determination of gap junctional intercellular communication by capacitance measurements* Pflügers Archiv **1996**, *431*.
[340] Bar-Yehuda, D.,A. Korngreen, *Space-Clamp Problems When Voltage Clamping Neurons Expressing Voltage-Gated Conductances* Journal of Neurophysiology **2008**, *99*.
[341] Ko, H., S.B. Hofer, B. Pichler, K.A. Buchanan, P.J. Sjöström,T.D. Mrsic-Flogel, *Functional specificity of local synaptic connections in neocortical networks* Nature **2011**, *473*.
[342] Qi, G., D. Yang, C. Ding,D. Feldmeyer, *Unveiling the Synaptic Function and Structure Using Paired Recordings From Synaptically Coupled Neurons* Frontiers in Synaptic Neuroscience **2020**, *12*.

[343] Rienecker, K.D., R.G. Poston,R.N. Saha, *Merits and limitations of studying neuronal depolarization-dependent processes using elevated external potassium* ASN neuro **2020**, *12*.
[344] Housley, G.D., A. Bringmann,A. Reichenbach, *Purinergic signaling in special senses* Trends in Neurosciences **2009**, *32*.
[345] Docherty, R.J., J.C. Yeats,A.S. Piper, *Capsazepine block of voltage-activated calcium channels in adult rat dorsal root ganglion neurones in culture* Br J Pharmacol **1997**, *121*.
[346] Sun, D., Z. Luo, Y. Kong, R. Huang,Q. Li, *Force-Regulated Calcium Signaling of Lymphoid Cell RPMI 8226 Mediated by Integrin α4β7/MAdCAM-1 in Flow* Biomolecules **2023**, *13*.
[347] Gui, P., X. Wu, S. Ling, S.C. Stotz, R.J. Winkfein, E. Wilson, G.E. Davis, A.P. Braun, G.W. Zamponi,M.J. Davis, *Integrin receptor activation triggers converging regulation of Cav1.2 calcium channels by c-Src and protein kinase A pathways* J Biol Chem **2006**, *281*.
[348] Li, F., T.H. Park, G. Sankin, C. Gilchrist, D. Liao, C.U. Chan, Z. Mao, B.D. Hoffman,P. Zhong, *Mechanically induced integrin ligation mediates intracellular calcium signaling with single pulsating cavitation bubbles* Theranostics **2021**, *11*.
[349] Hu, S.,N. Wang, *Control of stress propagation in the cytoplasm by prestress and loading frequency* Mol Cell Biomech **2006**, *3*.
[350] Kamranvar, S.A., D.K. Gupta, A. Wasberg, L. Liu, J. Roig,S. Johansson, *Integrin-Mediated Adhesion Promotes Centrosome Separation in Early Mitosis* Cells **2022**, *11*.
[351] Chang Chien, C.Y., S.H. Chou,H.H. Lee, *Integrin molecular tension required for focal adhesion maturation and YAP nuclear translocation* Biochem Biophys Rep **2022**, *31*.
[352] Wu, Y., C. Whiteus, C.S. Xu, K.J. Hayworth, R.J. Weinberg, H.F. Hess,P. De Camilli, *Contacts between the endoplasmic reticulum and other membranes in neurons* Proceedings of the National Academy of Sciences **2017**, *114*.
[353] Li, Z., K.-I. Okamoto, Y. Hayashi,M. Sheng, *The importance of dendritic mitochondria in the morphogenesis and plasticity of spines and synapses* Cell **2004**, *119*.
[354] Yalçın, B., L. Zhao, M. Stofanko, N.C. O'Sullivan, Z.H. Kang, A. Roost, M.R. Thomas, S. Zaessinger, O. Blard,A.L. Patto, *Modeling of axonal endoplasmic reticulum network by spastic paraplegia proteins* Elife **2017**, *6*.
[355] Smith, G.M.,G. Gallo, *The role of mitochondria in axon development and regeneration* Developmental neurobiology **2018**, *78*.
[356] Sargent, P.B., *What distinguishes axons from dendrites? Neurons know more than we do* Trends in Neurosciences **1989**, *12*.
[357] Sanes, J.R.,M. Yamagata, *Many Paths to Synaptic Specificity* Annual Review of Cell and Developmental Biology **2009**, *25*.
[358] Cruikshank, S.J., M. Hopperstad, M. Younger, B.W. Connors, D.C. Spray,M. Srinivas, *Potent block of Cx36 and Cx50 gap junction channels by mefloquine* Proceedings of the National Academy of Sciences **2004**, *101*.
[359] Seemann, N., A. Welling,I. Rustenbeck, *The inhibitor of connexin Cx36 channels, mefloquine, inhibits voltage-dependent Ca(2+) channels and insulin secretion* Mol Cell Endocrinol **2018**, *472*.
[360] el Manira, A., J. Tegnér,S. Grillner, *Calcium-dependent potassium channels play a critical role for burst termination in the locomotor network in lamprey* J Neurophysiol **1994**, *72*.
[361] Bagur, R.,G. Hajnóczky, *Intracellular Ca2+ Sensing: Its Role in Calcium Homeostasis and Signaling* Molecular Cell **2017**, *66*.
[362] Juhaszova, M., P. Church, M.P. Blaustein,E.F. Stanley, *Location of calcium transporters at presynaptic terminals* Eur J Neurosci **2000**, *12*.
[363] Lytton, J., M. Westlin, S.E. Burk, G.E. Shull,D.H. MacLennan, *Functional comparisons between isoforms of the sarcoplasmic or endoplasmic reticulum family of calcium pumps* J Biol Chem **1992**, *267*.
[364] Boyman, L., H. Mikhasenko, R. Hiller,D. Khananshvili, *Kinetic and Equilibrium Properties of Regulatory Calcium Sensors of NCX1 Protein** Journal of Biological Chemistry **2009**, *284*.
[365] Strata, F., M. Atzori, M. Molnar, G. Ugolini, F. Tempia,E. Cherubini, *A pacemaker current in dye-coupled hilar interneurons contributes to the generation of giant GABAergic potentials in developing hippocampus* Journal of Neuroscience **1997**, *17*.

[366] Sebastian, C., H. Gregory, I.N. James,E.P. Alberto, *Synergy between Electrical Coupling and Membrane Properties Promotes Strong Synchronization of Neurons of the Mesencephalic Trigeminal Nucleus* The Journal of Neuroscience **2012**, *32*.

[367] Barral, J.,A. D Reyes, *Synaptic scaling rule preserves excitatory–inhibitory balance and salient neuronal network dynamics* Nature Neuroscience **2016**, *19*.

[368] Rincón Montes, V., *Development, characterization, and application of intraretinal implants*. 2021, Bioelektronik.

[369] Keating, C.E.,D.K. Cullen, *Mechanosensation in traumatic brain injury* Neurobiol Dis **2021**, *148*.

[370] DeKosky, S.T.,B.M. Asken, *Injury cascades in TBI-related neurodegeneration* Brain injury **2017**, *31*.

[371] Perea, G., M. Navarrete,A. Araque, *Tripartite synapses: astrocytes process and control synaptic information* Trends in neurosciences **2009**, *32*.

[372] Abu Shihada, J., M. Jung, S. Decke, L. Koschinski, S. Musall, V. Rincón Montes,A. Offenhäusser, *Highly Customizable 3D Microelectrode Arrays for In Vitro and In Vivo Neuronal Tissue Recordings* Advanced Science **2024**, *11*.

[373] Pouzat, C., M. Delescluse, P. Viot,J. Diebolt, *Improved spike-sorting by modeling firing statistics and burst-dependent spike amplitude attenuation: a Markov chain Monte Carlo approach* J Neurophysiol **2004**, *91*.

[374] Zhang, Y., M. Rózsa, Y. Liang, D. Bushey, Z. Wei, J. Zheng, D. Reep, G.J. Broussard, A. Tsang, G. Tsegaye, S. Narayan, C.J. Obara, J.-X. Lim, R. Patel, R. Zhang, M.B. Ahrens, G.C. Turner, S.S.H. Wang, W.L. Korff, E.R. Schreiter, K. Svoboda, J.P. Hasseman, I. Kolb,L.L. Looger, *Fast and sensitive GCaMP calcium indicators for imaging neural populations* Nature **2023**, *615*.

**Eidesstattliche Erklärung**

**Declaration of Authorship**

I, Bogdana Cepkenovic,

declare that this thesis and the work presented in it are my own and has been generated by me as the result of my own original research.

Hiermit erkläre ich an Eides statt / I do solemnely swear that:

1. This work was done wholly or mainly while in candidature for the doctoral degree at this faculty and university;

2. Where any part of this thesis has previously been submitted for a degree or any other qualification at this university or any other institution, this has been clearly stated;

3. Where I have consulted the published work of others or myself, this is always clearly attributed;

4. Where I have quoted from the work of others or myself, the source is always given. This thesis is entirely my own work, with the exception of such quotations;

5. I have acknowledged all major sources of assistance;

6. Where the thesis is based on work done by myself jointly with others, I have made clear exactly what was done by others and what I have contributed myself;

7. Parts of this work have been published before as:

    - Shokoohimehr, P.#, Cepkenovic, B.#, Milos, F., Bednár, J., Hassani, H., Maybeck, V., Offenhäusser, A. High-Aspect-Ratio Nanoelectrodes Enable Long-Term Recordings of Neuronal Signals with Subthreshold Resolution. Small. (2022) DOI: https://doi.org/10.1002/smll.202200053 (#-equally contributed)

    - Bogdana Cepkenovic, Florian Friedland, Erik Noetzel, Vanessa Maybeck, Andreas Offenhäusser. Single-neuron mechanical perturbation evokes calcium plateaus that excite and modulate the network. Scientific Reports (2023). DOI: 10.1038/s41598-023-47090-z

    - Parts of this work are in preparation for publication as:
      Bogdana Cepkenovic, Vanessa Maybeck, Andreas Offenhäusser. Decoding Neuronal Firing Rates: Unraveling the Interplay Between Calcium Signals and Membrane Events